SYSTEM ANALYSIS OF A NUMERICAL PREDICTOR-CORRECTOR AEROCAPTURE GUIDANCE ARCHITECTURE

by

Rohan Deshmukh

A Dissertation

Submitted to the Faculty of Purdue University

In Partial Fulfillment of the Requirements for the degree of

Doctor of Philosophy

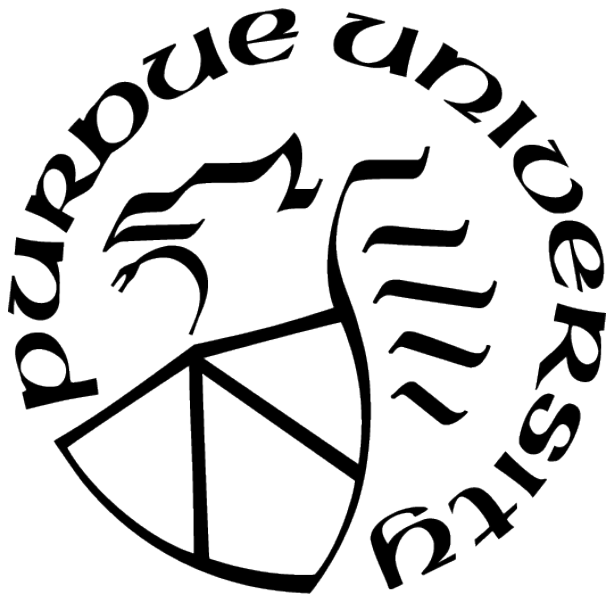

School of Aeronautics and Astronautics

West Lafayette, Indiana

May 2021

THE PURDUE UNIVERSITY GRADUATE SCHOOL
STATEMENT OF COMMITTEE APPROVAL

Dr. David A. Spencer, Chair

School of Aeronautics and Astronautics

Dr. James Longuski

School of Aeronautics and Astronautics

Dr. Michael Grant

School of Aeronautics and Astronautics

Dr. Soumyo Dutta

NASA Langley Research Center

Approved by:

Dr. Gregory Blaisdell

To my parents, Gajanan and Kavita. To my sister, Trisha.

"Rohan work hard, play often, and always follow your dream." - Astronaut Dr. Roger K. Crouch, Payload Specialist on STS-83 and STS-94

ACKNOWLEDGMENTS

I express my greatest gratitude to my advisor, Dr. David A. Spencer, for his dedicated mentorship and guidance over the past five years at Purdue University and three years beforehand at Georgia Institute of Technology. The numerous research projects, meetings, and discussions that I have had with him have immensely helped my growth as an aerospace engineer. I would also like to thank the members of the Space Flight Projects Laboratory, Dr. Sylvain Renevey, Dr. Justin Mansell, Jannuel Cabrera, Tom Cunningham, Arly Black, Samatha Dickmann, Dr. Jay Iuliano, Mitchell Dominguez, Juan Maldonado, Michael Thompson, Mayank Aggarwal, Mac Goggin, Ben Hilker, Brandon Smail, and Dr. Anthony Cofer for all of their collaboration, support, renaissance discussions, and friendship.

I would like to thank Purdue University and the School of Aeronautics and Astronautics for their financial support in the form of multiple teaching and research assistanships during my studies. Among the faculty, I would like to thank my committee members Dr. James Longuski and Dr. Michael Grant for both their truly memorable AAE 507/508/607 and AAE 590 classes as well as their suggestions and guidance regarding my work. I would also like to thank my mentor at NASA Dr. Soumyo Dutta for his invaluable discussion, guidance, and feedback on both my academic and professional work.

There are numerous people that I would like to thank that helped me with the completion of the dissertation as an abscentia student at NASA Langley Research Center. Firstly, I would like to express my sincere gratitude to branch chief Dr. Ron Merski for providing the encouragement and support for completion of the dissertation while beginning my professional career. I would also like to thank Dr. Chris Karlgaard and Jeremy Shidner of Analytical Mechanics Associates for their support. I would like to thank Alicia Cianciolo, Dick Powell, Dr. Rafael Lugo, Dr. Justin Green, and Michelle Munk for all of their technical guidance and feedback.

Lastly, this work could not have been completed with the unwavering support of my friends and family. Above all, I express my thanks to my parents and sister, Gajanan, Kavita, and Trisha, for nurturing my enthusiasm for space exploration and supporting me every step of the way in my academic and professional journey. To the countless friends I

have made from my childhood in Fairfax, undergrad at Georgia Tech, and graduate school at Purdue. Thank You.

TABLE OF CONTENTS

LIST OF TABLES

LIST OF FIGURES

ABBREVIATIONS

AC	aerocapture
BC	ballistic coefficient
BCR	ballistic coefficient ratio
BAM	bank angle modulation
DFC	direct force control
DM	drag modulation
DMCV	continuously-variable drag modulation
DMSJ	stagged-jettision drag modulation
EFPA	entry flight-path angle
FADS	flush air data system
GN&C	guidance, navigation, and control
IMU	inertial measurement unit
L/D	lift-to-drag ratio
MSL	Mars Science Laboratory
NASA	National Aeronautics and Space Administration
TPS	thermal protection system
3DOF	3 degrees of freedom
6DOF	6 degrees of freedom

ABSTRACT

Aerocapture has been envisioned as a potential orbit insertion technique for planetary destinations with an atmosphere. Despite not being flight proven technique, many studies found in the literature and recent mission proposals have employed aerocapture into their respective mission designs. The potential varying levels of trajectory dispersions experienced during atmospheric flight at each destination drives the need for robust and fuel-efficient guidance and control solutions. Existing guidance algorithms have relied on tracking precomputed reference trajectories, which are computed using significant simplifications to the flight mechanics, are not generally designed to be fuel-efficient, and require tedious performance gain tuning. When simulated with higher levels of uncertainty, the existing algorithms have been shown to produce large orbit insertion errors. Furthermore, existing flight control methodologies have been limited in scope to bank angle modulation. While some studies have introduced new methodologies, such as drag modulation and direct force control, they haven't been tested at the same level of rigor as the existing methods. Advances in on-board computational power are allowing for modern guidance and control solutions, in the form of numerical predictor-corrector algorithms, to be realized. This dissertation presents an aerocapture guidance architecture based on a numerical predictor-corrector algorithm. Optimal control theory is utilized to formulate and numerically obtain fuel-minimizing flight control laws for lifting and ballistic vehicles. The unified control laws are integrated into a common guidance algorithm. The architecture is utilized to conduct Monte Carlo simulation studies of Discovery-class and SmallSat-class aerocapture missions at various planetary destinations.

1. INTRODUCTION

This chapter surveys the concept of aerocapture from its historical conception to modern day definition. In particular, a overview of the current technology state of aerocapture guidance, navigation, and control is presented.

1.1 Aerocapture Overview

Aerocapture is a mission concept envisioned for orbit insertion about planetary bodies that have a substantial atmosphere. This concept offers the potential to reduce both propulsive orbit insertion costs and time-of-flight to orbit by utilizing the atmosphere for capturing an inbound hyperbolic trajectory. Like other aeroassist techniques including aerobraking and aerogravity assist, aerocapture utilizes the planetary atmosphere for orbital energy dissipation. During atmospheric flight, the spacecraft is actively guided to ensure sufficient energy is dissipated and the desired orbit plane is achieved once atmospheric exit is reached. After exiting the atmosphere, a series of propulsive burns are conducted to raise the orbit's periapsis out of the atmosphere, correct errors in orbit's apoapsis, and adjust the orbital plane (defined by either wedge angle[1] or inclination). Figure 1.1 provides a visualization of the aerocapture mission concept.

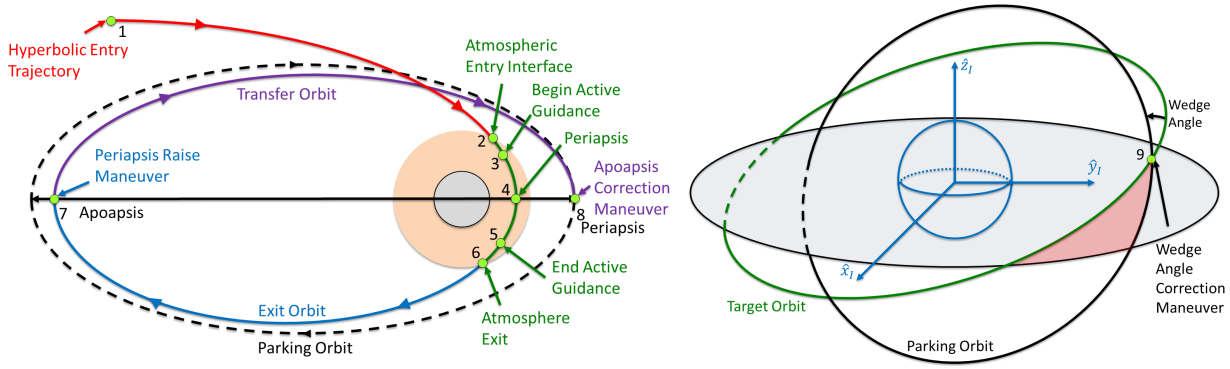

Figure 1.1. Aerocapture concept of operations

The historical development of aerocapture stems from research in aeroassisted orbital transfer. One of the earliest pioneering work was that of Howard London, who demonstrated

[1]↑Spherical angle between current orbit's and target orbit's angular momentum vectors

in his work the possibility of achieving orbital plane change at a lower cost than a fully propulsive maneuver by utilizing aerodynamic forces [1]. Much of the literature in aeroassist can be categorized into three categories: 1) inclination change maneuvers, 2) energy reduction maneuvers, and 3) planetary flyby applications [2]. Aerocapture falls under the second category. Following the successes of the Apollo program, the National Aeronautics and Space Administration (NASA) developed concepts for crewed missions to Mars. Aerocapture, not to be confused with aerobraking in the early literature, was studied as a potentially enabling orbit insertion technique. One such study assessed and demonstrated the feasibility of Martian aerocapture using an Apollo-based vehicle [3]. Other studies conducted investigation utilizing high lift-to-drag (L/D) vehicles and discovered significant improvement in the delivery corridor width can be achieved [4], [5]. At the time, the overwhelming consensus was that aerocapture can significantly reduce the propellant mass needed for orbit insertion both at Mars and at other planetary destinations. In the mission design of the 2001 Mars Orbiter, aerocapture was initially selected as the planned orbit insertion mode. However, the failures of the Mars Climate Orbiter and Mars Polar Lander in 1999 derailed any further flight implementation of aerocapture. Since then, a more conservative risk-based approach has been taken by NASA regarding missions that employ atmospheric flight. Once propulsively captured into orbit, aerobraking has been successfully demonstrated at both Venus and Mars for lowering orbit apogee by a handful of orbiters [6]. Some studies have shown using a probabilistic risk assessment that aerocapture can have lower computed risk posture than aerobraking [7]. In order to produce larger amounts of ΔV, aerocapture trajectories need to descend deeper into the atmosphere as compared to aerobraking trajectories. Fortunately, atmospheric probes deployed at Venus, Mars, Jupiter, and Titan have allowed for a better understanding of the planetary atmospheres over a wide range of altitudes. Additionally, orbital flybys of Venus, Mars, Jupiter, Saturn, Titan, Uranus, and Neptune have also provided valuable science data regarding the chemical composition of these atmosphere. In all, each source of data has allowed for improvements in the knowledge of planetary atmosphere and in turn has helped to reduce the potential risk posture posed by aerocapture.

From these improvement in 2004, NASA conducted a thorough systems engineering analysis of aerocapture at Venus [8], Mars [9], Titan [10], and Neptune [11].The overall goals of

these design reference mission (DRM) studies was to develop baseline mission concepts, assess the feasibility and reliability of aerocapture, and identify areas of technological improvement given the current state at the time. Table 1.1 provides a comparison between the mission designs for each planetary destination. With regards to the orbit insertion performance capability at each destination, these studies serve as the current state-of-the-art and will be subsequently referred to in later sections of this dissertation.

Table 1.1. Comparison of 2004 NASA aerocapture studies

	Venus	**Mars**	**Titan**	**Neptune**
Target Orbit Altitude (km x km)	300 x 300	500 x 500	1700 x 1700	3986 x 430,000
Target Orbit Inclination (deg)	90	45	100	153
Vehicle	Satellite	Sample return vehicle	Satellite	Satellite
Entry Velocity (km/s)	11.25	7.15	6.5	29
L/D	0.25	0.25	0.25	0.8
Ballistic Coefficient (kg/m^2)	138	365	90	895
Entry Mass (kg)	1088	8279	1026	1834
Payload/Entry Mass Fraction	72.5%	85.6%	58.5%	51.7%
Aeroshell Geometry	70° Sphere-Cone	70° Sphere-Cone	70° Sphere-Cone	Flat Bottom Ellipsled
GN&C Algorithm	HYPAS	HYPAS	HYPAS	HYPAS
Theoretical Corridor Width (deg)	1.55	2.42	3.5	2.27
Enhancing Technologies	Guidance algorithm	TPS	Guidance algorithm	None
Strongly Enhancing Technologies	TPS	None	TPS Atmosphere Modeling	Guidance and Control algorithm Alpha modulation Atmosphere Modeling
Enabling Technologies	None	None	None	TPS

At each destination, aerocapture was shown to be feasible and robust with the given mission design. For Venus, Mars, and Titan, the NASA studies concluded that heritage blunt-body sphere-cone aeroshells provide the sufficient control ability. For Neptune, a higher L/D aeroshell via a slender body ellipsled was determined to be needed. The technological areas of further investment are categorized as either enhancing, strongly enhancing, or enabling. Thermal Protection System (TPS) is shown to be enhancing for Mars, strongly enhancing for Venus, and enabling for Neptune. Since 2004, numerous landers at both Mars and Titan and recent advancements in TPS technology may make these finding outdated. Due to the much higher aerodynamic heating environments at both Venus and Neptune, investments in high-performance TPS materials are warranted. With regards to atmospheric modeling, the data provided by the Cassini orbiter and Huygens probe since the 2004 studies can serve to significantly improve the atmospheric knowledge of Titan thereby potentially enhancing aerocapture performance. Due to the only flight data source from the 1979 flyby of Neptune, the atmospheric knowledge of Neptune is limited. With regards to guidance and control, the current methods are generally sufficient for each destination with some destination po-

tentially achieving enhanced performance with further improvements. More details on this specific technology area are explained in the subsequent sections.

Additional complementary studies were conducted to further quantify the benefit of aerocapture for orbit insertion at other planetary destinations and target orbits as compared to alternatives [12]. The results from the study indicate that mission sets of low circular orbit insertion at Jupiter inside the rings and radiation belt (differing from Galileo's highly elliptical orbit insertion), high circular orbit insertion at Saturn for ring observations (differing from Cassini highly elliptical orbit insertion), elliptical orbit insertion at Uranus for Titania flybys, and elliptical orbit insertion at Neptune for Triton flybys, cannot be accomplished in a cost-effective manner without utilizing aerocapture while missions sets at Venus, Mars, and Titan can be enhanced by aerocapture through generous increase in payload delivered to orbit for the same launch vehicle. In 2016, a panel of aerocapture technologists conducted a technical assessment of the current state of aerocapture [13]. The objectives of the assessments included identifying the key technology areas needed for future aerocapture orbital missions and determining if a technology demonstration mission is needed. Many key finding were produced from the study and can be found in [14]. A portion of the findings relevant to this dissertation are listed as follows. Firstly, no precursor technology demonstration mission is needed to flight prove aerocapture as the current technology state is ready for flight implementation at Venus, Mars, and Titan. For Uranus and Neptune, further technological development in the field of advanced guidance and control methods is needed. Secondly, trade studies and DRM updates are needed in advance of flight implementation. Such trade studies may investigate the range of potential aeroshell configurations and flight control techniques to help better define technological requirements. Thirdly, determining whether techniques beyond heritage hypersonic guidance and control are needed would be a beneficial risk-mitigation activity.

1.2 State-of-the-Art Overview

The risk and reliability of planetary aerocapture is heavily driven by technology. One of these technology areas is guidance, navigation, and control (GN&C). Aerocapture consists of sequence of events that are heavily linked with GN&C [15]. On hyperbolic approach, the vehicle is guided to a desired atmospheric interface point, which is defined at the location when the vehicle enters the atmosphere. The delivery accuracy to this point is influenced by the deep space navigation utilized in determining the final trajectory correction maneuver burn before atmospheric flight begins. Once within the sensed atmosphere, the vehicle guidance actively steers the vehicle by modulating the flight control surfaces such that atmospheric exit is reached on the desired trajectory. To account for unforeseeable atmospheric perturbations, the vehicle's strapdown navigation system senses the vehicle's acceleration and subsequently determines the appropriate corrections to the onboard trajectory model. Upon exiting the atmosphere, propulsive correction burns are conducted to raise periapsis out of the atmosphere and correct for any remaining trajectory targeting errors. This state-of-the-art assessment will primarily address the atmospheric flight phase of aerocapture.

1.2.1 Navigation Methods

Aerocapture navigation consists of the set of instruments that provide in-situ measurements of the vehicle's state, position, and velocity. The navigation can be broken up into two phases, approach navigation and in-flight navigation.

Approach Navigation

Approach navigation pertains to vehicle orbital determination that occurs before atmospheric interface while in the central body's sphere-of-influence. The vehicle travels on a hyperbolic approach trajectory that targets atmospheric entry at the interface point, commonly defined by a vector in the B-plane [16]. Figure 1.2 provides an example graphical representation of the B-plane targeting for a Titan aerocapture trajectory.

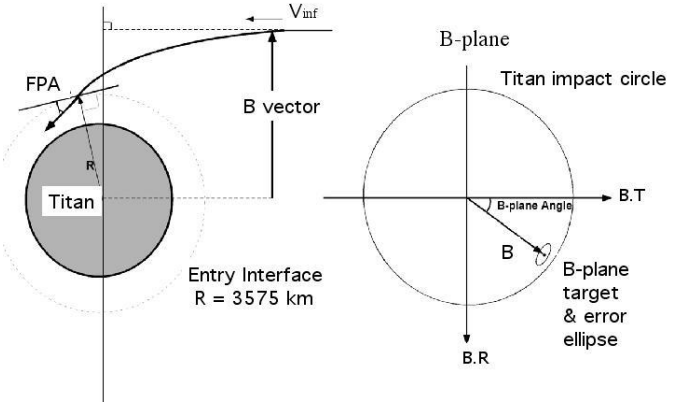

Figure 1.2. Sample B-Plane targeting visual. Image taken from Reference [16]

Trajectory correction maneuvers are conducted prior to the interface point. Using Earth-based radiometric and/or in-orbit optical data, estimates of the vehicle's position and velocity can be obtained. The combination of orbit determination and maneuver execution errors define the delivery errors at entry interface. Figure 1.3 provides a sample of such delivery errors mapped to the entry interface for entry flight path angle (EFPA) and inertial entry velocity.

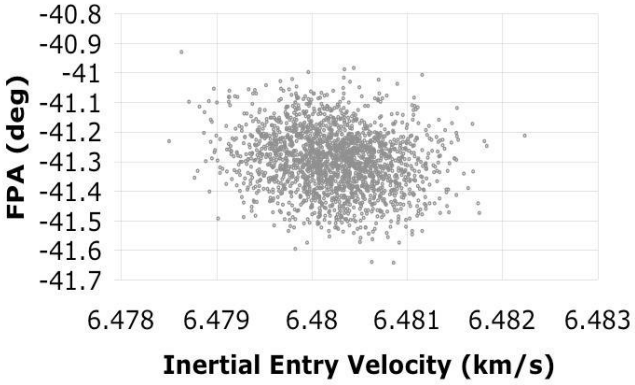

Figure 1.3. Sample entry state dispersion distribution for Titan. Image taken from Reference [16]

The resulting delivery errors can significantly impact the subsequent aerocapture trajectory. The impact of the errors are typically assessed using dispersions in Monte Carlo simulations. In particular, the impact of EFPA errors is commonly studied in aerocapture

and EDL literature since it generally has the largest variance and effect on the entry trajectory. Table 1.2 provides a comparison between EDL and aerocapture entry flight path angle errors found in the literature.

Table 1.2. Comparison of entry flight path angle delivery accuracy

	Mission	Entry Radius/Altitude	Nominal EFPA	3σ Error	Source
EDL	Pathfinder	3522.2 km	-14.2°	±1°	[17]
	Phoenix	3522.2 km	-13°	±0.2°	[18]
	MER	3522.2 km	-11.5°	±0.2°	[19]
	MSL	3522.2 km	-15.2°	±0.11°	[20]
	InSight	3522.2 km	-12°	±0.21°	[21]
	Galileo	450 km*	-8.6°	±0.6°	[22]
	Cassini/Huygens	4174.58 km	-63°	±3.0°	[23]
Aerocapture	Venus	6201.8 km	-6.12°	±0.4°	[8]
	Mars	3522.2 km	-12.731°	±0.35°	[9]
	Titan	3574.7 km	-36.03°	±0.6°	[10]
	Neptune	1000 km*	-12.818°	±0.51°	[11]

* Altitude defined relative to 1 bar atmospheric pressure

Many times, the delivery accuracy requirements are formulated as a function of EFPA. From the statistical distribution of EFPA, the $\pm 3\sigma$ variation about the nominal value is reported. The aerocapture vehicle should be designed with sufficient control authority to mitigate this delivery error. As a first-order metric, the vehicle's theoretical entry flight path angle corridor width is computed and compared against the delivery error. The corridor width is defined by range of flight path angles about the nominal that allows for the target apoapsis altitude to be reached given the vehicle's control capability. Figure 1.4 provides a sample corridor width contours computed for a Neptune aerocapture mission set for differing vehicle L/D and entry velocities. As an example, given a delivery error spread of 1.02° found in Table 1.2, the contours in Figure 1.4 might suggest that low entry velocities with vehicles with low L/D may not have enough control capability to overcome the anticipated delivery dispersion.

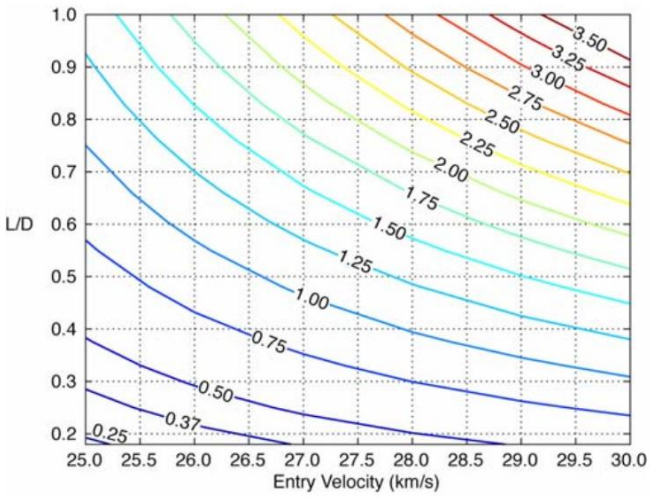

Figure 1.4. Sample entry flight path angle corridor width contours (in degrees). Image taken from Reference [24]

In-Flight Navigation

In-flight navigation pertains to estimates of the vehicle's state throughout the aerocapture sequence. A strapdown inertial measurement unit (IMU) can provide measurements of the vehicle's sensed translational and rotational accelerations. Integration of these measurements can provide estimates for the vehicle's attitude, position, and velocity along the aerocapture trajectory. Furthermore, the addition of measurements from flush air data systems (FADS), (e.g. pressure ports that measure the aeroshell pressure distribution during flight), allows for on-board atmospheric estimates to be conducted and be utilized in on-board trajectory model updates [25]. Effectively, the in-flight navigation system provides the closed-loop feedback to the guidance algorithm. Feedback errors are driven by measurement error. Because of the need for sensor specifications, most aerocapture guidance studies have assumed perfect state knowledge for simulating in-flight navigation.

1.2.2 Flight Control Methods

Aerocapture flight control consists of the actuators that influence the vehicle's motion during atmospheric flight. This is accomplished by influencing the aerodynamic forces generated by the vehicle, which include lift, $\vec{L}$, drag, $\vec{D}$, and side-force, $\vec{Q}$, as shown in Figure 1.5.

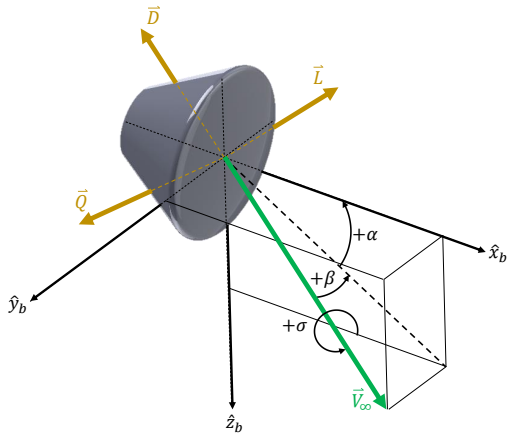

Figure 1.5. Aerodynamic forces produced during aerocapture

The different types of flight control can be classified as either lifting or ballistic flight control. In lifting flight control, the vehicle's lift vector is utilized to influence the motion of the vehicle. This can be achieved through rotation of the vector or direct control over its magnitude. Lifting flight control can also control the lateral motion of the vehicle. This can be accomplished by inducing a lateral component of the lift vector through rotation or by generating aerodynamic side-force. The two types of lifting flight control studied in literature include bank angle modulation and direct force control. In ballistic flight control, the vehicle's drag vector is primarily used to control the orbital energy (e.g. periapsis and apoapsis altitudes). This is primarily achieved through control over the vehicle's ballistic coefficient. The two types of ballistic flight control studied in literature include staged jettison drag modulation and continuously-variable drag modulation.

Bank Angle Modulation

Bank angle modulation (BAM) utilizes bank angle, σ, as the primary flight control. As shown in Figure 1.5, σ is the clock angle of rotation of the lift vector about the free-stream velocity vector, $\vec{V}_\infty$. Full lift vector up orientation arises at 0° (12 o'clock) while full lift vector down orientation arises at 180° (6 o'clock). The rotation of the lift vector about these two orientations allows for lateral motion about the velocity vector to be induced. For aerocapture, BAM generates coupled downrange and crossrange motion where downrange motion is utilized for handling the orbital energy while crossrange motion is utilized for handling the orbit plane. The BAM aerocapture concept of operations is shown in Figure 1.6.

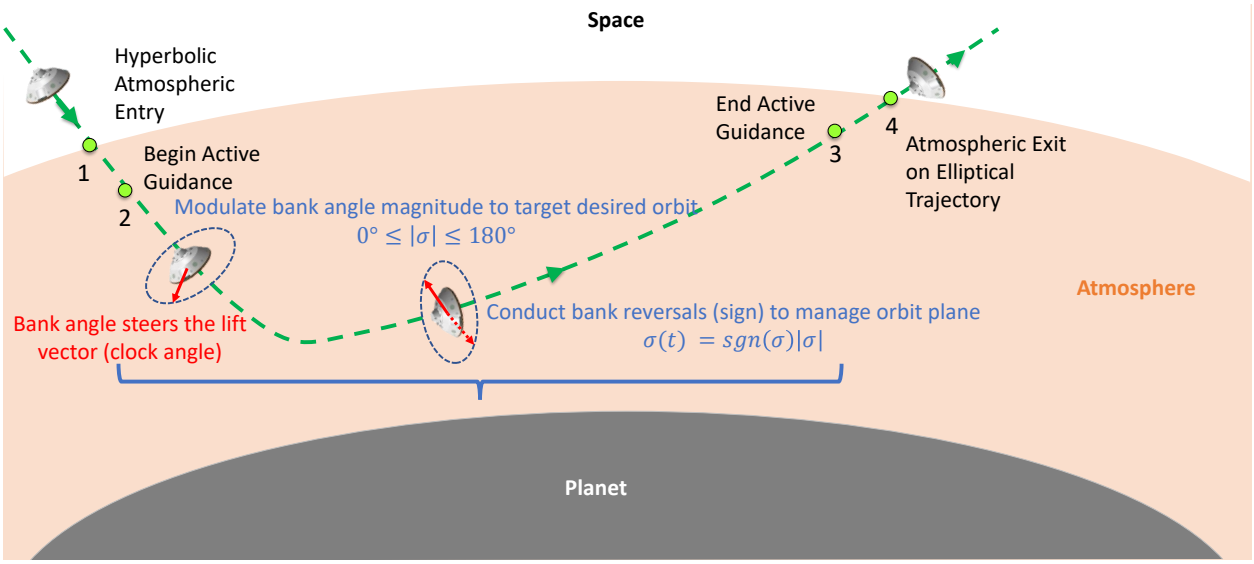

Figure 1.6. Bank angle modulated aerocapture concept of operations

The guidance determines both the magnitude, $|\sigma|$, of the bank angle based upon achieving the desired orbital energy and its corresponding sign, $sgn(\sigma)$, for management of the orbit plane. Commonly, the sign is computed from separate tuned lateral logic module in the guidance algorithm.

Because of the dependence on the lift vector, BAM can only be applied to a lifting-body. Typically, the vehicle is configured at a constant non-zero L/D by trimming the angle of attack. The L/D and the imposed clock-angle limits on σ determine aero-maneuverability of the vehicle. In EDL and aeroassist literature, BAM is the most commonly studied flight

control. In addition, BAM has been implemented in numerous EDL missions. Portions of the Apollo entry guidance were formulated utilizing bank angle as the steering mechanism [26]. Mars Science Laboratory (MSL) utilized bank angle commands for compensating trajectory dispersions during hypersonic entry at Mars [27]. The Mars 2020 mission utilized a MSL-derived bank angle guidance [21].

Direct Force Control

Direct force control (DFC) is a proposed and promising flight control methodology. It utilizes the combination of angle of attack, α, and side-slip angle, β, as the primary flight controls. This independent aerodynamic angle modulation can be accomplished propulsively using thrusters, aerodynamically using flaps or other external actuators, or mechanically using center of gravity offsets. As shown in Figure 1.5, α and β orient the free-stream velocity vector with respect to the vehicle's principal body axes. This enables full decomposition of horizontal, side, and vertical motion with respect to these axes. The concept of operation of DFC aerocapture is shown in Figure 1.7.

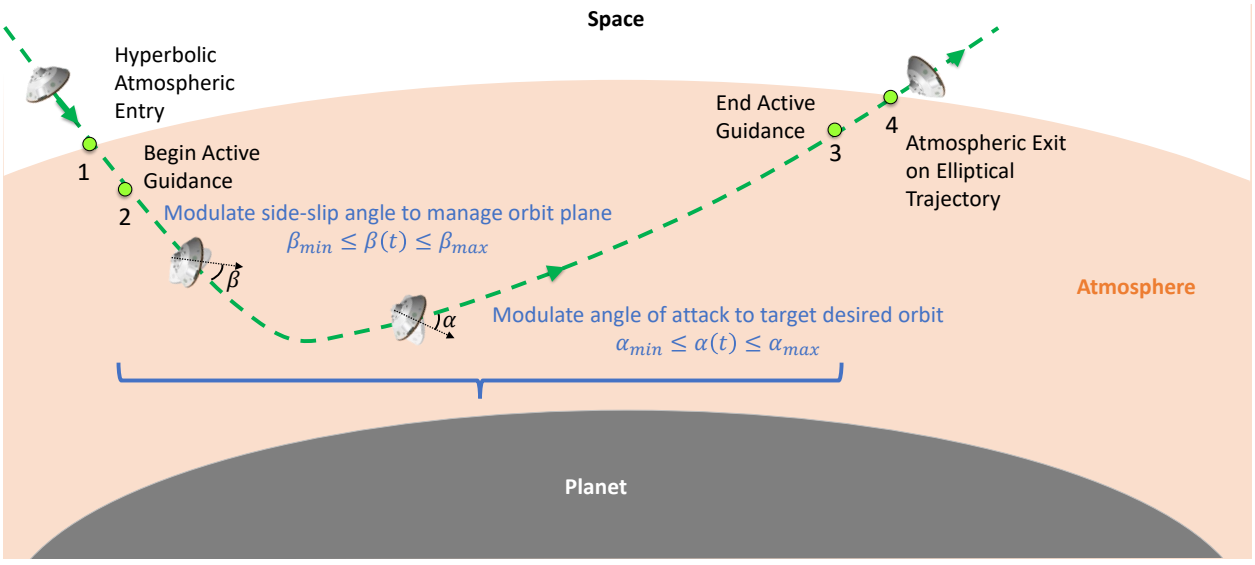

Figure 1.7. Direct force control aerocapture concept of operations

For aerocapture, DFC decouples the downrange and crossrange motion. Angle of attack is utilized for handling the orbital energy while side-slip angle is utilized for handling the orbit

plane. Like BAM, DFC is primarily applicable to lifting bodies. However, the modulation of angle of attack enables DFC higher control authority over the vehicle's L/D. The overall performance of DFC is linked to the vehicle's aerodynamics and control actuator limits on α and β.

Despite the potential benefits of an decoupled flight control strategy, there is limited literature on DFC for aerocapture applications. Some early studies investigated hybrid bank and angle of attack flight control. In this configuration, angle of attack is utilized to modify the vehicle's L/D and bank angle provides the crossrange motion. Angle of attack modulation was integrated into the U.S. Space Shuttle bank-based re-entry guidance for aeroheating regulation and short-period trajectory reference tracking [28]. Lafleur et al., demonstrated the potential benefit of adding angle of attack modulation to an existing Mars bank angle entry-to-terminal state guidance for achieving maximum altitude at a given termination Mach number [29]. Jits et al., demonstrated the validity of a blended angle of attack and bank angle aerocapture flight control methodology for Mars aerocapture [30] and thermal protection system design for Neptune aerocapture [31]. Starr et al., discovered reduced aerocapture risk and propellant consumption associated with the introduction of small angle of attack modulation capability to existing Neptune bank angle guidance [32]. In these studies, it was discovered that performance gains can be achieved through introduction of angle of attack modulation. More recently, DFC has seen some developments in EDL and aerocapture applications. Cianciolo et al, investigated the application of DFC for precision-landing of Mars human-class payloads and demonstrated reductions in the landing ellipse error can be achieved [33]. Matz et al., developed DFC flight control laws for application on Mars aerocapture mission sets [34]. Deshmukh et al., demonstrated that DFC can enable Neptune aerocapture using blunt body aeroshells [35].

Achieving control over angle of attack and side-slip angle have also been considered in the literature. Korzun et. al, investigated the effectiveness of mechanically-deployed trim tabs on blunt bodies for controlling the hypersonic angle of attack during flight [36]. This trim tab design was considered for implementation on MSL during EDL [37]. The recent Pterodactyl project at NASA aims at augmenting the current capability of the Adaptive Deployable Entry and Placement Technology (ADEPT) vehicle platform to achieve DFC

flight control. The project investigated the mechanical design trade space between achieving DFC flight control with either flaps, center of mass offsets, or RCS thrusters [38]. The study concluded that flaps and RCS thrusters provide promising control system capability without much compromise to vehicle mass [39]. The Hypersonic Inflatable Aerodynamic Decelerator (HIAD) vehicle platform has also seen recent analysis on achieving DFC flight control. As part of the Mars Entry, Descent, and Landing Architecture Study, DFC flight control using aerodynamic flap and morphing shape designs was shown to be mechanically feasible [40].

Drag Modulation

Drag Modulation (DM) is a recently studied flight control stratergy for aerocapture. The principal performance metric of DM is the vehicle's ballistic coefficient, BC, which is defined in Equation (1.1) where m is the vehicle mass, C_D is the vehicle coefficient of drag, and A_{ref} is the vehicle aerodynamic reference area. Ballistic coefficient is commonly defined as the ratio of the inertial to drag forces.

$$BC = \frac{m}{C_D A_{ref}} \tag{1.1}$$

An increase in BC implies either an increase in the influence of the inertial forces or a decrease in the influence of the drag forces. The converse holds for a decrease in BC. In particular, the drag force influences the rate of orbital energy depletion via the velocity vector during atmospheric flight. Assuming no mass change, BC can be controlled though changes in C_D and/or A_{ref} to allow for control over the downrange performance of the trajectory. Consequently, DM on its own cannot actively orient the aerodynamic force vectors to regulate crossrange motion. Despite the potential limitation in aero-maneuverability, the potential simplicity of DM allows for application on non-lifting vehicles. Aerobraking orbiters at Venus and Mars utilized a form of DM via solar panels during atmospheric flight for reducing their apoapsis altitudes. With regards to aerocapture applications, DM can be potentially utilized to augment the aeroshell geometry utilized during flight. Recent flight tests of HIAD [41] and ADEPT [42] have demonstrated the feasibility of utilizing deployable aeroshell by

either inflation or mechanical deployment, respectively. Consequently, much of the DM flight control literature has utilized HIAD or ADEPT aeroshell platforms.

Two potential DM flight control techniques have be studied in the literature: staged jettison (DMSJ) and continuously-variable (DMCV). DMSJ is a flight control strategy where discrete control over the aerocapture trajectory arises from jettison(s) of a single or multiple large area drag skirt(s). Figure 1.8 depicts the concept of operations of DMSJ for a single drag skirt but the description can be generally extended to multi-staged jettisons.

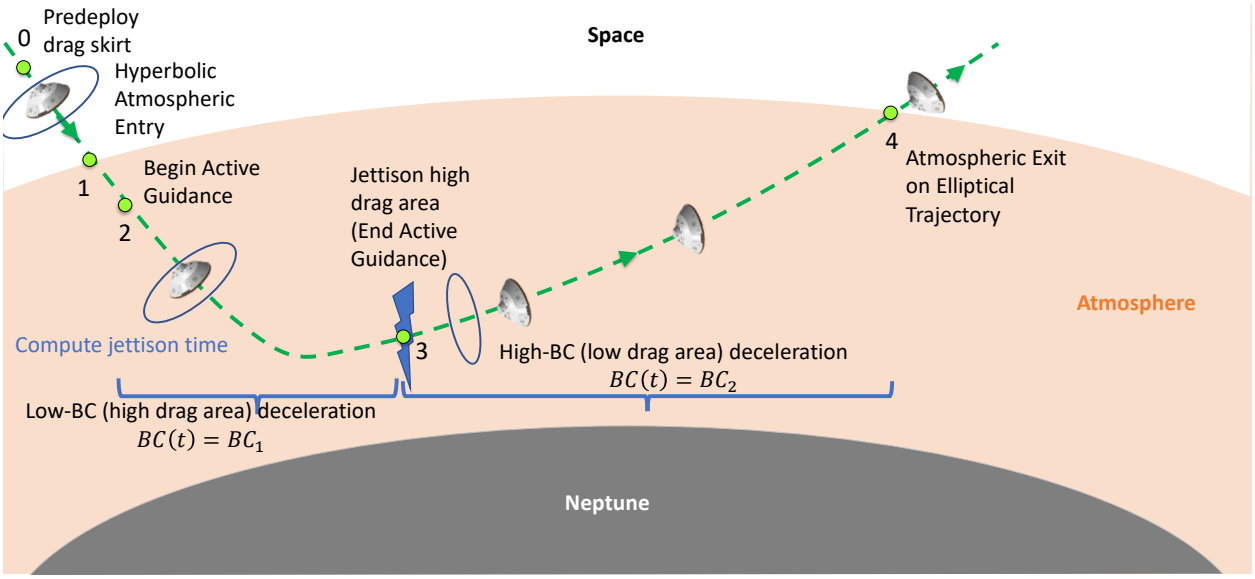

Figure 1.8. Staged Jettison drag modulated aerocapture concept of operations

Before the jettison time, the vehicle is configured with a large drag skirt that corresponds to the lower ballistic coefficient. The guidance algorithm determines jettison time such that the targeted orbit is met at atmospheric exit. At the jettison time, the vehicle jettisons the large drag skirt and flies with the lower reference area that corresponds to the larger ballistic coefficient. Despite being simplistic, jettison systems are potentially vulnerable to dispersions as no control authority is left after the last jettison to correct for further trajectory dispersions. On the other hand, DMCV provides continuous flight control throughout the trajectory. As shown in Figure 1.9, CV systems have the capability of modulating the ballistic coefficient to any value within a prescribed control bound. The CV system may expand/contract the aeroshell geometry, similar to opening and closing an umbrella, by

mechanical actuation to achieve the necessary BC determined by the guidance algorithm that achieves the targeted orbit at atmospheric exit. This system produces the highest control authority out of all the DM concepts but is more mechanically complex due to the required mechanical actuation capability. Simulation results from ADEPT show that CV systems utilizing a mechanically deployable and retractable aeroshell may be feasible [43].

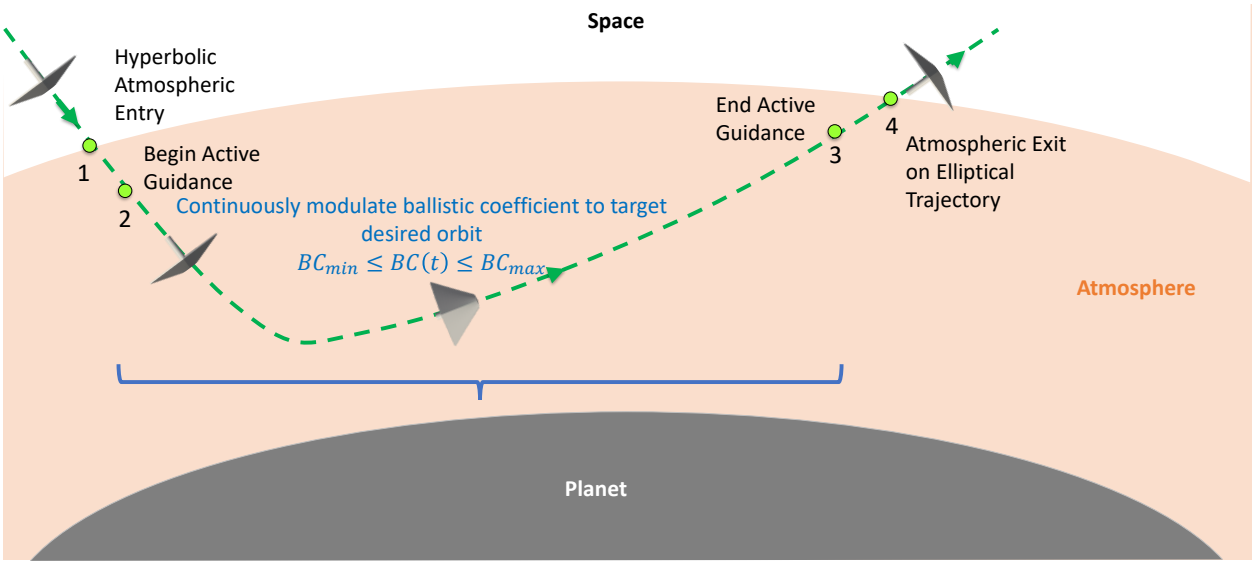

Figure 1.9. Continuously variable drag modulated aerocapture concept of operations

DM flight control has been recently studied for aerocapture applications. Some of the earliest studies investigated the application of an inflatable hypersonic decelerator known as a ballute. The large drag area produced allowed for the potential to achieve the necessary ΔV dissipation while achieving lower aerodynamic heating. Due to this potential performance advantage, some studies have proposed the application of ballute aerocapture at Neptune where the ballute is jettisoned in a DMSJ manner to provide the sufficient orbit insertion capability [44], [45]. Putnam et al., identified both DMSJ and DMCV to be viable at Mars and Titan while noting that improvements in thermal protection system are needed for application at Venus [46]. To mitigate the potential risk associated with single-stage DMSJ, Roelke et. al, investigated the application of multi-staged DMSJ and showed improvement in orbit insertion performance can be achieved [47]. Werner et al., formulated a SmallSat-based DMSJ vehicle for aerocapture application at Earth and Mars [48]. Similarly, Austin

el al., has formulated a SmallSat-based DMSJ vehicle using a trailing-ADEPT and high performance flexible TPS for aerocapture at Venus [49]. Despite being identified by Putnam et al. as the highest performing DM flight controls, DMCV has not been widely addressed in the literature.

1.2.3 Guidance

The objective of the aerocapture guidance is to steer the vehicle from atmospheric entry to exit such that the vehicle's trajectory at atmospheric exit matches the targeted apoapsis altitude. The vehicle's flight computer runs the guidance algorithm at a prescribed frequency, typically between 0.1-1 Hz with variations depending on the flight control and planetary destination. The guidance is driven by the flight control law, which must be closed-loop due to the presence of in-flight trajectory dispersions. Typically, a feedback controller is designed where trajectory estimations are derived from in-flight navigation data and are used to update the on-board trajectory model each guidance cycle. Furthermore, the guidance must be designed to be both robust to additional dispersions, such as delivery state errors, as well as be computationally efficient due to the potentially limited on-board computational power. Overall, the performance and reliability of aerocapture is driven by the designed guidance algorithm. As a result, much emphasis has been placed on guidance algorithms in literature. The guidance strategies studied in literature can be categorized into three methodologies: 1) Reference-based tracking, 2) Analytical Predictor-Corrector, and 3) Numerical Predictor-Corrector.

Reference-Based Tracking

Reference-based tracking (RBT) guidance algorithms rely on the principle of having a pre-computed on-board nominal flight profile. To mitigate trajectory dispersions from the nominal profile, the RBT guidance commands trajectory corrections to steer back on profile. Overall, the accuracy and robustness of the strategy depends on the designed nominal profile. The Apollo capsules utilized an RBT guidance for Earth skip-entry [50]. The earliest aerocapture guidance designs utilized RBT. In support of the Orbital Transfer Vehicle

employing aeroassist techniques, an adaptive RBT guidance logic modeled after Apollo skip-entry was developed in 1983 [51]. In support of the Mars 2001 Orbiter, an aerocapture terminal point guidance was investigated in 1998 [52]. RBT guidance algorithms utilize a perturbation feedback controller that aims to bring the perturbed trajectory back to the nominal profile. Equation 1.2 provides a sample update equation for bank angle used by RBT algorithms. The controller works on feedback terms relating to altitude rate, $\dot{h}$, and/or drag acceleration, D. The feedback terms have gains associated to them, G_d and G_h, that must be performance-tuned to the specific mission profile. In general, the laborious gain tuning and difficulty in selection of a nominal profile for obtaining values such as σ_{ref}, D_{ref}, and $\dot{h}_{ref}$, limits the guidance modularity and robustness of RBT algorithms.

$$\cos(\sigma_{cmd}) = \cos(\sigma_{ref}) + G_d(D - D_{ref}) - G_h(\dot{h} - \dot{h}_{ref}) \tag{1.2}$$

Analytical Predictor-Corrector

Predictor-Corrector algorithms utilized in aerocapture guidance are a simplistic control optimization routine. Utilizing a constant univariate control variable, the predictor predicts the trajectory from the current vehicle location to atmospheric exit by utilizing the atmospheric flight equations of motion. At atmospheric exit the objective function, e.g. apoapsis altitude, and other performance metrics are computed. The corrector utilizes optimization techniques, including unconstrained and constrained methods, to correct the control variable until the objective function is minimized and/or orbit insertion constraints are satisfied. For the case of analytical predictor-correctors (APC), analytical solutions to the equations of motion are utilized by the predictor. For example, lifting bodies may utilize solutions obtained from equilibrium glide [53] and ballistic bodies may utilize the Allen-Eggers solutions [54]. In each formulation of analytical solutions, many fundamental assumptions, such as small flight path angle, uncoupled longitudinal and lateral dynamics, and exponential atmospheric density model, are made to simplify the highly non-linear and coupled atmospheric flight differential equations. Although analytical expressions are ideally sought and allow for significant reduction in computational complexity, the accuracy of assumptions utilized in

the aerocapture flight regime may limit the accuracy and performance of the APC guidance strategies. A variety of APC algorithms have been studied in literature. A hybrid RBT and APC algorithm, known as the Analytic Drag Aerocapture Guidance (ADAC), was proposed by Cerimele and Gamble in 1985 [55]. Successful proof-of-concept demonstration of ADAC and performance benefit over RBT algorithms enabled its proposed application on the 2001 Mars Surveyor Program [56]. ADAC was later renamed the Hybrid Predictor-Corrector Aerocapture Scheme (HYPAS) and over time has been extensively applied in numerical simulations at numerous aerocapture planetary destinations [57]. HYPAS was utilized as the guidance algorithm for all the 2004 NASA aerocapture studies. More detailed performance analysis of HYPAS was conducted at Titan [58] and Neptune [59]. Due to its rigorous testing at numerous planetary destinations, HYPAS can be though of as the current state-of-the-art guidance algorithm for aerocapture. A visual representation of the phases of HYPAS is shown in Figure 1.10. The first phase consists of the capture phase where the bank angle is commanded to achieve equilibrium glide conditions. Once a specified velocity is reached, the second (exit) phase begins where the bank angle is adjusted assuming a constant altitude to analytically compute the necessary exit velocity that achieves the desired apoapsis. For this phase, a RBT solution is utilized to update the bank commands.

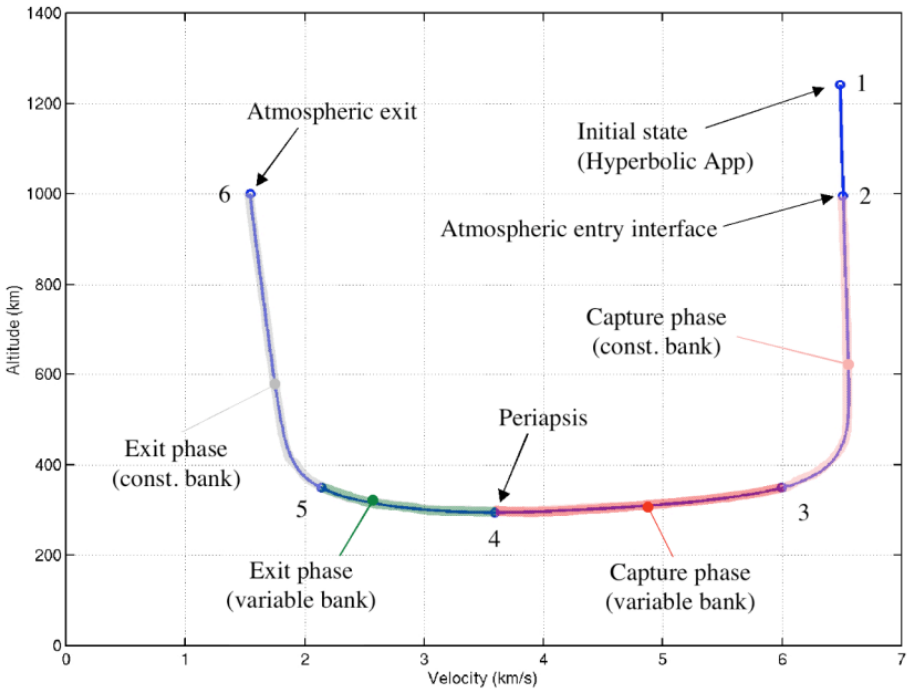

Figure 1.10. HYPAS guidance concept of operations. Image taken from Reference [10]

Numerical Predictor-Corrector

Unlike an APC, a numerical predictor-corrector (NPC) fully integrates the governing non-linear differential equations. This allows for the highest level of accuracy in trajectory prediction and correction at the price of computational cost and convergence guarantees. The increasing advancements in space-rated flight computer computational power may enable the applicability of on-board NPC algorithms. For the Aeroassist Flight Experiment in 1988, Gamble et al., proposed the utilization of an NPC for aerocapture guidance [60]. In 1992, Braun and Powell designed an NPC guidance algorithm for Mars aerocapture. Their 3DOF BAM guidance algorithm enabled robust and accurate apoapsis targeting and orbit plane control as well as incorporated a modest load relief logic [61]. The same algorithm was investigated in 6DOF and demonstrated that the addition of vehicle dynamics does not impact mission feasibility in the presence of atmospheric density uncertainties and vehicle aerodynamic mispredictions [62]. Furthermore, Powell applied the designed NPC guidance algorithm to the 2001 Mars Surveyor Program and demonstrated its applicability for both

3DOF and 6DOF Monte Carlo simulations [63]. The recently designed Fully Numerical Predictor Aerocapture Guidance (FNPAG) demonstrated predictive path handling for Earth aerocapture applications [64] and human-scale vehicle Mars aerocapture [65].

Trajectory optimization forms the foundation of NPC algorithms. The optimization problem can be formulated as the desire to exit the atmosphere on the targeted orbit while not violating any structural or aerothermal limits. Trajectory path constraints on g-loading, convective heating, and integrated heat load are rarely enforced due to their high variability caused by a stochastic and potentially unknown planetary atmosphere. Rather, the trajectory results from numerical simulations are utilized for formulating thermal protection system and structural requirements. Almost every designed NPC algorithm in literature seeks the control input(s) that minimizes the apoapsis orbit insertion error and regulates the orbit plane error. A critical drawback to this problem formulation is the lack of consideration of the periapsis raise maneuver cost. Aerocapture requires a propulsive periapsis raise burn at minimum, which can be potentially expensive depending on the target orbit and planetary destination. A potential solution to this limitation is to formulate the trajectory optimization in terms of minimizing the two-burn combination of the periapsis raise and apoapsis correction maneuvers. This formulation still preserves the apoapsis targeting as zero apoapsis error constitutes zero apoapsis correction maneuver cost. This new optimal aerocapture problem formulation for NPC guidance has been investigated primarily for BAM. Miele et al., investigated the optimal trajectories for the Aeroassited Flight Experiment and discovered through simulation a two-subarc bang-bang bank angle control law provides the ΔV minimal orbit insertion trajectory [66]. This work was further expanded to investigate similar fuel optimal trajectories but with the addition of angle of attack. Miele et al., introduced a decomposition technique that separates the longitudinal motion control to angle of attack and lateral motion to bank angle and shows numerically under certain underlying assumptions the optimal control law is constant for each flight control [67]. Lafleur et al., presented the formulation of a two-burn ΔV-minimization mode utilizing a constant bank angle input in the PreGuid+A NPC guidance algorithm [68]. Lu et al., investigated the optimal aerocapture problem utilizing optimal control theory and mathematically demonstrated that the optimal flight control law for BAM is bang-bang. A two-phase NPC guidance algorithm was

formulated and was demonstrated numerically to provide a significant propellant savings over the PreGuid+A NPC guidance algorithm [69]. This last work lays the foundations for the research objectives and approach of the proposed investigation described in the next section.

1.2.4 Limitation of the Approaches

The current methods for aerocapture GN&C can be thought of to be sufficient for aerocapture. As shown in Table 1.1, Mars is identified where current navigation methods, HYPAS guidance algorithm, and bank angle modulation flight control don't need further technological investments. For Venus, Reference [8] states that "improvements in the guidance system to further vehicle performance robustness to accommodate the small atmospheric scale height at Venus was identified as an enhancing technology". For Titan, Reference [10] noted that "existing guidance algorithms have been demonstrated to provide acceptable performance, improvements could provide increase robustness". At Neptune, improvements in guidance algorithms and α modulation are identified as a strongly enhancing technologies. Reference [11] noted for both existing guidance algorithms that they "have been demonstrated to provide adequate performance. However, improvements are possible to improve performance" as well as noted for α modulation that it "reduces the dispersions in apoapsis, provides additional and more rapid response to density perturbations, and provides additional margin for trim angle of attack uncertainties". A common theme from the excerpts is the need for the guidance algorithm to be robust to potentially high levels of uncertainty. Due to the number of missions to Mars, Mars may have much lower set of uncertainties than Neptune. Likewise, the planetary atmospheres of each planet are inherently different thus making it important for aerocapture guidance algorithm to be modular to these differences. Rather than utilizing assumptions to the fundamental equations of motion like that of HYPAS, fully integrating these equations in an NPC-manner may provide to be a better choice.

The design of aerocapture GN&C is very much control-specific. BAM is a commonly used lifting flight control methodology. From the previous paragraph, modulating angle of attack was identified as having the capability improve aerocapture performance and robustness.

However, limited analysis has further investigated this flight control in the form of DFC. Likewise, drag modulated aerocapture has mostly been studied in the form of staged-jettison yet continuously-variable, with its potential robustness advantages, has lacked much further analysis. Consequently, the analysis on advanced flight control techniques of DFC and DMCV may lead to improvements in both aerocapture performance and robustness. In order to assess such a benefit, a common architecture must be developed. However, much of the literature has been focused on independent developments of GN&C technology. This makes it difficult to conduct qualitative and quantitative comparisons between different flight control methodologies on the same playing-field.

Despite the potential advantage of NPC algorithms over the current state-of-the-art, many of the NPC algorithms found in the literature pose trajectory optimization in the form of apoapsis targeting. This leaves the periapsis raise maneuver unchecked thereby leading to trajectories that potentially have higher ΔV. Some authors have reformulated the NPC algorithms to be ΔV minimizing but have not formulated such flight control laws for DFC and drag modulation nor have assessed this benefit at different planetary destinations. This thesis will provide a framework to addressing these current limitations to aerocapture GN&C technology.

1.3 Contributions of This Dissertation

The primary contribution of this dissertation is the development of a modular aerocapture guidance architecture that encompasses optimal control theory and NPC algorithm to enable trade studies of aerocapture design reference missions.

1.3.1 Development of ΔV-Minimizing aerocapture flight control laws

This dissertation develops ΔV-minimizing flight-control laws for utilization in the NPC guidance architecture. The optimal aerocapture problem is formulated to ascertain the flight control laws for DM and DFC that minimize the in-plane two-burn ΔV cost. A similar problem has been formulated previously for BAM by Lu et al. [69] and will serve as the primary reference for the problem formulation. However, the work by Lu et al. utilizes

many simplifying assumptions, including the simplification of the flight dynamics, that are not appropriate for the generalization of aerocapture guidance. Furthermore, the work by Lu et al. does not fully solve the optimal aerocapture problem. In this dissertation, the full optimal aerocapture problem is formulated utilizing optimal control theory. A well-defined two-point boundary value problem is formulated with the necessary algebraic expressions for the state and co-state dynamics defined along with the optimal flight control law. Numerical solutions to the optimal aerocapture problem for each flight control are computed. The results are used in comparison to NPC-based solutions to determine its level of performance and computational cost.

1.3.2 Formulation of a unified NPC guidance architecture

The similar flight control laws for BAM, DFC, and DM, enables a generalized numerical predictor-corrector algorithm to be formulated. Unlike existing works that have developed individual flight control algorithms, the algorithm in this work is developed to allow for seamless simulation of aerocapture trajectories using different flight control laws under a single common framework. The algorithm is integrated into a closed-loop guidance architecture that allows for 3DOF aerocapture GN&C performance and robustness assessment in a Monte Carlo environment. Having a common framework is essential for enabling controlled Monte Carlo experiments where the same sets of dispersions and guidance routine can be assessed on each candidate vehicle design.

1.3.3 Systems Analysis of Aerocapture design reference missions

The intended consequence of designing a modular aerocapture guidance architecture is the capability to perform mission trade studies without the reliance on multiple independently designed guidance algorithms. The modularity enables various vehicle payloads, including satellite and SmallSats, vehicle designs, including rigid and morphable aeroshells, flight controls, and planetary destinations to be simulated in a 3DOF environment. A series of Monte Carlo experiments are conducted to quantify each mission design robustness and orbit insertion performance to varying levels of prescribed trajectory dispersions. Such

experiments include the application of elevated atmospheric density dispersions and delivery state errors. The results from the trade studies will help further define technological requirements need in preparation for future aerocapture flight projects.

1.3.4 Dissertation Outline

Chapter 1 has provided the motivation and literature review for the current methods of aerocapture GN&C. Chapter 2 highlights the theory and background of formulation of ΔV-minimizing aerocapture flight control laws. Chapter 3 formulates the modular NPC guidance architecture. Chapter 4 documents the numerous aerocapture mission studies conducted using the architecture. Chapter 5 summarizes significant results and suggests directions for future work.

2. THEORY AND BACKGROUND

This chapter highlights the theory and background of formulation of fuel-minimizing aerocapture flight control laws.

2.1 Atmospheric Flight Mechanics

The equations of motion for atmospheric flight are important differential equations in spaceflight mechanics. They define the vehicle's flight dynamics in the presence of atmospheric and gravitational forces. Such forces are important in aerocapture GN&C with regards to understanding how each flight control affects the vehicle's trajectory as well as understanding the stability of the vehicle. For non-thrusting spacecraft, the central body's gravity and atmosphere are the two primary external forces acting on the vehicle. The planet itself can be oblate leading to non-uniform gravitational acceleration, rotates about its axis of rotation at a prescribed angular rate, and can have a unique atmospheric profile. Therefore to achieve mission success, it is vital that the equations of motion for atmospheric flight be derived and understood in the context of the mission application.

2.1.1 Derivation of kinematic equations of motion

The kinematic equations of motion define the point-mass evolution of the spacecraft's position and velocity. These 3DOF differential equations have been thoroughly studied in the literature [53], [66], [67], [70]. However, the existing derivations have all utilized a Newtonian dynamics approach: F=ma. Such an approach requires proper formulation of coordinate frames, including an inertial frame, coordinate transformations, and expressions for time derivatives of non-inertial vectors. As a result, the Newtonian-based derivation can become cumbersome and tedious, especially when higher-order dynamical models are introduced. The objective of this derivation is to utilize Lagrange's equations to derive the same equations of motion as found in literature while demonstrating its elegance in deriving further expansions to the equations, including introduction of planetary oblateness and aerodynamic side-force. As a point of reference, this derivation is validated against

the existing Newtonian-based derivation found in *Hypersonic and Planetary Entry Flight Mechanics* by Vinh, Busemann, and Culp [70].

Problem Formulation

Figure 2.1 illustrates the vehicle motion during atmospheric flight in a spherical rotating planet. Let the inertial frame be defined by the planet-centered planet-fixed Basis I: $(\,\hat{\imath}\;\hat{\jmath}\;\hat{k}\,)$ where $\hat{k}$ is aligned with the planet's rotational axis, $\hat{\imath}$ points in the vernal equinox direction and $\hat{\jmath}$ is aligned with the planet's equatorial plane. The planet rotates about the inertial frame along the rotational axis at a constant rate of ω. Let the planet-relative frame be defined by the planet-centered rotating Basis P: $(\,\hat{x}\;\hat{y}\;\hat{z}\,)$ as shown in Figure 2.1. It is assumed that at time t = 0 the inertial and planet-relative frames are aligned. Basis P is important as the equations of motion are derived with respect to it. The planet-relative position vector $\vec{r_R}$ and velocity vector $\vec{V_R}$ are shown in Figure 2.1. These two kinematic vectors can be defined by a suite of six state-vector parameters: $(\,r\;\theta\;\phi\;v\;\gamma\;\psi\,)$ where r is the magnitude of the planet-relative position vector, θ is the planet-relative longitude (positive eastwards), ϕ is the planet-relative latitude (positive northwards), v is the magnitude of the planet-relative velocity vector, γ is the flight path angle of the planet-relative velocity vector (positive above the local horizon), and ψ is the heading angle of the planet-relative velocity vector (positive in direction of the local parallel).

Although Basis P can be utilized to formulate $\vec{r_R}$ and $\vec{V_R}$, it is more convenient to utilize the local horizon frame Basis H: $(\,\hat{x_H}\;\hat{y_H}\;\hat{z_H}\,)$ where $\hat{x_H}$ is aligned in the direction of $\vec{r_R}$, $\hat{y_H}$ is aligned in the direction of $\hat{y}$ and $\hat{z_H}$ completes the right-handed triad. In Basis H, the planet-relative position and velocity vectors are defined by the state-vector components as shown in Eq. (2.1) and Eq. (2.2).

$$\vec{r_R} = r\hat{x_h} \tag{2.1}$$

$$\vec{v_R} = (v\sin\gamma)\hat{x_h} + (v\cos\gamma\cos\psi)\hat{y_h} + (v\cos\gamma\sin\psi)\hat{z_h} \tag{2.2}$$

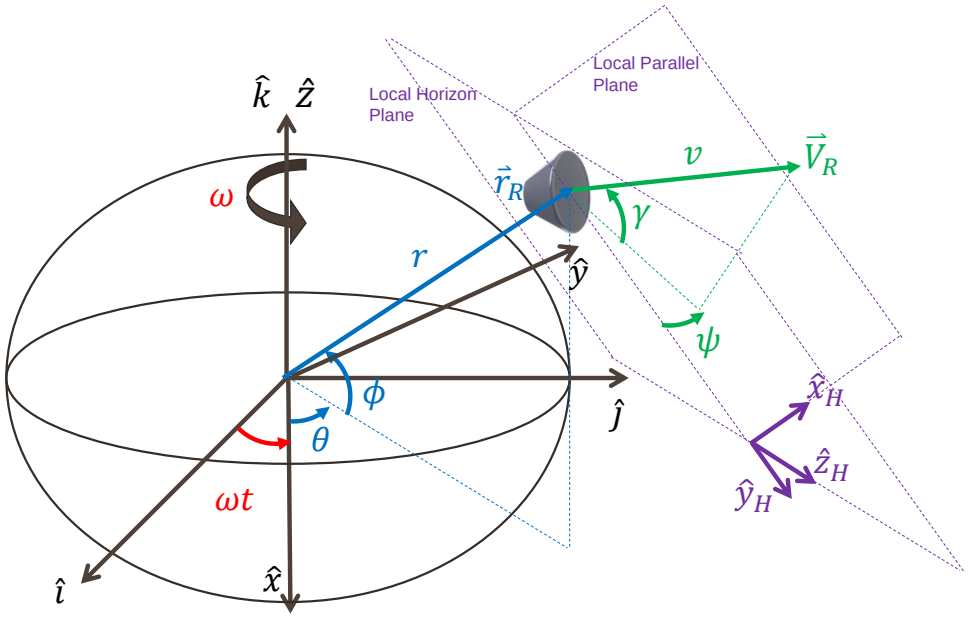

Figure 2.1. Planet-relative motion of a spacecraft during atmospheric flight

Both Basis P and Basis H are rotating with respect to Basis I. For the former, the angular velocity vector, $\vec{\omega}$, of Basis P with respect to Basis I in planet-relative coordinates is shown in Eq. (2.3).

$$\vec{\omega} = \omega \hat{z} \tag{2.3}$$

To transform Eq. (2.3) to local horizon coordinates, a change of coordinates matrix is utilized, which is shown in Eq. (2.4).

$$\begin{bmatrix} \hat{x_H} \\ \hat{y_H} \\ \hat{z_H} \end{bmatrix} = \begin{bmatrix} \cos\theta\cos\phi & \sin\theta\cos\phi & \sin\phi \\ -\sin\theta & \cos\theta & 0 \\ -\cos\theta\sin\phi & -\sin\theta\sin\phi & \cos\phi \end{bmatrix} \begin{bmatrix} \hat{x} \\ \hat{y} \\ \hat{z} \end{bmatrix} \tag{2.4}$$

Substituting Eq. (2.3) into right-hand side of Eq. (2.4) yields the angular velocity vector of Basis P with respect to Basis I in local horizon coordinates as shown in Eq. (2.5).

$$\vec{\omega} = (\omega \sin\phi)\hat{x_H} + (\omega \cos\phi)\hat{z_H} \tag{2.5}$$

The state vector parameters θ and ϕ can be utilized to model the angular velocity vector of Basis H with respect to Basis P. This angular velocity vector, $\vec{\Omega}$, is composed of two parts as shown in Eq. (2.6) where $\dot{\theta}$ and $\dot{\phi}$ are the *planet-relative* time derivatives of θ and ϕ.

$$\vec{\Omega} = \dot{\theta}\hat{z} - \dot{\phi}\hat{y_H} \tag{2.6}$$

Taking the first component of Eq. (2.6) and transforming to the local horizon frame using Eq. (2.4) yields the angular velocity vector of Basis H with respect to Basis P in local horizon coordinates as shown in Eq. (2.7).

$$\vec{\Omega} = (\dot{\theta}\sin\phi)\hat{x_H} - \dot{\phi}\hat{y_H} + (\dot{\theta}\cos\phi)\hat{z_H} \tag{2.7}$$

The last component in the problem formulation is the aerodynamic forces. During atmospheric flight, the spacecraft generates aerodynamic forces that can be modeled in either the body-frame or wind-frame. Let the body-frame be defined by Basis B: ($\hat{x_B}$ $\hat{y_B}$ $\hat{z_B}$) where the axes correspond to the principal axes of the vehicle's geometry as shown in Figure 2.2. Let the wind-frame be defined by Basis W: ($\hat{x_W}$ $\hat{y_W}$ $\hat{z_W}$) where $\hat{x_W}$ is aligned with the planet-relative velocity vector, $\hat{y_W}$ is aligned with the side-force vector and $\hat{z_W}$ is aligned anti-parallel to the lift vector. Both frames are related through the angle of attack, α, and side-slip angle, β.

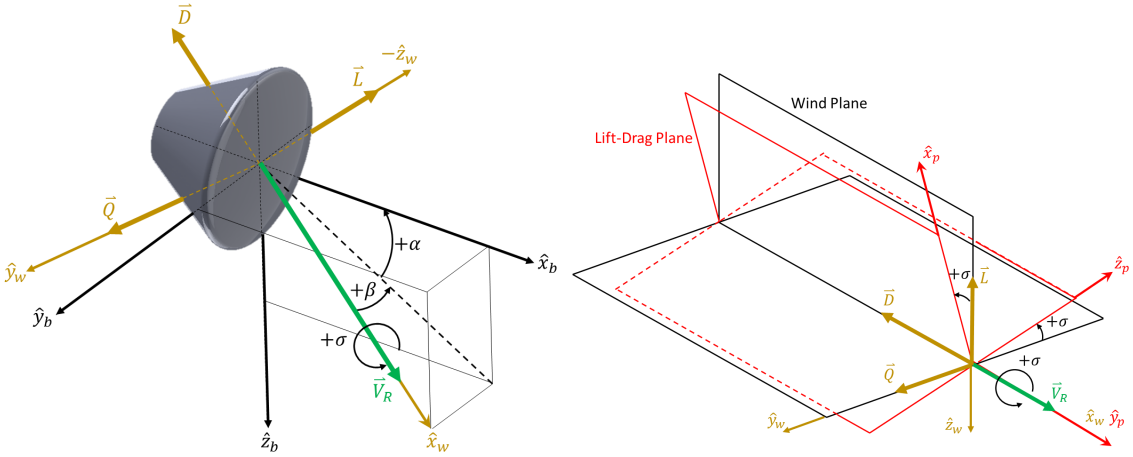

Figure 2.2. Visualization of aerodynamic forces generated by vehicle during planetary atmospheric flight. Modulating bank angle causes rotation of the lift-drag plane about the planet-relative velocity vector.

Since the drag vector, $\vec{D}$, is aligned anti-parallel to the relative-velocity vector, Eq. (2.2) can be utilized with the substitution v = -D to formulate the drag vector equation in the local horizon frame as shown in Eq. (2.8). Here, D is defined as the drag vector magnitude.

$$\vec{D} = (-D\sin\gamma)\hat{x_h} - (D\cos\gamma\cos\psi)\hat{y_h} - (D\cos\gamma\sin\psi)\hat{z_h} \tag{2.8}$$

To ascertain the lift vector equation, the influence of the vehicle's bank angle, σ, must be identified. Bank angle is defined as the rotation angle of the lift vector about the planet-relative velocity vector[1] (positive rotation in direction of relative-velocity vector) as shown in Figure 2.2. This causes an effective rotation of the lift-drag plane away from the wind plane. Let the lift-drag plane be defined by the vectors $\hat{x_P}$ and $\hat{y_P}$ in Basis L: ($\hat{x_P}$ $\hat{y_P}$ $\hat{z_P}$) as shown in Figure 2.2. By convention, full lift vector up occurs at 0° bank angle and full lift vector down occurs at 180° bank angle. The vertical component of lift, denoted by Lcos σ remains aligned with $\hat{x_P}$ while the out-of-plane component of lift, denoted by Lsin σ remains aligned with $\hat{z_P}$. Nevertheless, the lift vector in Basis L is defined as shown in Eq. (2.9) where L is the magnitude of the lift vector.

$$\vec{L} = (L\cos\sigma)\hat{x_P} + (L\sin\sigma)\hat{z_P} \tag{2.9}$$

The influence of bank angle on side-force, $\vec{Q}$, is addressed later in this section. The transformation matrix from Basis L to the Basis H can be formulated by a two-rotation sequence by angles ψ and γ resulting in the matrix shown in Eq. (2.10).

$$\begin{bmatrix} \hat{x_h} \\ \hat{y_h} \\ \hat{z_h} \end{bmatrix} = \begin{bmatrix} \cos\gamma & \sin\gamma & 0 \\ -\sin\gamma\cos\psi & \cos\gamma\cos\psi & -\sin\psi \\ -\sin\gamma\sin\psi & \cos\gamma\sin\psi & \cos\psi \end{bmatrix} \begin{bmatrix} \hat{x_P} \\ \hat{y_P} \\ \hat{z_P} \end{bmatrix} \tag{2.10}$$

Substituting Eq. (2.9) into right-hand side of Eq. (2.10) yields the lift vector expressed in local horizon coordinates as shown in Eq. (2.11).

$$\begin{aligned} \vec{L} = {} & (L\cos\sigma\cos\gamma)\hat{x_h} - (L\cos\sigma\sin\gamma\cos\psi + L\sin\sigma\sin\psi)\hat{y_h} \\ & - (L\cos\sigma\sin\gamma\sin\psi - L\sin\sigma\cos\psi)\hat{z_h} \end{aligned} \tag{2.11}$$

[1]↑Assume freestream and planet-relative velocity vectors are identical

Application of Lagrange's Equations

In classical dynamics, Lagrange's Equations provide an analytical assessment of the system dynamics meaning that the system as a whole can be described by scalar kinetic and potential energy functions. This is in contrast to Newtonian dynamics, commonly denoted as vectorial dynamics, where the forces and motion of individual parts of the systems are analyzed. For complex systems, solving for the constraint forces may be necessary when utilizing Newtonian dynamics; however, solving for such constraint forces is not necessary when using Lagrangian dynamics. Furthermore, the scalar functions are invariant to coordinate system chosen. On the contrary, the results obtained from Newtonian dynamics require an inertial coordinate frame to be specified. These philosophical differences make Lagrangian dynamics much more appealing for solving complex and difficult problems [71], [72].

The beauty of Lagrangian dynamics is that if the system being analyzed is holonomic, then the equations of motion of the system can be obtained from Lagrange's Equations, which is shown in Eq. (2.12).

$$\frac{d}{dt}\left(\frac{\partial \tilde{L}}{\partial \dot{q}_i}\right) - \frac{\partial \tilde{L}}{\partial q_i} = F_i \qquad (i = 1, 2, ..., n) \tag{2.12}$$

In Eq. (2.12), $\tilde{L}$ denotes the Lagrangian function, which is defined by the difference between the kinetic energy, T, and potential energy, V, of the system as shown in Eq. (2.13). F_i are the generalized forces not derivable from a potential function. One such example are aerodynamic forces.

$$\tilde{L} = T - V \tag{2.13}$$

The q_i are the generalized coordinates of the system. They can be chosen arbitrarily so as long as they are independent. For the atmospheric flight problem, let the generalized coordinates be the components of the inertial position vector, x_I, y_I, z_I, and the inertial

velocity vector, v_{x_I}, v_{y_I}, v_{z_I}, as expressed in the local horizon frame as shown in Eq. (2.14) and Eq. (2.15). In the local horizon frame, $x_I = \mathrm{r}$ and $y_I = z_I = 0$.

$$\vec{r_I} = x_I \hat{x_h} \tag{2.14}$$

$$\vec{v_I} = v_{x_I} \hat{x_h} + v_{y_I} \hat{y_h} + v_{z_I} \hat{z_h} \tag{2.15}$$

The kinetic energy of the system is defined by Eq. (2.16) utilizing the inertial velocity vector.

$$T = \frac{1}{2} m (\vec{v_I} \cdot \vec{v_I}) \tag{2.16}$$

The potential energy of the system is derivable from a scalar potential being the spherical gravity gradient of the central body. Denoting μ as the gravitational parameter of the planet, the potential energy of the system is modeled by Eq. (2.17). The effects of planetary oblateness are addressed later in this section.

$$V = -\frac{m\mu}{x_I} \tag{2.17}$$

The generalized forces come from lift and drag, which are modeled in the local horizon frame component-wise as shown in Eq. (2.18) and Eq. (2.19).

$$\vec{L} = L_x \hat{x_h} + L_y \hat{y_h} + L_z \hat{z_h} \tag{2.18}$$

$$\vec{D} = D_x \hat{x_h} + D_y \hat{y_h} + D_z \hat{z_h} \tag{2.19}$$

Summing the lift and drag forces yields the generalized force vector, $\vec{F}$, as shown in Eq. (2.20).

$$\vec{F} = \vec{L} + \vec{D} \tag{2.20}$$

Next, the Lagrangian is built by substituting Eq. (2.16) and Eq. (2.17) into Eq. (2.13) to yield Eq. (2.21).

$$\tilde{L} = \frac{1}{2}m({v_{x_I}}^2 + {v_{y_I}}^2 + {v_{z_I}}^2) + \frac{m\mu}{x_I} \tag{2.21}$$

Now, Lagrange's Equation is applied to the generalized coordinates. First, the partials of the Lagrangian (Eq. (2.21)) with respect to the inertial position vector (Eq. (2.14)) and inertial velocity vector (Eq. (2.15)) are taken with the corresponding results shown in Eq. (2.22) and Eq. (2.23), respectively. Note that $\vec{v_I} = \dot{\vec{r_I}}$ by definition.

$$\frac{\partial \tilde{L}}{\partial \vec{r_I}} = -\frac{\mu m}{r^2}\hat{x_h} \tag{2.22}$$

$$\frac{\partial \tilde{L}}{\partial \vec{v_I}} = (mv_{x_I})\hat{x_h} + (mv_{y_I})\hat{y_h} + (mv_{z_I})\hat{z_h} \tag{2.23}$$

Next, the inertial time derivative of Eq. (2.23) is taken. Rather than taking the derivative explicitly, this derivative is expanded to allow for the planet-relative position and velocity vectors to be introduced into the problem. Eq. (2.23) can be rewritten to yield Eq. (2.24) assuming constant mass.

$$\frac{d^I}{dt}(\frac{\partial \tilde{L}}{\partial \vec{v_I}}) = \frac{d^I}{dt}(m\vec{v_I}) = m\frac{d^I}{dt}(\vec{v_I}) \tag{2.24}$$

Using the Transport Theorem [73], the inertial time derivative of the inertial velocity vector can be decomposed into the planet-relative time derivative of the velocity vector plus the cross product of the rotation rate of the planet-relative frame with the velocity vector yielding Eq. (2.25).

$$\frac{d^I}{dt}(\vec{v_I}) = \frac{d^P}{dt}(\vec{v_I}) + \vec{\omega} \times \vec{v_I}. \tag{2.25}$$

The inertial velocity vector is the inertial time derivative of the position vector. Likewise, this time derivative can also be decomposed based off the planet-relative time derivative as

shown in Eq. (2.26) where planet-relative time derivative yields the planet-relative velocity vector.

$$\vec{v_I} = \frac{d^I}{dt}(\vec{r_I}) = \frac{d^P}{dt}(\vec{r_I}) + \vec{\omega} \times \vec{r_I} = \vec{v_R} + \omega \times \vec{r_I}. \tag{2.26}$$

Substituting Eq. (2.26) into Eq. (2.25), simplifying and substituting the result into Eq. (2.24) yields the inertial time derivative of the partial of the Lagrangian with respect to the inertial velocity vector as a function of the planet-relative velocity vector, planet-relative rotation rate vector, and planet-relative position vector (note that the planet-relative and inertial position vectors are the same when using local horizon coordinates) as shown in Eq. (2.27).

$$\frac{d^I}{dt}(\frac{\partial \tilde{L}}{\partial \vec{v_I}}) = m(\frac{d^P}{dt}(\vec{v_R}) + 2(\vec{\omega} \times \vec{v_R}) + \vec{\omega} \times (\vec{\omega} \times \vec{r_R})) \tag{2.27}$$

Finally, putting together the pieces of Lagrange's Equation(Eq. (2.12)) with Eq. (2.20), Eq. (2.22), and Eq. (2.27) yields Eq. (2.28).

$$m(\frac{d^P}{dt}(\vec{v_R}) + 2(\vec{\omega} \times \vec{v_R}) + \vec{\omega} \times (\vec{\omega} \times \vec{r_R})) + \frac{\mu m}{r^2}\hat{x_h} = \vec{F} \tag{2.28}$$

Eq. (2.28) represents the foundational equation for computing the planet-relative parameter differential equations. One can easily notice that the equation resembles a form that can be derived from the application of Newton's F=ma equation; in fact, this is precisely the case as Eq. (2.28) matches the form derived using a Newtonian method in Reference [70] pp. 22 Eq 2-13.

Now Lagrange's equations are utilized to obtain the planet-relative differential equations. The local horizon frame is used as the working frame. Let the planet-relative velocity vector be defined component-wise by Eq. (2.29).

$$\vec{v_R} = v_x\hat{x_h} + v_y\hat{y_h} + v_z\hat{z_h} \tag{2.29}$$

Because local horizon coordinates are utilized, the planet-relative time derivative found in Eq. (2.28) must be found using the Transport Theorem where the rotation rate of the local

horizon frame (Basis H) with respect to the planet-relative frame (Basis P) is incorporated as shown in Eq. (2.30).

$$\frac{d^P}{dt}(\vec{v_R}) = \dot{v_x}\hat{x_h} + \dot{v_y}\hat{y_h} + \dot{v_z}\hat{z_h} + \vec{\Omega} \times \vec{v_R} \tag{2.30}$$

Substituting Eq. (2.7) into Eq. (2.30) for $\vec{\Omega}$ yields Eq. (2.31).

$$\frac{d^P}{dt}(\vec{v_R}) = (\dot{v_x} - \dot{\phi}v_z - \dot{\theta}v_y\cos\phi)\hat{x_h} + (\dot{v_y} + \dot{\theta}v_x\cos\phi - \dot{\theta}v_z\sin\phi)\hat{y_h} + (\dot{v_z} + \dot{\phi}v_x + \dot{\theta}v_y\sin\phi)\hat{z_h} \tag{2.31}$$

Substituting Eq. (2.6) and Eq. (2.31) into Eq. (2.28) and decomposing the resulting vector equation about each coordinate axis yields three scalar differential equations as shown by Eq. (2.32), Eq. (2.33), and Eq. (2.34).

$$-D_x - L_x + \frac{\mu m}{r^2} + m(\dot{v_x} - \dot{\phi}v_z - \dot{\theta}v_y\cos\phi - 2v_y\omega\cos\phi - r\omega^2\cos\phi^2) \qquad (\hat{x_h}) \tag{2.32}$$

$$-D_y - L_y + m(\dot{v_y} + \dot{\theta}v_x\cos\phi - \dot{\theta}v_z\sin\phi - 2(v_x\omega\cos\phi - v_z\omega\sin\phi)) \qquad (\hat{y_h}) \tag{2.33}$$

$$-D_z - L_z + m(\dot{v_z} + \dot{\phi}v_x + \dot{\theta}v_y\sin\phi + 2v_y\omega\sin\phi + r\omega^2\cos\phi\sin\phi) \qquad (\hat{z_h}) \tag{2.34}$$

In Eq. (2.32), Eq. (2.33), and Eq. (2.34), the local horizon components of the planet-relative velocity vector are present. In fact, Eq. (2.2) provides the expression for these components as a function of the planet-relative parameters. Taking the time derivative

of Eq. (2.2) components yields three equations for $\dot{v_x}$, $\dot{v_y}$, and $\dot{v_z}$ as seen by Eq. (2.35), Eq. (2.36), and Eq. (2.37).

$$\dot{v_x} = \dot{v}\sin\gamma + v\cos\gamma\dot{\gamma} \tag{2.35}$$

$$\dot{v_y} = \dot{v}\cos\gamma\cos\psi - v\sin\gamma\cos\psi\dot{\gamma} - v\cos\gamma\sin\psi\dot{\psi} \tag{2.36}$$

$$\dot{v_z} = \dot{v}\cos\gamma\sin\psi - v\sin\gamma\sin\psi\dot{\gamma} + v\cos\gamma\cos\psi\dot{\psi} \tag{2.37}$$

Eq. (2.8) and Eq. (2.11) provide the necessary expressions for D_x, D_y, D_z, L_x, L_y, and L_z. There are six unknowns ($\dot{r}$, $\dot{\theta}$, $\dot{\phi}$, $\dot{v}$, $\dot{\gamma}$, and $\dot{\psi}$) with only three equations from Eq. (2.35), Eq. (2.36), and Eq. (2.37).

The remaining three equations can be computed by linking known $\vec{v_R}$ to the planet-relative time derivative of the position vector $\vec{r_R}$. Using the Transport Theorem, the planet-relative time derivative of Eq. (2.1) is taken where the rotation rate of the local horizon frame (Basis H) with respect to the planet-relative frame (Basis P) is incorporated as shown in Eq. (2.38).

$$\frac{d^P}{dt}(\vec{r_R}) = \dot{r}\hat{x_h} + \vec{\Omega}\times\vec{r_R} = \dot{r}\hat{x_h} + r\dot{\theta}\cos\phi\hat{y_h} + \dot{\phi}\hat{z_h} \tag{2.38}$$

Equating Eq. (2.38) to Eq. (2.2) and solving for $\dot{r}$, $\dot{\theta}$, and $\dot{\phi}$ yields the Kinematic Scalar Differential Equations as shown by Eq. (2.39), Eq. (2.40), and Eq. (2.41). These differential equations represent the evolution of the planet-relative position vector. The position vector magnitude rate of change (or altitude rate of change) depends on the flight path angle. For positive flight path angles, the altitude rate is positive thereby indicating increase in altitude. Conversely, negative flight path angles result in negative altitude rate and thereby indicate decrease in altitude. The planet-relative longitude and latitude rates differ with regards to longitude and heading angle terms. Longitude does not appear explicitly in these kinematic

equations nor will they appear in the force equations below. As a result, longitude can be classified as an ignorable coordinate.

$$\dot{r} = v \sin \gamma \tag{2.39}$$

$$\dot{\theta} = \frac{v \cos \gamma \cos \psi}{r \cos \phi} \tag{2.40}$$

$$\dot{\phi} = \frac{v \cos \gamma \sin \psi}{r} \tag{2.41}$$

Finally, expressions found from Eq. (2.39), Eq. (2.40), and Eq. (2.41) are used to solve for $\dot{v}$, $\dot{\gamma}$, and $\dot{\psi}$ with the results shown below in Eq. (2.42), Eq. (2.43), and Eq. (2.44). These three equations represent the force equations that explain the evolution of the planet-relative velocity vector. The velocity vector magnitude rate of change is influenced by both gravity and the aerodynamic drag. The flight path angle sign dictates gravity's influence on the increase or decrease in the rate of change of velocity. Drag decreases the rate of change of velocity. In the flight path angle dynamics, gravity acts to counteract the centripetal acceleration of the trajectory ($\frac{v^2}{r}$) while the bank angle serves to control the lift vector's effect. Likewise, bank angle also influences the lift vector's effect on the heading angle dynamics. Steering the lift vector to the right of the velocity vector (positive bank) increases the rate of change of heading angle while steering to the left (negative bank) decreases the rate of change of the heading angle. Present in all three equations is the influence of the planet's rotation rate (ω). The $2\omega v$ term is the Coriolis acceleration and directly influences the flight path angle and heading angle evolution.

$$\dot{v} = -\frac{D}{m} - \frac{\mu \sin(\gamma)}{r^2} + r\omega^2 \cos(\phi)(\sin(\gamma)\cos(\phi) - \cos(\gamma)\sin(\psi)\sin(\phi)) \tag{2.42}$$

$$\begin{aligned} v\dot{\gamma} = \frac{L\cos(\sigma)}{m} - \frac{\mu\cos(\gamma)}{r^2} + r\omega^2\cos(\phi)(\sin(\gamma)\sin(\psi)\sin(\phi) + \cos(\gamma)\cos(\phi)) \\ + \frac{v^2\cos(\gamma)}{r} + 2v\omega\cos(\psi)\cos(\phi) \end{aligned} \tag{2.43}$$

$$v\dot{\psi} = \frac{L\sin(\sigma)}{m\cos(\gamma)} - \frac{(r\omega^2)\cos(\psi)\sin(\phi)\cos(\phi)}{\cos(\gamma)} - \frac{v^2\cos(\gamma)\cos(\psi)\tan(\phi)}{r} + 2v\omega(\tan(\gamma)\sin(\psi)\cos(\phi) - \sin(\phi)) \tag{2.44}$$

The results obtained from the application of Lagrangian dynamics can be compared to an existing derivation produced using Newtonian dynamics. A comparison of the Kinematic Scalar Differential Equations from Eq. (2.39), Eq. (2.40), and Eq. (2.41) to Reference [70] pp. 26 Eq 2-28 indicate complete mathematical agreement. Similarly, comparison of the force equations from Eq. (2.42), Eq. (2.43), and Eq. (2.44) to Reference [70] pp. 27 Eq 2-31 indicate complete mathematical agreement. Therefore, it has been shown and verified that the equations of motion for atmospheric flight in a spherical planet can be successfully derived using Lagrangian dynamics.

Further Expansion to the Equations of Motion

The equations of motion have been derived for atmospheric flight in a spherical rotating planet. It was assumed that the central body is perfectly spherical with a spherical gravity potential (i.e. gravitational acceleration strictly a function of radial distance only). However, not every planet is a perfect sphere but rather resembles an ellipsoid. The oblateness of the planet due to non-uniform distribution of mass leads to non-radial gravitational acceleration components. Zonal harmonics can be utilized to model such a non-uniform gravity potential. Consequently, this modification can be handled in the equation of motion derivation by modifying the potential energy of the system. Furthermore, it was shown that bank angle can be utilized as a flight control parameter for influencing the equations of motion. During atmospheric flight, the vehicle can also modulate its aerodynamic reference area, its angle of attack, and/or its side-slip angle to influence the equations of motion. All three of these parameters affect the aerodynamic forces; but, the latter introduces an additional force not modeled by the current derivation. This force is side-force and along with lift and drag complete an orthogonal force triad. Consequently, this modification can be handled in the equation of motion derivation by adding side-force to the generalized forces. These

two components are included in this derivation to demonstrate the simplistic approach in improving the fidelity of the equations of motion utilizing Lagrangian dynamics.

Planetary Oblateness

To introduce planetary oblatness into the model, the central body is modeled by an ellipsoid where R_e is the equatorial radius and R_p is the polar radius. Spherical coordinates (r, θ, ϕ) are still utilized to model the position vector. The velocity vector parameterization (v, γ, ψ) is unaffected by this modification. The potential energy of the system is derived from the gravitational potential function, U. Using zonal harmonics, the gravitational potential for an oblate ellipsoidal planet can be approximated as shown in Eq. (2.45). Despite the gravitational potential being truncated to the J_2 zonal term, the potential can be readily expanded to incorporate additional perturbation terms.

$$U = -\frac{\mu\left(J_2\left(\frac{R_e}{r}\right)^2\left(\frac{3}{2} - \frac{9\sin^2(\phi)}{2}\right) + 1\right)}{r} \tag{2.45}$$

Eq. (2.45) models latitudinal gravitational potential in addition to the radial component. The modified potential energy of the system can be modeled using Eq. (2.46). Note that if J_2 is zero, then the existing potential energy of the system, Eq. (2.17), can be obtained.

$$V = mU \tag{2.46}$$

The Lagrangian is modified by substituting Eq. (2.46) into Eq. (2.13). The planetary oblateness only affects the potential energy of the system and subsequently the partial of the Lagrangian with respect to the inertial position vector, Eq. (2.22). Because this partial derivative only depends on the potential energy of the system, it can be decomposed using the chain rule to incorporate the planet-relative components defining the potential function as shown in Eq. (2.47).

$$\frac{\partial L}{\partial \vec{r_I}} = \frac{\partial L}{\partial r}\hat{x_h} + \frac{1}{r}\frac{\partial L}{\partial \phi}\hat{z_h} \tag{2.47}$$

Expanding the scalar partial derivatives with respect to r and ϕ yields Eq. (2.48) and Eq. (2.49).

$$\frac{\partial L}{\partial r} = -m\frac{\partial U}{\partial r} \tag{2.48}$$

$$\frac{\partial L}{\partial \phi} = -m\frac{\partial U}{\partial \phi} \tag{2.49}$$

Indeed, these partial derivatives of the gravitational potential function yield the radial and latitudinal gravitational accelerations, g_r and g_ϕ, as shown in Eq. (2.50) and Eq. (2.51).

$$\frac{\partial U}{\partial r} = \frac{\mu}{r^2}(1 + J_2(\frac{R_e}{r})^2)(\frac{3}{2} - \frac{9}{2}\sin^2\phi) = g_r \tag{2.50}$$

$$\frac{1}{r}\frac{\partial U}{\partial \phi} = \frac{\mu}{r^2}(J_2(\frac{R_e}{r})^2)(3\sin\phi\cos\phi) = g_\phi \tag{2.51}$$

Thus, the expanded partial derivative represents the gravitational force of the planet derived from a potential function as shown in Eq. (2.52).

$$\frac{\partial L}{\partial \vec{r_I}} = -mg_r\hat{x_h} - mg_\phi\hat{z_h} \tag{2.52}$$

Aerodynamic Side-Force

During atmospheric flight, side force can be generated by side-slipping the vehicle. This can be thought of as yawing the vehicle by modulating the side-slip angle β as shown in Figure 2.2. Like lift, modulating bank angle results in a rotation of the side force about the relative-velocity vector. Nevertheless, the side force vector in Basis L is defined as shown in Eq. (2.53) where Q is the magnitude of the side force vector.

$$\vec{Q} = (Q\sin\sigma)\hat{x_P} - (Q\cos\sigma)\hat{z_P} \tag{2.53}$$

Eq. (2.53) is subsequently transformed to local horizon coordinates via Eq. (2.10). The resulting expression is appended to the generalized force expression, Eq. (2.20).

Atmospheric Winds

During atmospheric flight, atmospheric winds can be present. The speed of these winds can vary depending on the planetary atmosphere. Generally, these winds are much smaller when compared to the vehicle's velocity. The aerodynamic forces produced by the vehicle are dependent on the freestream velocity vector, $\vec{v}_\infty$. In the absence of winds, the relative-velocity vector matches the freestream vector; thus, the absence of winds were assumed in the previous derivation. Commonly, the wind vector is defined by its north-south, east-west, and down-up components. These components refer to a reference frame known as the North-East-Down frame. Let the frame be defined by Basis NED: $(\,\hat{N}\ \hat{E}\ \hat{D}\,)$ where $\hat{N}$ is aligned anti-parallel to $\vec{y_H}$, $\hat{E}$ is aligned in the direction of $\hat{z_H}$ and $\hat{D}$ completes the right-handed triad. The wind vector, $\vec{v_w}$, can be mathematically modeled by Eq. (2.54) where v_N, v_E, and v_D represent the positive wind components in the north, east, and down directions respectively.

$$\vec{v_w} = v_N\hat{N} + v_E\hat{E} + v_D\hat{D} \tag{2.54}$$

Using the orientation of Basis NED to Basis H, the wind vector can be expressed in the local horizontal frame as shown by Eq. (2.55)

$$\vec{v_w} = -v_D\hat{x_H} + -v_N\hat{y_H} + v_E\hat{z_H} \tag{2.55}$$

The freestream velocity vector can then simply be computed by subtracting the relative-velocity vector, Eq. (2.2), from the wind vector, Eq. (2.55). Doing so yields Eq. (2.56)

$$\vec{v}_\infty = (v\sin\gamma + v_D)\hat{x_h} + (v\cos\gamma\cos\psi + v_N)\hat{y_h} + (v\cos\gamma\sin\psi - v_E)\hat{z_h} \tag{2.56}$$

Modified Equations of Motion

The new expressions for potential energy and side force are substituted into Lagrange's equations. The same methodology as that presented in this section is applied. The modifications only affect the resulting force equations and not the kinematic equations. The resulting force equations from solving Lagrange's equations are shown in Eq. (2.57), Eq. (2.58), and Eq. (2.59).

$$\dot{v} = -\frac{D}{m} - g_r \sin\gamma - g_\phi \cos\gamma \sin\psi + r\omega^2 \cos\phi(\sin\gamma\cos\phi - \cos\gamma\sin\psi\sin\phi) \tag{2.57}$$

$$\begin{aligned} v\dot{\gamma} = {} & \frac{L\cos\sigma}{m} + \frac{Q\sin\sigma}{m} + (\frac{v^2}{r} - g_r)\cos\gamma + g_\phi \sin\gamma\sin\psi \\ & + r\omega^2\cos\phi(\sin\gamma\sin\psi\sin\phi + \cos\gamma\cos\phi) + 2v\omega\cos\psi\cos\phi \end{aligned} \tag{2.58}$$

$$\begin{aligned} v\dot{\psi} = {} & \frac{L\sin\sigma}{m\cos\gamma} - \frac{Q\cos\sigma}{m\cos\gamma} - g_\phi\frac{\cos\psi}{\cos\gamma} - \frac{r\omega^2\cos\psi\sin\phi\cos\phi}{\cos\gamma} \\ & - \frac{v^2\cos\gamma\cos\psi\tan\phi}{r} + 2v\omega(\tan\gamma\sin\psi\cos\phi - \sin\phi) \end{aligned} \tag{2.59}$$

The resulting force equations are identical to those presented previously with the exception of the terms arising from the introduction of side force and planetary oblateness. The relative-velocity vector magnitude dynamics are influenced by both the radial and latitudinal gravitational acceleration but is not influenced directly by side force. On the contrary, both flight path angle and heading angle dynamics are directly influenced by side force. Bank angle regulates the sign and determines whether lift and side force constructively or destructively oppose one another's influence on the respective dynamics. For a full-lift vector up or down trajectory, the flight path angle dynamics are directly influenced by lift vector only while the heading angle dynamics are directly influenced by side-force vector only. The latitudinal gravitational acceleration influences both flight path angle and heading angle dynamics.

In summary, the 3DOF kinematic equations of motion for atmospheric flight in an ellipsoidal rotating planet are modeled using Eq. (2.39), Eq. (2.40), Eq. (2.41), Eq. (2.57),

Eq. (2.58), and Eq. (2.59). These equations represent a cylindrical parameterization of the time-evolution of the planet-relative position and velocity vectors.

2.1.2 Derivation of rotational equations of motion

The rotational equations of motion represent the evolution of the vehicle attitude. In addition to controlling the trajectory of the vehicle, it is important that the vehicle attitude is controlled as well. The vehicle's attitude is influenced by external torques that act to rotate the vehicle about its center of mass. During atmospheric flight, the two primary torques include aerodynamic and propulsive moments. Figure 2.3 illustrates the aerodynamic forces and moments produced by the vehicle.

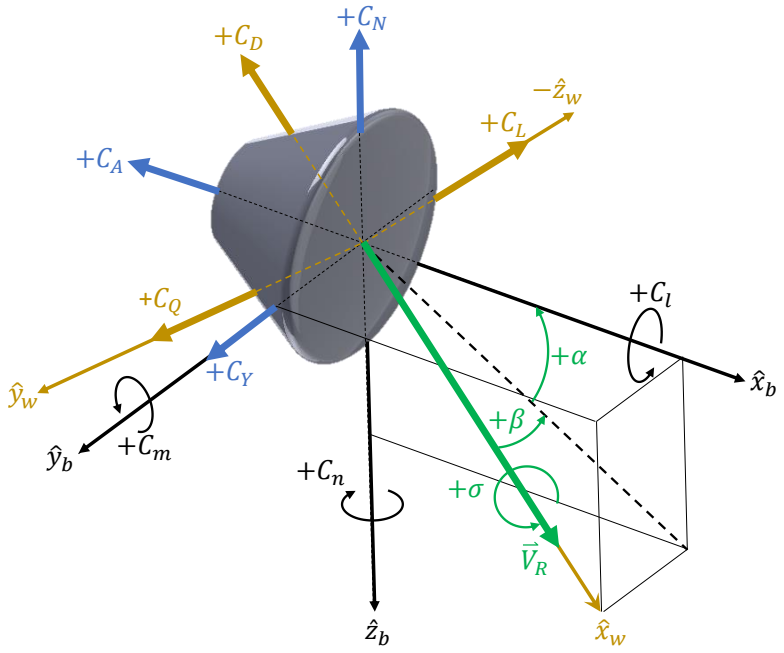

Figure 2.3. Visualization of vehicle aerodynamic force and moments coefficients generated by vehicle during planetary atmospheric flight.

Rotational Dynamics

To derive the rotational dynamics of the vehicle during flight, Euler's equation of motion is utilized as shown by Eq. (2.60) where $\vec{M}$ are the external moments acting on the vehicle and $\vec{H}$ is the vehicle's angular momentum vector. The reference frame utilized include: inertial frame (Basis I), body-frame (Basis B), and wind-frame (Basis W). The definition of each frame can be found in Section 2.1.1.

$$\sum \vec{M} = \frac{d^I}{dt}(\vec{H}) \tag{2.60}$$

The angular momentum vector itself is defined by Eq. (2.61) where $\vec{\omega}_b$ is the angular velocity vector of the body-frame to the inertial frame and $\bar{\bar{I}}_b$ is the vehicle inertia tensor with respect to the body axis.

$$\vec{H} = \bar{\bar{I}}_b \vec{\omega}_b \tag{2.61}$$

Depending on the body axes chosen, the inertia tensor may be diagonal or fully defined. The former case is generally true when the body axes are aligned with the principal axes. This is generally the case for most aerocapture vehicles. Eq. (2.62) defines a generalized fully defined inertia tensor.

$$\bar{\bar{I}}_b = \begin{bmatrix} I_{xx} & I_{xy} & I_{xz} \\ I_{xy} & I_{yy} & I_{yz} \\ I_{xz} & I_{yz} & I_{zz} \end{bmatrix} \tag{2.62}$$

The angular velocity vector can be decomposed with respect to each body axis. Eq. (2.63) highlights this decomposition where $\dot{s}$ is the roll rate, $\dot{p}$ is the pitch rate, and $\dot{q}$ is the yaw rate.

$$\vec{\omega}_b = \dot{s}\hat{x}_b + \dot{p}\hat{y}_b + \dot{q}\hat{z}_b \tag{2.63}$$

To obtain the inertial time derivative of the angular momentum vector, the Transport Theorem is applied. When taking this time derivative of Eq. (2.61), the inertia tensor is

assumed to be time-invariant. This is generally a good first-order assumption for aerocapture vehicles. The result of the integration is subsequently combined with Eq. (2.60) with its vector components shown in Eq. (2.64).

$$\begin{aligned}
M_l &= I_{xy}\ddot{p} + I_{xz}\ddot{q} + I_{xx}\ddot{s} - \dot{q}\left(I_{yy}\dot{p} + I_{yz}\dot{q} + I_{xy}\dot{s}\right) + \dot{p}\left(I_{yz}\dot{p} + I_{zz}\dot{q} + I_{xz}\dot{s}\right) \\
M_m &= I_{yy}\ddot{p} + I_{yz}\ddot{q} + I_{xy}\ddot{s} + \dot{q}\left(I_{xy}\dot{p} + I_{xz}\dot{q} + I_{xx}\dot{s}\right) - \dot{s}\left(I_{yz}\dot{p} + I_{zz}\dot{q} + I_{xz}\dot{s}\right) \\
M_n &= I_{yz}\ddot{p} + I_{zz}\ddot{q} + I_{xz}\ddot{s} - \dot{p}\left(I_{xy}\dot{p} + I_{xz}\dot{q} + I_{xx}\dot{s}\right) + \dot{s}\left(I_{yy}\dot{p} + I_{yz}\dot{q} + I_{xy}\dot{s}\right)
\end{aligned} \tag{2.64}$$

Given the external moments, the body-frame rotational accelerations can be solved for. Eq. (2.66), Eq. (2.67), Eq. (2.65) provides the general-form solution to the body-frame rotational dynamics of the vehicle where $\ddot{p}$, $\ddot{q}$, $\ddot{s}$ are the pitch, yaw, and roll accelerations respectively.

$$\begin{aligned}
\ddot{s} = -\frac{1}{I_{xz}den}[&I_{xx}I_{xy}I_{xz}I_{yz}\dot{p}\dot{s} + I_{xx}I_{xy}I_{xz}I_{zz}\dot{q}\dot{s} - I_{xx}I_{xz}^2I_{yy}\dot{p}\dot{s} - I_{xx}I_{xz}^2I_{yz}\dot{q}\dot{s} + I_{xy}^2I_{xz}I_{yz}\dot{p}^2 \\
&- I_{xy}^2I_{xz}I_{yz}\dot{s}^2 + I_{xy}^2I_{xz}I_{zz}\dot{p}\dot{q} - I_{xy}I_{xz}^2I_{yy}\dot{p}^2 + I_{xy}I_{xz}^2I_{yy}\dot{s}^2 + I_{xy}I_{xz}^2I_{zz}\dot{q}^2 \\
&- I_{xy}I_{xz}^2I_{zz}\dot{s}^2 - I_{xy}I_{xz}I_{yy}I_{yz}\dot{p}\dot{s} + I_{xy}I_{xz}I_{yy}I_{zz}\dot{q}\dot{s} - 2I_{xy}I_{xz}I_{yz}^2\dot{q}\dot{s} \\
&- I_{xy}I_{xz}I_{yz}I_{zz}\dot{p}\dot{s} + I_{xy}I_{xz}I_{yz}M_n - I_{xy}I_{xz}I_{zz}^2\dot{q}\dot{s} - I_{xy}I_{xz}I_{zz}M_m \\
&- I_{xz}^3I_{yy}\dot{p}\dot{q} + I_{xz}^3(-I_{yz})\dot{q}^2 + I_{xz}^3I_{yz}\dot{s}^2 + I_{xz}^2I_{yy}^2\dot{p}\dot{s} + I_{xz}^2I_{yy}I_{yz}\dot{q}\dot{s} \\
&- I_{xz}^2I_{yy}I_{zz}\dot{p}\dot{s} - I_{xz}^2I_{yy}M_n + 2I_{xz}^2I_{yz}^2\dot{p}\dot{s} + I_{xz}^2I_{yz}I_{zz}\dot{q}\dot{s} + I_{xz}^2I_{yz}M_m \\
&+ I_{xz}I_{yy}^2I_{zz}\dot{p}\dot{q} - I_{xz}I_{yy}I_{yz}^2\dot{p}\dot{q} - I_{xz}I_{yy}I_{yz}I_{zz}\dot{p}^2 + I_{xz}I_{yy}I_{yz}I_{zz}\dot{q}^2 \\
&- I_{xz}I_{yy}I_{zz}^2\dot{p}\dot{q} + I_{xz}I_{yy}I_{zz}M_l + I_{xz}I_{yz}^3\dot{p}^2 - I_{xz}I_{yz}^3\dot{q}^2 + I_{xz}I_{yz}^2I_{zz}\dot{p}\dot{q} \\
&- I_{xz}I_{yz}^2M_l]
\end{aligned} \tag{2.65}$$

$$\begin{aligned}\ddot{p} = -\frac{1}{den}[& - I_{xx}^2 I_{yz}\dot{p}\dot{s} - I_{xx}^2 I_{zz}\dot{q}\dot{s} + I_{xx}I_{xy}I_{xz}\dot{p}\dot{s} - I_{xx}I_{xy}I_{yz}\dot{p}^2 + I_{xx}I_{xy}I_{yz}\dot{s}^2 - I_{xx}I_{xy}I_{zz}\dot{p}\dot{q} \\ & + I_{xx}I_{xz}^2\dot{q}\dot{s} - I_{xx}I_{xz}I_{yz}\dot{p}\dot{q} - I_{xx}I_{xz}I_{zz}\dot{q}^2 + I_{xx}I_{xz}I_{zz}\dot{s}^2 + I_{xx}I_{yy}I_{yz}\dot{p}\dot{s} + I_{xx}I_{yz}^2\dot{q}\dot{s} \\ & + I_{xx}I_{yz}I_{zz}\dot{p}\dot{s} - I_{xx}I_{yz}M_n + I_{xx}I_{zz}^2\dot{q}\dot{s} + I_{xx}I_{zz}M_m + I_{xy}^2 I_{xz}\dot{p}^2 - I_{xy}^2 I_{xz}\dot{s}^2 \\ & - I_{xy}^2 I_{zz}\dot{q}\dot{s} + 2I_{xy}I_{xz}^2\dot{p}\dot{q} - I_{xy}I_{xz}I_{yy}\dot{p}\dot{s} + I_{xy}I_{xz}I_{zz}\dot{p}\dot{s} + I_{xy}I_{xz}M_n - I_{xy}I_{yy}I_{zz}\dot{p}\dot{q} \\ & + I_{xy}I_{yz}I_{zz}\dot{p}^2 - I_{xy}I_{yz}I_{zz}\dot{q}^2 + I_{xy}I_{zz}^2\dot{p}\dot{q} - I_{xy}I_{zz}M_l + I_{xz}^3\dot{q}^2 - I_{xz}^3\dot{s}^2 - 2I_{xz}^2 I_{yz}\dot{p}\dot{s} \\ & - I_{xz}^2 I_{zz}\dot{q}\dot{s} - I_{xz}^2 M_m + I_{xz}I_{yy}I_{yz}\dot{p}\dot{q} - I_{xz}I_{yz}^2\dot{p}^2 + I_{xz}I_{yz}^2\dot{q}^2 - I_{xz}I_{yz}I_{zz}\dot{p}\dot{q} \\ & + I_{xz}I_{yz}M_l]\end{aligned} \tag{2.66}$$

$$\begin{aligned}\ddot{q} = -\frac{1}{den}[& I_{xx}^2 I_{yy}\dot{p}\dot{s} + I_{xx}^2 I_{yz}\dot{q}\dot{s} - I_{xx}I_{xy}^2\dot{p}\dot{s} - I_{xx}I_{xy}I_{xz}\dot{q}\dot{s} + I_{xx}I_{xy}I_{yy}\dot{p}^2 - I_{xx}I_{xy}I_{yy}\dot{s}^2 \\ & + I_{xx}I_{xy}I_{yz}\dot{p}\dot{q} + I_{xx}I_{xz}I_{yy}\dot{p}\dot{q} + I_{xx}I_{xz}I_{yz}\dot{q}^2 - I_{xx}I_{xz}I_{yz}\dot{s}^2 - I_{xx}I_{yy}^2\dot{p}\dot{s} - I_{xx}I_{yy}I_{yz}\dot{q}\dot{s} \\ & + I_{xx}I_{yy}M_n - I_{xx}I_{yz}^2\dot{p}\dot{s} - I_{xx}I_{yz}I_{zz}\dot{q}\dot{s} - I_{xx}I_{yz}M_m + I_{xy}^3\left(-\dot{p}^2\right) + I_{xy}^3\dot{s}^2 \\ & - 2I_{xy}^2 I_{xz}\dot{p}\dot{q} + I_{xy}^2 I_{yy}\dot{p}\dot{s} + 2I_{xy}^2 I_{yz}\dot{q}\dot{s} - I_{xy}^2 M_n - I_{xy}I_{xz}^2\dot{q}^2 + I_{xy}I_{xz}^2\dot{s}^2 \\ & - I_{xy}I_{xz}I_{yy}\dot{q}\dot{s} + I_{xy}I_{xz}I_{zz}\dot{q}\dot{s} + I_{xy}I_{xz}M_m + I_{xy}I_{yy}I_{yz}\dot{p}\dot{q} - I_{xy}I_{yz}^2\dot{p}^2 + I_{xy}I_{yz}^2\dot{q}^2 \\ & - I_{xy}I_{yz}I_{zz}\dot{p}\dot{q} + I_{xy}I_{yz}M_l + I_{xz}^2 I_{yy}\dot{p}\dot{s} - I_{xz}I_{yy}^2\dot{p}\dot{q} + I_{xz}I_{yy}I_{yz}\dot{p}^2 - I_{xz}I_{yy}I_{yz}\dot{q}^2 \\ & + I_{xz}I_{yy}I_{zz}\dot{p}\dot{q} - I_{xz}I_{yy}M_l]\end{aligned} \tag{2.67}$$

The above equations have a common denominator term, denoted *den*. Its equation is represented by Eq. (2.68)

$$den = -I_{xx}I_{yy}I_{zz} + I_{xx}I_{yz}^2 + I_{xy}^2 I_{zz} - 2I_{xy}I_{xz}I_{yz} + I_{xz}^2 I_{yy} \tag{2.68}$$

If the body-axes are assumed to be principal axes such that I_{xy}, I_{xz}, and I_{yz} are zero, then the rotational dynamics simplify significantly. Substituting these conditions into Eq. (2.66), Eq. (2.67), and Eq. (2.65) yield the principal axes rotational equations of motion as shown

in Eq. (2.69). The remainder of this derivation will retain the assumption of principal axes. If non-principal axes are desired, the analysis can still utilize the same methodology.

$$\begin{aligned} \ddot{s} &= \frac{M_l + (I_{yy} - I_{zz})\,\dot{p}\dot{q}}{I_{xx}} \\ \ddot{p} &= \frac{M_m + (I_{zz} - I_{xx})\,\dot{q}\dot{s}}{I_{yy}} \\ \ddot{q} &= \frac{M_n + (I_{xx} - I_{yy})\,\dot{p}\dot{s}}{I_{zz}} \end{aligned} \tag{2.69}$$

Eq. (2.69) can be numerically integrated to provide the vehicle attitude evolution with respect to the principal body axis. For applications of aerodynamic control surfaces, it maybe desirable to express the vehicle attitude with respect to the wind-axes. Both axes can be related through angle of attack and side-slip angle. In fact, these two angles along with bank angle serve as Eulerian rotational angles. Using Figure 2.3 as a reference, the change of coordinates matrix from wind to body can be computed, which is shown in Eq. (2.70).

$$\begin{bmatrix} \hat{x_b} \\ \hat{y_b} \\ \hat{z_b} \end{bmatrix} = \begin{bmatrix} \cos\alpha\cos\beta & -\cos\alpha\sin\beta & -\sin\alpha \\ \sin\beta & \cos\beta & 0 \\ \sin\alpha\cos\beta & -\sin\alpha\sin\beta & \cos\alpha \end{bmatrix} \begin{bmatrix} \hat{x_w} \\ \hat{y_w} \\ \hat{z_w} \end{bmatrix} \tag{2.70}$$

The angular velocity vector of Basis W with respect to Basis I can be modeled by Eq. (2.71) where $\dot{\sigma}$ is the bank angle rate of change, $\dot{\alpha}$ is the angle of attack rate of change, and $\dot{\beta}$ is the rate of change of side-slip.

$$\vec{\omega}_w = \dot{\sigma}\hat{x_w} + \dot{\alpha}\hat{y_w} + \dot{\beta}\hat{z_w} \tag{2.71}$$

Substituting Eq. (2.71) into Eq. (2.70) allows for the wind-frame angular velocity to be related to the body-frame angular velocity. To link the angular accelerations, the time

derivative of this substitution is taken. Doing so component-wise yields Eq. (2.72), Eq. (2.73), and Eq. (2.74).

$$\begin{aligned}\ddot{s} = [&- \dot{\alpha}\dot{\sigma}\sin(\alpha)\cos(\beta) - \dot{\beta}\dot{\sigma}\cos(\alpha)\sin(\beta) + \dot{\alpha}^2\sin(\alpha)\sin(\beta) - \dot{\alpha}\dot{\beta}\cos(\alpha) \\ &-\dot{\alpha}\dot{\beta}\cos(\alpha)\cos(\beta) - \ddot{\alpha}\cos(\alpha)\sin(\beta) - \ddot{\beta}\sin(\alpha) + \ddot{\sigma}\cos(\alpha)\cos(\beta)]\end{aligned} \tag{2.72}$$

$$\ddot{p} = [- \dot{\alpha}\dot{\beta}\sin(\beta) + \ddot{\alpha}\cos(\beta) + \dot{\beta}\dot{\sigma}\cos(\beta) + \ddot{\sigma}\sin(\beta)] \tag{2.73}$$

$$\begin{aligned}\ddot{q} = [&- \dot{\beta}\dot{\sigma}\sin(\alpha)\sin(\beta) + \dot{\alpha}\dot{\sigma}\cos(\alpha)\cos(\beta) - \dot{\alpha}\dot{\beta}\sin(\alpha) + \dot{\alpha}^2(-\cos(\alpha))\sin(\beta) \\ &-\dot{\alpha}\dot{\beta}\sin(\alpha)\cos(\beta) - \ddot{\alpha}\sin(\alpha)\sin(\beta) + \ddot{\beta}\cos(\alpha) + \ddot{\sigma}\sin(\alpha)\cos(\beta)]\end{aligned} \tag{2.74}$$

Using Eq. (2.72), Eq. (2.73), , Eq. (2.74), and Eq. (2.71), expressions for $\ddot{s}$, $\ddot{p}$, $\ddot{q}$, $\dot{s}$, $\dot{p}$, and $\dot{q}$ can be substituted into Eq. (2.69). Solving for $\ddot{\alpha}$, $\ddot{\beta}$, and $\ddot{\sigma}$ yields the wind-frame rotational equations of motion for as shown in Eq. (2.75), Eq. (2.76), and Eq. (2.77).

$$\begin{aligned}\ddot{\sigma} = &-\sin(\beta)[\dot{\beta}\dot{\sigma}\cos(\beta) - \dot{\alpha}\dot{\beta}\sin(\beta) - \frac{M_m}{I_{yy}} \\ &+\frac{I_{zz} - I_{xx}}{I_{yy}}(\dot{\sigma}\cos(\alpha)\cos(\beta) - \dot{\beta}\sin(\alpha) - \dot{\alpha}\cos(\alpha)\sin(\beta))(\dot{\beta}\cos(\alpha) \\ &+\sin(\alpha)\left(\dot{\sigma}\cos(\beta) - \dot{\alpha}\sin(\beta)\right))] - \frac{\cos(\beta)}{4I_{xx}}[-4M_l\cos(\alpha) \\ &+\frac{1}{I_{zz}}[-4I_{xx}M_n\sin(\alpha) - 2\dot{\beta}\cos(2\alpha)(I_{xx} - I_{zz})(I_{xx} - I_{yy} + I_{zz})(\dot{\alpha}\cos(\beta) \\ &+\dot{\sigma}\sin(\beta)) + 2\dot{\beta}(\dot{\sigma}\sin(\beta)\left(I_{xx}^2 - I_{xx}(I_{yy} + 2I_{zz}) + I_{zz}(I_{zz} - I_{yy})\right) \\ &+\dot{\alpha}\left(\cos(\beta)\left(-I_{zz}(2I_{xx} + I_{yy}) + I_{xx}(I_{xx} - I_{yy}) + I_{zz}^2\right) - 2I_{xx}I_{zz}\right)) \\ &+\sin(2\alpha)(I_{xx} - I_{zz})(I_{xx} - I_{yy} + I_{zz})\left(\left(\dot{\alpha}^2 - \dot{\sigma}^2\right)\sin(2\beta) - 2\dot{\alpha}\dot{\sigma}\cos(2\beta)\right)]]\end{aligned} \tag{2.75}$$

$$
\begin{aligned}
\ddot{\alpha} = \frac{\cos^2(\beta)}{I_{xx}I_{yy}I_{zz}}[&I_{xx}I_{zz}\dot{\beta}^2\sin(\alpha)\cos(\alpha)\sec(\beta)\left(I_{xx}-I_{zz}\right)\\
&+\frac{1}{4}\sec(\beta)[-4I_{xx}I_{yy}M_n\sin(\alpha)\tan(\beta)+4I_{xx}I_{zz}M_m-4I_{yy}I_{zz}M_l\cos(\alpha)\tan(\beta)\\
&-\sin(2\alpha)(I_{xx}-I_{zz})(\dot{\sigma}-\dot{\alpha}\tan(\beta))[\dot{\alpha}\sin(2\beta)(I_{xx}-I_{yy})(I_{yy}-I_{zz})\\
&+\dot{\sigma}(-\cos(2\beta)(I_{xx}-I_{yy})(I_{yy}-I_{zz})+I_{zz}(I_{xx}+I_{yy})+I_{yy}(I_{xx}-I_{yy}))]]\\
&+\frac{1}{2}\dot{\beta}[-2\dot{\alpha}\tan(\beta)[I_{yy}I_{zz}\cos^2(\alpha)(I_{xx}\sec(\beta)+I_{yy}-I_{zz})\\
&+I_{xx}I_{yy}\sin^2(\alpha)(-I_{xx}+I_{yy}+I_{zz}\sec(\beta))+I_{xx}I_{zz}\sin^4(\alpha)(I_{xx}-I_{zz})\\
&+I_{xx}I_{zz}\cos^4(\alpha)(I_{zz}-I_{xx})]+\dot{\sigma}[2I_{xx}\sin^2(\alpha)(-I_{zz}\left(\sin^2(\alpha)(I_{zz}-I_{xx})+I_{yy}\right)\\
&-I_{yy}\tan^2(\beta)(-I_{xx}+I_{yy}+I_{zz}))+I_{yy}I_{zz}\cos^2(\alpha)\sec^2(\beta)(-2I_{xx}\\
&+\cos(2\beta)(I_{yy}-I_{zz})-I_{yy}+I_{zz})+2I_{xx}I_{zz}\cos^4(\alpha)(I_{zz}-I_{xx})]]]
\end{aligned}
\tag{2.76}
$$

$$
\begin{aligned}
\ddot{\beta} = \frac{1}{4I_{xx}I_{zz}}[&4I_{xx}M_n\cos(\alpha)-4\dot{\alpha}I_{xx}I_{zz}\dot{\sigma}\cos(\beta)\\
&+2\cos(2\beta)\dot{\alpha}\dot{\sigma}(I_{xx}^2-I_{xx}I_{yy}+I_{zz}(I_{zz}-I+yy))-4I_{zz}M_l\sin(\alpha)+4\dot{\alpha}^2I_{xx}I_{zz}\sin(\beta)\\
&-2\dot{\beta}\sin(2\alpha)(I_{xx}-I_{zz})(I_{xx}-I_{yy}+I_{zz})\left(\dot{\alpha}\cos(\beta)+\dot{\sigma}\sin(\beta)\right)\\
&+\left(\dot{\sigma}^2-\dot{\alpha}^2\right)\sin(2\beta)\left(I_{xx}^2-I_{xx}I_{yy}+I_{zz}(I_{zz}-I_{yy})\right)\\
&+\cos(2\alpha)(I_{xx}-I_{zz})(I_{xx}-I_{yy}+I_{zz})\left(\left(\dot{\sigma}^2-\dot{\alpha}^2\right)\sin(2\beta)+2\dot{\alpha}\dot{\sigma}\cos(2\beta)\right)]
\end{aligned}
\tag{2.77}
$$

Even with the assumption of principal axes, the above equations illustrate the highly coupled attitude dynamics as expressed in the wind-frame. The advantage of utilizing the wind-frame over the body-frame for expressing the attitude dynamics is that the dynamics can be directly mapped to both the flight control variables as well as the kinematic flight dynamics. For BAM and DFC, the dynamics of the control variables of σ, α, and β are explicitly modeled. This can allow for the flight controller to be designed using these governing dynamics for the purpose of achieving the control commands from the guidance algorithm.

Additionally, the wind-frame attitude dynamics naturally couple with the kinematics equations of motion to provide a full 6DOF characterization of the flight dynamics.

External Moments

The forces and moments acting on the vehicle act at the aerodynamic reference point, $(\,x_{ref}\;\;y_{ref}\;\;z_{ref}\,)$, which can be offset from the center of mass, $(\,x_{cg}\;\;y_{cg}\;\;z_{cg}\,)$. The offset distance is normalized by reference length, d, when computing the aerodynamic coefficient induced moments. The aerodynamic pitch, yaw, and roll moments about Basis B are modeled using Eq. (2.78), Eq. (2.79), Eq. (2.80) respectively. In these three equations, q_∞ is the freestream dynamic pressure.

$$\vec{M}_{m,aero} = \left[C_m + C_A\left(\frac{z_{cg} - z_{ref}}{d}\right) - C_N\left(\frac{x_{cg} - x_{ref}}{d}\right)\right] q_\infty A_{ref} d \tag{2.78}$$

$$\vec{M}_{n,aero} = \left[C_n - C_Y\left(\frac{x_{cg} - x_{ref}}{d}\right) - C_A\left(\frac{y_{cg} - y_{ref}}{d}\right)\right] q_\infty A_{ref} d \tag{2.79}$$

$$\vec{M}_{l,aero} = \left[C_l + C_N\left(\frac{y_{cg} - y_{ref}}{d}\right) + C_Y\left(\frac{z_{cg} - z_{ref}}{d}\right)\right] q_\infty A_{ref} d \tag{2.80}$$

In addition to the natural moments produced by the vehicle, external moments can be produced through the deflection of aerodynamic control surfaces or propulsively through RCS thrusters. These external pitch, yaw, and roll moments about Basis B are modeled using Eq. (2.81), Eq. (2.82), Eq. (2.83) respectively. The effectiveness of the aerodynamic control surfaces is directly dictated by the dynamic pressure while the effectiveness of the RCS thrusters as generally invariant to dynamic pressure.

$$\vec{M}_{m,ext} = q_\infty A_{ref} d C_{m,acs} + M_{m,RCS} \tag{2.81}$$

$$\vec{M}_{n,ext} = q_\infty A_{ref} d C_{n,acs} + M_{n,RCS} \tag{2.82}$$

$$\vec{M}_{l,ext} = q_\infty A_{ref} dC_{l,acs} + M_{l,RCS} \tag{2.83}$$

Putting all together, the pitch, yaw, and roll moments can be computed using Eq. (2.84), Eq. (2.85), and Eq. (2.86). These equations are used as inputs into the rotational equations of motion.

$$M_m = M_{m,aero} + M_{m,ext} \tag{2.84}$$

$$M_n = M_{n,aero} + M_{n,ext} \tag{2.85}$$

$$M_l = M_{l,aero} + M_{l,ext} \tag{2.86}$$

This completes the derivation of the rotational equations of motion. Subsequent analysis in this dissertation will focus on 3DOF translational motion. The rotational equations of motion are provided in this dissertation to demonstrate the coupled dynamics between the flight controls of interest (BAM with σ, DFC with α and β) and the attitude of the vehicle. The future work related to studies on 6DOF motion can utilize these equations.

2.1.3 Analytical Hypersonic Aerodynamics

Motivation

Understanding the vehicle aerodynamic properties are a fundamental characteristic needed for aerocapture. This understanding can be accomplished through application of computational fluid dynamic (CFD) codes that simulate the flow physics. A typical aerocapture trajectory consists of a large range of velocities and atmosphere densities. As a result, numerous CFD runs would need to be conducted for a single aerocapture trajectory. The trajectories can vary depending on the vehicle chosen and the planetary destination assessed. The cumulative result is a laborious and potentially computationally-expensive process for assessing the vehicle aerodynamics.

Fortunately, first-order methods have been developed for assessing the vehicle aerodynamics. Aerocapture trajectories spend nearly their entire flight profile in the hypersonic flow regime. Subsequently, the hypersonic aerodynamics can be sufficiently approximated using Newtonian flow theory [74]. Issac Newton in his work *Principia* [75] first introduced the concept of modeling flow of a fluid as a system of particles moving in uniform motion. If a body is introduced to the flowfield, then the particles would impact the body in a manner such that the momentum perpendicular to the body is lost and the momentum tangential to the body is conserved. The momentum transfer normal to body leads to a pressure force that the fluid exerts on the body. Assuming pressure as the only force imparted by the fluid onto to body leads to the formulation of a sine-squared law for the pressure coefficient C_p.

$$C_p = 2sin^2(\eta) \tag{2.87}$$

In Eq. (2.87), C_p depends only on the local inclination of the flow to the body and not on the freestream properties itself. At hypersonic speeds, the presence of a bow shock upstream of the vehicle affects the motion of the particles. Lees suggested a modification to the theory in which the conditions at the stagnation point are met [76]. This modified Newtonian theory has Eq. (2.87) written in the form of Eq. (2.88) where K is equal to the maximum value of the pressure coefficient evaluated at the stagnation point of the normal shock.

$$C_p = Ksin^2(\eta) \tag{2.88}$$

Using normal shock relations, K can written in the form of Eq. (2.89) where M_∞ is the freestream Mach number and $\bar{\gamma}$ is the specific gas constant of the freestream.

$$K = \frac{2}{\bar{\gamma}M_\infty^2}\left(\frac{\left(\frac{(\bar{\gamma}+1)^2M_\infty^2}{4\bar{\gamma}M_\infty^2-2(\bar{\gamma}-1)}\right)^{\frac{\bar{\gamma}}{\bar{\gamma}-1}}(1-\bar{\gamma}+2\bar{\gamma}M_\infty^2)}{\bar{\gamma}+1}-1\right) \tag{2.89}$$

With modified Newtonian theory, C_p and thus the vehicle aerodynamics depend on the freestream properties. For $M_\infty \to \infty$, Eq. (2.89) converges to

$$K = \left[\frac{(\gamma+1)^2}{4\gamma}\right]^{\frac{\gamma}{\gamma-1}} \left[\frac{4}{\gamma+1}\right] \tag{2.90}$$

For $\gamma = 1$, Eq. (2.90) equals 2. This indicates that traditional Newtonian theory can be recovered under a certain set of assumptions. Modified Newtonian is generally more accurate for predicting pressure distributions over blunt bodies as compared to slender bodies. Conversely, traditional Newtonian is generally more suitable for application on slender bodies. The subtle differences in the models can be attributed to constant K.

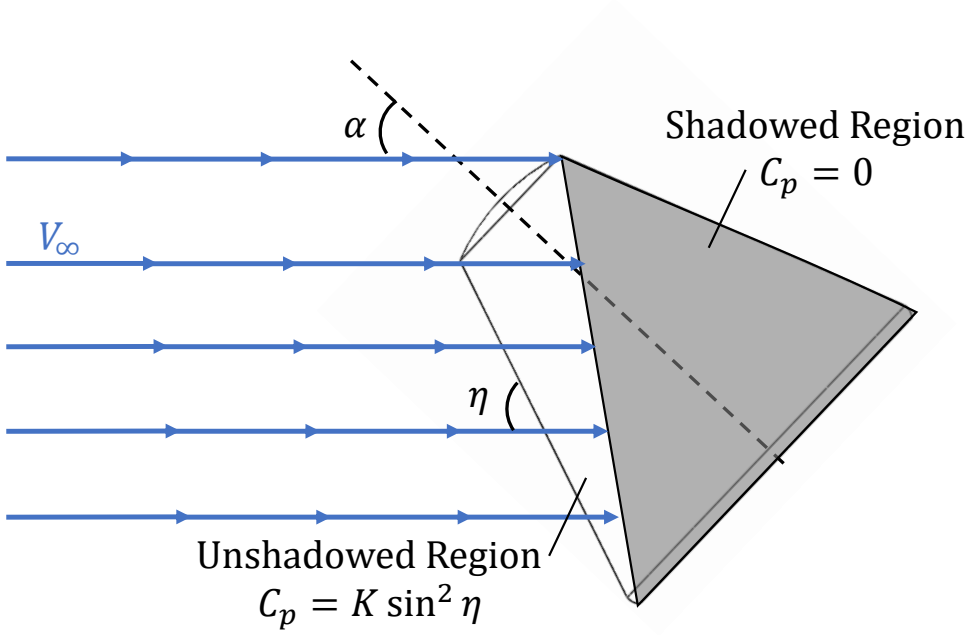

Figure 2.4. Newtonian Aerodynamics Visualization. Imaged adapted from [74]

Figure 2.4 shows a high-level representation of the Newtonian aerodynamics model. For portions of the body that are not exposed to the flowfield, known as the shadowed region, no momentum transfer occurs and thus $C_p = 0$. Integrating the pressure coefficient around the body surface in the unshadowed region allows for the vehicle aerodynamic forces and moments to be computed. The result of Newtonian flow theory is that the aerodynamics can be parameterized based off the *shape* of the vehicle. For simple shapes, exact analytical

relations for the vehicle aerodynamics can be achieved. This lends itself to use in the mathematical formulation of aerocapture flight control laws. It is important to keep in mind that Newtonian flow theory provides an *inviscid* solution to the hypersonic aerodynamics. Viscous effects, such as shock-body and shock-boundary layer interactions, that tend to worsen the aerodynamic capability of the vehicle are not captured in the theory. These effects are typically assessed using CFD codes. The subsequent errors in vehicle aerodynamics can be can be addressed in a Monte Carlo setting though simulation of aerodynamic uncertainty.

Methodology

The application of Newtonian theory to hypersonic vehicle aerodynamics has been studied extensively in literature [77]–[80]. The methodology utilized in this work will generally follow the methodology introduced by Grant [81] and will focus on sphere-cone aeroshell geometries assuming flight conditions that lead to no shadowed regions. To handle analytical integration, *Mathematica* is utilized.

The methodology decomposes a vehicle aeroshell into basic shapes. A sphere-cone consists of a hemispherical nose and a conical frustrum. For each shape, a series of five steps are conducted to obtain their respective body-frame aerodynamic coefficients.

In the first step, the surface of the shape is parameterized such that a position vector, r, is defined by two independent variables, u and v. Using vector calculus, the surface normal vector can be calculated using $\vec{r}_u \times \vec{r}_v$ where $r_u = \frac{\partial \vec{r}}{\partial u}$ and $r_v = \frac{\partial \vec{r}}{\partial v}$. Additionally, the differential area of the surface, dA, under which the analytical integration occurs can be computed by $dA = ||\vec{r}_u \times \vec{r}_v||$.

In the second step, the pressure coefficient is computed. From Figure 2.4, the $\sin(\eta)$ can be computed by $\sin(\eta) = \hat{V}_\infty^T \hat{n}$. The unit normal vector, $\hat{n}$ can be computed by $\hat{n} = \frac{\vec{r}_u \times \vec{r}_v}{dA}$. In the wind-frame, the free-stream velocity vector is $\vec{V}_\infty = -V_\infty \hat{x}_w$. Transforming to the body-frame using Eq. (2.70) yields

$$\vec{V}_\infty = V_\infty[-\cos(\alpha)\cos(\beta)\hat{x}_b - \sin(\beta)\hat{y}_b - \sin(\alpha)\cos(\beta)\hat{z}_b] \tag{2.91}$$

The third step is to compute the surface integrals for calculations of the body-frame aerodynamic force and moment coefficients. The aerodynamic coefficients are computed using Eq. (2.92) and the moment coefficients are computed using Eq. (2.93). The reference area, A_{ref}, is selected as the projected area of the shape on the y-z plane. For sphere-cone shapes, this area is typically circular. The reference length, l_{ref}, is selected to be the maximum span of the shape in the x-direction.

$$\begin{bmatrix} -C_A \\ C_Y \\ -C_N \end{bmatrix} = \frac{1}{A_{ref}} \iint_S C_p \begin{bmatrix} \hat{n}^T \hat{x} \\ \hat{n}^T \hat{y} \\ \hat{n}^T \hat{z} \end{bmatrix} dA \tag{2.92}$$

$$\begin{bmatrix} C_l \\ C_m \\ C_n \end{bmatrix} = \frac{1}{A_{ref} l_{ref}} \iint_S C_p \begin{bmatrix} (\vec{r} \times \vec{n})^T \hat{x} \\ (\vec{r} \times \vec{n})^T \hat{y} \\ (\vec{r} \times \vec{n})^T \hat{z} \end{bmatrix} dA \tag{2.93}$$

The fourth step is the superposition of shapes to form the aeroshell. Due to varying sizes of each shape, the aerodynamic coefficients and moments are scaled using a common reference area and length. For a sphere-cone, the common reference area and length is assumed to be the overall sphere-cone reference area and overall sphere-cone span, respectively.

The fifth step is the transformation of body-frame aerodynamic coefficients to the wind-frame and simplification of the analytic equations. This step is not explicitly utilized by Grant in his work. This step is intended to link the analytical expressions obtained from the Newtonian aerodynamic model to the formulation of aerocapture flight control laws. The analytical results from Eq. (2.92) can be rotated to the wind-frame using the inverse of Eq. (2.70). The resulting equations are non-linear and define the vehicle's lift, drag, and side-force coefficients as functions of the freestream conditions, via K , aeroshell geometry, as well as angle of attack and side-slip angle. The latter terms may appear as trigonometric terms in the aerodynamic equations. This makes it difficult to obtain closed-form control laws for DFC, especially when root-solving an equation of the form $A\cos(\alpha) + B\sin(\alpha) = 0$ for α. For a sphere-cone, it is common for small angles about zero total angle of attack to be commanded. At this reference point, a first-order and second-order Taylor Series approx-

imation is done to simplify the non-linear expressions into simpler mathematical forms. The accuracy of these approximations is explored.

Morphable Sphere-Cone

A morphable sphere-cone consists of a rigid hemispherical nose and a morphable conical frustrum as shown in Figure 2.5. The key difference from a traditional sphere-cone is that the conical frustrum's cone angle can change. A base cone angle, $\delta_{c,base}$ can be selected to enable a smooth transition between the nose and frustrum; but, modifying the cone angle from the base will lead to non-smooth transition. At the transition point, $\omega_{max} = 90° - \delta_{c,base}$. This variant of the sphere-cone is envisioned for application on DMCV aerocapture vehicles where modulating the cone angle from the base can allow for the vehicle ballistic coefficient to change through the reduction in the vehicle drag coefficient and reference area. Due to the morphing geometry, the aeroshell payload fairing is cylindrical. The aeroshell nose radius is thereby constrained by the diameter of the cylinder, d, such that $d = r_n \sin(\omega_{max})$. During launch, the aeroshell stows into a compact form such $\delta_c = 0$ and length of aeroshell is $r_n\,(1 - \cos(\omega_{max})) + S$. A morphable sphere-cone has a constant conical frustrum diagonal length, S, rather than a constant r_c. This leads to the geometry being fully defined by S, d, and $\delta_{c,base}$.

A polar parameterization of the nose is utilized. Parameters include the elevation angle in the $\hat{x}_b - \hat{z}_b$ plane, which ranges from 0° to ω_{max}, and rotational angle in the $\hat{y}_b - \hat{z}_b$ plane, which ranges from 0° to 360°. Circular reference area of radius r_n and reference length of r_n is assumed for the nose. A cylindrical parametrization of conical frustrum is utilized. Parameters include the cross-sectional radius in the $\hat{y}_b - \hat{z}_b$, which ranges from $r_n \sin(\omega_{max})$ to r_c, and rotational angle in the $\hat{y}_b - \hat{z}_b$ plane, which ranges from 0° to 360°. Circular reference area of radius r_c is assumed for the frustrum. The reference length of the frustrum is computed geometrically to be $\frac{r_n \sin(\omega_{max})}{\tan(\delta_c)}$. Superposition of the two shapes is done with a circular base reference area of radius r_c and base reference length equal to the reference length of the frustrum plus $r_n\,(1 - \cos(\omega_{max}))$. Note that r_n and r_c are both utilized to

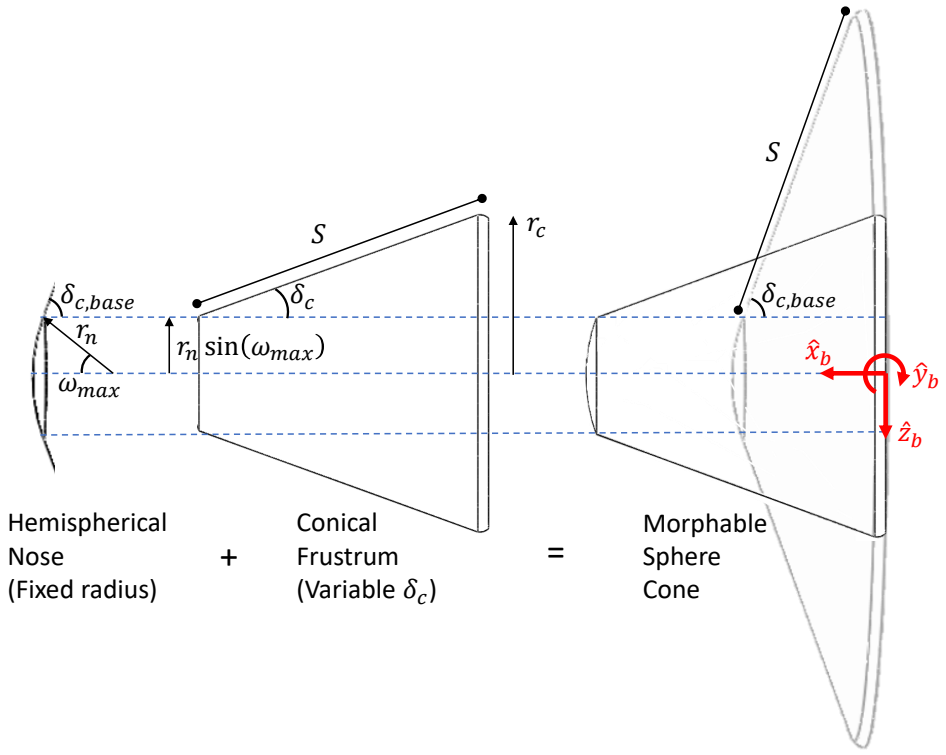

Figure 2.5. Morphable Sphere-Cone Shape Decomposition

provide a natural analogy to the rigid sphere-cone. Geometrical relations to d and S include $r_n = \frac{d}{\sin(\omega_{\max})}$ and $r_c = S\sin(\delta) + r_n \sin(\omega_{max})$.

The resulting full non-linear analytical aerodynamic coefficient equations are shown in Eq. (2.94), Eq. (2.95), and Eq. (2.96). For zero total angle of attack, C_D is non zero. For zero angle of attack, C_L equals zero. Likewise for zero side-slip angle, C_Q equals zeros. These are simple sanity checks on the analytical expressions that produce results expected for an axisymmetrical sphere-cone.

$$
\begin{aligned}
C_D = \frac{K\cos(\alpha)\cos(\beta)}{64 r_c^2}\Big[&\Big(-2\cos(2\delta_c)\left(6\cos^2(\alpha)\cos(2\beta)+3\cos(2\alpha)-1\right)+\cos(2(\alpha-\beta))\\
&+\cos(2(\alpha+\beta))+2\cos(2\alpha)+2\cos(2\beta)+10\Big)\left(2r_c^2-r_n^2\cos(2\delta_{c,base})-r_n^2\right)\\
&+2r_n^2\cos^2(\delta_{c,base})\Big(2\cos^2(\alpha)\cos(2\beta)(5-3\cos(2\delta_{c,base}))\\
&+\cos(2\alpha)(5-3\cos(2\delta_{c,base}))+\cos(2\delta_{c,base})+9\Big)\\
&-16\tan(\beta)\sin(2\beta)\left(\cos^2(\delta_c)\left(-2r_c^2+r_n^2\cos(2\delta_{c,base})+r_n^2\right)-r_n^2\cos^4(\delta_{c,base})\right)\\
&+16\tan(\alpha)\sin(2\alpha)\cos^2(\beta)\left(\cos^2(\delta_c)\left(2r_c^2-r_n^2\cos(2\delta_{c,base})-r_n^2\right)+r_n^2\cos^4(\delta_{c,base})\right)\Big]
\end{aligned}
\tag{2.94}
$$

$$C_L = \frac{K\sin(\alpha)}{64r_c^2}\Big[16\sin(2\alpha)\cot(\alpha)\cos^2(\beta)\left(\cos^2(\delta_c)\left(2r_c^2 - r_n^2\cos(2\delta_{c,base}) - r_n^2\right)\right.$$
$$\left. + r_n^2\cos^4(\delta_{c,base})\right) - \left(-2\cos(2\delta_c)\left(6\cos^2(\alpha)\cos(2\beta) + 3\cos(2\alpha) - 1\right) + \cos(2(\alpha-\beta))\right.$$
$$\left. + \cos(2(\alpha+\beta)) + 2\cos(2\alpha) + 2\cos(2\beta) + 10\right)\left(2r_c^2 - r_n^2\cos(2\delta_{c,base}) - r_n^2\right)$$
$$+ 2r_n^2\cos^2(\delta_{c,base})\left(2\cos^2(\alpha)\cos(2\beta)(5 - 3\cos(2\delta_{c,base}))\right.$$
$$\left. + \cos(2\alpha)(5 - 3\cos(2\delta_{c,base})) + \cos(2\delta_{c,base}) + 9\right)\Big] \tag{2.95}$$

$$C_Q = \frac{K\cos(\alpha)\sin(\beta)}{64r_c^2}\Big[\left(-2\cos(2\delta_c)\left(6\cos^2(\alpha)\cos(2\beta) + 3\cos(2\alpha) - 1\right) + \cos(2(\alpha-\beta))\right.$$
$$\left. + \cos(2(\alpha+\beta)) + 2\cos(2\alpha) + 2\cos(2\beta) + 10\right)\left(2r_c^2 - r_n^2\cos(2\delta_{c,base}) - r_n^2\right)$$
$$+ 2r_n^2\cos^2(\delta_{c,base})\left(2\cos^2(\alpha)\cos(2\beta)(5 - 3\cos(2\delta_{c,base}))\right.$$
$$\left. + \cos(2\alpha)(5 - 3\cos(2\delta_{c,base})) + \cos(2\delta_{c,base}) + 9\right)$$
$$+ 16\tan(\alpha)\sin(2\alpha)\cos^2(\beta)\left(\cos^2(\delta_c)\left(2r_c^2 - r_n^2\cos(2\delta_{c,base}) - r_n^2\right) + r_n^2\cos^4(\delta_{c,base})\right)$$
$$+ 16\sin(2\beta)\cot(\beta)\left(\cos^2(\delta_c)\left(-2r_c^2 + r_n^2\cos(2\delta_{c,base}) + r_n^2\right) - r_n^2\cos^4(\delta_{c,base})\right)\Big] \tag{2.96}$$

The resulting full non-linear analytical body-frame aerodynamic moment equations are shown in Eq. (2.97), Eq. (2.98), and Eq. (2.99). As expected for an axisymmetrical sphere-cone, the roll moment coefficient is zero. For zero angle of attack, C_m is zero. Likewise for zero side-slip angle, C_n is zero.

$$C_l = 0 \tag{2.97}$$

$$C_m = \frac{K\sin(2\alpha)\cos^2(\beta)\cot(\delta_c)}{24r_c^2(\cot(\delta_c)(r_c - r_n\cos(\delta_{c,base})) + r_n(-\sin(\delta_{c,base})) + r_n)}(r_c$$
$$- r_n\cos(\delta_{c,base}))\left(6r_c\cos(2\delta_c)(r_c + r_n\cos(\delta_{c,base}))\right.$$
$$\left. - 2\left(r_c^2 + r_c r_n\cos(\delta_{c,base}) + 2r_n^2\cos(2\delta_{c,base}) + 2r_n^2\right)\right) \tag{2.98}$$

$$C_n = \frac{K\cos(\alpha)\sin(2\beta)\cot(\delta_c)}{12r_c^2(\cot(\delta_c)(r_c - r_n\cos(\delta_{c,base})) + r_n(-\sin(\delta_{c,base})) + r_n)}(r_c - r_n\cos(\delta_{c,base}))\left(r_c^2\right.$$
$$\left. - 3r_c\cos(2\delta_c)(r_c + r_n\cos(\delta_{c,base})) + r_c r_n\cos(\delta_{c,base}) + 2r_n^2\cos(2\delta_{c,base}) + 2r_n^2\right) \tag{2.99}$$

The pitching stability derivative can be computed by taking the partial of Eq. (2.98) with respect to α. The yawing stability derivative can be computed by taking the partial of Eq. (2.99) with respect to β. The roll stability derivative can be computed by taking the partial of Eq. (2.97) with respect to β. However do so would be trivial. The resulting pitching and yawing stability derivatives are shown in Eq. (2.100) and Eq. (2.101).

$$\begin{aligned} C_{m_\alpha} = \frac{K\cos(2\alpha)\cos^2(\beta)\cot(\delta_c)}{12r_c^2(\cot(\delta_c)(r_c - r_n\cos(\delta_{c,base})) + r_n(-\sin(\delta_{c,base})) + r_n)}(r_c \\ - r_n\cos(\delta_{c,base}))\left(6r_c\cos(2\delta_c)(r_c + r_n\cos(\delta_{c,base}))\right. \\ \left. - 2\left(r_c^2 + r_c r_n\cos(\delta_{c,base}) + 2r_n^2\cos(2\delta_{c,base}) + 2r_n^2\right)\right) \end{aligned} \tag{2.100}$$

$$\begin{aligned} C_{n_\beta} = \frac{K\cos(\alpha)\cos(2\beta)\cot(\delta_c)}{6r_c^2(\cot(\delta_c)(r_c - r_n\cos(\delta_{c,base})) + r_n(-\sin(\delta_{c,base})) + r_n)}(r_c - r_n\cos(\delta_{c,base}))\left(r_c^2\right. \\ \left. - 3r_c\cos(2\delta_c)(r_c + r_n\cos(\delta_{c,base})) + r_c r_n\cos(\delta_{c,base}) + 2r_n^2\cos(2\delta_{c,base}) + 2r_n^2\right) \end{aligned} \tag{2.101}$$

The ability of a morphable sphere-cone to modulate ballistic coefficient can be numerically simulated using the analytical Newtonian aerodynamic solutions. To validate the solutions, the Configuration Based Aerodynamics (CBAERO) tool is utilized [82]. CBAERO is a widely-used software for conceptual vehicle aero-thermodynamic analysis. It utilizes a panel method approach for computation of pressure distribution over a gridded surface mesh of the aeroshell geometry. The validation process utilizing CBAERO is identical to the one outlined by Grant [81]. CAD geometries of the aeroshell at each deflected cone angle is produced and is subsequently meshed for each CBAERO run.

A conceptual morphable sphere-cone geometry is assumed such that $\delta_{c,base} = 70°$, $r_n = 5.848m$, and $S = 3.5m$. The value for K is assumed to be 2 for illustrative purposes. The total angle of attack is assumed to be zero degrees to emulate ballistic flight. Using Eq. (2.94) to obtain C_D and the geometrical relationship between r_c and S to obtain A_{ref}, the ballistic coefficient can be computed as a function of δ_c. The ballistic coefficient ratio is assumed to be defined as the ballistic coefficient divided by the ballistic coefficient at $\delta_{c,base}$. Figure 2.6 depicts the ballistic coefficient ratio and ballistic coefficient trends for modulation of the aeroshell cone angle. The analytical solutions are shown to be in well agreement with the

CBAERO runs. Trends indicate a quadratic growth in BCR and ballistic coefficient with reductions in cone angle.

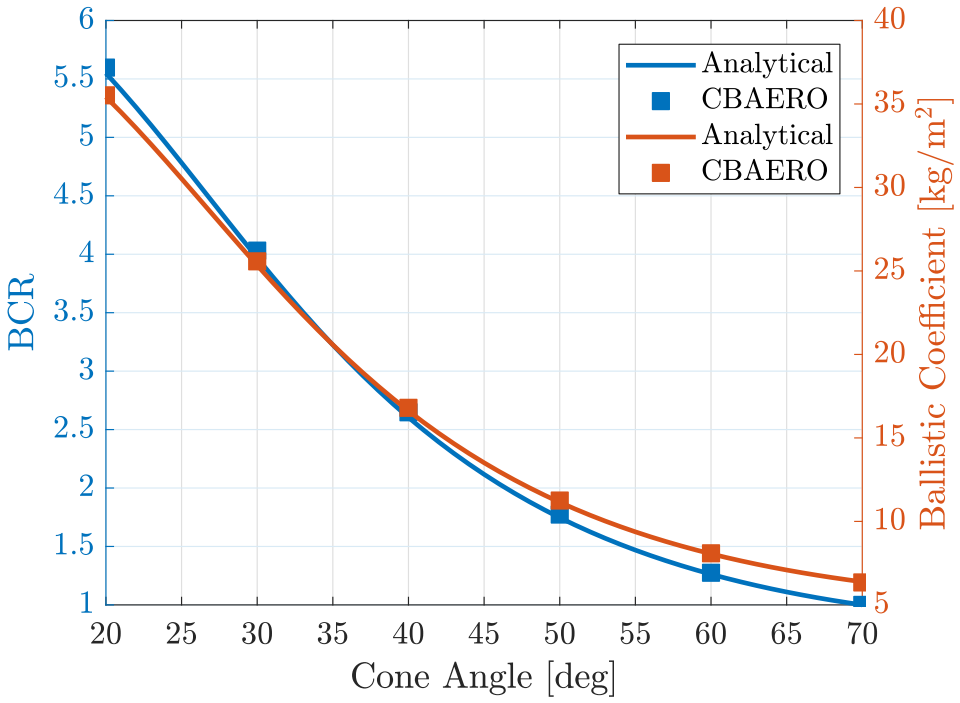

Figure 2.6. Morphable sphere-cone ballistic flight validation

With the analytical model validated, vehicle design trade studies can be conducted. Given a prescribed cone angle bounds, the control capability of a ballistic trajectory can be influenced by the geometrical form-factor of the morphable sphere-cone. Launch vehicle payload fairing constraints impose constraints on the geometry of the sphere-cone. The conical frustrum diagonal length influences the stowed length of the aeroshell where this stowed length must conform to the maximum value specified by the fairing constraint. Due to the lack of a backshell, the satellite payload must be housed inside of the cylindrical payload fairing. The cylinder's diameter, d, is influenced by the form-factor of the satellite. Commonly, the satellite's antenna is the largest sized component and must be contained within the aeroshell. Consequently, d must be properly sized to allow for proper stowage. Different satellite classes may utilize differently sized antennas. Discovery-class satellites delivered to orbit may have antennas with diameters greater than 1m. Small Satellites

delivered to orbit may have antennas with diameters less than 1m. Figure 2.7 and Figure 2.8 depict the morphable sphere-cone design trade space for Satellite and SmallSat payloads.

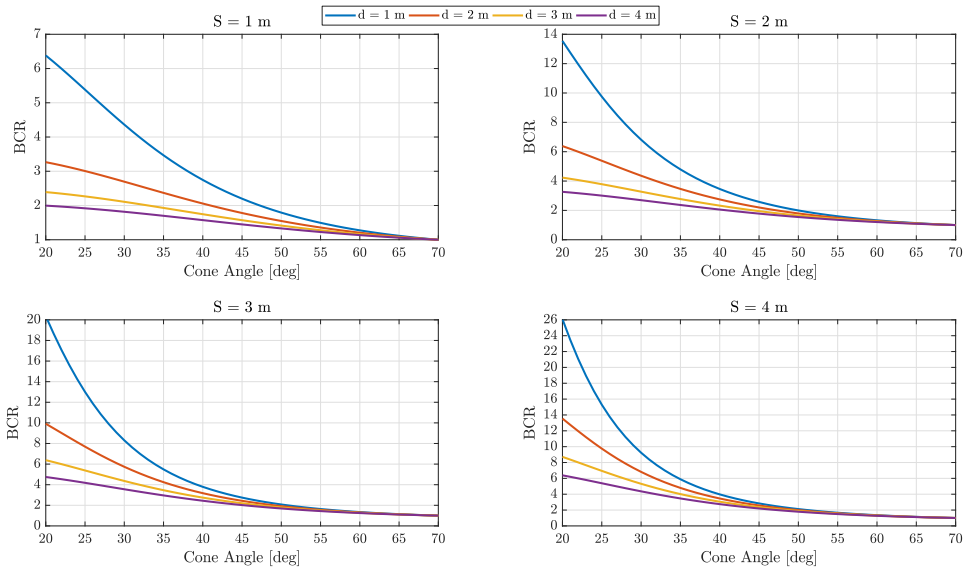

Figure 2.7. Ballistic Coefficient Ratio control capability for different morphable sphere-cone geometries housing Satellite-class payloads

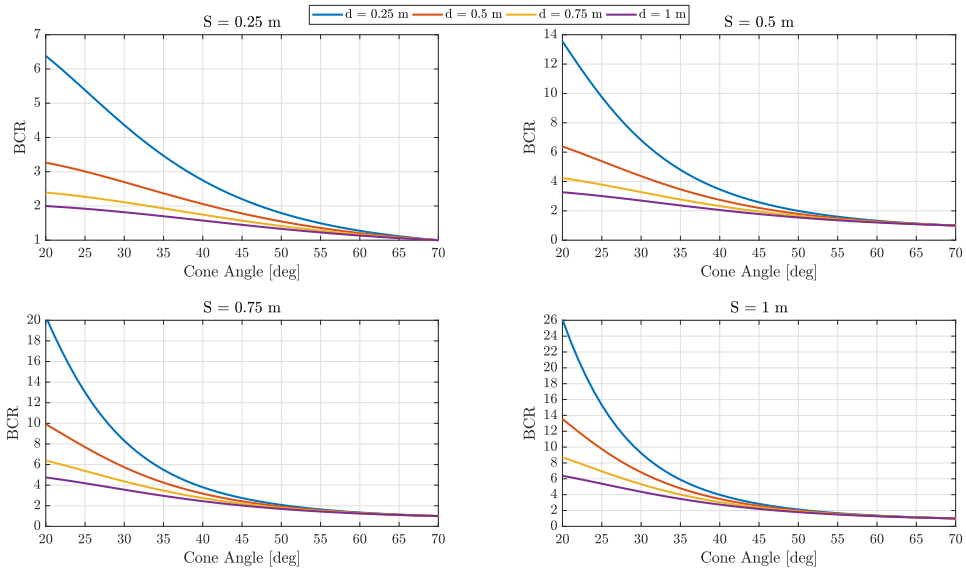

Figure 2.8. Ballistic Coefficient Ratio control capability for different morphable sphere-cone geometries housing SmallSat-class payloads

Despite having different values for S and d, both sets of data produce nearly identical trends and results. For a given value of S and cone angle, decreasing d increases the BCR capability. Similarly for a given value of d and cone angle, increasing S increases the BCR capability. This trend suggests the largest BCR values can be achieved by making the morphable sphere-cone more slender through reduction in nose radius and increase in the overall deflected length of the aeroshell. A caveat to the increase in BCR is the potential increase in aerodynamic heating. Subsequently, the TPS capability utilized by the aeroshell may cap the achievable BCR.

Rigid Sphere-Cone

The geometrical formulation of a rigid sphere-cone is nearly identical to a morphable sphere-cone. The only difference is $\delta_{c,base} = \delta_c$. This leads to a smooth transition between the hemispherical blunt nose and conical frustrum as shown in Figure 2.9. Overall, the sphere-cone geometry can be fully defined by r_c, r_n, and δ_c.

The application of Newtonian aerodynamics methods yields identical analytical solutions for the aerodynamic coefficient, moment, and stability derivative equations as the morphable aeroshell solutions with the substitution $\delta_{c,base} = \delta_c$. Using the full non-linear wind-frame aerodynamics, a first and second-order Taylor Series approximation is done about zero total angle of attack. The resulting expressions are shown in Eq. (2.102) and Eq.(2.103). The second-order model is identical to the first-order model except for C_D, which is quadratic with respect to α and β. The first-order model produces C_D that is not an explicit function of α and β while producing C_L to be a linear function of α as well as C_Q to be a linear function of β.

$$\begin{aligned} C_D &= \frac{K}{16r_c^2}(-\left(3\alpha^2+3\beta^2-1\right)\left(4\cos(2\delta_c)\left(r_n^2-2r_c^2\right)+r_n^2\cos(4\delta_c)\right) \\ &\quad +8r_c^2-3r_n^2\left(3\alpha^2+3\beta^2-1\right)) \\ C_L &= -\frac{\alpha K}{8r_c^2}\left(4\cos(2\delta_c)\left(r_n^2-2r_c^2\right)+r_n^2(\cos(4\delta_c)+3)\right) \\ C_Q &= \frac{\beta K}{8r_c^2}\left(4\cos(2\delta_c)\left(r_n^2-2r_c^2\right)+r_n^2(\cos(4\delta_c)+3)\right) \end{aligned} \tag{2.102}$$

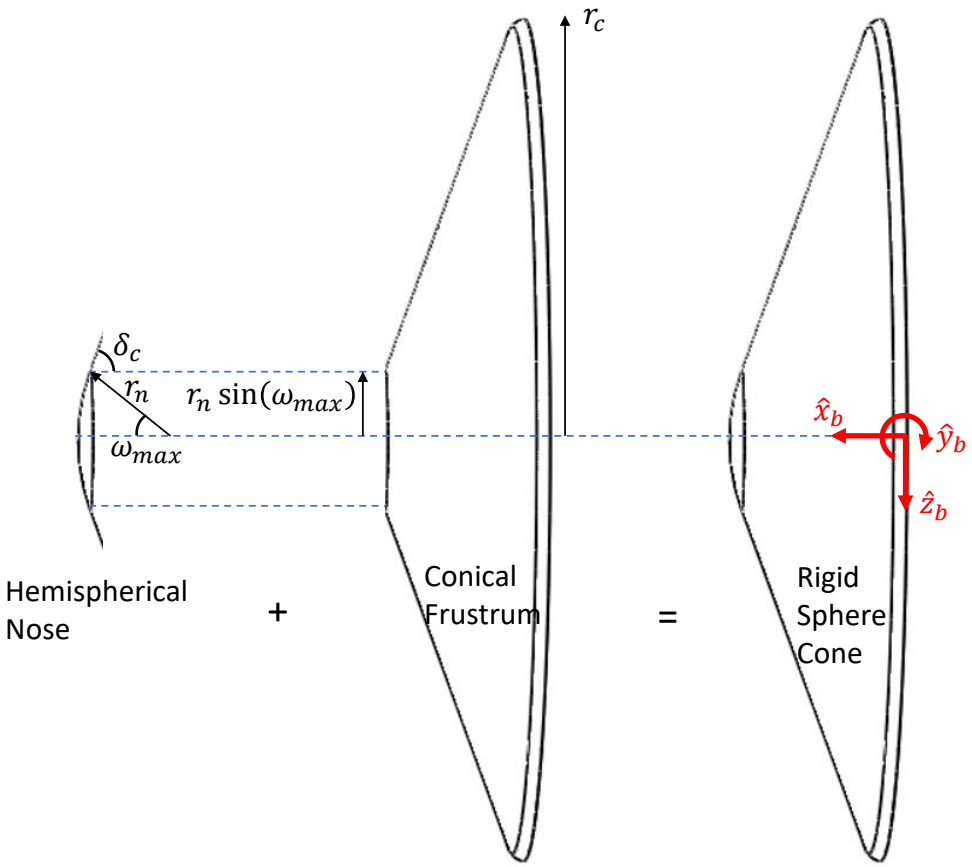

Figure 2.9. Rigid Sphere-Cone Shape Decomposition

$$
\begin{aligned}
C_D &= \frac{K}{16r_c^2}\left(4\cos(2\delta_c)\left(r_n^2 - 2r_c^2\right) + 8r_c^2 + r_n^2\cos(4\delta_c) + 3r_n^2\right) \\
C_L &= -\frac{\alpha K}{8r_c^2}\left(4\cos(2\delta_c)\left(r_n^2 - 2r_c^2\right) + r_n^2(\cos(4\delta_c) + 3)\right) \\
C_Q &= \frac{\beta K}{8r_c^2}\left(4\cos(2\delta_c)\left(r_n^2 - 2r_c^2\right) + r_n^2(\cos(4\delta_c) + 3)\right)
\end{aligned}
\tag{2.103}
$$

The accuracy of the analytic Newtonian models can be compared numerically to a higher-fidelity aerodynamic model. An MSL-derived aeroshell geometry is assumed such that $\delta_c = 70°$, $r_n = 1.125m$, and $r_c = 2.25m$. The MSL aerodatabase is utilized as the high-fidelity aerodynamic model [83]. The aerodatabase contains static hypersonic and supersonic aerodynamic coefficient data for a wide range of Mach numbers and total angles of attack. The continuum data is generated using the Langley Aerothermal Upwind Relaxation Algorithm (LAURA) viscous CFD code. The aerodatabase is queried for a wide range of

angles of attack and side-slip angles at a constant Mach number of 20. For this value and specific gas constant of Mars atmosphere of 1.3, Eq. (2.89) provides $K = 1.89$.

Figure 2.10 provides a comparison of the aerodynamic coefficients and Figure 2.11 provides the corresponding coefficient percent error from the MSL aerodatabase solution. For zero side-slip angle, the full analytic model for C_L agrees well within 10% of the aerodatabase solution. The linear and 2nd order models for C_L generally agree well within 10% of the aerodatabase solution up until $\pm 15°$. For angles of attack past this point, the two models tend to overestimate C_L. At $\pm 30°$, both models overestimate C_L by 50%. For zero angle of attack, all three models for C_Q agree well within 10% of the aerodatabase solution for side-slip angles as high as $\pm 10°$. For zero side-slip angle, varying trends can be seen for C_D and L/D. The analytical solutions underestimate C_D for α near zero. This can be attributed to the viscous drag contributions not captured by the inviscid Newtonian solutions. Nevertheless, the full model generally agrees well within 5% of the aerodatabase solution. The linear model accuracy for C_D significantly degrades the further moved away from zero angle of attack. At $\pm 10°$, $\pm 20°$, and $\pm 30°$, the error is within 5%, 20%, and 50%, respectively. On the contrary, the 2nd order model generally agrees well with the aerodatabase with the error within 5% for the range of angles of attack simulated. The consequence of the inaccuracy with the linear model is primarily an underestimation of the vehicle ballistic coefficient. Despite this inaccuracy, the linear model agree very well with the aerodatabase with regards to L/D for the range of angles of attack simulated. This trend can also be seen with the full model. The 2nd order model agrees well with the aerodatabase up until $\pm 15°$. Angles of attack past this point lead to the 2nd order model overestimating L/D with an error of 50% at $\pm 30°$.

Figure 2.12 provides an extension of the aerodynamic coefficient profiles to the complete range of angles of attack and side-slip angles. Non-zero side-slip introduces non-linearity into the C_L contours that increase for large angles of attack. Similar observation can be seen in the C_Q contours where non-linearity increases for large side-slip angles. The 2nd order model agrees well with the aerodatabase with regards to C_D over the entire simulated domain. Likewise, the linear model agrees well with the aerodatabase with regards to L/D.

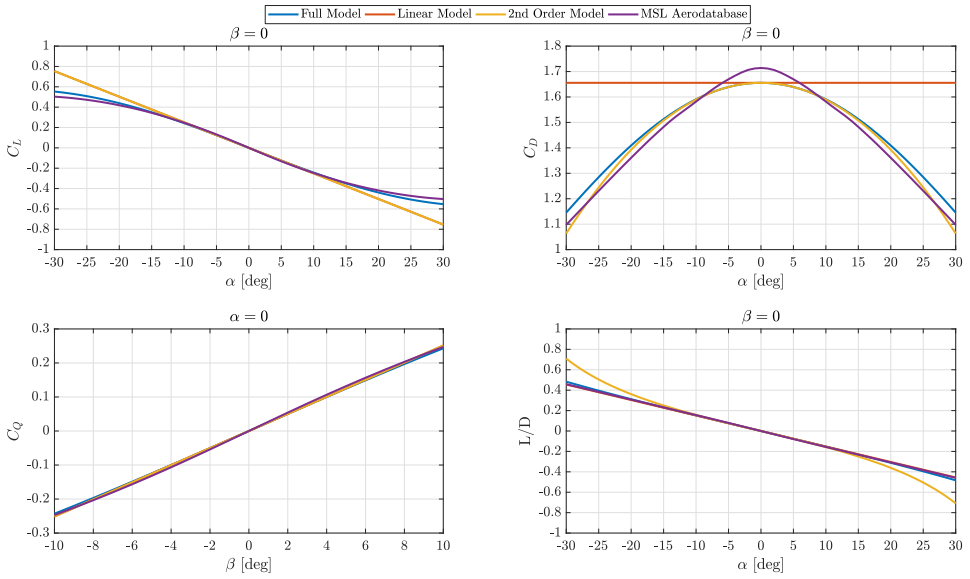

Figure 2.10. Comparison of analytical aerodynamic profiles for MSL-derived aeroshell

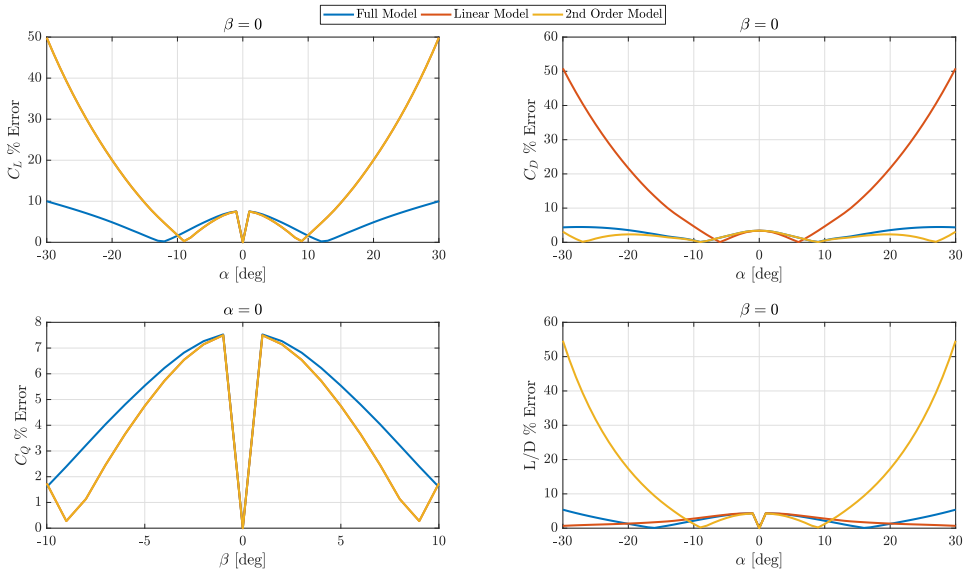

Figure 2.11. Percent Error of analytical aerodynamic profiles from MSL aerodatabase

The full model can be shown to provide an excellent agreement for the vehicle aerodynamic coefficients as compared to the aerodatabase solution.

In summary, analytical aerodynamics for a sphere-cone aeroshell can be ascertained using Newtonian aerodynamic theory. As compared to higher-fidelity aerodynamic models, the inviscid analytical solutions provide a sufficient approximation to the hypersonic aero-

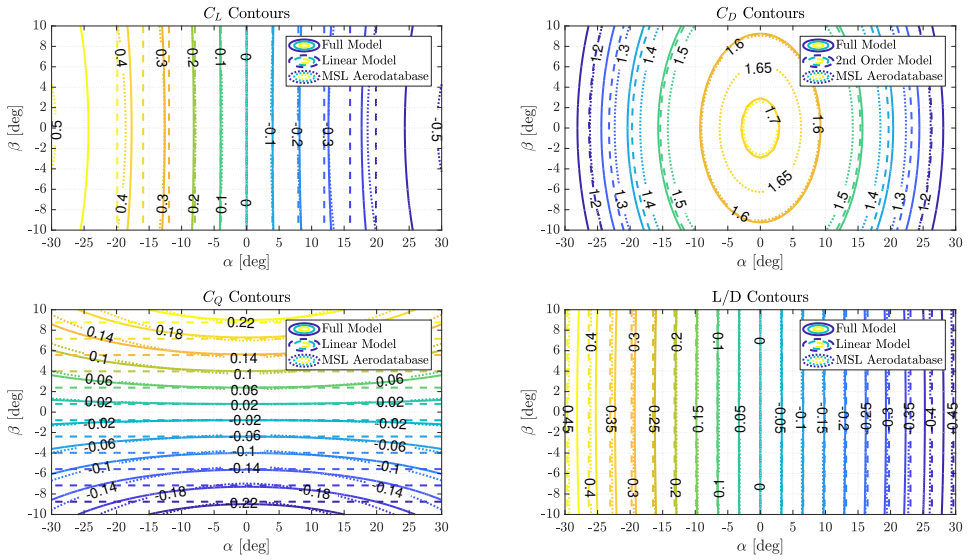

Figure 2.12. Comparison of analytical aerodynamic contours for MSL-derived aeroshell

dynamics. Simplifications to the resulting non-linear analytical expressions allows for 1st and 2nd order expressions, which are mathematically easier to manipulate, to be generated. Both models provide good estimations of C_Q for a wide range of angles of attack but small range of side-slip angles. The 2nd order model provides a much better representation of the drag coefficient but a poorer representation of the L/D as compared to the simplistic 1st order model. Achieving proper estimation of vehicle L/D is primarily important for lifting flight control. Consequently, the application of a linear aerodynamics model for formulating DFC flight control laws is suitable.

2.1.4 Planetary Atmospheres

The performance and robustness of aerocapture is planet-dependent. Each planetary destination has a distinct atmosphere and gravity well that can affect the outcome of the orbit insertion. In this section, the planetary geodesy and atmosphere of potential planetary destinations for aerocapture are introduced. The planetary destinations highlighted include Venus, Earth, Mars, Titan, and Neptune.

The gravitational well of each planetary destination is unique. The level of fidelity of each destination will depend on the current understanding. Commonly, a zonal harmonic gravity

model is used as an engineering model. As most planetary bodies are not perfect spheres, ellipsoidal representations are utilized. The zonal harmonics are modeled using Legendre polynomials. The polynomials are utilized in the formulation of the gravitational potential. Eq. (2.45) provided a sample mathematical construct of the gravitational potential with utilization of the 2nd order Legendre polynomial. This truncates the zonal terms up to the J_2 term. This model neglects potential tesseral terms are they are generally much smaller than the J_2 term. Table 2.1 shows a comparison of the gravitational model parameters between each planetary destination.

Table 2.1. Comparison of planetary gravity models. Values obtained from NASA Planetary Fact Sheets (https://nssdc.gsfc.nasa.gov/planetary/planetfact.html)

	Venus	Earth	Mars	Titan	Neptune
Gravitational Parameter, km^3/s^2	324859	398600	42828	8980	6836527
J_2 zonal term, nd	4.5E-06	1.1E-03	2.0E-03	3.2E-05	3.4E-03
Rotational Rate, rad/s	3.0E-07	7.3E-05	7.1E-05	4.6E-06	1.1E-04
Equatorial Radius, km	6052	6378	3396	2575	24764
Polar Radius, km	6052	6357	3376	2575	24341
Escape Velocity, km/s	10.4	11.2	5.0	2.6	23.5

Both Venus and Earth have similar gravitational wells as indicated by the gravitational parameter. This results in similar escape velocities for each planet, which for the same entry velocity indicates similar dissipated ΔV requirements needed for elliptical orbit insertion. Moreover, Venus has a much slower rotation rate, much smaller J_2 zonal term, and has a more spherical shape as compared to Earth. As compared to Earth, Mars has a much weaker gravity well and smaller escape velocity but has similar J_2 zonal term and rotation rate. Due to its diminutive mass, Titan has a weak gravity well. This leads to a very small escape velocity. Size-wise, Titan is somewhat comparable to Mars being 800 km smaller in radius. Like Venus, Titan is nearly spherical with a small J_2 zonal term and slow rotation rate. The sheer mass of the ice-giant Neptune leaves it in a category of its own. The immense gravity well yields significantly higher escape velocity. Out of the five planetary destinations, Neptune exhibits the fastest rotation completing 1 revolution in 16 hrs. The J_2 zonal term of Neptune is comparable in magnitude to Earth and Mars.

The atmospheres of each planetary destination are unique as well. Table 2.2 highlights the atmospheric chemical composition comparison between each planetary atmosphere.

Table 2.2. Comparison of planetary atmospheres. Values obtained from NASA Planetary Fact Sheets (https://nssdc.gsfc.nasa.gov/planetary/planetfact.html)

	Venus	Earth	Mars	Titan	Neptune
Atmosphere Composition	96.5% CO_2 3.5% N_2	78.1% N_2 21.0% O_2	95.1% CO_2 2.6% N_2	94.2% N_2 5.6% CH_4	80% H_2 19% He

Both Venus and Mars are carbon dioxide-rich atmospheres with small amounts of nitrogen. Earth and Titan are nitrogen-rich atmosphere with Earth's having a significant contribution due to oxygen. As an ice-giant, Neptune contains a hydrogen-based atmosphere with significant contribution due to helium. The atmospheric properties of each planet are modeled using the Global Reference Atmospheric Models (GRAM). The GRAM models are engineering-level atmospheric models that have been developed and utilized by NASA for aerocapture studies [84]. Earth-GRAM is developed for Earth using a mixture of datasets from satellite, rocket, balloon and remote sensing data [85]. Mars-GRAM is developed using both the NASA Ames Mars General Circulation Model and the University of Michigan Mars Thermospheric General Circulation Model, and has been validated using radio science flight data [86]. Venus-GRAM is developed on the Venus International Reference Atmosphere, which incorporate flight data obtained from atmospheric probes and in-orbit measurements [87]. Titan-GRAM is developed using engineering model profile envelopes developed by Yelle et. al [88]. Despite the existence of current flight data from the Cassini/Huygens mission, the current Titan-GRAM version does not incorporate the data. Neptune-GRAM is a basic engineering model derived from Voyager observations and limited Earth-based measurements [89].

Figure 2.13 provides a comparison of the nominal atmospheric profiles generated by the GRAM models for each planetary destination. The density profiles illustrate the uniqueness of each planetary atmosphere. At Venus, the density rapidly increases with small reductions in altitude. Conversely, Mars exhibits a slow increase despite having similar chemical composition as Venus. Titan and Neptune both have dense atmosphere that have sufficient

density at much higher altitudes as that of Venus, Earth, and Mars. The Yelle maximum and minimum profiles are also plotted for both planets. These profiles are meant to exhibit the range of uncertainty in each planet's nominal atmospheric profile. As Figure 2.13 shows, the uncertainty is the most pronounced at high altitudes and gradually tapers down as the altitude decreases.

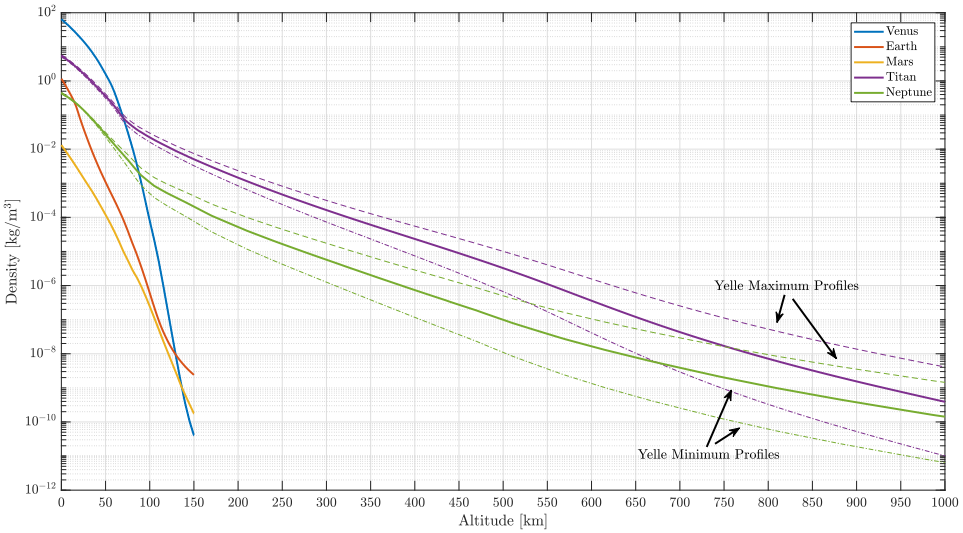

Figure 2.13. Sample nominal atmospheric density profiles generated by GRAM models for each planetary destination. Altitude range selected from atmospheric interface to surface.

Another important quantity that can be derived from the GRAM models is density scale height. The scale height is a metric utilizes to assess how much altitude is needed to change the density by a factor of e in an isothermal atmosphere. The smaller the number, the faster the atmosphere density changes. Commonly, scale height is used in exponential density models. From hydrostatic equilibrium and a constant temperature atmosphere, an analytical density model can be derived of the form shown in Eq. (2.104) where ρ_0 is the reference density, h_0 is the reference altitude, and H_ρ is the density scale height. With this model, density ρ becomes a function of altitude h.

$$\rho = \rho_0 \exp \frac{-(h - h_0)}{H_\rho} \tag{2.104}$$

Despite the advantages of being a continuous-function, the model's accuracy is limited by the scale height chosen. In existing APC guidance algorithms, a constant scale height assumption along with an exponential atmospheric model is commonly made. Figure 2.14 provides a sample density scale height profile computed from nominal atmospheric profiles using each GRAM model. For certain altitudes and planets, the constant scale height assumption might be adequate. But, the assumption in general is not accurate. The potential consequence of an incorrect scale height can result in an overestimation of the atmosphere leading to insufficient orbital energy depletion.

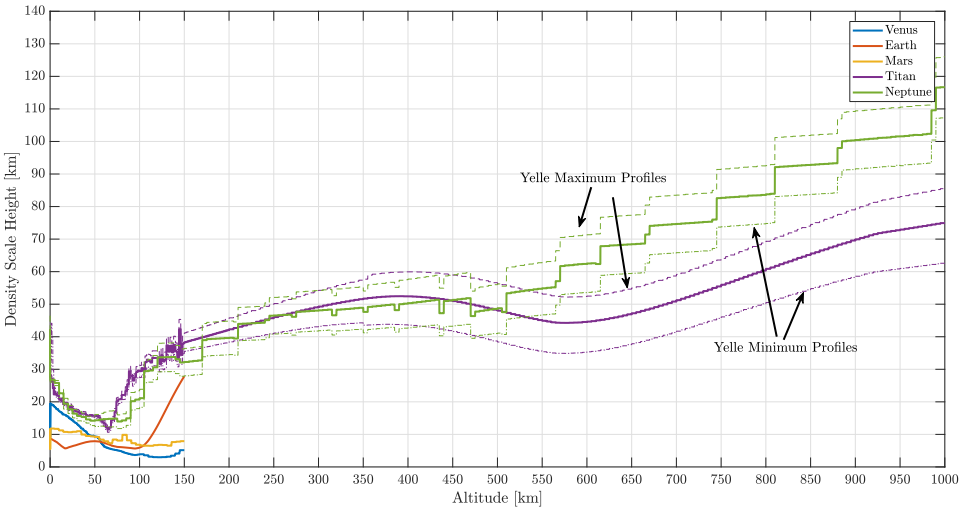

Figure 2.14. Sample nominal atmospheric density scale height profiles generated by GRAM models for each planetary destination.

Atmospheric uncertainty is an important environmental perturbation that can affect both the performance and robustness of aerocapture. Figure 2.15 provides a comparison of sample atmospheric uncertainties generated by each GRAM model. The uncertainties at Venus, Earth, and Mars exhibit a tornado-like structure with large density perturbation at high altitudes that taper down with decreasing altitude. The relative uncertainty in atmospheric knowledge of Titan and Neptune, as compared to Venus, Earth, and Mars, adds an additional risk to aerocapture performance that must be addressed. Figure 2.15 also shows the uncertainties applied to the Yelle minimum and maximum profiles. For both destinations, the potential density perturbations can be as high as 10 times mean profile.

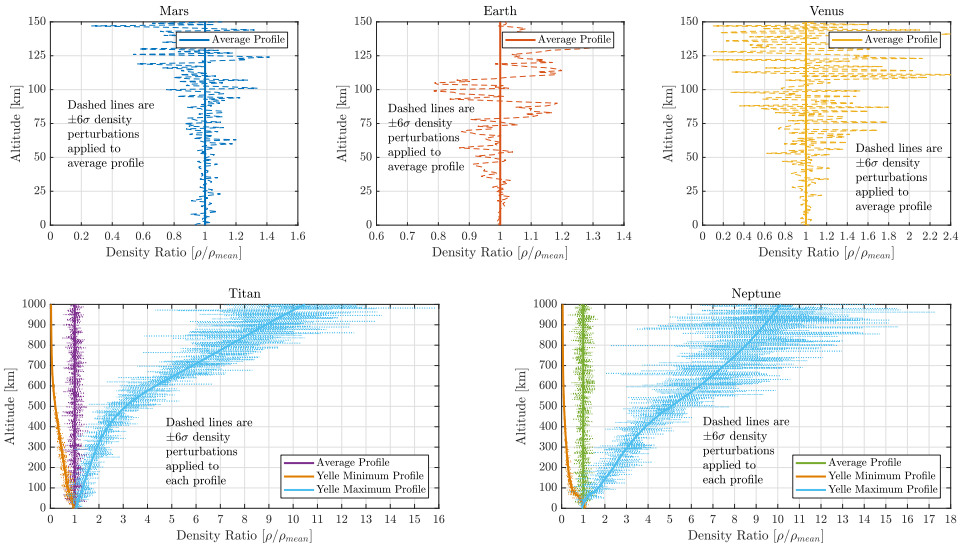

Figure 2.15. Atmospheric uncertainty simulated using GRAM models for each planetary destination

In addition to atmospheric perturbations, atmospheric winds can potentially impact the vehicle during atmospheric flight. Figure 2.16 shows a sample set of atmospheric winds generated by each GRAM model. The wind speeds significantly vary for each planetary destination. At Mars and Earth, the winds are relatively small in magnitude and are expected to be much smaller than the velocity of the vehicle. At Venus, Titan, and Neptune, the winds can potentially be of excess of 100 m/s.

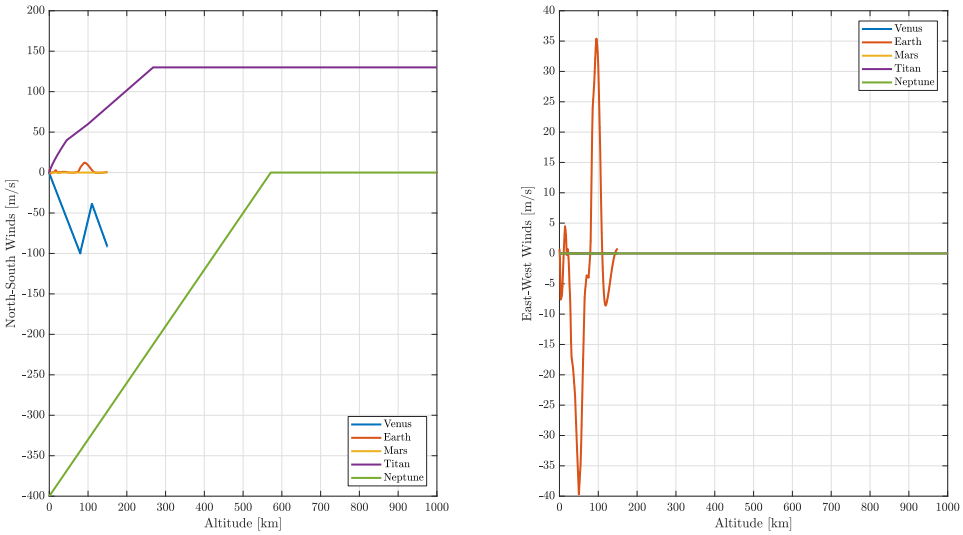

Figure 2.16. Sample atmospheric wind profiles generated by GRAM models for each planetary destination.

2.1.5 Aerothermodynamic Heating and Aerodynamic Loading

In this section, models for estimating aerothermodynamic heating and aerodynamic loading are presented.

Aerothermodynamic Heating

Heat transfer is an important physical phenomena that occurs during aerocapture. During hypersonic flight, the majority of the trajectory's energy is dissipated through aerothermodynamic heat transfer. The heat transfer from the flowfield to the vehicle is predominantly convective and radiative [90]. The aeroshell's thermal protection system must be designed with the proper material to withstand the peak heat flux while being thick enough to withstand the integrated heat load over the duration of the atmospheric pass. The selection of vehicle shape and TPS material can affect certain aspects of the heating. Slender vehicles tend to have higher L/D and larger convective heating than blunt vehicles. The strong detached shock waves associated with blunt bodies significantly dissipate the flowfield energy. This results in an increase in the chemical energy of gas directly in front of the vehicle geometry. Although most of the energy is convected to the vehicle wake, some energy is

convected to the vehicle surface. The increase in chemical energy may disassociate and ionize the gas leading to radiation being emitted. The heat flux imparted on the TPS material may produce chemical reactions through the form of ablation yielding catalytic heating. Furthermore, boundary layer interaction with the shock wave and potentially shock-shock interactions produced by protruding aerosurfaces may serve to increase the heating imparted on the vehicle. The assessment of aerocapture aerothermodynamic heating is best done using high-fidelity CFD codes. However similar to the aerodynamic CFD codes, achieving solutions over the entire trajectory is time and computationally expensive. Fortunately, some engineering methods exists that allow for a simplified assessment of the heating environment.

Convective heat transfer models assess the heat flux at the stagnation point of a hemispherical nose of radius r_n. Fay and Riddell [91] developed analytic expressions using boundary layer and stagnation point theories. This model consisted of flowfield properties that are not generally known without a full analytic solution of the flowfield. Both Chapman [92] as well as Sutton and Graves [93] developed analytical models relating stagnation point convective heat flux of a fully catalytic wall to freestream and geometrical properties. The latter model, shown mathematically in Eq. (2.105), has been widely used in conceptual design for estimating convective heat flux, $\dot{q}_c$. The Sutton-Graves constant, k, varies for each planetary destination. The values assumed in this dissertation are shown in Table 2.3. The model indicates that for the same freestream conditions, the convective heat flux increases as the nose radius of the aeroshell decreases. Likewise, the heat flux increases with the square root of density but increases with cube of velocity.

$$\dot{q}_c = k \left(\frac{\rho}{r_n} \right)^{\frac{1}{2}} V^3 \tag{2.105}$$

Table 2.3. Sutton-Graves Constants for Convective Heat Flux Model

	Venus	Earth	Mars	Titan	Neptune
k, $\frac{kg^{0.5}}{m}$	1.986e-4	1.74153e-4	1.898e-4	1.7407e-4	6.79e-5

Radiative heat transfer models similarly assess the heat flux at the stagnation point of a hemispheric nose. However, the engineering models are more complicated due to the

associated gas chemistry. A common model utilized in radiative heat flux estimates is the Tauber-Sutton model [94]. The model consists of the mathematical form shown in Eq. (2.106) where $\dot{q}_r$ is the stagnation point radiative heat flux, C is the Tauber-Sutton constant that depends on the planetary atmosphere, $f(V)$ is tabulated data that depends on velocity, and a and b are functions that depends on density and velocity. The model indicates a linear relationship between $\dot{q}_r$ and r_n for a values greater than zero. Larger nose radii may increase the radiative heat flux imparted on the aeroshell. Nevertheless, the challenge with utilizing this model is its dependence on tabulated and empirical model fits to limited experimental data. This in turn limits its applicability for utilization on aerocapture trajectories where no experimental data is present as well as its range of validity for given experimental data. Better calculations can be achieved using CFD codes beyond the scope of this dissertation. As a result, radiative heating calculations are omitted in this dissertation.

$$\dot{q}_r = C r_n^a \rho^b f(V) \tag{2.106}$$

The total integrated heat load imparted on the vehicle can be assessed by numerically integrating the heat flux over the entire trajectory. The stagnation point is utilized to assess heat load. Neglecting radiative heat flux, the integrated heat load, J, can be estimated using Eq. (2.107) where $\dot{q}$ is the total stagnation point heat flux.

$$J = \int_{t_0}^{t_f} \dot{q}\, dt \tag{2.107}$$

Aerodynamic Loading

Aerodynamic loading pertains to the sensed aerodynamic forces experienced during atmospheric flight. The load factor, n, can be calculated using Eq. (2.108) where the root sum square of the sensed lift, a_L, drag, a_D, and side-force, a_Q, accelerations as expressed in Earth g's.

$$n = \sqrt{a_L^2 + a_D^2 + a_Q^2} \tag{2.108}$$

For cases where no side-force is present, Eq. (2.108) can be written as a function of BC and L/D as shown in Eq. (2.109) where g_0 is Earth sea-level gravitational acceleration. In this form, it can be seen that the load factor increases with increasing vehicle L/D and decreases with increasing vehicle BC.

$$n = \frac{\rho v^2}{2BCg_0}\sqrt{\left(\frac{L}{D}\right)^2 + 1} \tag{2.109}$$

2.2 Optimal Aerocapture

This section provides the derivation and numerical solution of fuel-minimizing flight control laws pertaining to bank angle modulation, direct force control, and drag modulation.

2.2.1 Problem formulation

Cost Functional Definition

To ascertain the ΔV-minimizing flight control laws, the cost functional must first be defined. From the aerocapture problem depicted in Figure 1.1, the cost functional, P, can be defined in many ways. Existing cost functional formulations for aerocapture guidance have almost entirely minimized the apoapsis radius error using a form shown by Eq. (2.110) where r_a is the post aerocapture apoapsis radius and r_a^t is the target apoapsis radius.

$$P = \left|r_a - r_a^t\right| \tag{2.110}$$

A limitation to this approach is the periapsis raise maneuver cost remains unchecked, which can be expensive depending on the planetary destination and target periapsis radius, r_p^t. An alternative approach is to explicitly incorporate the periapsis raise maneuver into the cost function. The periapsis raise maneuver, ΔV_1 in Eq. (2.111), can be modeled using two-body orbital mechanics where the maneuver depends on r_a, r_a^t, r_p^t, as well as the semi-major axis, a, and central body gravitational constant, μ.

$$|\Delta V_1| = \sqrt{2\mu}\left[\left|\sqrt{\frac{1}{r_a} - \frac{1}{r_a + r_p^t}} - \sqrt{\frac{1}{r_a} - \frac{1}{2a}}\right|\right] \tag{2.111}$$

The apoapsis correction maneuver, ΔV_2 in Eq. (2.112), can also be similarly defined. Note that when $r_a = r_a^t$ the apoapsis correction maneuver is zero. This indicates that if the the apoapsis radius boundary condition is not explicitly enforced, then the apoapsis correction maneuver should be incorporated into the cost function.

$$|\Delta V_2| = \sqrt{2\mu}\left[\left|\sqrt{\frac{1}{r_p^t} - \frac{1}{r_p^t + r_a^t}} - \sqrt{\frac{1}{r_p^t} - \frac{1}{r_a + r_p^t}}\right|\right] \tag{2.112}$$

To visualize the orbit insertion cost at each planetary destination, a parametric evaluation of Eq. (2.111), Eq. (2.112), and Eq. (2.114) is conducted over a range of different inertial exit flight path angles and velocities. Figure 2.17, Figure 2.18, Figure 2.19, Figure 2.20, and Figure 2.21 depict the trade space for Venus, Earth, Mars, Titan, and Neptune respectively. In each figure the targeted apoapsis contour, denoted by the red dashed line, is superimposed on the in-plane ΔV and periapsis altitude subplots. These contours are representative of what the current state-of-the-art guidance optimization algorithms seek to achieve. Despite achieving the proper apoapsis, the resulting exit conditions may achieve larger in-plane ΔV costs associated with more negative post-aerocapture periapsis altitudes. The resulting penalty can vary between each planet. At Venus, the in-plane ΔV can increase by as much as 300 m/s with respect to the theoretical minimum value. Similar calculations show an increase by as much as 220 m/s, 100 m/s, 140 m/s, and 90 m/s for Earth, Mars, Titan, and Neptune, respectively. Of course, some exit conditions may not be feasible. The theoretical minimum for each planet arises at a flight path angle of zero, which indicates the exit state is at periapsis. Since the in-bound hyperbolic trajectory must fly through the atmosphere, the subsequent periapsis altitude must be inside of the atmosphere making achieving this theoretical minimum solution physically impossible. Moreover, lower in-plane ΔV/higher periapsis altitudes can be achieved on the red contours with smaller exit flight angles. As a result, the aerocapture guidance algorithm must seek to remain on these contours while ensuring the post-aerocapture periapsis altitude is as positive as possible.

Furthermore, the additional contours in the figures below also show the sensitivity of the orbit insertion performance to deviations from the superimposed red dashed contour. The addition of trajectory dispersions can cause these small deviations to arise. For the same

exit flight path angle, small errors in the orbital energy depletion (e.g. exit velocity) can potentially cause larger errors in the post-aerocapture apoapsis altitude. Similar observation can be seen for small errors in exit flight path angle for a given exit velocity. Despite the potential apoapsis altitude errors on the order of a few hundreds of km (with the exception of Neptune which itself is a few tens of thousands of km), the resulting in-plane ΔV cost (e.g. apoapsis correction cost) may increase on the order of a few tens of m/s. On the contrary, a change in a few hundreds of km in periapsis altitude will lead to a substantial increase in the in-plane ΔV cost (e.g. periapsis raise cost).

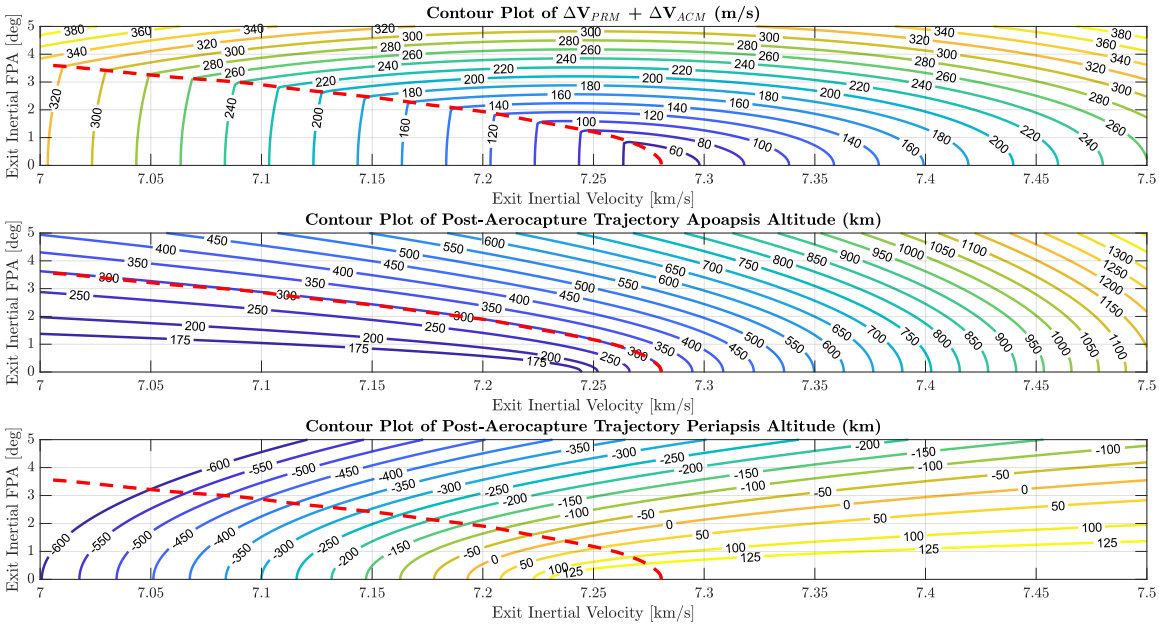

Figure 2.17. Orbit insertion trade space for Venus aerocapture into a 300 km circular orbit

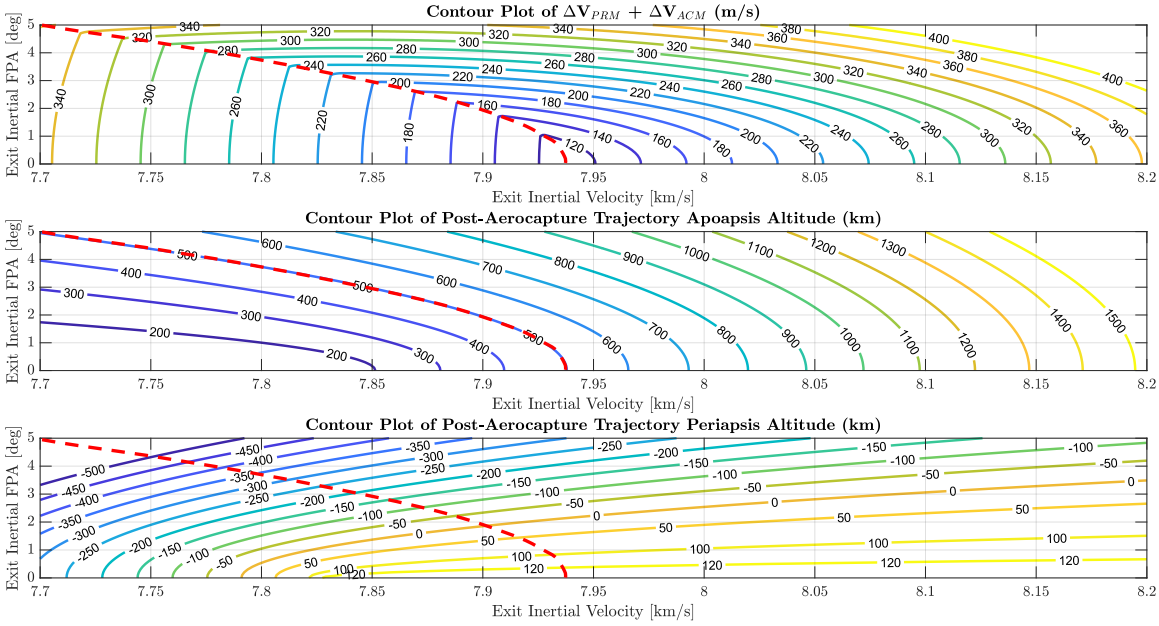

Figure 2.18. Orbit insertion trade space for Earth aerocapture into a 500 km circular orbit

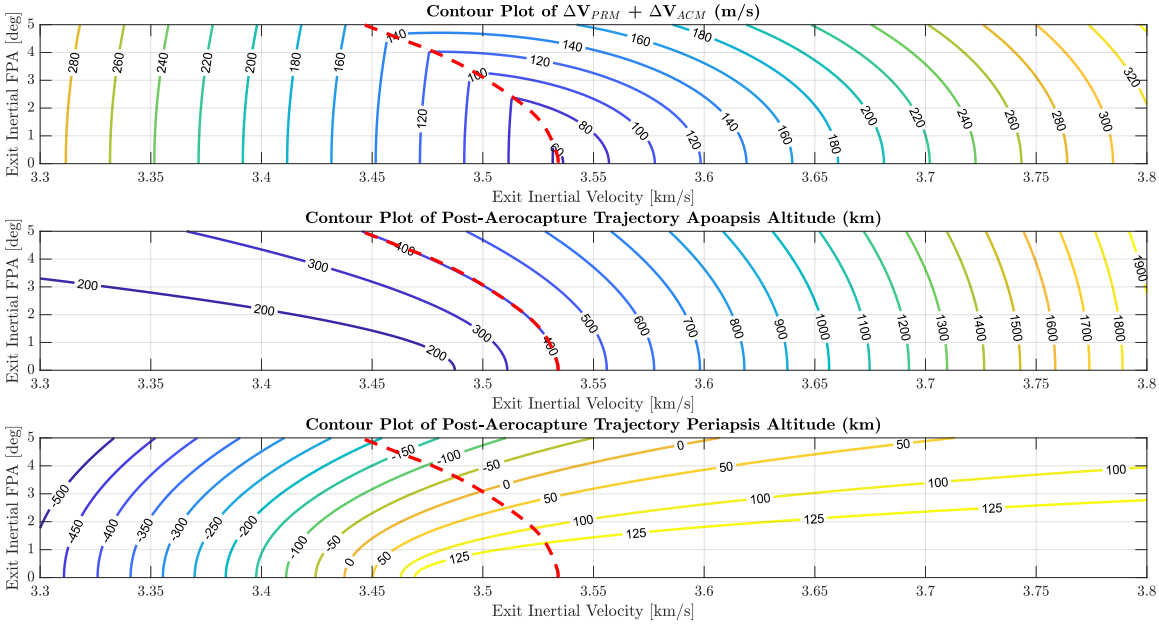

Figure 2.19. Orbit insertion trade space for Mars aerocapture into a 400 km circular orbit

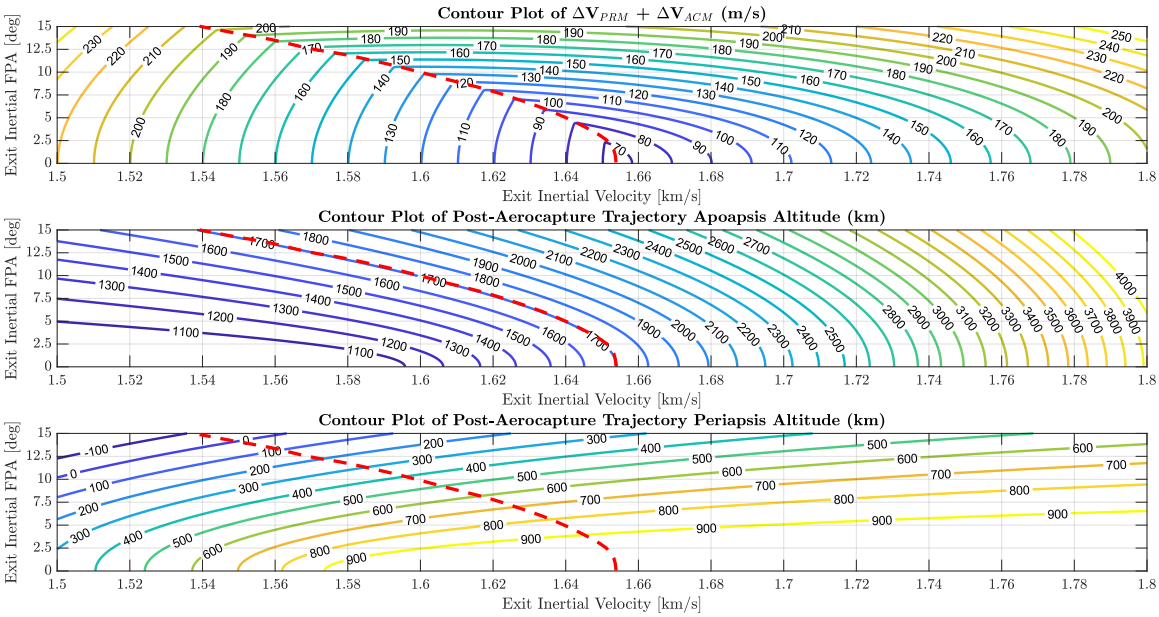

Figure 2.20. Orbit insertion trade space for Titan aerocapture into a 1700 km circular orbit

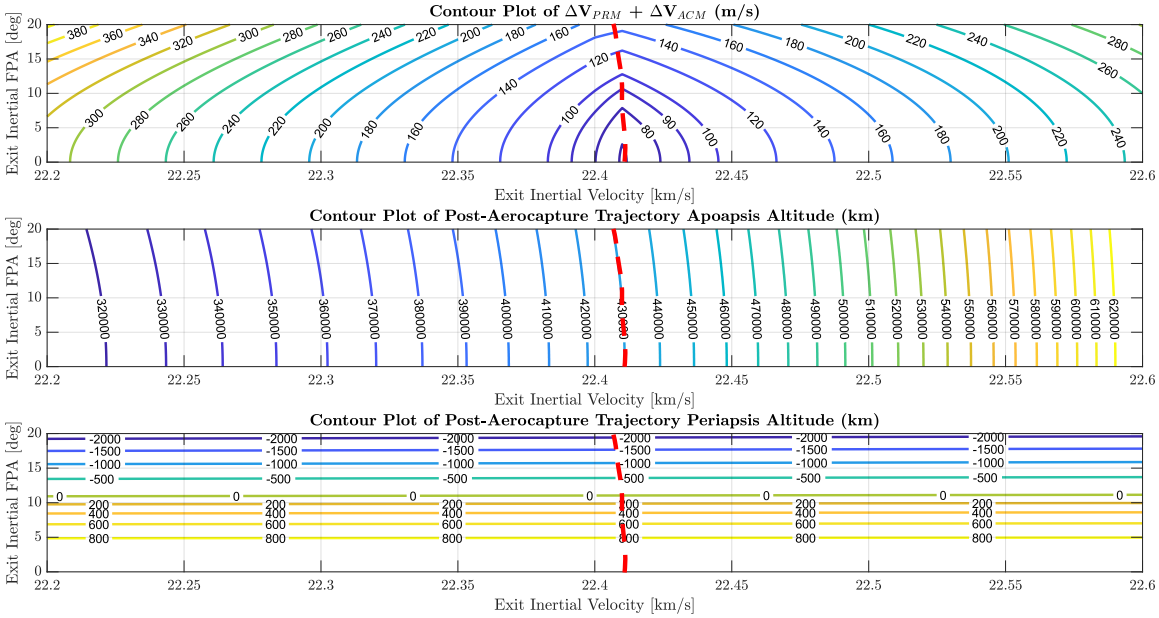

Figure 2.21. Orbit insertion trade space for Neptune aerocapture into a 3986 x 430000 km orbit

In the optimal aerocapture formulation derived in this section, the apoapsis radius boundary condition is enforced in the problem formulation. Formally, the formulation seeks the optimal flight control law that minimizes the absolute value of the propulsive periapsis raise maneuver with a cost functional defined by Eq. (2.113).

$$P = |\Delta V_1| \tag{2.113}$$

After exiting the atmosphere, the governing flight dynamics of the vehicle can be modeled using two-body orbital mechanics. Subsequently, post-aerocapture orbital parameters can be mapped to the *inertial* state vector at atmospheric exit. The semi-major axis and apoapsis radius are functions of the position vector magnitude, r, inertial flight path angle, γ_I, and inertial velocity vector magnitude, v_I, as computed at atmospheric exit.

$$a = \frac{\mu}{\frac{2\mu}{r} - {v_I}^2} \tag{2.114}$$

$$r_a = a\left[1 + \sqrt{1 - \frac{\left(v_I \; r\cos\left(\gamma_I\right)\right)^2}{\mu a}}\right] \tag{2.115}$$

The atmospheric flight dynamics of the aerocapture vehicle can be modeled using the 3DOF dynamics for flight relative to an ellipsoidal rotating planet. These differential equations model the evolution of the *planet-relative* position and velocity vector from atmospheric entry to exit. These two vectors can be parameterized by a set of six generalized coordinates where r is the position vector magnitude, θ is the planeto-centric longitude, ϕ is the planeto-centric latitude, V is the planet-relative velocity vector magnitude, γ is the flight path angle of the planet-relative velocity vector, and ψ is the azimuth angle of the planet-relative velocity vector.

$$\vec{x} = \begin{bmatrix} r & \theta & \phi & V & \gamma & \psi \end{bmatrix}^T \tag{2.116}$$

The state vector equations of motion can be written in the form $\dot{\vec{x}} = f(\vec{x}, \vec{u}, t)$ where $\vec{u}$ is the flight control vector and t is time. The coupled differential equations for the state vector

components can be found in Eq. (2.39), Eq. (2.40), Eq. (2.41), Eq. (2.57), Eq. (2.58), and Eq. (2.59). The equations include vehicle aerodynamics and destination dependent terms. The wind-frame aerodynamic terms include lift, L, drag, D, and side-force, Q. Each term depends on the atmospheric density, the freestream velocity, and the aerodynamic reference area. The corresponding aerodynamic coefficients may depend on the Mach number, angle of attack and side-slip angle.

$$L = \frac{1}{2}\rho V_{\infty}^{2} A_{ref} C_{L}\left(M, \alpha, \beta\right) \tag{2.117}$$

$$D = \frac{1}{2}\rho V_{\infty}^{2} A_{ref} C_{D}\left(M, \alpha, \beta\right) \tag{2.118}$$

$$Q = \frac{1}{2}\rho V_{\infty}^{2} A_{ref} C_{Q}\left(M, \alpha, \beta\right) \tag{2.119}$$

In this analysis, a few assumptions are made regarding the aerodynamic and destination dependent terms. The aerodynamic coefficients are assumed to come from the analytical expressions introduced in the previous section. Due to the high orbital velocities associated with aerocapture, the Mach Independence principle is applied to the vehicle aerodynamics. This yields the aerodynamic coefficients as solely functions of angle of attack and side-slip angle. The presence of winds are neglected such that $V_{\infty} \approx V$. Atmospheric density is assumed to be a strong function of position only with the values calculated from the nominal density profile produced by each planet respective GRAM model. A oblate gravity model with zonal harmonics up to the J_2 term is assumed. The model was introduced in the previous section with the radial and latitudinal gravitational accelerations modeled using Eq. (2.50) and Eq. (2.51).

Since the state vector is defined using planet-relative parameters and the cost functional is defined using inertial parameters, conversion relations between the two are needed. From Reference [66], the transformation from planet-relative to inertial coordinates are shown in Eq. (2.120). The equations can be used for converting numerical integration result at atmospheric exit to inertial coordinates for subsequent calculations of cost functional. Note

that when the rotation rate of the planet approaches zero, then $\theta_I \approx \theta$, $v_I \approx v$, $\gamma_I \approx \gamma$, and $\psi_I \approx \psi$. This trend is leveraged in the bank angle formulation.

$$\begin{aligned} r_I &= r \\ \theta_I &= \theta + \omega t \\ \psi_I &= \psi \\ v_I &= \sqrt{v^2 + 2\omega r v \cos\gamma \cos\psi \cos\phi + (\omega r \cos\phi)^2} \\ \tan\gamma_I &= \frac{v \sin\gamma}{\sqrt{(v\cos\gamma)^2 + 2\omega r v \cos\gamma \cos\psi \cos\phi + (\omega r \cos\phi)^2}} \\ \tan\psi_I &= \frac{v \cos\gamma \sin\psi}{(v\cos\gamma\cos\psi + \omega r \cos\phi)} \end{aligned} \tag{2.120}$$

Conversely, from Reference [66], the transformation from inertial to planet-relative coordinates are shown in Eq. (2.121). The equations can be used for converting atmospheric entry state from an inbound hyperbolic trajectory to the initial conditions for numerical integration of the planet-relative state vector.

$$\begin{aligned} r &= r_I \\ \theta &= \theta_I - \omega t \\ \psi &= \psi_I \\ v &= \sqrt{v_I^2 - 2\omega r_I v_I \cos\gamma_I \cos\psi_I \cos\phi_I + (\omega r_I \cos\phi_I)^2} \\ \tan\gamma &= \frac{v_I \sin\gamma_I}{\sqrt{(v_I\cos\gamma_I)^2 - 2\omega r_I v_I \cos\gamma_I \cos\psi_I \cos\phi_I + (\omega r_I \cos\phi_I)^2}} \\ \tan\psi &= \frac{v_I \cos\gamma_I \sin\psi_I}{(v_I\cos\gamma_I\cos\psi_I - \omega r_I \cos\phi_I)} \end{aligned} \tag{2.121}$$

In addition to minimizing the in-plane ΔV at atmospheric exit, it might be desired to enforce the orbital inclination. This can be enforced in the problem formulation as a terminal constraint of the form shown in Eq. (2.122) where i^t is the targeted inclination.

$$i(\vec{x}_{exit}) - i^t = 0 \tag{2.122}$$

The exit inclination, $i(\vec{x}_{exit})$, can be computed using inertial state vector components as shown in Eq. (2.123).

$$\cos i = cos\phi_I \cos \psi_I \tag{2.123}$$

For circular target orbits the inclination correction maneuver, $\Delta \mathrm{V}_3$, can be simply computed using Eq. (2.124).

$$|\Delta V_3| = 2\sqrt{\frac{\mu}{r_a^t}} \sin\left(\frac{|i - i^t|}{2}\right) \tag{2.124}$$

For elliptical target orbits, the corresponding inclination correction burn is slightly more complicated. Assuming burn at the line of nodes, $\Delta \mathrm{V}_3$ can be computed using Eq. (2.125) where v_N and γ_N are the orbital velocity and orbital flight path angle at line of nodes crossing [95].

$$|\Delta V_3| = 2v_N \cos(\gamma_N) \sin\left(\frac{|i - i^t|}{2}\right) \tag{2.125}$$

With the cost functional, state vector dynamics, and orbit insertion boundary constraints defined, the next step is the application of optimal control theory. The theory is derived from the application of calculus of variations to the optimal control problem. Its solutions, which minimize the cost functional, are known as the Euler-Lagrange equations. The optimal aerocapture control problem can be formulated as a two-point boundary value problem where the initial states, $\vec{x}_0$, are prescribed, the terminal constraints, $\vec{\Psi}\left(\vec{x}\left(t_f\right), t_f\right)$, are enforced, and the evolution of the state with the control inputs are defined by the state dynamics, $\dot{\vec{x}}$. The flight control(s) are explicitly bounded by upper and lower constraints. The mathematical setup of a general inequality-constrained optimal control problem is shown below where the cost functional, including terminal, $\varphi\left(\vec{x}\left(t_f\right), t_f\right)$, and path cost, $\int_{t_0}^{t_f} \tilde{L}\left(\vec{x}, \vec{u}, t\right) dt$, is defined in Eq. (2.126), the state dynamics and initial state are defined in Eq. (2.128), the terminal boundary constraints are defined in Eq. (2.129), and control vector component inequality constraints are defined in Eq. (2.130). The initial time is fixed but the final time is free to

vary. The objective is to obtain the optimal control time history, $\vec{u}^{*}(t)$, that minimizes the cost functional such that the imposed constraints are satisfied.

Minimize

$$P = \varphi\left(\vec{x}\left(t_f\right), t_f\right) + \int_{t_0}^{t_f} \tilde{L}\left(\vec{x}, \vec{u}, t\right) dt \tag{2.126}$$

Subject to:

$$t_0 = 0,\ t_f \text{ free} \tag{2.127}$$

$$\dot{\vec{x}} = f\left(\vec{x}, \vec{u}, t\right),\ \vec{x}\left(t_0\right) = \vec{x}_0 \tag{2.128}$$

$$\vec{\Psi}\left(\vec{x}\left(t_f\right), t_f\right) = 0 \tag{2.129}$$

$$u_i^{min} \leq u_i\left(t\right) \leq u_i^{max},\ i = 1, \ldots p \tag{2.130}$$

Applying the mathematical definition of the optimal control problem to aerocapture yields:

Minimize

$$P = |\Delta V_1| \left(\vec{x} \left(t_f \right), t_f \right) \tag{2.131}$$

Subject to:

$$t_0 = 0,\ t_f\ free \tag{2.132}$$

$$\dot{\vec{x}} = \begin{bmatrix} \dot{r} & \dot{\theta} & \dot{\phi} & \dot{v} & \dot{\gamma} & \dot{\psi} \end{bmatrix},\ \vec{x}\left(t_0\right) = \begin{bmatrix} r_0 & \theta_0 & \phi_0 & v_0 & \gamma_0 & \psi_0 \end{bmatrix} \tag{2.133}$$

$$\Psi_1 \left(\vec{x} \left(t_f \right), t_f \right) = r(t_f) - r_{exit} = 0 \tag{2.134}$$

$$\Psi_2 \left(\vec{x} \left(t_f \right), t_f \right) = r_a(\vec{x}_f) - r_a^t = 0 \tag{2.135}$$

$$\Psi_3 \left(\vec{x} \left(t_f \right), t_f \right) = i(\vec{x}_f) - i^t = 0 \tag{2.136}$$

$$|\sigma|_{min} \leq |\sigma|(t) \leq |\sigma|_{max} \tag{2.137}$$

$$BC_{min} \leq BC(t) \leq BC_{max} \tag{2.138}$$

$$\alpha_{min} \leq \alpha(t) \leq \alpha_{max},\ \beta_{min} \leq \beta(t) \leq \beta_{max} \tag{2.139}$$

The first step in solving the problem is the definition of the Hamiltonian, H, which is mathematically constructed using Eq. (2.140). In this equation the Lagrangian, $\tilde{L}\left(\vec{x}, \vec{u}, t\right)$, that appears in the path cost is summed with the state vector dynamics through the introduction of Lagrange multipliers, $\vec{\lambda}$.

$$H\left(\vec{x}, \vec{u}, \vec{\lambda}, t\right) = \tilde{L}\left(\vec{x}, \vec{u}, t\right) + \vec{\lambda}^T f\left(\vec{x}, \vec{u}, t\right) \tag{2.140}$$

The resulting Hamiltonian definition for the optimal aerocapture problem is shown in Eq. (2.141).

$$H = \lambda_r \dot{r} + \lambda_\theta \dot{\theta} + \lambda_\phi \dot{\phi} + \lambda_V \dot{V}\left(\alpha, \beta, BC\right) + \lambda_\gamma \dot{\gamma}\left(\sigma, \alpha, \beta, BC\right) + \lambda_\psi \dot{\psi}\left(\sigma, \alpha, \beta, BC\right) \tag{2.141}$$

The next step is to apply the Euler-Lagrange solutions to the optimal control problem [96]. The first solution, as shown in Eq. (2.142), provides the algebraic differential equations for the unknown Lagrange multipliers.

$$\dot{\vec{\lambda}}^T = -\frac{\partial H}{\partial \vec{x}} \tag{2.142}$$

The differential equations for the Lagrange multipliers require initial conditions. They can be obtained from applying the transversality condition. The condition is an algebraic constraint based off the Hamiltonian and augmented terminal cost. The latter, defined in Eq. (2.143), combines the terminal cost with the terminal constraints via additional *constant* unknown multipliers, $\vec{\eta}$ [97].

$$\vec{\Phi}\left(t_f, \vec{x}_f\right) = \varphi\left(\vec{x}\left(t_f\right), t_f\right) + \vec{\eta}^T \vec{\Psi}\left(\vec{x}\left(t_f\right), t_f\right) \tag{2.143}$$

For a fixed initial time and free final time problem, the transversality condition takes the form shown in Eq. (2.144). In order for the final time to vary, dt_f cannot equal zero. Consequently, the first enclosed term in Eq. (2.144) must equal zero. This provides the necessary conditions for determining the final time. The advantage of this adjoined method is that the incorporation of $\vec{\eta}$ allows for the terminal state vector to vary. This means that $d\vec{x}_f$ cannot equal zero *for all* its components. This allows then for the second bracketed term in Eq. (2.144) to be used directly in determining all of the initial conditions for the Lagrange multiplier differential equations.

$$\left(H_f + \frac{\partial \varphi}{\partial t_f} + \vec{\eta}^T \frac{\partial \Psi}{\partial t_f}\right) dt_f - \left(\frac{\partial \varphi}{\partial \vec{x}_f} + \vec{\eta}^T \frac{\partial \Psi}{\partial \vec{x}_f} - \vec{\lambda}_f^T\right) d\vec{x}_f = 0 \tag{2.144}$$

If Eq. (2.130) were not enforced, then the second Euler-Lagrange solution, as shown in Eq. (2.145), can be applied. This solution provides the optimal control laws for each control variable.

$$\frac{\partial H}{\partial \vec{u}} = 0 \tag{2.145}$$

With the explicit enforcement of bounded control, the optimal can be potentially ascertained through the application of Pontryagin's Minimum Principle [98]. The principle assumes that the control vector $\vec{u}$ lies within the set U of m-dimensional Euclidean space during time interval $[t_0, t_f]$ and is piecewise continuous. In other words, the control vector lies within the imposed bounds during the time interval. If the bounded optimal control, $\vec{u}^*(t)$, causes the cost functional to be minimized and the problem is normal such that the co-state vector, $\vec{\lambda}(t)$, does not equal the zero vector over a finite time interval in $[t_0, t_f]$, then Pontryagin's Minimum Principle mathematically states that

$$H[t, \vec{x}^*(t), \vec{u}^*(t), \vec{\lambda}(t)] \leq H[t, \vec{x}^*(t), \vec{u}(t), \vec{\lambda}(t)] \tag{2.146}$$

Eq. (2.146) illustrates the concept that the Hamiltonian, as computed on the optimal trajectory $\vec{x}^*$, must be minimized by the control input. In applying the principle, assume that the Hamiltonian can be written into the compact form as shown in Eq. (2.147). Without loss of generality, assume a single control input. In this form, the Hamiltonian is *linear* with respect to the control input and H_1 is known as the switch function.

$$H = H_0 + H_1 u_1 \tag{2.147}$$

Since H_0 is not directly influenced by control, the control input must be determined based off the sign of the switching function. Applying Pontryagin's Minimum Principle leads to Eq. (2.148). The case in which the switching function is zero for a finite time period is known as a singular arc. If shown to not exist, then the optimal control law resembles a "bang-bang" structure in which the control switches from one control bound to the other as controlled by its respective switching function. This result can be extended to more control inputs if they can be put into the form of Eq. (2.147)

$$u_1^* = \begin{cases} u_{1,min}, & \text{if } H_1 > 0 \\ u_{1,max}, & \text{if } H_1 < 0 \\ \in [u_{1,min}, u_{1,max}], & \text{if } H_1 \equiv 0 \text{ in } [t_1, t_2] \subset [t_0, t_f] \end{cases} \tag{2.148}$$

2.2.2 Regularized Optimal Control

Although the "bang-bang" optimal control law may appear to be simplistic, it is in general difficult to obtain numerical solutions due to the lack of knowledge on the number of control switches and numerical values for the switching function(s). In order to alleviate the challenges in obtaining a potentially feasible optimal control law for bounded control, a regularized optimal aerocapture guidance problem is formulated. The methodology reformulates the problem through introduction of saturation functions and control regularization.

Saturation Functions

The motivation for investigating the application of saturation functions for handing control bounds comes from [99]. The objective of the control saturation function is to replace the two-sided control inequality constraint with a single equality constraint that *implicitly* bounds the control. The resulting control saturation function is shown in Eq. (2.149) where w_i is the saturation control. The saturation control implicitly bounds the actual control as $\Xi_i \rightarrow u_i^{max}$ for $w_i \rightarrow \infty$ and $\Xi_i \rightarrow u_i^{min}$ for $w_i \rightarrow -\infty$.

$$\Xi_i\left(w_i\right) = u_i^{max} - \frac{u_i^{max} - u_i^{min}}{1 + exp\left(\frac{4w_i}{u_i^{max} - u_i^{min}}\right)} \tag{2.149}$$

This smooth and monotonically increasing function allows for the two-sided inequality constraint to be converted into a single equality constraint as shown in Eq. (2.150).

$$g_i\left(u_i, w_i\right) = u_i - \Xi_i\left(w_i\right) = 0 \tag{2.150}$$

Enforcing the equality constraint is done by adjoining it to the Hamiltonian via additional unknown Lagrange multipliers π_i. This allows for an unconstrained optimal control solution to be formulated; consequently, the optimal control solution from the Euler-Lagrange equations can utilized. Applying the equation yields Eq. (2.151) in addition to Eq. (2.145).

These two equations along with Eq. (2.150) provide the algebraic expressions for obtaining u_i, w_i, and π_i.

$$\frac{\partial H}{\partial w_i} = 0 \tag{2.151}$$

Control Regularization

The original cost functional in Eq. (2.126) does not depend on the saturation control vector, $\vec{w}$. As a result, a two-norm control regulator cost is added to the cost functional as shown in Eq. (2.152). Furthermore, to minimize the original control effort, the original control, $\vec{u}$, is added to the regulator cost. Note that the addition of $\vec{u}$ is a modification to the existing theory derived in [99]. This is done to obtain a quadratic growth property for the optimal aerocapture cost function, which does not explicitly depend on $\vec{u}$. In the numerical simulation results, ΔV_u denotes the regularized control cost $\epsilon \int_{t_0}^{t_f} ||\vec{u}||_2^2 + ||\vec{w}||_2^2 dt$.

$$\bar{P}\left(\vec{u}, \vec{w}, \epsilon\right) = P\left(\vec{u}\right) + \epsilon \int_{t_0}^{t_f} ||\vec{u}||_2^2 + ||\vec{w}||_2^2 dt \tag{2.152}$$

The regularization constant, ϵ, serves as a penalty multiplier to account for the unbounded $\vec{w}$. Furthermore, the addition of $\vec{u}$ provides a level of convexity to the optimal control problem where ϵ can also be though of as analogous to the Lipschitz constant. Because ϵ is user-defined, its affect on the numerical simulations is investigated later in this section.

With the regularized cost functional defined, the Hamiltonian definition can be revised, as shown in Eq. (2.153).

$$H\left(\vec{x}, \vec{u}, \vec{w}, \vec{\lambda}, \vec{\pi}, t\right) = L\left(\vec{x}, \vec{u}, t\right) + \epsilon\left(||\vec{u}||_2^2 + ||\vec{w}||_2^2\right) + \vec{\lambda}^T f\left(\vec{x}, \vec{u}, t\right) + \vec{\pi}^T g\left(\vec{u}, \vec{v}\right) \tag{2.153}$$

The co-state dynamics are computed using Eq. (2.142). The transversality condition, Eq. (2.144), is used for both obtaining the terminal conditions for the co-state variables as well as the condition for free final time, with the corresponding expressions denoted by

Eq. (2.154) and Eq. (2.155) respectively. Both equations are computed at the unknown final time, t_f.

$$\vec{\lambda}^T(t_f) = \left.\frac{\partial \varphi}{\partial x}\right|_{t_f} + \vec{\eta}^T \left.\frac{\partial \vec{\Psi}}{\partial x}\right|_{t_f} \tag{2.154}$$

$$H\left(x, \vec{u}, \vec{w}, \vec{\lambda}, \vec{\pi}, t\right)\Big|_{t_f} = -\left.\frac{\partial \varphi}{\partial t}\right|_{t_f} - \vec{\eta}^T \left.\frac{\partial \vec{\Psi}}{\partial t}\right|_{t_f} \tag{2.155}$$

The remaining expressions needed for a well-defined two-point boundary value problem come from the control.

Control Dynamics

Although Eq. (2.145), Eq. (2.150), and Eq. (2.151) provide the expressions for the remaining unknown parameters, the expressions are highly non-linear and coupled. As a result, closed-form expressions for the optimal control are difficult to obtain. Furthermore, numerical root-solving techniques may not be able to solve the expression with a high-level of fidelity. If a differential equation can be obtained for the control variables, then a high-fidelity solution can be obtained through numerical integration given an initial condition. This section highlights a procedure for obtaining the control dynamics based of a similar procedure introduced in [100].

From Eq. (2.151), expressions for π_i as a function of w_i can be obtained. The expressions are substituted into the Hamiltonian. Subsequently, using Eq. (2.145) allows for expressions for u_i as a function of w_i to be obtained. From these latter expressions, the total time derivative of u_i is obtained through the application of the chain rule as shown in Eq. (2.156).

$$\dot{u}_i = \frac{\partial u_i}{\partial t} + \frac{\partial u_i}{\partial \vec{x}}\dot{x} + \frac{\partial u_i}{\partial \vec{\lambda}}\dot{\vec{\lambda}} + \frac{\partial u_i}{\partial w_i}\dot{w}_i \tag{2.156}$$

Because the imposed equality constraints in Eq. (2.150) equals zero, its corresponding total time derivatives must also equal zero. Application of the chain rule and rearrangement of variables yields Eq. (2.157).

$$\frac{\partial g_i}{\partial u_i}\dot{u}_i + \frac{\partial g_i}{\partial w_i}\dot{w}_i = -\frac{\partial g_i}{\partial t} - \frac{\partial g_i}{\partial \vec{x}}\dot{\vec{x}} - \frac{\partial g_i}{\partial \vec{\lambda}}\dot{\vec{\lambda}} \tag{2.157}$$

Using Eq. (2.156) and Eq. (2.157) allows for unique control differential equations for $\dot{w}_i$ and $\dot{u}_i$ to be determined. The initial conditions are defined such that Eq. (2.150) is held. The control differential equations are numerically integrated with the state and co-state dynamics. With expressions for π_i known, a well-defined two-point boundary value problem is posed.

Numerical Solution Setup

The two-point boundary value problem is numerically solved using *MATLAB* bvp5c function. The function utilizes a fifth order finite difference collocation algorithm for solving the boundary value problem [101]. The function requires an initial guess for the collocation algorithm, a separate function defining the problem's differential equations, and another separate function defining the problem's initial and terminal boundary conditions. Variable time-step numerical integration is conducted with a relative and absolute tolerance of 1e-3. The numerical accuracy of the solution highly depends on the initial guess. The guess is generated by propagating the state vector dynamics to atmospheric exit with a constant control solution for each flight control analyzed. With a time history guess for the state and the control, the co-state time history guess is generated by backwards propagating the co-state dynamics to atmospheric entry given the known co-state terminal conditions. The regularization control time history guess is determined by using the constant control solution and solving for the regularization control via Eq. (2.150). This initial guess approach was noted to be sufficient for producing a numerical solution for large values of epsilon. Note that no mesh refinement is conducted on the initial guess or any further simulation runs. A continuation approach is utilized where the previous bvp5c solution is utilized as an initial guess until the solution achieved a maximum residual error of 1e-3. Each control methodology

analyzed are numerically solved using a decreasing sequence of regularization constant values. The previous constant value solution is utilized as an initial guess to the current constant value and a continuation approach is conducted. This decreasing sequence is conducted to numerically demonstrate the regularized optimal control solution convergence to the known "bang-bang" control structure.

The function defining the problem's differential equations include the state, co-state, control, and regularization control dynamics. The function defining the boundary conditions include the known entry state, enforced terminal boundary conditions, derived free final time condition, derived co-state terminal values, and saturation function equality constraints. The unknown parameters that are optimized are the final time and the terminal constraint Lagrange multipliers. The algebra for these differential equations and boundary conditions is solved using *Mathematica*.

2.2.3 Bank angle flight control laws

For BAM, the primary control is assumed to be σ. The vehicle is trimmed at zero β such that no side-force is produced and is trimmed at a non-zero α such that the vehicle produces lift. From Eq. (2.58) and Eq. (2.59), σ is a trigonometric function appearing in both $\dot{\gamma}$ and $\dot{\psi}$. The coupled control makes it difficult to mathematically obtain the optimal trajectories. As a result, simplifications to the flight profile and assumptions on the control scheme are needed.

The derivation of the optimal bank angle control laws was first introduced by Lu et al. [69]. In his work, many fundamental assumptions are made regarding the optimal aerocapture problem formulation. Firstly, the cost functional and terminal constraints are assumed to explicitly depend on the terminal values of the *longitudinal* variables r_f, v_f, and γ_f. Consequence of this assumption is the inclination terminal constraint is not explicitly enforced. Secondly, the state-vector dynamics are simplified through neglecting small magnitudes associated with planetary rotation and non-spherical gravity. The accuracy of this assumption may vary depending on the planetary destination but the consequence of it is that the the

state-vector dynamics decouple into longitudinal and lateral terms as denoted by Eq. (2.158) and Eq. (2.159), respectively.

$$\begin{aligned} \dot{r} &= v\sin(\gamma) \\ \dot{v} &= -\frac{D}{m} - \frac{\mu\sin(\gamma)}{r^2} \\ v\dot{\gamma} &= \frac{L}{m}\cos(\sigma) + \left(v^2 - \frac{\mu}{r}\right)\frac{\cos(\gamma)}{r} \end{aligned} \tag{2.158}$$

$$\begin{aligned} \dot{\theta} &= \frac{v\cos\gamma\cos\psi}{r\cos\phi} \\ \dot{\phi} &= \frac{v\cos\gamma\sin\psi}{r} \\ v\dot{\psi} &= \frac{L\sin(\sigma)}{m\cos(\gamma)} - \frac{v^2}{r}\cos(\gamma)\cos(\psi)\tan(\phi) \end{aligned} \tag{2.159}$$

The longitudinal dynamics in Eq. (2.158) are not explicit functions of lateral variables θ, ϕ, or ψ and are controlled by the $\cos(\sigma)$. The bank angle itself can be mathematically represented by $\sigma = sgn(\sigma)|\sigma|$ with the relations that $\cos(\sigma) = \cos(|\sigma|)$ and $\sin(\sigma) = sgn(\sigma)\sin(|\sigma|)$. This decomposition lends itself to the control strategy of having the optimal aerocapture problem provide the solution to $|\sigma|$ while separate lateral logic determines the $sgn(\sigma)$ necessary for managing the inclination error.

For BAM problem formulation, the control variable is defined as $u = \cos(|\sigma|)$. Its bounds are dictated by the imposed bounds on $|\sigma|$ as shown by Eq. (2.160).

$$\begin{aligned} 0 \leq \sigma_{min} \leq |\sigma|(t) \leq \sigma_{max} \leq \pi \\ -1 \leq u_{min} \leq u\,(t) \leq u_{max} \leq\ 1 \end{aligned} \tag{2.160}$$

Optimal Control Law

To ascertain the BAM optimal control laws, the Hamiltonian is first formulated using Eq. (2.141) and omitting state-vector dynamics and co-state variable terms associated with lateral variables. The control variable appears only in $\dot{\gamma}$ as a linear function. This relationship allow for the Hamiltonian to be written in the general form of Eq. (2.147) where H_1 is represented by Eq. (2.161).

$$H_1 = \lambda_\gamma \frac{\rho V_\infty}{2BC} \frac{L}{D} \tag{2.161}$$

Inspecting the switching function shows that it is a function of the flight path angle co-state variable as well as other terms related to the flow-field and vehicle. The latter terms are always positive and non-zero thus indicating that the optimal angle of attack flight control is primarily influenced by the sign of the former term. Formally, the bank angle optimal control law has a "bang-bang" structure denoted by Eq. (2.162). The potential non-existence of the singular arc solution for BAM can be found in [69] and is not re-produced in the Appendix section of this dissertation.

$$u^* = \begin{cases} u_{min}, & \text{if } H_1 > 0 \\ u_{max}, & \text{if } H_1 < 0 \end{cases} \tag{2.162}$$

Regularized Optimal Control Solution

The optimal BAM flight control is numerically solved using regularized optimal control. The methodology is applied to aerocapture mission sets at Venus, Earth, Mars, Titan, and Neptune. The simulation parameters utilized can be found in Table 2.4. In particular, the vehicle L/D and BC are selected to be representative of prospective vehicle designs at each planetary destination. Furthermore, the longitudinal entry states and target orbits are also selected to be similar to existing mission sets. Due to the assumed decoupled lateral dynamics, the corresponding initial lateral states are selected such that the entry trajectory is equatorial at each planetary destination.

Table 2.4. Bank Angle Modulation Optimal Aerocapture Simulation Parameters

Category	Variable	Venus	Earth	Mars	Titan	Neptune
Entry State	r_0, km	6201.800	6503.136	3546.190	3575.000	25764.000
	θ_0, deg	0.000	350.854	342.226	7.239	0.000
	ϕ_0, deg	0.000	0.000	0.000	0.000	0.000
	v_0, km/s	11.250	11.095	5.253	6500.000	31.474
	γ_0, deg	-5.815	-5.186	-10.500	-36.118	-12.5
	ψ_0, deg	0.000	0.000	0.000	0.000	0.000
Exit State	h_f, km	150	125	150	1000	1000
Target Orbit	h_p^t, km	300	500	400	1700	3986
	h_a^t, km	300	500	400	1700	430000
Vehicle	L/D	0.25	0.25	0.25	0.25	0.5
	BC, kg/m^2	60	85	60	90	120
	$[\sigma_{min}, \sigma_{max}]$, deg	$[0, 180]$	$[0, 180]$	$[0, 180]$	$[0, 180]$	$[0, 180]$

Figure 2.22 provides a comparison of the optimal bank angle modulation control laws for decreasing values of ϵ at each planetary destination. The control laws are inherently unique for each planet but do exhibit similar trends with respect to ϵ. For decreasing sequence of ϵ, the optimal control approaches a "bang-bang" structure. For Venus, Earth, Mars, and Neptune, the bank angle switches from maximum values to minimum value and may switch back to the max value. This second switch is more evident in the Earth and Neptune datasets. Conversely, Titan exhibits bank angle switch from minimum to maximum value. This observation demonstrates that bounds in which the bank angle switches to and from can depend on the planetary destination. This may lead to difficulty in obtaining a numerical solution using the known "bang-bang" control law from Eq. (2.162) as the initial guess may assume the wrong switch. On the other hand, the regularized optimal control results makes no such assumption allowing for numerical solutions to be obtained while allowing for the expected control structure to be generally converged upon.

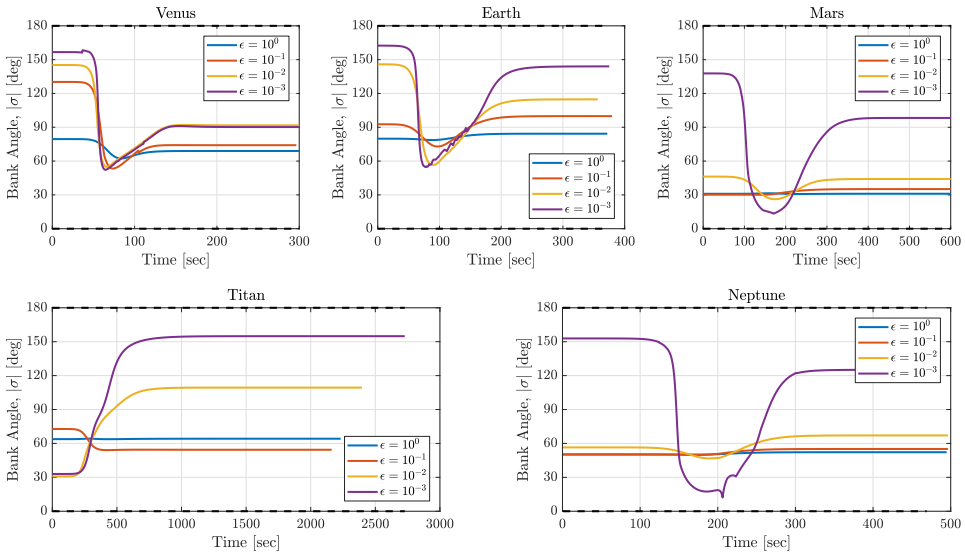

Figure 2.22. Regularized bank angle optimal control solutions for planetary aerocapture. Black dashed lines are imposed control constraints

Figure 2.23 provides a sample trajectory solution for BAM optimal aerocapture. Although not all BAM solutions are presented, the general trends can be deciphered from the single numerical solution. The trajectory shows the time evolution of the state and co-state vectors corresponding to $\epsilon = 10^{-3}$ result for Titan. The blue plots denote the longitudinal state variables while the black plots denote the subsequent lateral state variables solved for using the longitudinal state vector solution. These lateral variable solutions represent their natural evolution if no bank angle reversal logic is implemented to control the inclination error. Despite having no physical significance, the co-state vector influences the bank angle inputs that control the state vector. The control solution for this corresponding trajectory is shown in Figure 2.24. The saturation control allows for the bank angle to remain bounded through the enforcement of the control equality constraint g_1. The subsequent time history of the constraint is shown to be close to zero with some small numerical error within the specified error tolerance. Furthermore, the Hamilton time history is shown to be nearly zero, which validates the finding from calculus of variation of a constant zero Hamiltonian.

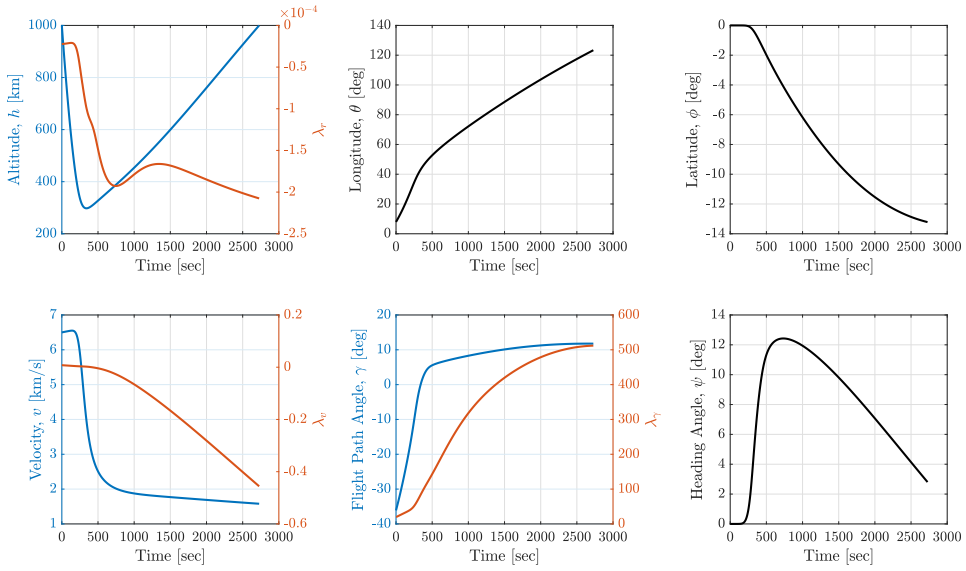

Figure 2.23. Sample Titan bank angle modulation optimal aerocapture trajectory solution

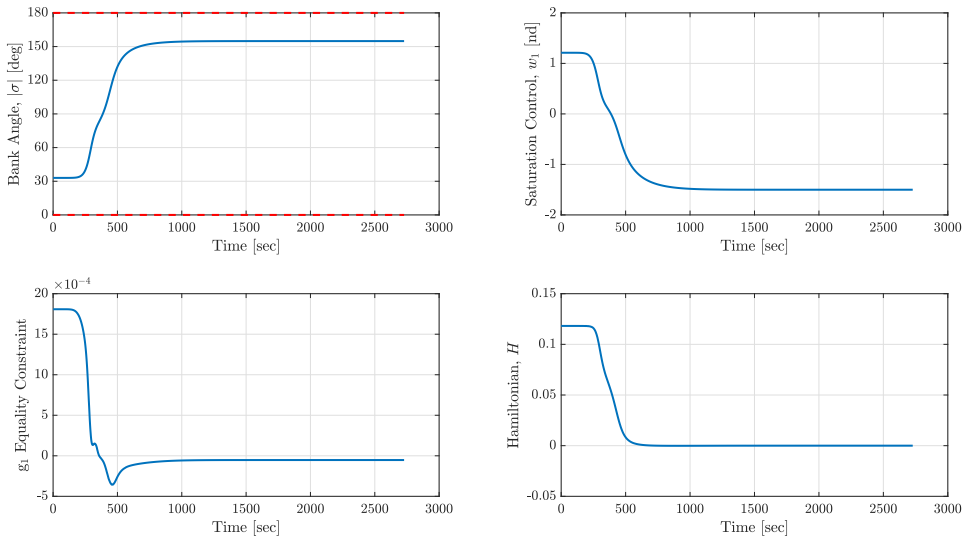

Figure 2.24. Sample Titan bank angle modulation optimal aerocapture control solution. Red dashed lines are control constraint limits

Table 2.5 tabulates the orbit insertion performance and computation cost of each of the BAM solutions. Each run is shown to produce minimal apoapsis error thus indicating that the corresponding terminal constraint is met. The corresponding apoapsis correction maneuver is thereby minimized. The small maximum error indicates sufficient quality of the numerical solutions. For decreasing sequence of ϵ, the regularized cost decreases with

some affect to the periapsis raise maneuver cost. This trend indicates two things. Firstly, the cost functional utilized by the regularization methodology converges to the original cost functional posed in the optimal aerocapture formulation thus indicating that optimal control law that minimizes the original cost function can be converged upon. Secondly, each ϵ solution produces a unique and admissible control time history that achieves the desired terminal constraints. At Neptune, the resulting periapsis raise costs doesn't significantly change with decreasing ϵ. Venus and Titan exhibit modest decreases in periapsis raise cost while Earth and Mars exhibits a minute decrease. The relative magnitude of the decrease can be significant with the largest ΔV reduction around 30 m/s.

The computational cost of achieving optimal BAM control is representative by the number of *odefun* calls. Each function call is analogous to the number of numerical integrations utilized by the collocation solver. Table 2.5 shows that a large number of integrations are needed to achieve even a single solution. Despite achieving the optimal BAM control law, the regularized optimal control approach is too computationally expensive to be implemented on-board an aerocapture vehicle.

Table 2.5. Regularized Bank Angle Optimal Aerocapture Solution Data

Planet	ϵ	$r_{a_{error}}$ (km)	ΔV_2 (m/s)	ΔV_1 (m/s)	ΔV_u (m/s)	$\bar{P}$ (m/s)	Max Error	# *odefun* calls
Venus	1E+00	6.077E-04	1.711E-04	122.779	77.552	200.331	8.948E-05	86945
	1E-01	1.439E-03	4.052E-04	129.664	10.569	140.233	2.847E-02	102748
	1E-02	3.787E-06	1.066E-06	107.258	1.212	108.470	3.174E-02	90769
	1E-03	8.613E-03	2.424E-03	110.153	0.989	111.141	6.691E-02	94269
Earth	1E+00	1.529E-03	4.232E-04	140.945	14.014	154.958	5.821E-04	73758
	1E-01	4.674E-02	1.293E-02	137.989	1.887	139.876	3.888E-03	90652
	1E-02	9.475E-04	2.622E-04	141.300	2.050	143.350	1.039E-02	83335
	1E-03	1.413E-02	3.911E-03	136.547	0.608	137.156	1.630E-01	101387
Mars	1E+00	8.511E-06	1.883E-06	118.819	1500.483	1619.302	7.012E-04	83787
	1E-01	9.093E-04	2.011E-04	118.232	135.689	253.921	1.103E-03	91707
	1E-02	2.237E-06	4.948E-07	117.546	9.891	127.437	5.115E-04	90769
	1E-03	3.550E-03	7.853E-04	113.175	0.600	113.775	1.396E-02	98683
Titan	1E+00	5.597E-08	4.744E-09	189.314	916.821	1106.135	1.354E-05	211666
	1E-01	5.117E-02	4.337E-03	195.469	149.172	344.641	6.605E-04	246125
	1E-02	5.890E-01	4.992E-02	173.174	7.613	180.786	6.838E-03	207099
	1E-03	7.796E-04	6.607E-05	156.299	7.201	163.500	2.849E-03	207600
Neptune	1E+00	1.096E-05	1.516E-08	88.154	459.319	547.473	1.765E-04	80505
	1E-01	1.203E-04	1.663E-07	88.039	42.591	130.631	2.428E-04	109101
	1E-02	8.628E-04	1.193E-06	87.910	2.840	90.750	4.076E-04	106492
	1E-03	3.486E-02	4.820E-05	89.054	0.756	89.810	3.869E-02	120576

2.2.4 Drag modulation flight control laws

For drag modulation, the primary control is assumed to be BC. The vehicle is assumed to be trimmed at zero angle of attack, side-slip angle, and bank angle such that no lift or side-force is generated. Due to lack of out-of-plane control authority, the inclination terminal boundary condition is omitted. Substituting the definition of ballistic coefficient, Eq. (1.1), into definition of drag, Eq. 2.118 and dividing by m yields Eq. (2.163).

$$\frac{D}{m} = \frac{\rho V_\infty^2}{2BC} \tag{2.163}$$

In Eq. (2.163), BC is inversely proportional to the drag acceleration. Assuming constant mass, BC can be changed through combination of C_D and A_{ref}. These two components are in fact linear with respect to the drag acceleration. Consequently, the optimal control formulation assumes the an auxiliary control variable uBC such that $uBC = \frac{1}{BC}$. For DM, BC is bounded by an upper and lower limit. Converted to uBC, the control bounds imposed are given by Eq. (2.164).

$$uBC_{min} \leq uBC\,(t) \leq uBC_{max} \tag{2.164}$$

Optimal Control Law

To ascertain the DM optimal control laws, the Hamiltonian is first formulated using Eq. (2.141). Given zero lift and side-force vehicle configuration, uBC appears only in $\dot{V}$. Due to uBC linear relationship to the term $\frac{D}{m}$ found in Eq. 2.57, the Hamiltonian can be written to be the form of Eq. (2.147) where H_1 can be written by Eq. (2.165).

$$H_1 = -\lambda_v \frac{\rho V_\infty^2}{2} \tag{2.165}$$

Inspecting the switching function shows that it is a function of both the freestream dynamic pressure as well as the velocity co-state variable. The former term is always positive thus indicating that the optimal DM flight control is primarily influenced by the sign of the latter term. Formally, the optimal control law has a "bang-bang" structure denoted by

Eq. (2.166). The potential non-existence of the singular arc solution for DM is proved in Appendix A.0.1.

$$uBC^* = \begin{cases} uBC_{min}, & \text{if } H_1 > 0 \\ uBC_{max}, & \text{if } H_1 < 0 \end{cases} \tag{2.166}$$

Regularized Optimal Control Solution

The optimal DM flight control is numerically solved using regularized optimal control methodology highlighted in the previous section. The methodology is applied to aerocapture mission sets at Venus, Earth, Mars, Titan, and Neptune. The simulation parameters utilized can be found in Table 2.6. In particular, the ballistic coefficient range is selected to representative of prospective vehicle designs at each planetary destination. Furthermore, the entry states and target orbits are also selected to be similar to existing mission sets.

Table 2.6. Drag Modulation Optimal Aerocapture Simulation Parameters

Category	Variable	Venus	Earth	Mars	Titan	Neptune
Entry State	r_0, km	6201.800	6503.136	3546.190	3575.000	25764.000
	θ_0, deg	0.000	350.854	342.226	7.239	344.818
	ϕ_0, deg	-9.132	-5.243	0.000	-35.544	-6.862
	v_0, km/s	11.250	11.095	5.253	6500.000	31.482
	γ_0, deg	-5.349	-5.855	-11.156	-33.759	-9.772
	ψ_0, deg	-90.000	-30.785	0.000	-102.323	-156.603
Exit State	h_f, km	150	125	150	1000	1000
Target Orbit	h_p^t, km	300	500	400	1700	3986
	h_a^t, km	300	500	400	1700	430000
Vehicle	L/D	0	0	0	0	0
	$[BC_{min}, BC_{max}]$, kg/m^2	$[10, 50]$	$[75, 375]$	$[60, 300]$	$[10, 50]$	$[10, 50]$

Figure 2.25 provides a comparison of the optimal drag modulation control laws for decreasing values of ϵ at each planetary destination. The control laws are inherently unique for each planet but do exhibit similar trends with respect to ϵ. For decreasing sequence of ϵ, the optimal control converges to a "bang-bang" structure where the ballistic coefficient switches from its maximum value to its minimum value briefly and then switches back to the maximum value. This trend suggests that ballistic coefficient undergoes two control switches, which otherwise would not be known a-priori if the problem was solved using the known

"bang-bang" control law from Eq. (2.166). Nonetheless, the regularized optimal control results is shown to produce the expected structure.

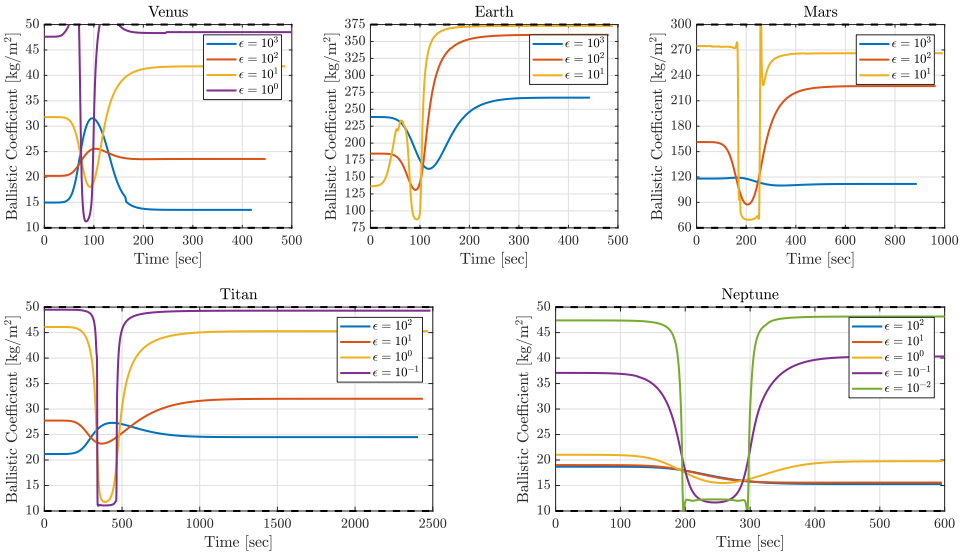

Figure 2.25. Regularized drag modulation optimal control solutions for planetary aerocapture. Black dashed lines are imposed control constraints

Figure 2.26 provides a sample trajectory solution for DM optimal aerocapture. Although not all DM solutions are presented, the general trends can be deciphered from the single numerical solution. The trajectory shows the time evolution of the state and co-state vectors corresponding to $\epsilon = 10^{-2}$ result for Neptune. Despite having no physical significance, the co-state vector influences the ballistic coefficient inputs that control the state vector. The control solution for this corresponding trajectory is shown in Figure 2.27. The saturation control allows for the ballistic coefficient to remain bounded through the enforcement of the control equality constraint g_1. The subsequent time history of the constraint is shown to be close to zero with some small numerical error within the specified error tolerance. Furthermore, the Hamilton time history is shown to be nearly zero, which validates the finding from calculus of variation of a constant zero Hamiltonian.

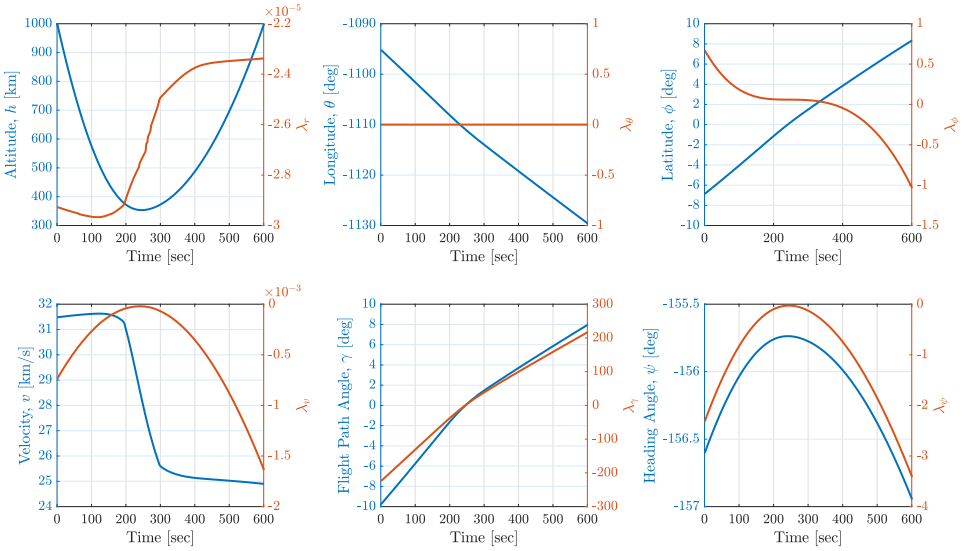

Figure 2.26. Sample Neptune drag modulation optimal aerocapture trajectory solution

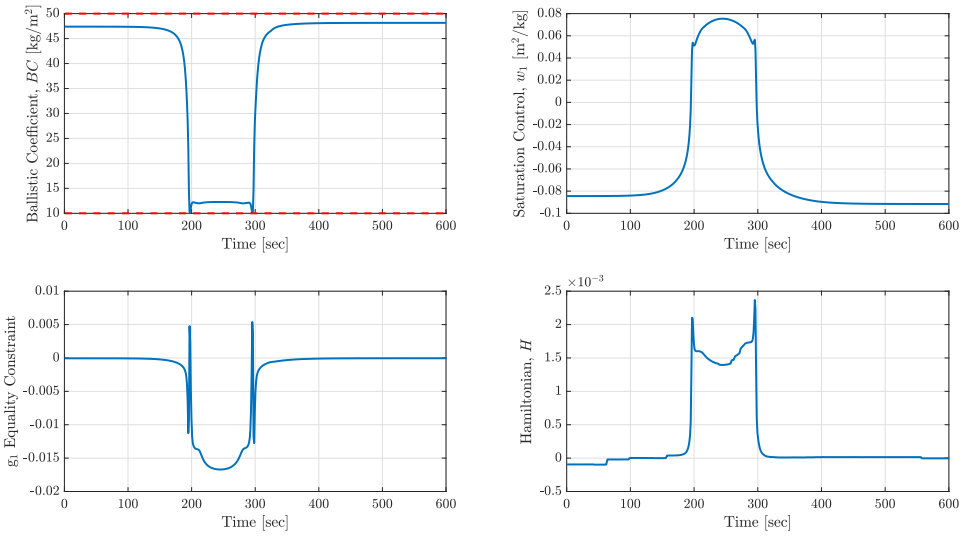

Figure 2.27. Sample Neptune drag modulation optimal aerocapture control solution. Red dashed lines are control constraint limits

Table 2.7 tabulates the orbit insertion performance and computation cost of each of the DM solutions. Each run is shown to produce minimal apoapsis error thus indicating that the corresponding terminal constraint is met. The corresponding apoapsis correction maneuver is thereby minimized. The small maximum error indicates sufficient quality of the numerical solutions. For decreasing sequence of ϵ, the regularized cost decreases with some affect to the periapsis raise maneuver cost. This trend indicates two things. Firstly, the cost functional

utilized by the regularization methodology converges to the original cost functional posed in the optimal aerocapture formulation thus indicating that optimal control law that minimizes the original cost function can be converged upon. Secondly, each ϵ solution produces a unique and admissible control time history that achieves the desired terminal constraints. At Neptune, the resulting periapsis raise costs doesn't significant change but does decrease with decreasing ϵ. Venus, Titan, and Mars exhibit modest decreases in periapsis raise cost while Earth exhibits a minute decrease. The relative magnitude of the decrease is still not a significant game-changer in terms of propellant mass savings.

The computational cost of achieving optimal DM control is representative by the number of *odefun* calls. Each function call is analogous to the number of numerical interactions utilized by the collocation solver. Table 2.7 shows that a immensely large number of interactions are needed to achieve even a single solution. Despite achieving the optimal DM control law, the regularized optimal control approach is too computationally expensive to be implemented on-board an aerocapture vehicle.

Table 2.7. Regularized Drag Modulation Optimal Aerocapture Solution Data

Planet	ϵ	$r_{a_{error}}$ (km)	ΔV_2 (m/s)	ΔV_1 (m/s)	ΔV_u (m/s)	$\bar{P}$ (m/s)	Max Error	# *odefun* calls
Venus	1E+03	1.750E-02	4.927E-03	80.153	1931.050	2011.202	5.930E-02	51733
	1E+02	1.779E-06	5.006E-07	74.834	98.449	173.283	2.123E-04	43724
	1E+01	6.338E-04	1.784E-04	69.715	17.080	86.795	2.815E-04	49973
	1E+00	5.173E-02	1.456E-02	67.631	3.827	71.458	3.250E-01	54861
Earth	1E+03	3.244E-04	8.975E-05	136.801	19.294	156.095	2.779E-04	82509
	1E+02	1.227E-03	3.394E-04	134.442	5.523	139.965	2.201E-03	83826
	1E+01	9.497E-05	2.628E-05	134.034	1.155	135.189	3.498E-02	69090
Mars	1E+03	2.580E-06	5.708E-07	93.319	73.467	166.786	4.844E-04	103765
	1E+02	1.733E-07	3.834E-08	89.156	10.724	99.880	1.093E-04	84524
	1E+01	1.509E-02	3.338E-03	87.564	2.756	90.320	3.863E-02	98966
Titan	1E+02	1.779E-07	1.508E-08	164.650	511.029	675.679	5.288E-06	256792
	1E+01	8.458E-07	7.169E-08	162.397	54.040	216.437	8.840E-05	227375
	1E+00	1.099E-05	9.313E-07	158.929	13.445	172.374	1.614E-05	234808
	1E-01	5.290E-04	4.484E-05	157.956	3.099	161.054	1.005E-02	308119
Neptune	1E+02	6.953E-07	9.604E-10	82.758	220.741	303.499	2.127E-06	36095
	1E+01	3.493E-07	4.839E-10	82.755	21.571	104.326	3.719E-06	25948
	1E+00	7.161E-03	9.901E-06	82.728	1.738	84.466	2.610E-06	57556
	1E-01	1.504E-02	2.080E-05	82.634	0.217	82.852	3.686E-04	63830
	1E-02	2.167E-02	2.997E-05	82.616	0.049	82.665	4.085E-02	76570

2.2.5 Direct Force Control flight control laws

For DFC, two independent control variables of α and β are used for assessing the optimal angle of attack and side-slip angle control laws, respectively. The vehicle is assumed to be trimmed at zero bank angle such that only α and β control the vehicle's trajectory during flight. Each control variable is bounded by an upper and lower limit as shown by Eq. (2.167) and Eq. (2.168).

$$\alpha_{min} \leq \alpha(t) \leq \alpha_{max} \tag{2.167}$$

$$\beta_{min} \leq \beta(t) \leq \beta_{max} \tag{2.168}$$

In the mathematical formulation of the DFC optimal aerocapture problem, a key assumption is made regarding the vehicle aerodynamics. In 2.1.3, analytical aerodynamic expressions relating the aerodynamic coefficients to α and β are presented. These expressions allow for the DFC control variables to be explicitly incorporated into the optimal control formulation. A linear aerodynamics model is assumed in this analysis. The model arises from a first-order Taylor Series approximation of the resulting non-linear analytical aerodynamics model. The accuracy of the linear model is good for a reasonable range of α and β values around zero degree total angle of attack. This may make the model favorable for application on blunt body aeroshells. A generalized form of the linear model is shown in Eq. (2.169). The terms C_{L_α}, C_{D_0}, and C_{Q_β} are functions of the vehicle geometry and flow-field properties. This form is assumed in the optimal control formulation.

$$\begin{aligned} C_L &= C_{L_\alpha}\alpha \\ C_D &= C_{D_0} \\ C_Q &= C_{Q_\beta}\beta \end{aligned} \tag{2.169}$$

Optimal Control Law

To ascertain the DFC optimal control laws, the Hamiltonian is first formulated using Eq. (2.141). From Eq. (2.169), α primarily controls the lift coefficient while β primarily controls the side-force coefficient. Given zero bank angle vehicle configuration, α appears only in $\dot{\gamma}$ while β appears only in $\dot{\psi}$. These relationships allow for the Hamiltonian to be written in the general form of Eq. (2.147) expanded to two control variables where u_1 refers to α and u_2 refers to β. H_1 and H_2 can then be represented by Eq. (2.170) and Eq. (2.171) respectively.

$$H_1 = \lambda_\gamma \frac{\rho V_\infty}{2m} A_{ref} C_{L_\alpha} \tag{2.170}$$

$$H_2 = -\lambda_\psi \frac{\rho V_\infty}{2m \cos(\gamma)} A_{ref} C_{Q_\beta} \tag{2.171}$$

Inspecting the angle of attack switching function, H_1, shows that it is a function of the flight path angle co-state variable as well as other terms related to the flow-field and vehicle. The latter terms are always positive an non-zero thus indicating that the optimal angle of attack flight control is primarily influenced by the sign of the former term. Formally, the angle of attack optimal control law has a "bang-bang" structure denoted by Eq. (2.172). The potential non-existence of the singular arc solution for both angle of attack and side-slip angle is provided in Appendix A.0.2.

$$\alpha^* = \begin{cases} \alpha_{min}, & \text{if } H_1 > 0 \\ \alpha_{max}, & \text{if } H_1 < 0 \end{cases} \tag{2.172}$$

A similar inspection of the side-slip angle switch function, H_2 can be done with the observation that optimal side-slip angle control is primarily influenced by the azimuth angle co-state variable as well as the control has a "bang-bang" structure denoted by Eq. (2.173).

$$\beta^* = \begin{cases} \beta_{min}, & \text{if } H_2 > 0 \\ \beta_{max}, & \text{if } H_2 < 0 \end{cases} \tag{2.173}$$

Regularized Optimal Control Solution

The optimal DFC flight control is numerically solved using regularized optimal control. The methodology is applied to aerocapture mission sets at Venus, Earth, Mars, Titan, and Neptune. The simulation parameters utilized can be found in Table 2.8. In particular, the vehicle's aeroshell mass, geometry, and imposed control constraints are selected to be representative of prospective blunt body vehicle designs at each planetary destination. Furthermore, the entry states and target orbits are also selected to be similar to existing mission sets.

Table 2.8. Direct Force Control Optimal Aerocapture Simulation Parameters

Category	Variable	Venus	Earth	Mars	Titan	Neptune
Entry State	r_0, km	6201.800	6503.136	3546.190	3575.000	25764.000
	θ_0, deg	0.000	350.854	168.454	7.938	345.879
	ϕ_0, deg	-9.928	-5.186	-8.493	-38.062	-7.362
	v_0, km/s	11.250	11.095	5.303	6500.000	31.474
	γ_0, deg	-5.815	-5.791	-10.800	-36.118	-10.485
	ψ_0, deg	-90.000	-30.795	-30.222	-102.742	-156.603
Exit State	h_f, km	150	125	150	1000	1000
Target Orbit	h_p^t, km	300	500	400	1700	3986
	h_a^t, km	300	500	400	1700	430000
	i^t, km	90	30	30	100	153
Vehicle	m, kg	1500	180	1500	1500	2200
	δ_c, deg	70	70	70	70	70
	r_n, m	1.125	0.3	1.125	0.9375	1.125
	r_c, m	4.5	1.35	4.5	3.75	4.5
	$[\alpha_{min}, \alpha_{max}]$, deg	$[-20, 20]$	$[-20, 20]$	$[-20, 20]$	$[-20, 20]$	$[-30, 30]$
	$[\beta_{min}, \beta_{max}]$, deg	$[-5, 5]$	$[-5, 5]$	$[-5, 5]$	$[-5, 5]$	$[-5, 5]$

Figure 2.28 and Figure 2.29 provides a comparison of the optimal direct force control laws for decreasing values of ϵ at each planetary destination. The control laws are inherently unique for each planet but do exhibit similar trends with respect to ϵ. For decreasing

sequence of ϵ, the optimal control for both angle of attack and side-slip angle converge to a "bang-bang" structure. The bounds in which the angle of attack and side-slip angle switch between varies with each planet. This observation would lead to difficulty in producing an initial guess for solving for the optimal control numerically utilizing Eq. (2.172) and Eq. (2.173). Nonetheless, the regularized optimal control results is shown to produce the expected structure.

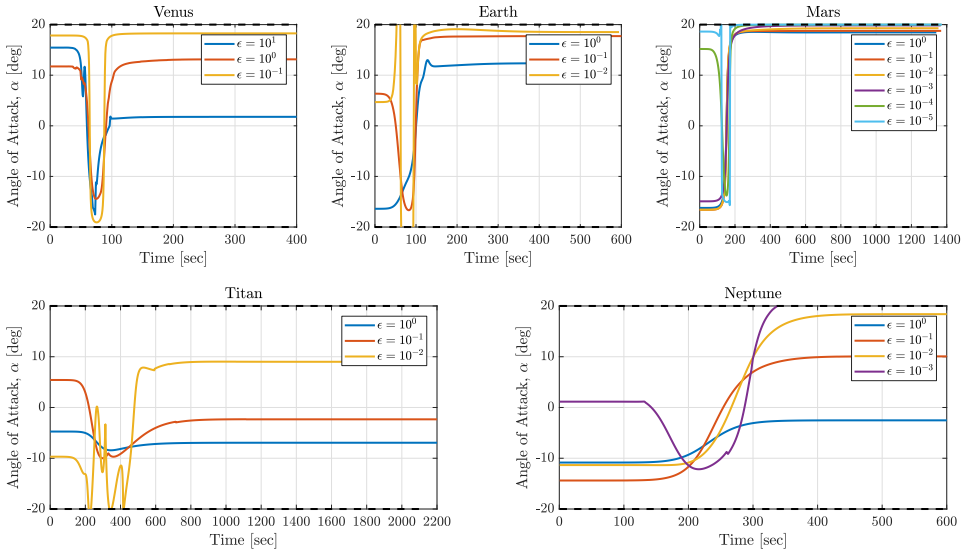

Figure 2.28. Regularized angle of attack optimal control solutions for planetary aerocapture. Black dashed lines are imposed control constraints

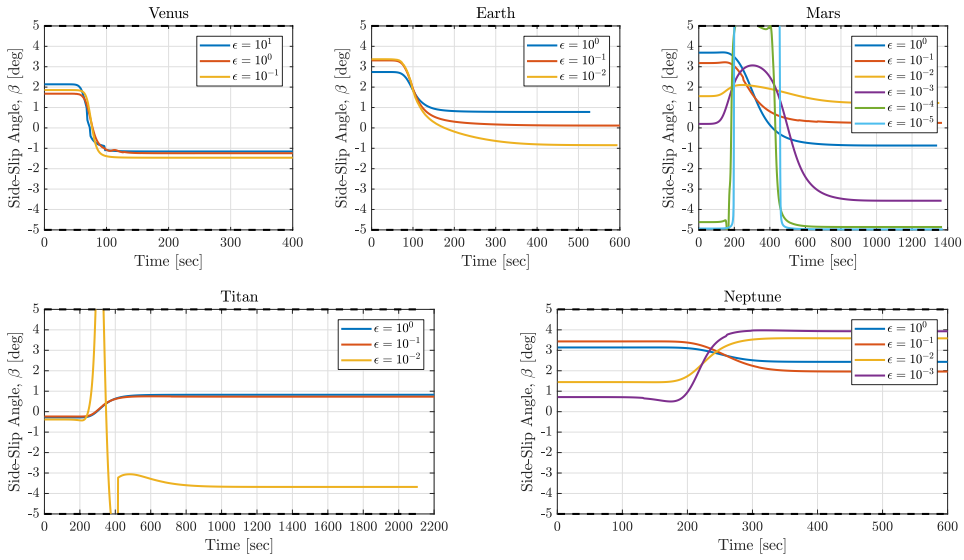

Figure 2.29. Regularized side-slip angle optimal control solutions for planetary aerocapture. Black dashed lines are imposed control constraints

Figure 2.30 provides a sample trajectory solution for DFC optimal aerocapture. Although not all DFC solutions are presented, the general trends can be deciphered from the single numerical solution. The trajectory shows the time evolution of the state and co-state vectors corresponding to $\epsilon = 10^{-5}$ result for Mars. Despite having no physical significance, the co-state vector influences the angle of attack and side-slip angle inputs that control the state vector. The control solution for this corresponding trajectory is shown in Figure 2.31. The saturation controls w_1 and w_2 allows for angle of attack and side-slip angle to respectively remain bounded. This is enforced through the control equality constraints g_1 and g_2. The subsequent time history of the constraint is shown to be close to zero with some small numerical error within the specified error tolerance. Furthermore, the Hamilton time history is shown to be nearly zero, which validates the finding from calculus of variation of a constant zero Hamiltonian.

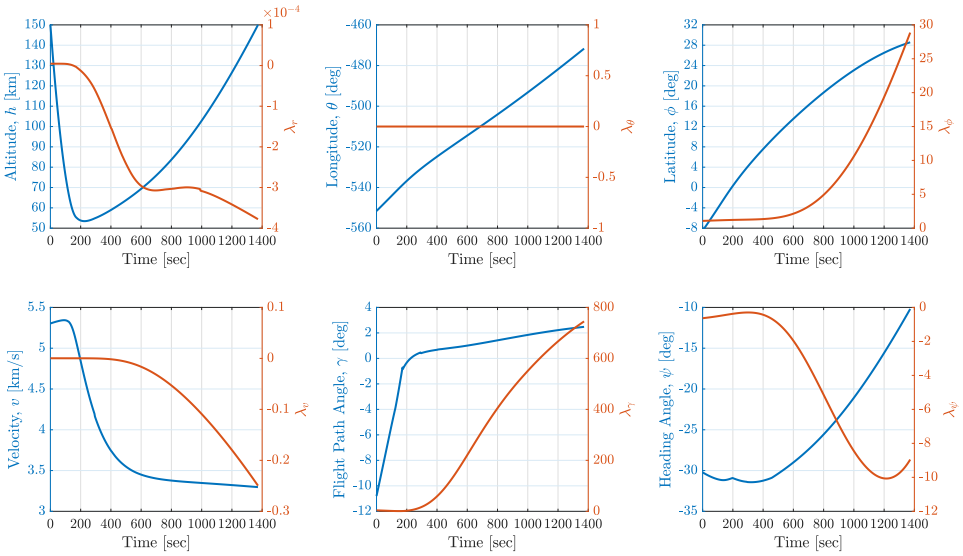

Figure 2.30. Sample Mars direct force control optimal aerocapture trajectory solution

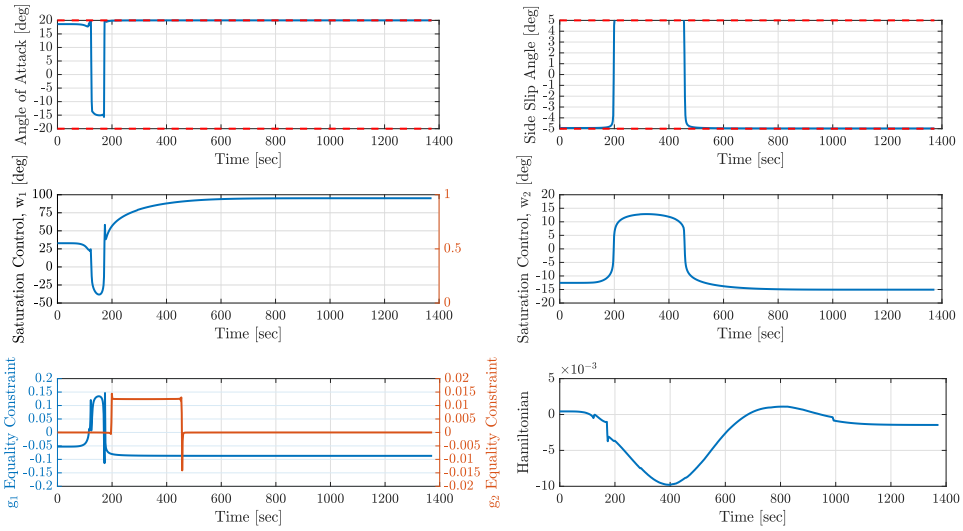

Figure 2.31. Sample Mars direct force control optimal aerocapture control solution. Red dashed lines are control constraint limits

Table 2.9 tabulates the orbit insertion performance and computation cost of each of the DFC solutions. Each run is shown to produce minimal apoapsis and inclination error thus indicating that the corresponding terminal constraints are met. The corresponding apoapsis and inclinations correction maneuvers are thereby minimized. The small maximum error indicates sufficient quality of the numerical solutions.

For decreasing sequence of ϵ, the regularized cost generally decreases with little affect to the periapsis raise maneuver cost. The Venus dataset does show a decreasing trend with the first two values of epsilon but the last value increase. This increase can be attributed to the sensitivity of the numerical solution to the initial guess. Otherwise, the decreasing trend can be seen with the rest of the planetary destinations thereby allowing for convergence to the original cost functional optimal solution. For Mars and Neptune, minute reductions in the periapsis raise cost are achieved with reductions in ϵ. Although this formally demonstrates the convergence to the minimal cost functional, the relative magnitude of the decrease is still not a significant game-changer in terms of propellant mass savings. In fact, it demonstrates that DFC control inputs close to the theoretical optimal can potentially achieve both the desired orbit and at similar propellant cost.

The computational cost of achieving optimal DM control is representative by the number of *odefun* calls. Each function call is analogous to the number of numerical integrations utilized by the collocation solver. Table 2.9 shows that a immensely large number of integrations are needed to achieve even a single solution. Despite achieving the optimal DFC control law, the regularized optimal control approach is too computationally expensive to be implemented on-board an aerocapture vehicle.

Table 2.9. Regularized Direct Force Control Optimal Aerocapture Solution Data

Planet	ϵ	$r_{a_{error}}$ (km)	i_{error} (km)	ΔV_2 (m/s)	ΔV_3 (m/s)	ΔV_1 (m/s)	ΔV_u (m/s)	$\bar{P}$ (m/s)	Max Error	# *odefun* calls
Venus	1E+01	6.270E-01	2.931E-05	1.765E-01	3.659E-03	76.846	87.123	163.969	5.495E-02	86331
	1E+00	1.659E-01	7.669E-06	4.670E-02	9.573E-04	66.822	57.244	124.066	5.746E-03	99848
	1E-01	2.722E-03	1.437E-07	7.661E-04	1.794E-05	71.367	65.961	137.328	7.932E-04	90074
Earth	1E+00	5.305E-03	4.852E-02	1.468E-03	6.446E+00	121.863	56.954	178.817	2.872E-01	45118
	1E-01	1.033E-01	1.093E-02	2.858E-02	1.452E+00	119.006	16.314	135.320	4.503E-02	42979
	1E-02	7.639E-02	7.337E-03	2.114E-02	9.748E-01	118.989	2.176	121.164	1.080E+00	47021
Mars	1E+00	1.798E-06	4.108E-08	3.977E-07	2.408E-06	79.270	523.701	602.972	1.923E-04	107091
	1E-01	2.640E-02	4.266E-03	5.841E-03	2.501E-01	79.303	58.711	138.014	7.012E-03	91680
	1E-02	5.009E-04	6.740E-05	1.108E-04	3.951E-03	79.071	7.077	86.148	6.631E-04	98900
	1E-03	2.102E-06	2.517E-09	4.651E-07	1.476E-07	78.886	1.152	80.037	3.555E-05	95566
	1E-04	7.431E-02	9.852E-03	1.644E-02	5.775E-01	78.849	0.202	79.051	1.825E-02	111260
	1E-05	3.540E-03	4.698E-04	7.831E-04	2.754E-02	78.810	0.033	78.843	5.652E-01	109804
Titan	1E+00	1.648E-05	6.696E-07	1.397E-06	1.694E-05	191.303	67.638	258.941	2.590E-05	246146
	1E-01	5.385E-02	7.863E-03	4.564E-03	1.989E-01	189.026	2.189	191.215	7.647E-03	316689
	1E-02	1.328E+00	4.780E-01	1.125E-01	1.209E+01	191.166	2.423	193.589	2.039E-01	321004
Neptune	1E+00	7.737E-04	5.470E-08	1.070E-06	3.702E-06	84.854	21.536	106.390	6.314E-05	60099
	1E-01	1.078E+01	6.415E-04	1.491E-02	4.341E-02	83.803	5.343	89.146	7.317E-04	82764
	1E-02	1.122E-01	6.724E-06	1.552E-04	4.550E-04	83.854	1.056	84.910	2.561E-05	72325
	1E-03	1.561E+01	9.479E-04	2.158E-02	6.415E-02	83.724	0.305	84.030	1.395E-02	76130

2.2.6 Discussion

In the previous section, it was numerically demonstrated that regularized optimal control allows for the optimal aerocapture problem to be solved. For each flight control analyzed, the numerical solutions provide excellent orbit insertion performance and meet all the imposed initial and terminal boundary conditions. However, the fundamental assumption of introducing the original control, $\vec{u}$, with the saturation control, $\vec{w}$, in the control regulator was made. This was done to provide a quadratic cost function that exhibits a quadratic growth property, which is a property of strongly convex functions. The periapsis raise maneuver cost is not an explicit function of $\vec{u}$. By introducing u along with the regularization constant, a quadratic cost functional, $\tilde{P}(\vec{u}, \epsilon)$, is achieved as shown in Eq. (2.174).

$$\tilde{P}(\vec{u}, \epsilon) = |\Delta V_1| + \epsilon \int_{t_0}^{t_f} ||\vec{u}||_2^2 dt \tag{2.174}$$

The quadratic growth property can be mathematically formulated using Eq. (2.175)

$$C_2||\vec{u} - \vec{u}^*||_2^2 \leq \tilde{P}(\vec{u}, \epsilon) - \tilde{P}(\vec{u}^*, \epsilon), u_i \in \left[u_i^{min}\ u_i^{max}\right] \tag{2.175}$$

Graichen et al[99], proves in Theorem 2 that this property holds if it is assumed that

1. $\tilde{P}(\vec{u}, \epsilon)$ has an optimal solution, $\vec{u}^*$, that minimizes $\tilde{P}(\vec{u}, \epsilon)$
2. $\bar{P}\left(\vec{u}^k, \vec{w}^k, \epsilon^k\right)$ has a bounded state and control solutions, $\vec{x}^k$ and $\vec{u}^k$, for each regularization constant, ϵ^k used in a decreasing sequence
3. $\tilde{P}(u, \epsilon)$, is continuous in $u_i \in [u_i^{min}\ u_i^{max}]$ and state dynamics, $\dot{\vec{x}}$, are Lipschitz with respect to the $\vec{x}$ and $\vec{u}$

For the optimal aerocapture problem, all three assumptions are valid. Assumptions 1 and 2 are numerically demonstrated with the various solutions computed. Assumption 3 is valid for the imposed control bounds and state vector dynamics that are Lipschitz continuous in $\vec{x}$ and $\vec{u}$. The consequence of exhibiting a quadratic growth property is convergence to the optimal solution. For the decreasing sequence of ϵ^k such that $\lim_{k\to\infty} \epsilon^k = 0$, the control, $\vec{u}^k$, and state histories, $\vec{x}^k$ converge to the optimal control and state histories. Graichen et

al[99] additionally proved in Theorem 1 that for the same decreasing sequence of ϵ^k, the regularized optimal control converges to the original optimal cost functional, P^* as shown by Eq. (2.176).

$$\begin{aligned} \lim_{k\to\infty} \bar{P}\left(\vec{u}^k, \vec{w}^k, \epsilon^k\right) &= P^* \\ \lim_{k\to\infty} \tilde{P}\left(\vec{u}^k, \epsilon^k\right) &= P^* \\ \lim_{k\to\infty} \epsilon^k \int_{t_0}^{t_f} ||\vec{u}||_2^2 + ||\vec{w}||_2^2 dt & \end{aligned} \tag{2.176}$$

The numerical results presented for each flight control methodology at different planetary destinations validates these two theorems. The regularized cost functional exhibits a quadratic growth property for increasing ϵ^k as seen in Table 2.5, Table 2.7, and Table 2.9. As ϵ^k is reduced, the regularized cost functional converges to the periapsis raise cost. Furthermore, the control law solutions converge to the "bang-bang" optimal solutions. Overall, regularized optimal control problem formulation allows for the bounded optimal flight control laws pertaining to BAM, DM, and DFC to be numerically solved for at various planetary destinations.

2.2.7 Application of Results to Onboard Guidance

The solution method presented in this section could be integrated into a closed-loop architecture in the form of a Model Predictive Controller (MPC). During each guidance cycle, the collocation solver determines the optimal control input from the current state to atmospheric exit. The control input along with the state dynamics are subsequently integrated forward in time until the next guidance cycle. Due to unforeseeable trajectory dispersions, a feedback controller provides the necessary model updates for the next guidance iteration and the collocation solver repeats the optimization process. Although a valid guidance methodology, the sheer computational cost of achieving even a single collocation solution may dissuade the utilization of a MPC for achieving optimal aerocapture guidance.

The application optimal control theory to BAM, DM, and DFC does provide invaluable insight into the *structure* of the optimal control. This common "bang-bang" structure can be leveraged in formulating a unified guidance strategy that attempts to achieve aerocapture

trajectories that are as close to the optimal as possible. From the numerical simulations of the regularized optimal control, it was shown that trajectories that are not exactly the pure "bang-bang" optimal solution achieve the necessary orbit insertion performance at similar periapsis raise cost. If the control switch time between two assumed control bounds, e.g. upper and lower, is used as the control input in a "bang-bang" fashion, then the trajectory optimization can be potentially solved using univariate parameter optimization. This indirect approach may allow for a closed-loop guidance methodology to be formulated that is orders-of-magnitude computationally cheaper to implement.

3. DESIGN OF A NPC AEROCAPTURE ARCHITECTURE

This chapter highlights the formulation of the modular NPC aerocapture guidance architecture.

3.1 NPC Algorithm

In Chapter 2, fuel minimizing aerocapture ΔV control laws for DFC, BAM, and DM are derived. Under certain underlying assumptions, the control laws for each flight control law are found to have the same "bang-bang" structure. Consequently, a unified trajectory optimization algorithm can be developed in the form of a numerical predictor-corrector. The NPC works by *numerically* integrating the equations of motion from the vehicle's current state using a univariate parameter relating to the control structure or control itself. This is done to *predict* the cost functional at the terminal state. The *corrector* optimizes the parameter to minimize the post-aerocapture in-plane ΔV using parameter optimization techniques. Separate lateral logic for BAM and DFC is utilized to minimize the orbit plane error. The aerocapture guidance runs the algorithm at a prescribed frequency set by the flight computer. Figure 3.1 provides a high-level overview of the designed NPC algorithm.

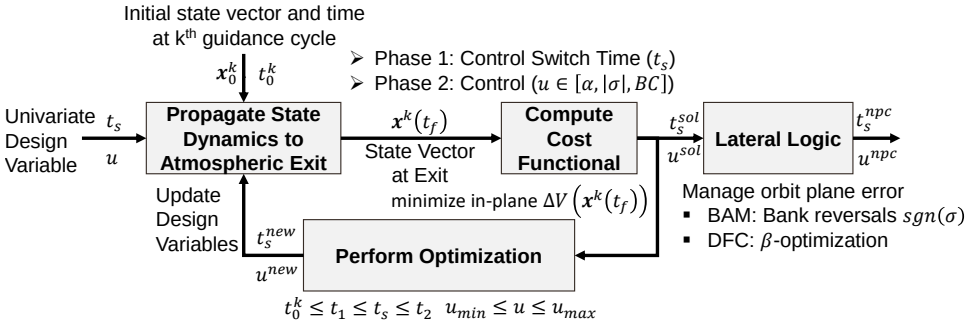

Figure 3.1. NPC algorithm overview

3.1.1 Phased structure

The designed NPC algorithm utilizes a two-phased active guidance structure, Phases 1 and 2, to determine the necessary control commands. Both of these phases occur while the vehicle is in the sensed atmosphere, which is defined by a sensed deceleration from the vehicle's IMU of 0.01 g's. Phases 0 and 3 are defined from atmospheric entry to the g-load trigger and g-load trigger to atmospheric exit, respectively. During these two phases, no active guidance is conducted and a constant control input is commanded.

During Phase 1, the control switch time is optimized to minimize the cost functional. The minimum and maximum control limits utilized in Phase 1 are selected to be a subset of the theoretical control limit capability of the vehicle. This is done to allow for control margin after Phase 1 keeping robustness into consideration. For BAM, the control is assumed to switch from lift up configuration (σ_{min}) to lift down configuration (σ_{max}). Similarly for DFC, the control is assumed to switch from lift up (α_{min}) to lift down (α_{max}) configurations. For DM, the control is assumed to switch from maximum drag configuration (BC_{min}) to minimum drag configuration (BC_{max}). Assuming continuously-variable systems employing morphable sphere-cone aeroshells, the minimum and maximum drag configurations can be correlated to max cone angle, ($\delta_{c,max}$), and min cone angle, ($\delta_{c,min}$) respectively. Note that Phase 1 only with the theoretical control limits allows for the jettison time for staged-jettison systems to be computed.

After the switch time is reached, Phase 2 begins where the flight control variable itself ($|\sigma|$ for BAM, α for DFC, BC via δ_c for DMCV) is optimized within the theoretical control limits to minimize the cost functional. This phase is added to allow for the guidance to account for unforeseeable trajectory dispersions experienced after the control switch is reached. Despite the trajectory potentially diverging from the optimal trajectory, the second phase allows for guidance robustness when operating in a potentially stochastic planetary atmosphere.

3.1.2 Parameter optimization

The optimal aerocapture problem can be converted into a *univariate* parameter optimization problem using the a-priori control law structure. The explicit enforcement of terminal boundary conditions can be eliminated with a few assumption. Firstly, the cost functional in Eq. (2.113) is modified to include the apoapsis correction cost such that $P = |\Delta V_1| + |\Delta V_2|$. This allows for the relaxation of the apoapsis radius boundary condition. Secondly, the inclination boundary condition is assumed to be handled by separate lateral logic explained later in the next section. Finally, a numerical integration cutoff at the atmospheric exit altitude is assumed. This allows for the relaxation of the terminal boundary condition on r. The cumulative affect of these assumptions are the formulation of a control bounded univariate parameter optimization with no explicit terminal boundary conditions.

Such a posed problem can be solved using a variety of optimization techniques. Since the in-plane ΔV cost functional is not an explicit function of the control parameters, calculus-based techniques would rely on numerical derivatives. Their computation adds to the computational complexity of the NPC algorithm since additional integrations of the equations of motion are needed as well as are potentially sensitive to the step size used in their calculation. Hyperbolic trajectories have infinite apoapsis radius and as a result the apoapsis correction cost is infinite. This may lead to infinite gradient calculations and convergence instability. As a result, non calculus-based approaches are preferred. Bracketing methods seek to determine the minimum of the cost functional on a control bounded interval without utilization of gradients. Golden section search utilizes the golden ratio in determining the next point to iterate on in the bracketing minimum search [102]. The convergence to a minimum is linear with respect to each successive function evaluation. The convergence speed can be potentially increased if the objective function exhibits a parabolic structure. With this assumption, an inverse parabolic interpolation can be utilized to determine the minimum point between the bracketed points of interest. Brent's method combines both Golden section search along with inverse parabolic interpolation to efficiently converge to a neighborhood of a *local* minimum [103]. Although this approach may not achieve a globally

optimal solution, the robustness and convergence benefits of this approach are significant for on-board application.

The designed NPC leverages Brent's method with an algorithm code found in [104]. During Phase 1 although the control switch time is not explicitly bounded, the lower and upper bounds are selected to correspond to captured elliptical trajectories. For Phase 2, the lower and upper bounds are selected to correspond to the respective control bounds of each flight control. The step tolerance utilized by the method is assumed to be 1e-3. To provide accurate calculations of the cost functional, a variable time-step integrator rather than a fixed-time step integrator is utilized. A variable order Adams-Bashforth-Moulton PECE integrator is utilized [105]. The relative and absolute tolerances are assumed to be 1e-6.

3.1.3 Lateral logic

The algorithm lateral logic is utilized for determining the sign of the bank angle (for BAM) or side-slip angle (for DFC). The objective of the logic is to determine the necessary commands such that orbit plane error is minimized *after* the in-plane optimization of $|\sigma|$ or α is completed. Consequently, the logic assumes the longitudinal and lateral flight dynamics can be controlled independently.

For BAM, $sgn(\sigma)$ is determined to null the orbit plane error. Producing bank reversals can be potentially expensive and demanding the the vehicle RCS system and as a result are limited to a prescribed number. The formulation of the BAM lateral logic is derived from the methodology introduced by Smith [106]. The method compares the ratio of the predicted inclination errors to a threshold value. The inclination errors are computed by numerically integrating the state vector dynamics from the current state in the trajectory to atmospheric exit using positive and negative signs of the current bank angle. The threshold is computed by raising the ratio of the current inclination error and prescribed final inclination error to the inverse of the number of available bank reversals left. The threshold allows for wiggle room with respect to the final inclination error and does not quickly saturate the number of bank reversals conducted. A final inclination error of 0.1° is assumed. The maximum

number of bank reversals is assumed to be five. Figure 3.2 provides a sample performance of the BAM lateral logic.

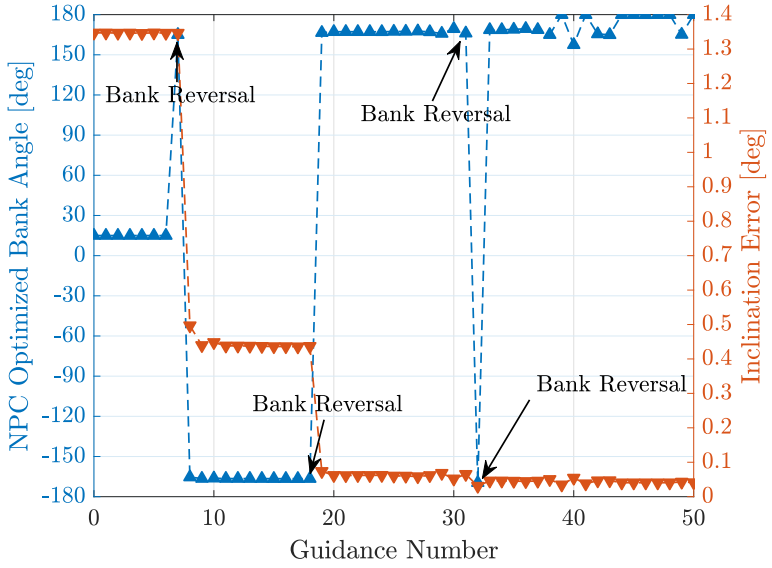

Figure 3.2. Example NPC lateral logic performance for BAM

For DFC, the orbit plane error is minimized using optimization of the side-slip angle itself. The parameter optimization formulated in the previous section is applied with $P = \sqrt{(i - i^t)^2}$. This methodology adds additional computational cost to the NPC algorithm for DFC, but may allow for precise control over the orbit plane error as shown in Figure 3.3.

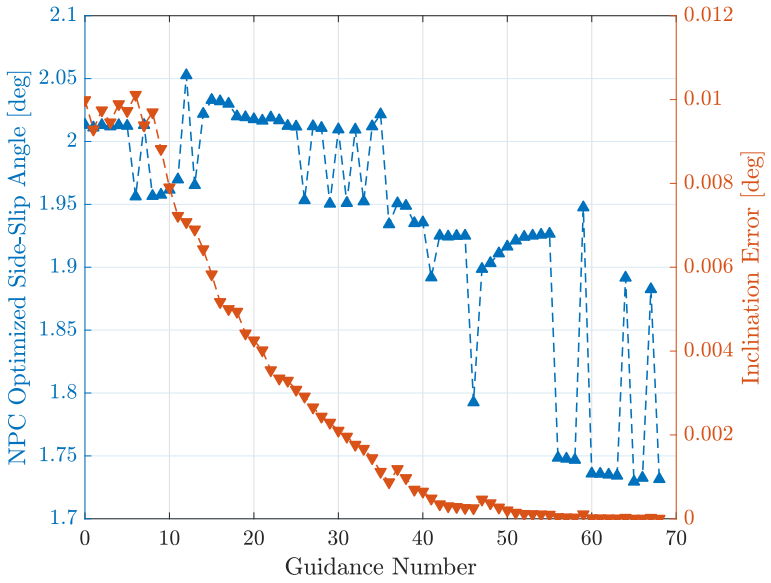

Figure 3.3. Example NPC lateral logic performance for DFC

3.1.4 Comparison to optimal trajectories

The aerocapture problems analyzed in Section 2.2 are numerically solved using the NPC algorithm. For the BAM comparison, no lateral logic is utilized by the NPC solutions. The guidance is called at a rate of 0.1 Hz for each flight control. During each guidance call, the same atmospheric density table as the one utilized by the optimal control solutions is utilized. Two NPC solution methods are conducted. The first method, denoted by Min ΔV, uses the two phase active guidance approach with the cost functional defined by in-plane ΔV. The second method, denoted by Min $r_{a_{error}}$, uses Phase 2 only during active guidance with a cost functional denoted by $P = \sqrt{(r_a - r_a^t)^2}$. This method is selected to emulate the cost functional utilized by current state-of-the-art NPC guidance algorithms.

In the subsequent sections for each flight control, the resulting periapsis raise cost (ΔV_1) for the Min ΔV NPC method may be slightly lower than the optimal trajectory solution at certain planets. This result is not be interpreted as the optimal trajectory not being truly optimal but rather an artifact of the collocation solution. Due to difficulty in achieving numerical solutions, a large integration tolerance of 1e-3 is utilized by the collocation solver. This is in contrast with the NPC, which utilized a much smaller integration tolerance of 1e-6.

Furthermore, no mesh refinement is used in the collocation solution process. Given the same utilized atmospheric density table for each planet, the differences in the numerical integration setup step size may lead to large enough differences in the atmospheric exit conditions that caused the observed results in periapsis raise cost. It is expected that both mesh refinement and reduction in integration tolerance used in the collocation solution process will reconcile these results.

Bank Angle Modulation

Figure 3.4 provides a comparison between the optimized bank angle control inputs at each planetary destination and Figure 3.5 provides a corresponding representation of each trajectory. The Min ΔV method generally produces a constant control command after the bank angle switch. The Min $r_{a_{error}}$ method also generally produces a constant control command. These trends are expected due to nonexistence of trajectory dispersions that otherwise would necessitate compensatory control command modifications. For Earth and Neptune, the more pronounced changes in control commands during Phase 2 can be attributed to the numerical sensitivity of the NPC cost functional to the control parameter. Since the optimization algorithm lacks derivative information, it can be possible for sub-optimal solutions to be produced. Nevertheless, these errors are mitigated as seen in the resulting orbital insertion performance found in Table 3.1.

The resulting NPC bank angle trajectory solutions do not significantly differ from the optimal trajectories with regards to altitude vs velocity and flight path angle vs velocity, with levels varying depending on the planet. At Venus, The optimal control solution and the min $r_{a_{error}}$ agree well in altitude and flight path angle while the Min ΔV produces a differing trajectory with an smaller exit flight path angle for a similar exit velocity. The latter is an observable trend produced with the Min ΔV solution as compared to the others. The terminal flight path angle can be identified to have a significant influence on achieving ΔV-minimizing trajectories. Both the optimal control solution and Min ΔV method exhibit lower terminal flight path angles than the Min $r_{a_{error}}$ method. This yields a lower periapsis raise ΔV for near zero apoapsis correction ΔV as shown in Table 3.1. As was shown in

Figure 2.17 for Venus, achieving an exit flight path angle near zero is beneficial for achieving higher post-aerocapture periapsis altitudes that are propulsively cheaper to raise.

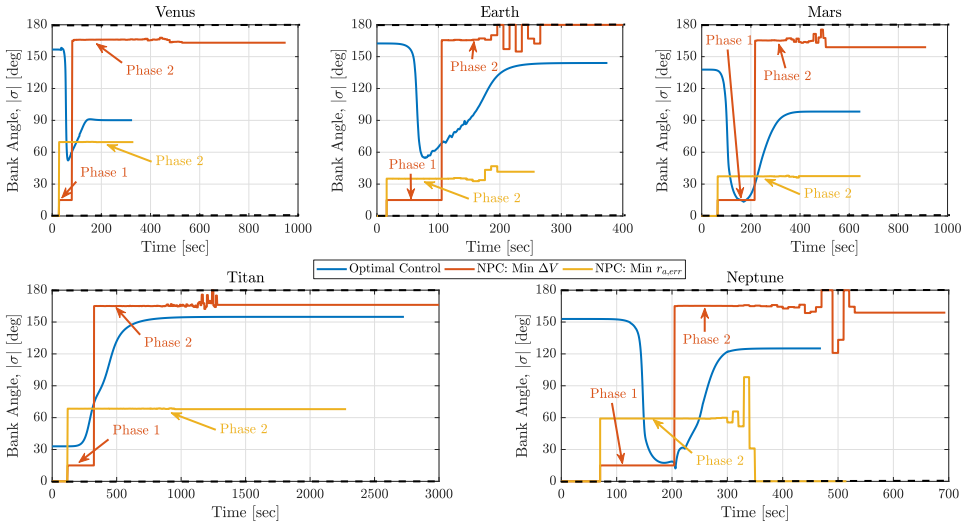

Figure 3.4. Comparison of bank angle control inputs between optimal control and NPC solutions. Black dashed lines are imposed control constraints

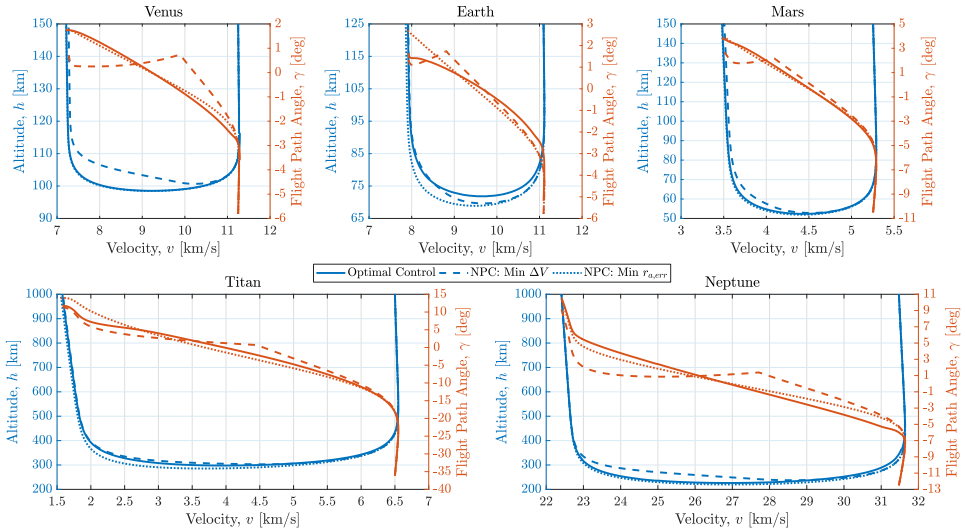

Figure 3.5. Comparison of bank angle trajectories between optimal control and NPC solutions

For BAM, all three numerical guidance solutions are sufficient with regards to orbit insertion. Both the optimal control and Min ΔV methods achieve lower periapsis raise maneuvers than the Min $r_{a_{error}}$ method. At all the destinations simulated, the Min ΔV NPC

solution produces a lower periapsis raise cost than the optimal solution. This difference can be attributed to the lack of mesh refinement used in the collocation solution process for the optimal control solutions. It is expected with further mesh refinement that the optimal control solutions will produce lower periapsis raise costs. With respect to Min ΔV method, the percent reduction in periapsis raise ΔV as compared to the Min $r_{a_{error}}$ method at Venus, Earth, Mars, Titan, and Neptune is 52%, 32%, 27%, 20%, and 5%, respectively. This result demonstrates the performance enhancement achieved by incorporating the periapsis raise maneuver into the cost functional. Furthermore, the NPC methods allow for a significant reduction in the number of numerical integration as compared to the optimal control solution. The percent fraction of the number of Min ΔV method numerical integrations to the optimal control solution at Venus, Earth, Mars, Titan, and Neptune is 0.8%, 0.5%, 0.7%, 0.8%, and 0.6%, respectively.

Table 3.1. Bank Angle Modulation Aerocapture Solution Data

Planet	Solution Method	$r_{a_{error}}$ (km)	ΔV_2 (m/s)	ΔV_1 (m/s)	# *odefun* calls
Venus	Optimal Control	8.613E-03	2.424E-03	110.155	94269
	NPC: Min ΔV	1.538E-02	4.329E-03	54.545	753
	NPC: Min $r_{a_{error}}$	9.177E-04	2.583E-04	112.815	194
Earth	Optimal Control	1.413E-02	3.911E-03	136.552	101387
	NPC: Min ΔV	2.250E-01	6.225E-02	128.615	466
	NPC: Min $r_{a_{error}}$	4.173E-02	1.155E-02	188.469	221
Mars	Optimal Control	3.550E-03	7.853E-04	113.176	98683
	NPC: Min ΔV	1.534E-02	3.393E-03	85.043	716
	NPC: Min $r_{a_{error}}$	5.969E-03	1.320E-03	116.838	375
Titan	Optimal Control	7.796E-04	6.607E-05	156.299	207600
	NPC: Min ΔV	3.399E-01	2.881E-02	149.559	1723
	NPC: Min $r_{a_{error}}$	3.301E-02	2.798E-03	186.805	932
Neptune	Optimal Control	3.486E-02	4.820E-05	89.055	120576
	NPC: Min ΔV	2.373E+00	3.281E-03	83.534	751
	NPC: Min $r_{a_{error}}$	8.299E+00	1.147E-02	88.040	440

Drag Modulation

Figure 3.6 provides a comparison between the optimized drag modulation control inputs at each planetary destination and Figure 3.7 provides a corresponding representation of each trajectory. The Min ΔV method generally produces a constant control command after the ballistic coefficient switch. The Min $r_{a_{error}}$ method also generally produces a constant control command, though pronounced control modifications are noted for Venus and Earth. The resulting NPC drag modulation trajectory solutions do not significantly differ from the optimal trajectories with regards to altitude vs velocity but differ with regards to flight path angle vs velocity. Like what was observed for BAM, the terminal flight path angle can be identified to have a significant influence on achieving ΔV-minimizing DM trajectories. Both the optimal control solution and Min ΔV method exhibit minutely lower terminal flight path angles than the Min $r_{a_{error}}$ method. This yields a lower periapsis raise ΔV for near zero apoapsis correction ΔV as shown in Table 3.2.

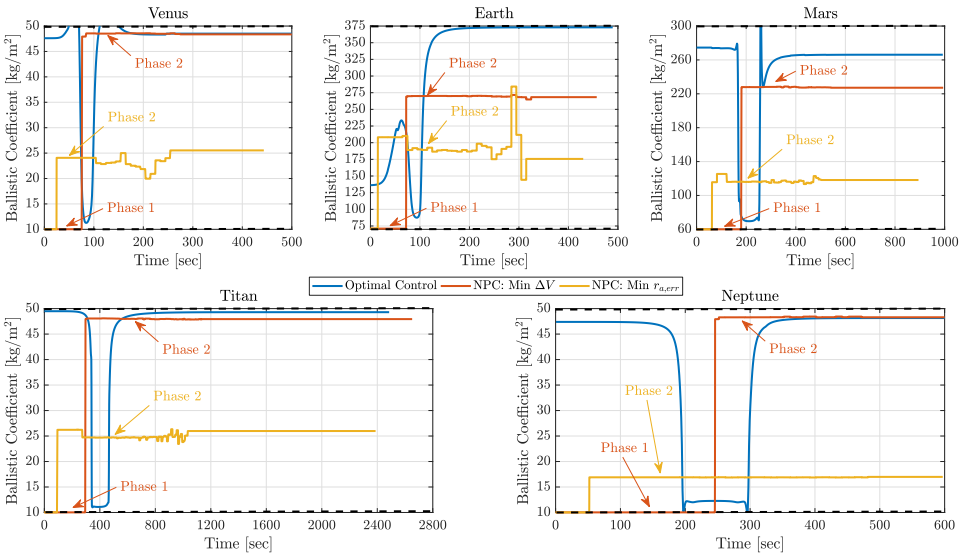

Figure 3.6. Comparison of drag modulation control inputs between optimal control and NPC solutions. Black dashed lines are imposed control constraints

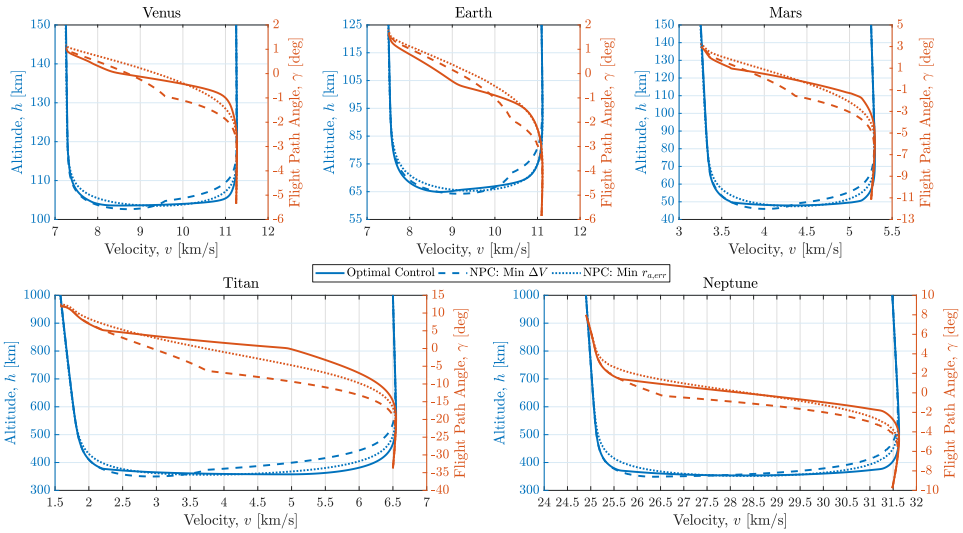

Figure 3.7. Comparison of drag modulation trajectories between optimal control and NPC solutions

For DM aerocapture data in Table 3.2, all three numerical guidance solutions are sufficient with regards to orbit insertion. Both the optimal control and Min ΔV methods achieve lower periapsis raise maneuvers than the Min $r_{a_{error}}$ method. At all the destinations simulated, the Min ΔV NPC solution produces a slightly higher periapsis raise cost than the optimal solution. This indicates that the utilized mesh in the optimal control solution is sufficient. With respect to Min ΔV method, the percent reduction in periapsis raise ΔV as compared to the Min $r_{a_{error}}$ method at Venus, Earth, Mars, Titan, and Neptune is 7%, 1%, 3%, 4%, and 0.05%, respectively. The percent reduction is smaller as compared to BAM but nonetheless demonstrates the performance enhancement achieved by incorporating the periapsis raise maneuver into the cost functional. Furthermore, the NPC methods allow for a significant reduction in the number of numerical integration as compared to the optimal control solution. The percent fraction of the number of Min ΔV method numerical integrations to the optimal control solution at Venus, Earth, Mars, Titan, and Neptune is 0.6%, 0.5%, 0.6%, 0.4%, and 0.8%, respectively. As compared to BAM, the number of numerical integrations is nearly half yet the percent fraction is nearly identical.

Table 3.2. Drag Modulation Aerocapture Solution Data

Planet	Solution Method	$r_{a_{error}}$ (km)	ΔV_2 (m/s)	ΔV_1 (m/s)	# *odefun* calls
Venus	Optimal Control	5.173E-02	1.456E-02	67.646	54861
	NPC: Min ΔV	5.790E-04	1.630E-04	70.075	328
	NPC: Min $r_{a_{error}}$	1.897E-01	5.341E-02	75.127	210
Earth	Optimal Control	9.497E-05	2.628E-05	134.034	69090
	NPC: Min ΔV	1.577E-03	4.365E-04	137.477	330
	NPC: Min $r_{a_{error}}$	9.873E-01	2.732E-01	138.987	292
Mars	Optimal Control	1.509E-02	3.338E-03	87.567	98966
	NPC: Min ΔV	2.839E-02	6.279E-03	89.911	561
	NPC: Min $r_{a_{error}}$	3.171E-01	7.014E-02	92.927	438
Titan	Optimal Control	5.290E-04	4.484E-05	157.956	308119
	NPC: Min ΔV	1.632E-01	1.383E-02	158.656	1205
	NPC: Min $r_{a_{error}}$	3.315E+00	2.808E-01	164.621	786
Neptune	Optimal Control	2.167E-02	2.997E-05	82.616	76570
	NPC: Min ΔV	5.036E+00	6.963E-03	82.705	621
	NPC: Min $r_{a_{error}}$	7.920E+00	1.095E-02	82.749	433

Direct Force Control

Figure 3.8 and Figure 3.9 provide a comparison between the optimized angle of attack and side-slip angle control inputs at each planetary destination and Figure 3.10 provides a corresponding representation of each trajectory. The Min ΔV method generally produces a constant control command after the angle of attack switch, though noticeable divergences can be seen for Mars and Neptune. The Min $r_{a_{error}}$ method also generally produces a constant control command, but with observable divergences for Venus and Neptune. The side-slip angle commands between the two NPC solutions are nearly identical as the same lateral logic is utilized. The resulting NPC direct force control trajectory solutions produce similar trends as BAM with regards to the altitude vs velocity and flight path angle vs velocity profiles. For Venus and Earth, the differences in the altitude vs velocity profiles are the most pronounced. But for the remaining planets, the profiles are similar. The altitude vs flight path angle profiles do exhibit visual variations at each planet. Like BAM and DM, the terminal flight path angle can be identified to have a significant influence on achieving ΔV-minimizing trajectories. Both the optimal control solution and Min ΔV method exhibit lower terminal flight path angles than the Min $r_{a_{error}}$ method. This yields a lower periapsis raise ΔV for near zero apoapsis correction ΔV as shown in Table 3.3.

For DFC aerocapture data in Table 3.3, all three numerical guidance solutions are sufficient with regards to orbit insertion. Both the optimal control and Min ΔV methods achieve

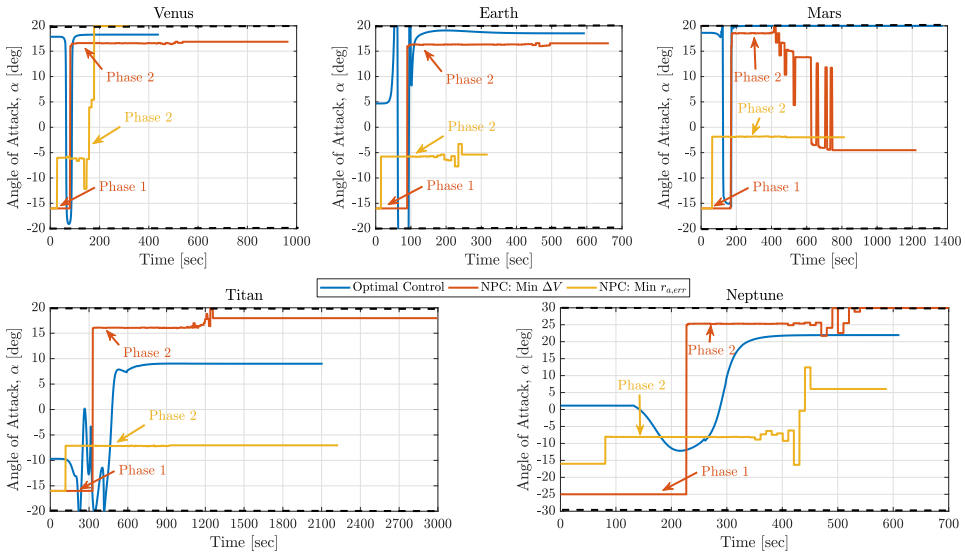

Figure 3.8. Comparison of angle of attack control inputs between optimal control and NPC solutions. Black dashed lines are imposed control constraints

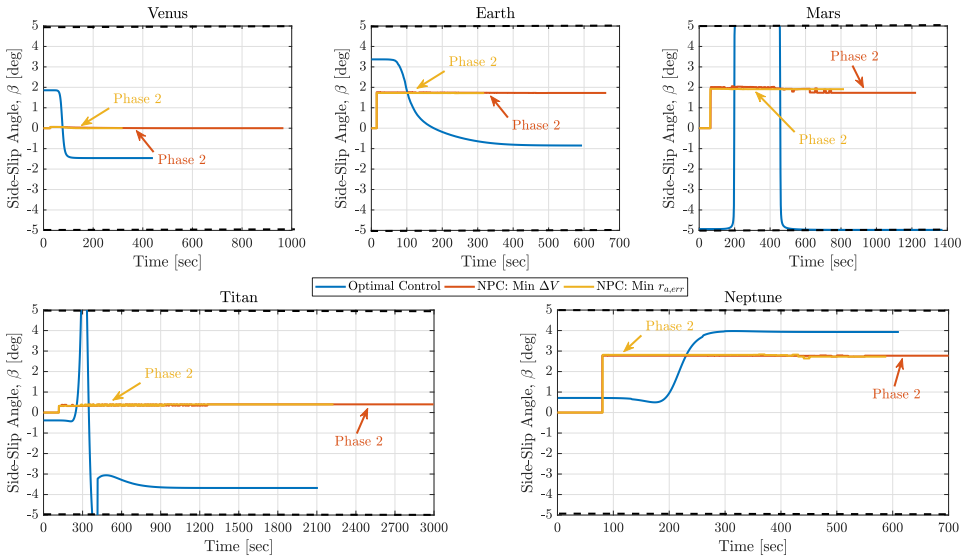

Figure 3.9. Comparison of side-slip angle control inputs between optimal control and NPC solutions. Black dashed lines are imposed control constraints

lower periapsis raise maneuvers than the Min $r_{a_{error}}$ method. At Venus, Titan, and Neptune, the Min ΔV NPC solution produces a lower periapsis raise cost than the optimal solution. This difference can be attributed to the lack of mesh refinement used in the collocation solution process for the optimal control solutions. It is expected with further mesh refinement

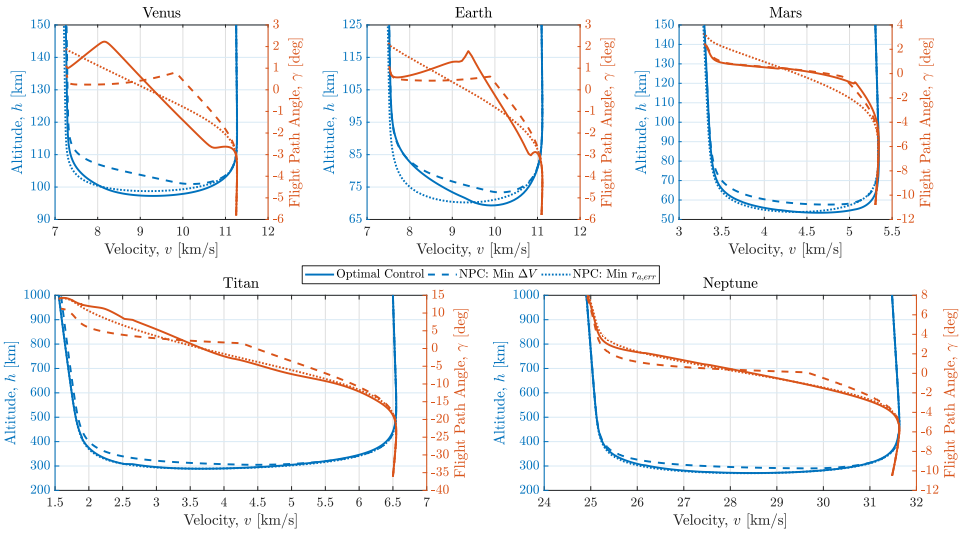

Figure 3.10. Comparison of direct force control trajectories between optimal control and NPC solutions

that the optimal control solutions will produce lower periapsis raise costs. With respect to Min ΔV method, the percent reduction in periapsis raise ΔV as compared to the Min $r_{a_{error}}$ method at Venus, Earth, Mars, Titan, and Neptune is 54%, 23%, 15%, 22%, and 3%, respectively. The percent reduction is smaller as compared to BAM but nonetheless demonstrates the performance enhancement achieved by incorporating the periapsis raise maneuver into the cost functional. Furthermore, the NPC methods allow for a significant reduction in the number of numerical integration as compared to the optimal control solution. The percent fraction of the number of Min ΔV method numerical integrations to the optimal control solution at Venus, Earth, Mars, Titan, and Neptune is 1.1%, 2.2%, 1.3%, 0.8%, and 1.5%, respectively. As compared to BAM, the number of numerical integrations and percent fraction is nearly double. This can be attributed to the additional NPC optimization cost due to an additional control parameter.

Table 3.3. Direct Force Control Aerocapture Solution Data

Planet	Solution Method	$r_{a_{error}}$ (km)	i_{error} (km)	ΔV_2 (m/s)	ΔV_3 (m/s)	ΔV_1 (m/s)	# *odefun* calls
Venus	Optimal Control	2.722E-03	1.437E-07	7.661E-04	1.794E-05	71.367	90074
	NPC: Min ΔV	2.819E-02	1.581E-07	7.935E-03	1.973E-05	54.245	1028
	NPC: Min $r_{a_{error}}$	1.352E-01	5.786E-08	3.807E-02	7.221E-06	117.671	298
Earth	Optimal Control	7.639E-02	7.337E-03	2.114E-02	9.748E-01	118.966	47021
	NPC: Min ΔV	1.772E-02	7.569E-07	4.904E-03	1.006E-04	119.045	1009
	NPC: Min $r_{a_{error}}$	7.713E-02	1.026E-06	2.134E-02	1.364E-04	154.827	422
Mars	Optimal Control	3.540E-03	4.698E-04	7.831E-04	2.754E-02	78.809	109804
	NPC: Min ΔV	2.711E-02	1.345E-06	5.996E-03	7.887E-05	79.997	1454
	NPC: Min $r_{a_{error}}$	6.975E-03	1.777E-07	1.543E-03	1.042E-05	94.302	741
Titan	Optimal Control	1.328E+00	4.780E-01	1.125E-01	1.209E+01	191.347	321004
	NPC: Min ΔV	1.706E+00	1.901E-04	1.447E-01	4.808E-03	148.766	2412
	NPC: Min $r_{a_{error}}$	4.143E-02	1.516E-04	3.512E-03	3.835E-03	189.673	1412
Neptune	Optimal Control	1.561E+01	9.479E-04	2.158E-02	6.415E-02	84.092	76130
	NPC: Min ΔV	2.832E+00	1.569E-07	3.916E-03	1.062E-05	82.942	1179
	NPC: Min $r_{a_{error}}$	5.144E+00	6.653E-07	7.113E-03	4.502E-05	85.279	769

Discussion on computational cost

The results presented in the preceding sections demonstrate the computational cost difference in obtaining ΔV-minimizing trajectories for each flight control analyzed. The NPC doesn't explicitly solve the optimal aerocapture problem but produces trajectories close to the theoretical optimal solution using the a-priori knowledge of the optimal control structure. Computing these trajectories using univariate parameter optimization, rather than collocation methods, allows for a significant reduction in the number of numerical integrations. The small reduction in ΔV cost associated with computing the optimal control solution does not warrant the order-of-magnitude increase in on-board computational cost. Due to the potentially fast guidance call rates, it is imperative that the on-board guidance algorithm obtain solutions efficiently and quickly. The computational cost associated with the NPC solutions are well within the current capability of on-board flight computers.

3.2 Closed-loop architecture

The NPC algorithm utilizes a simplified 3DOF trajectory model when computing the necessary control inputs. These may include a nominal GRAM atmospheric model, linear aerodynamics model, and decoupled longitudinal/lateral flight dynamics. The accuracy of these simplifications is rigorously tested using a truth model, which serves as the true trajectory model. The truth model may include the coupled longitudinal/lateral flight dynamics, full non-linear aerodynamic model, and dispersed GRAM atmospheric model. The latter term is an example of trajectory dispersions that can be present during flight. Other dispersions that are applied to the truth model include atmospheric winds, aerodynamic uncertainty, and vehicle attitude uncertainty. A flight actuator is implemented to simulate the time response of controls commanded by the NPC based off a maximum rate and acceleration limit. A feedback filter is utilized to provide closed-loop feedback to the NPC model. Figure 3.11 provides a high-level representation of the closed-loop NPC aerocapture guidance architecture. Overall, the architecture allows for a variety of different aeroshell configurations, vehicle flight controls, and planetary destinations to be readily simulated in a single environment.

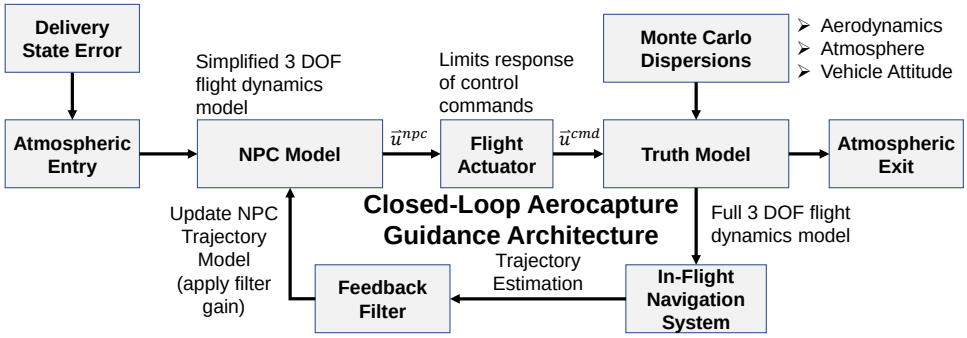

Figure 3.11. Closed-loop NPC aerocapture guidance architecture

3.2.1 Control command limiter

Flight control actuators, such as RCS thrusters and aerosurfaces, are utilized to achieve the desired NPC control commands. For BAM and DFC, the control variables are identical to the Eulerian angle respresenting the wind-frame attitude of the vehicle; thus, the actuators must act on the rotational dynamics of the vehicle. For a 3DOF simulation, the rotational response of the vehicle can be emulated using a control command limiter. It limits the time response of the control commands based off a maximum rate, $\dot{u}_{max}$, and acceleration, $\ddot{u}_{max}$. Using a second-order Taylor Series approximation of the control time response, the time history of the flight actuator can be modeled using Eq. (3.1) [107].

$$u(t) \approx u_0 + \dot{u}_{max}\Delta t + \frac{1}{2}\ddot{u}_{max}\Delta t^2 \tag{3.1}$$

This pseudo-actuator methodology has been widely utilized in aerocapture and EDL applications [32], [33], [108]–[110]. Figure 3.12 depicts the finite time response of control commands as passed from the NPC solution to the truth model for a single 10 second guidance cycle. Sample values for the rates and accelerations come from literature. For each flight control, the commands are able to be achieved within the simulated 10 second interval. If the guidance call rate were to be increased beyond 0.5 Hz (5 second interval), then the pseudo-actuator would not be able to reach the targeted command before the next guidance cycle. This could be reconciled by improving the actuator response via increase in its maximum rate and acceleration. Nevertheless, the example presented in Figure 3.12 illustrates the dependence of guidance rate to actuator selection.

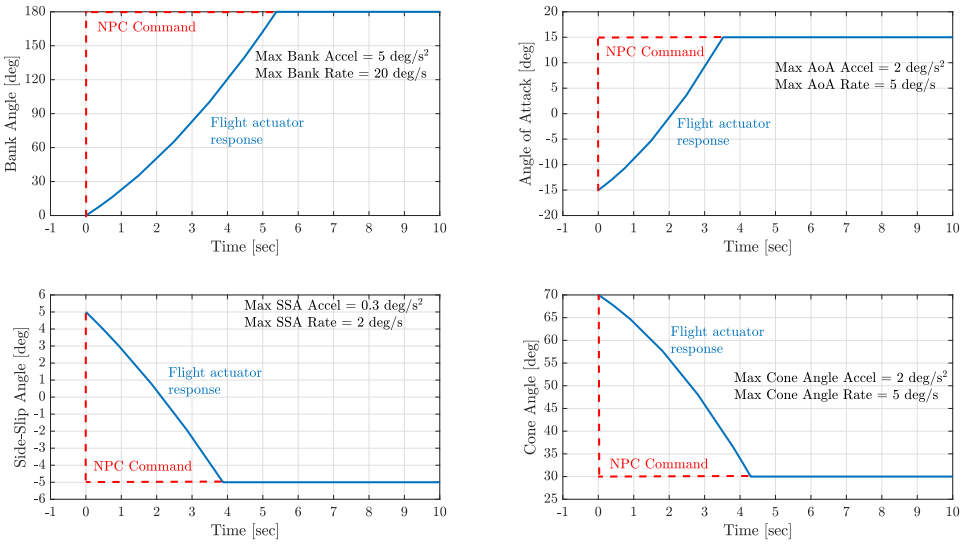

Figure 3.12. Example 3DOF flight actuator response to bank angle, angle of attack, side-slip angle, and cone angle NPC commands

3.2.2 Uncertainty estimator

The NPC guidance architecture is designed closed-loop in the sense that the NPC trajectory models are corrected in real-time based off sensed trajectory data from the in-flight navigation system. The navigation system may include integrated IMU and FADS instrumentation. Due to the reliance on instrumentation model specifications, perfect navigation knowledge is assumed by the in-flight navigation system. The knowledge is used to provide an estimate for the sensed aerodynamics accelerations during flight, which are subsequently compared against similar calculations using the current NPC trajectory model. A first-order fading memory filter is utilized to compute the update gain that is applied to the NPC trajectory model. Unlike the current state-of-the-art aerocapture guidance routines, a single user-defined gain is required that does not require gain tuning to achieve the desired closed-loop performance. The memory filter has been shown in literature to provide sufficient closed-loop performance for EDL and aerocapture guidance applications [69], [111], [112].

The principles of fading-memory filters can be traced to Kalman filters, which itself has been widely utilized in aerospace applications. The fading-memory filter has a recursive

structure that incorporates old estimates with current estimates of a parameter of interest. A first-order filter can be mathematically modeled using Eq. (3.2) where k is the current index in the sequence, G is a *constant* gain, $\hat{x}$ is the estimated parameter of interest, and x_{err} is the ratio of the current measurement to the old estimate [113].

$$\hat{x}_k = \hat{x}_{k-1} + (1 - G)(x_{err} - \hat{x}_{k-1}) \tag{3.2}$$

The mathematical structure of the fist-order memory filter is similar to a linear polynomial Kalman filter with the only difference being in the computation of G. The Kalman filter solves the Ricatti equations to obtain G and as a result the gain can be time-varying and can increase the computational cost of the filter. The selection of the constant value for G between 0 and 1 is generally arbitrary but is related to the bandwidth of the filter. Increasing the gain towards 1 reduces the bandwidth thereby increasing the importance of previous measurements. Although higher-order memory filters share similar constant gain properties as the first-order filter, they are generally less effective at attenuating measurement noise than a first-order filter. Due to the potential stochastic trajectory dispersions, a first-order filter is assumed. Figure 3.13 provides a high-level overview of the feedback filter structure.

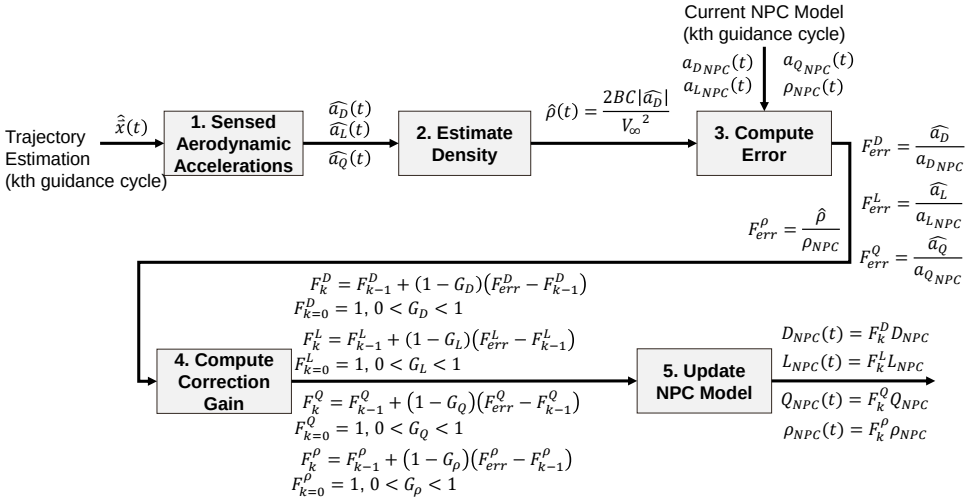

Figure 3.13. Feedback filter gain computation overview

The filter is utilized to compute the correction gains associated with the NPC model of lift-force, drag-force, and side-force. This is done by computing the errors of the respective force-accelerations between the current NPC model and current trajectory estimates. The calculation of the update gains are conducted every kth guidance cycle. An update gain for atmospheric density can be computed using a similar approach but only with drag acceleration. Ultimately, acceleration-based gains rather than density-based gains are utilized since aerodynamic acceleration measurements can capture uncertainty associated with aerodynamic coefficients, mass, and vehicle attitude, in addition to density dispersions.

A numerical example of the feedback filter as applied to DFC is shown in Figure 3.14. The example shows the NPC update gain calculations for two sets of perturbed Neptune aerocapture trajectories, denoted High and Low. The limited knowledge of Neptune atmospheric profile provides a good example to test the effectiveness of the feedback filter. The High trajectory corresponds to a higher-than-average 6σ perturbed atmospheric profile while the Low trajectory corresponds to a lower-than-average 6σ perturbed atmospheric profile. Figure 2.15 provides a visualization of sample atmospheric profiles with 6σ density dispersions applied where High trajectory correlates to Yelle maximum profile and Low trajectory correlates to Yelle min profile. For both trajectories, the NPC utilizes a nominal Neptune atmospheric profile, denoted by Average profile in Figure 2.15, with trajectory updates occurring at 0.1 Hz. Gain of 0.9 are used for each aerodynamic force as well as atmospheric density. Note that the latter gain is only used for illustrative purposes.

The top left subplot in Figure 3.14 shows the effectiveness of the memory filter in properly scaling the NPC atmospheric profile in the presence of high frequency density perturbations to nearly match the High and Low atmospheric profiles. The remaining three subplots show the evolution of the NPC gain updates each guidance cycle. For the High profile, each gain is generally greater than unity indicating an amplification of the NPC model's aerodynamic forces due to computing density values that are lower than the flight environment. Converse trend can be seen with the Low profile. The net effect of the update gains allows for each respective simulated trajectory to achieve Neptune aerocapture with apoapsis errors less than 10 km and inclination errors less than 0.1°.

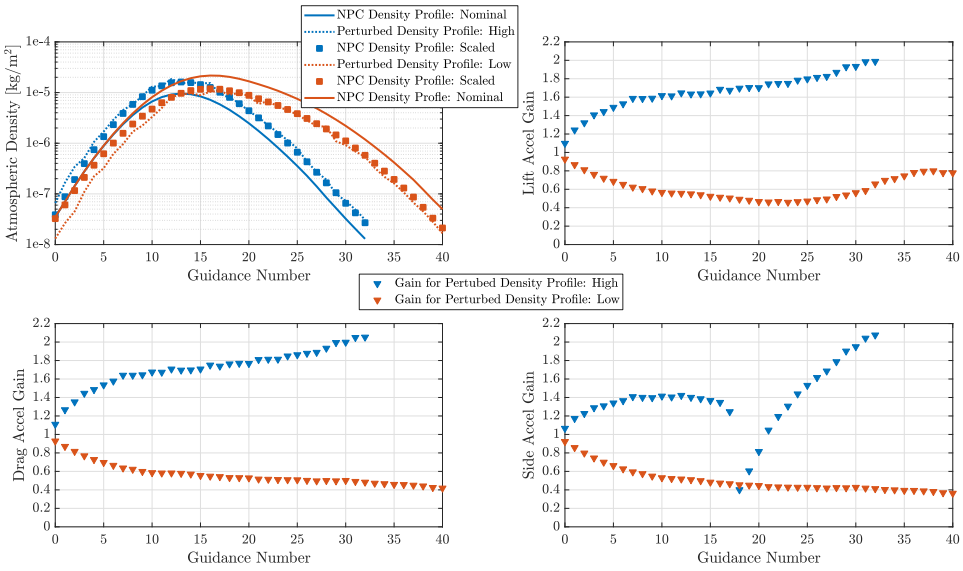

Figure 3.14. Example feedback filter gain calculations applied to two sets of perturbed density profiles at Neptune

3.2.3 Monte Carlo Integration

Monte Carlo simulations are employed to assess the robustness of each vehicle design at different planetary destinations. This is accomplish by integrating Monte Carlo methods into NPC aerocapture guidance architecture. Probabilistic parameters are inputted into the architecture during each simulation of a guided aerocapture trajectory. Thousands of trajectories are simulated to provide a sufficient statistical representation of the output parameters of interest. For 3DOF aerocapture, the probabilistic inputs include parameters associated with delivery state error at atmospheric entry, vehicle aerodynamic coefficient uncertainty, atmospheric profile uncertainty and density dispersions, as well as vehicle attitude dispersions. Each input has an associated probabilistic distribution function that is sampled during the simulations. The output parameters are associated with the orbit insertion performance of each aerocapture trajectory. Further details on the Monte Carlo setup utilized in the computational studies can be found in Chapter 4.

4. SYSTEM ANALYSIS OF AEROCAPTURE MISSION SETS

In this chapter, the NPC aerocapture guidance architecture is applied to numerically simulate aerocapture trajectories for two sets of vehicles at different planetary destinations. Monte Carlo simulations are conducted to assess the robustness and orbit insertion performance of each flight control option.

4.1 Lifting and Ballistic Aerocapture Trajectories

4.1.1 Theoretical Entry Flight Path Angle Corridor Width

An important metric for assessing aerocapture capability is the theoretical entry flight path angle corridor width. The width should be larger than the anticipated delivery state errors in inertial flight path angle ($\pm 3\sigma$). It is a direct function of the control capability of the vehicle. The control can be parametrized by the vehicle L/D for lifting trajectories and by the vehicle BCR for ballistic trajectories. Given a base BC, lifting vehicles see no change in BC while ballistic vehicles increase the BC up to a maximum value equal to BCR times the base BC (min BC assumed to be equal to base BC). Solving for the entry flight path angle that achieves the targeted orbit apoapsis using lift vector up/max BC, known as steep side, and lift vector down/min BC, known as shallow side, configurations allows for the corridor width to be computed. To normalize the comparison between lifting and ballistic trajectories, the same base BC is assumed. The corridor width trends are presented for each planetary destination using a wide range of entry velocities, base BC, vehicle L/D and BCR values. The peak stagnation point convective heat flux for a 1m nose radius amongst the steep and shallow trajectories is presented.

Venus

The corridor width assessment for Venus targets a 300 km circular orbit. Figure 4.1 depicts a comparison between the theoretical corridor width as function inertial entry velocity for different lifting and ballistic vehicles. The range of velocities analyzed as typical for Venus aerocapture mission sets. Note that Venus escape velocity is 10.36 km/s. Figure 4.1a illustrates that the corridor width for ballistic vehicles strongly increases with increasing BCR and slowly increases with increasing entry velocities. This indicates that the corridor can be most influenced by changes in ballistic control capability rather than changes in the arrival conditions. Figure 4.1b shows that the width strongly increases with both increasing L/D and entry velocity. The width produced by lifting vehicles are generally an order-of-magnitude bigger than the widths produced by ballistic vehicles. As an example, a ballistic vehicle with BCR=20 and entry velocity = 14 km/s is needed to match the width produced by a lifting vehicle with L/D=0.1 and entry velocity = 11.5 km/s. This indicates that for the targeted orbit, lifting vehicles are more favorable control-wise than ballistic vehicles.

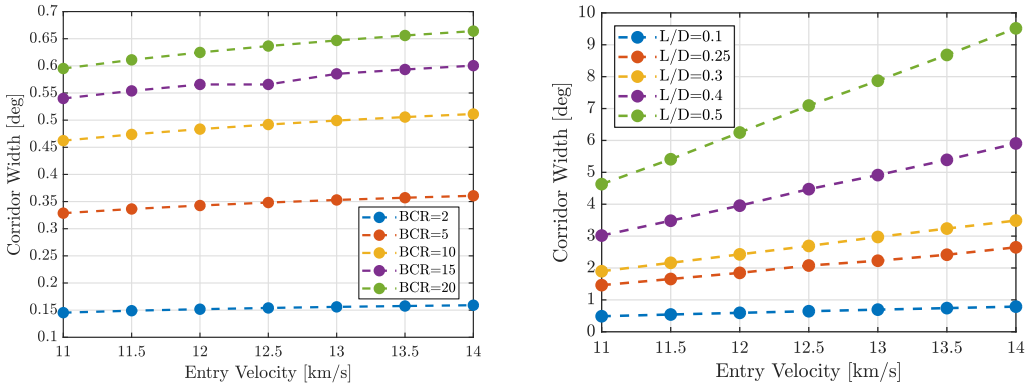

(a) Ballistic Vehicles (b) Lifting Vehicles

Figure 4.1. Venus corridor width as function of entry velocity and vehicle control for base BC=50 kg/m^2 and target apoapsis altitude of 300 km

The effect of base BC on the corridor trends for each set of trajectories is shown in Figure 4.2. An entry velocity of 11.5 km/s is assumed. For both Figure 4.2a and Figure 4.2b, modifying the base BC has little effect on the resulting width. Rather, the figures show the widths to be strong functions of the vehicle control parameters, being BCR and L/D

respectively. This suggests that the width is generally invariant to the vehicle mass since the base BC scales lineally with it. So, the expected corridor width between a SmallSat-class and Satellite-class payload at Venus, given same entry velocity, L/D or BCR, should generally be the same.

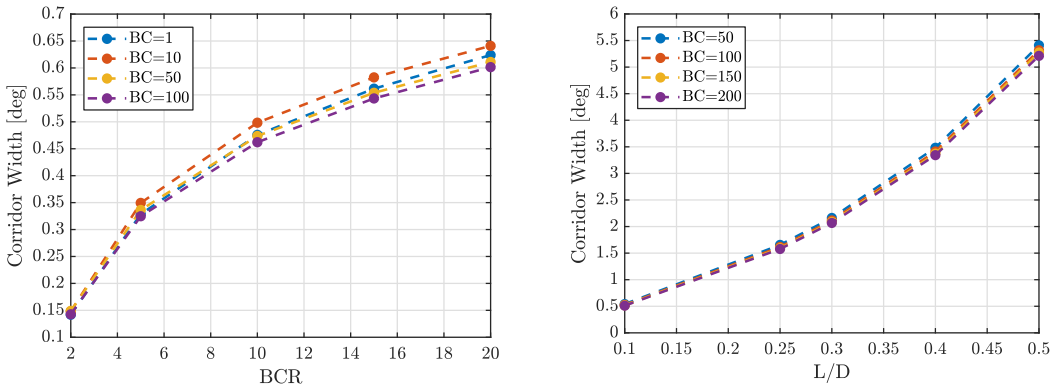

(a) Ballistic Vehicles

(b) Lifting Vehicles

Figure 4.2. Venus corridor width as function of vehicle control and base BC for 11.5 km/s entry velocity and target apoapsis altitude of 300 km

Modifying the base BC has the effect of shifting the middle entry flight path angle of the corridor and peak convective heat rate as shown in Figure 4.3. Increasing BC leads to steeper flight path angles as shown in Figure 4.3a and Figure 4.3b. For ballistic vehicles, increasing the BCR shifts the middle EFPA to be more steeper. Similar trend can be seen for lifting vehicles with L/D. Steeper EFPA yield higher convective heat rates. Figure 4.3c shows that increasing the vehicle BC, via increasing BCR or base BC, increases the heat rate. The rate of increase is amplified with higher base BC. Figure 4.3d shows that increasing L/D increases the peak heat rate. For Venus, the relatively large heat rate values may suggest that higher performance TPS material is needed. For low base BC and low BCR ballistic vehicles, the heat rates might be within the current TPS capabilities. But due to small corridor width produced by small BCR vehicles, larger BCR values might be sought for leading to an increase in the heat rate. For lifting vehicles, lowering the heat rate can be achieved with a high area aeroshell and low-L/D vehicle.

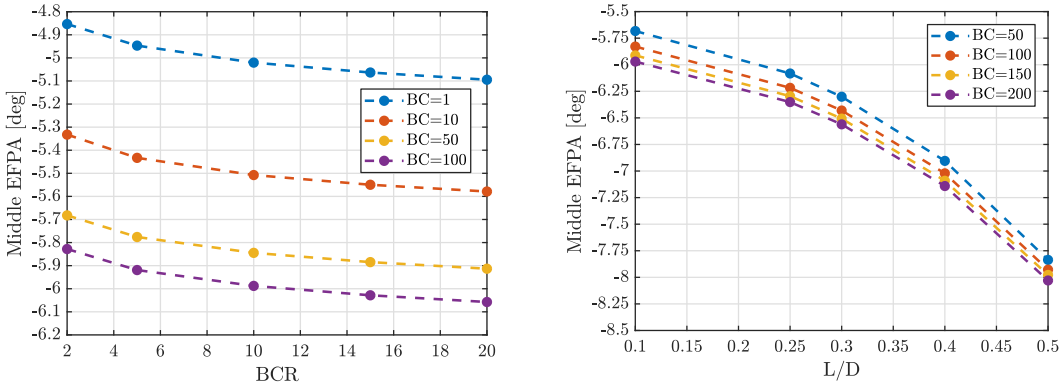

(a) Ballistic Vehicles

(b) Lifting Vehicles

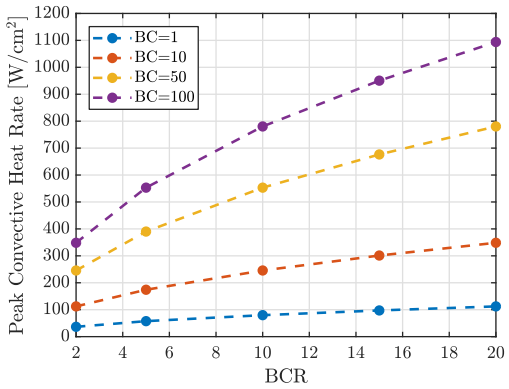

(c) Ballistic Vehicles

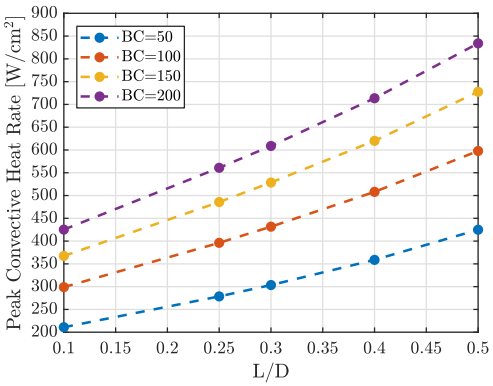

(d) Lifting Vehicles

Figure 4.3. Venus middle entry flight path angle and peak convective heat rate as function of vehicle control and base BC for 11.5 km/s entry velocity and target apoapsis altitude of 300 km

Earth

The corridor width assessment for Earth targets a 500 km circular orbit. Figure 4.4 depicts a comparison between the theoretical corridor width as function inertial entry velocity for different lifting and ballistic vehicles. The range of velocities analyzed as typical for Earth-return aerocapture mission sets. Note that Earth escape velocity is 11.12 km/s. Figure 4.4a illustrates that the corridor width for ballistic vehicles strongly increases with increasing BCR and slowly increases with increasing entry velocities, similar to Venus. Unlike Venus, the ballistic corridor widths at Earth for the same entry velocity and BCR value are generally twice as big. Figure 4.4b shows that the width strongly increases with both increasing L/D and entry velocity. This width is significantly larger than its ballistic vehicle counterpart. For

low-L/D vehicles, the widths produced at Earth and Venus are nearly the same. For higher L/D vehicles, the widths at Venus are much higher than at Earth. Given similar gravitational accelerations, the higher densities experienced at Venus can be potentially attributed to this difference in widths.

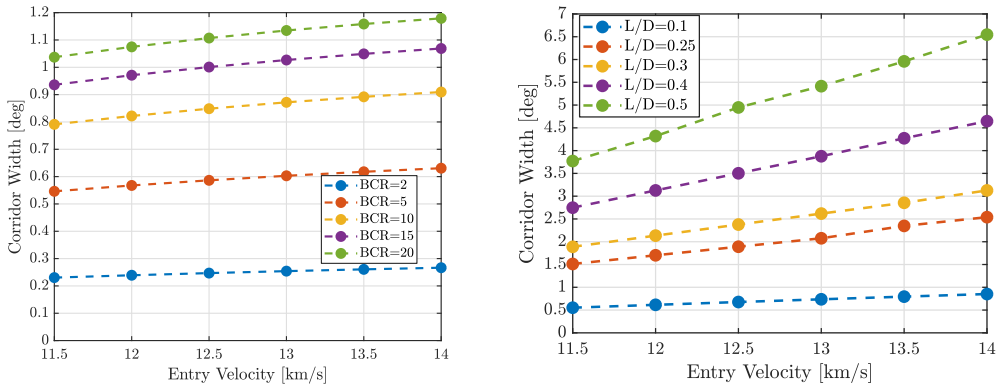

(a) Ballistic Vehicles (b) Lifting Vehicles

Figure 4.4. Earth corridor width as function of entry velocity and vehicle control for base BC=50 kg/m^2 and target apoapsis altitude of 500 km

The effect of base BC on the corridor trends for each set of trajectories is shown in Figure 4.5. An entry velocity of 11.5 km/s is assumed. For both Figure 4.5a and Figure 4.5b, modifying the base BC has little effect on the resulting width, similar to Venus.

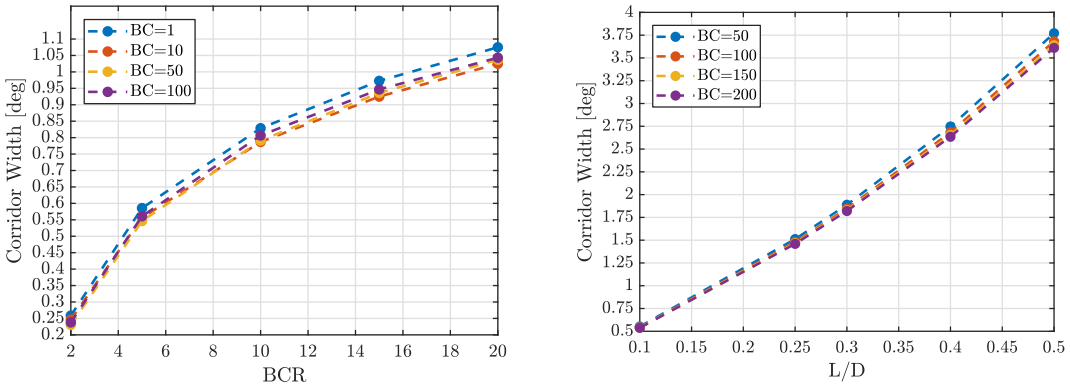

(a) Ballistic Vehicles (b) Lifting Vehicles

Figure 4.5. Earth corridor width as function of vehicle control and base BC for 11.5 km/s entry velocity and target apoapsis altitude of 500 km

The effect modifying base BC has on the middle entry flight path angle of the corridor and peak convective heat rate is shown in Figure 4.6. Increasing BC leads to steeper flight path angles as shown in Figure 4.6a and Figure 4.6b. Figure 4.6c shows that increasing the vehicle BC, via increasing BCR or base BC, increases the heat rate. Figure 4.6d shows that increasing L/D increases the peak heat rate. For Earth and the same entry velocity, the heat rates are comparable but slightly lower than those found for Venus.

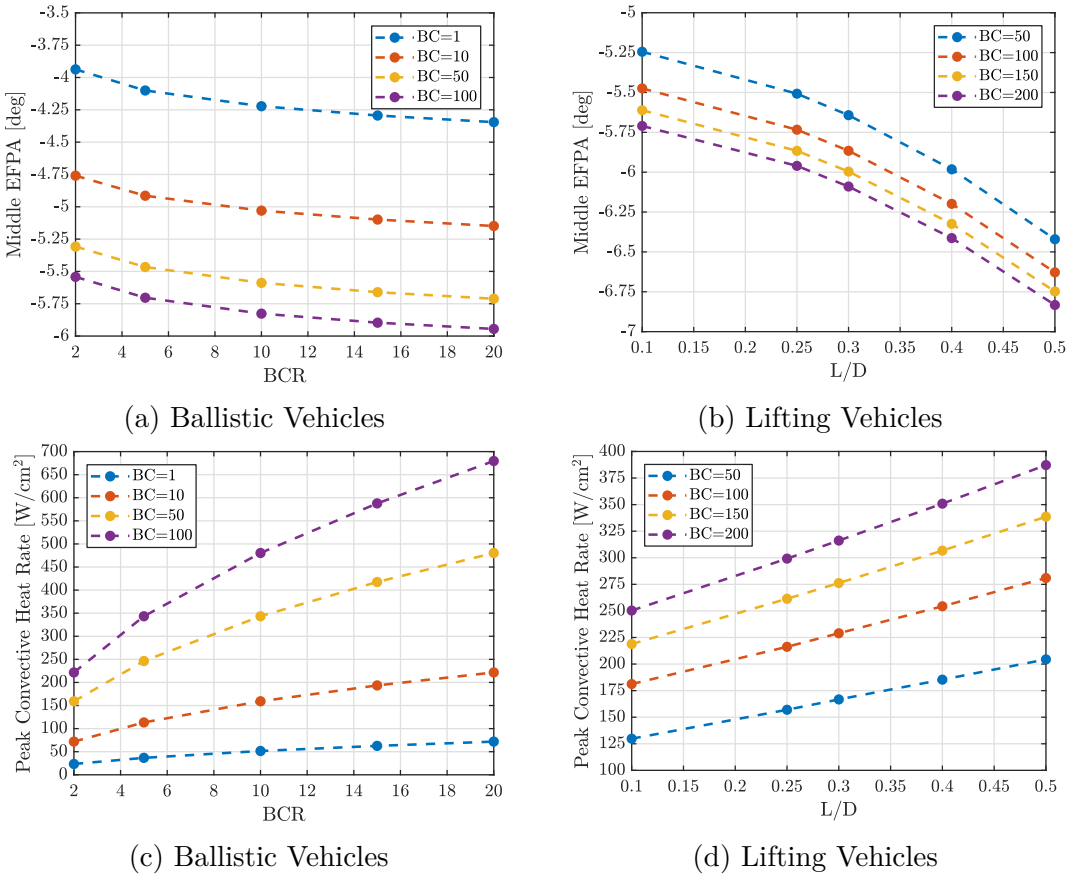

(a) Ballistic Vehicles

(b) Lifting Vehicles

(c) Ballistic Vehicles

(d) Lifting Vehicles

Figure 4.6. Earth middle entry flight path angle and peak convective heat rate as function of vehicle control and base BC for 11.5 km/s entry velocity and target apoapsis altitude of 300 km

Mars

The corridor width assessment for Mars targets a 400 km circular orbit. Figure 4.7 depicts a comparison between the theoretical corridor width as function inertial entry velocity for different lifting and ballistic vehicles. The range of velocities analyzed as typical for Mars aerocapture mission sets. Note that Mars escape velocity is 5.03 km/s. Figure 4.7a illustrates that the corridor width for ballistic vehicles strongly increases with increasing BCR and slowly increases with increasing entry velocities. Figure 4.7b shows that the width strongly increases with both increasing L/D and entry velocity. This width is generally larger than its ballistic vehicle counterpart. At lower entry velocities, a low-L/D vehicle has a similar width as a mid to high BCR vehicle (e.g. L/D=0.25 similar to BCR = 15 at 5.5 km/s). But for higher entry velocities, the lifting vehicles produce much larger widths. Despite the different entry velocities analyzed, the raw corridor width values and trends between Earth and Mars lifting and ballistic vehicles are quite similar.

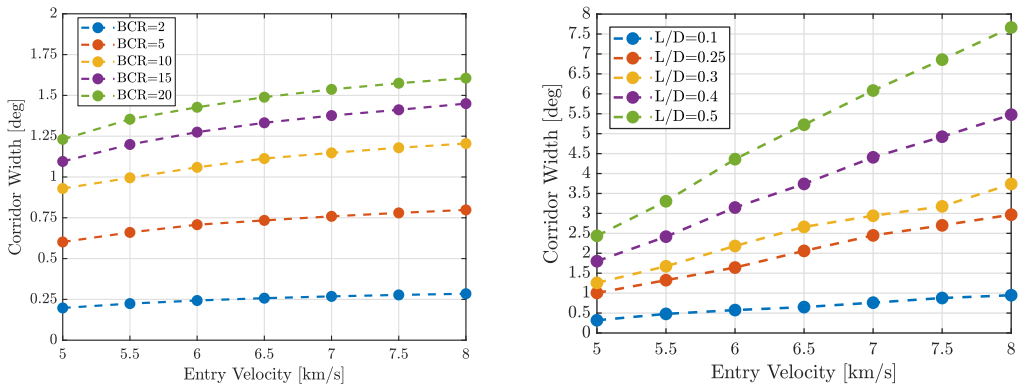

(a) Ballistic Vehicles (b) Lifting Vehicles

Figure 4.7. Mars corridor width as function of entry velocity and vehicle control for base BC=50 kg/m^2 and target apoapsis altitude of 400 km

The effect of base BC on the corridor trends for each set of trajectories is shown in Figure 4.8. An entry velocity of 5.5 km/s is assumed. In Figure 4.8a, increasing the base BC slightly increases the width for ballistic vehicles. However, Figure 4.8b shows that modifying the base BC on lifting vehicles has little effect on the resulting width.

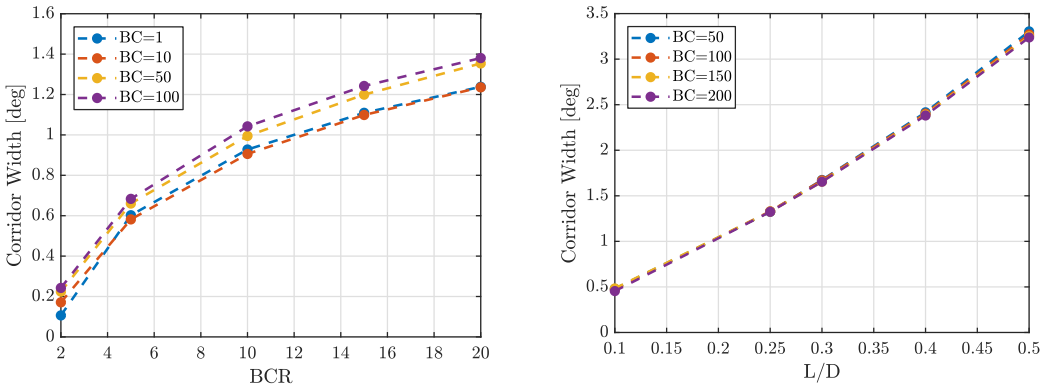

(a) Ballistic Vehicles

(b) Lifting Vehicles

Figure 4.8. Mars corridor width as function of vehicle control and base BC for 5.5 km/s entry velocity and target apoapsis altitude of 400 km

The effect modifying base BC has on the middle entry flight path angle of the corridor and peak convective heat rate is shown in Figure 4.9. Increasing BC leads to steeper flight path angles as shown in Figure 4.9a and Figure 4.9b. Figure 4.9c shows that increasing the vehicle BC, via increasing BCR or base BC, increases the heat rate. Figure 4.9d shows that increasing L/D increases the peak heat rate. For Mars, the heat rates are well within the current TPS technology capabilities.

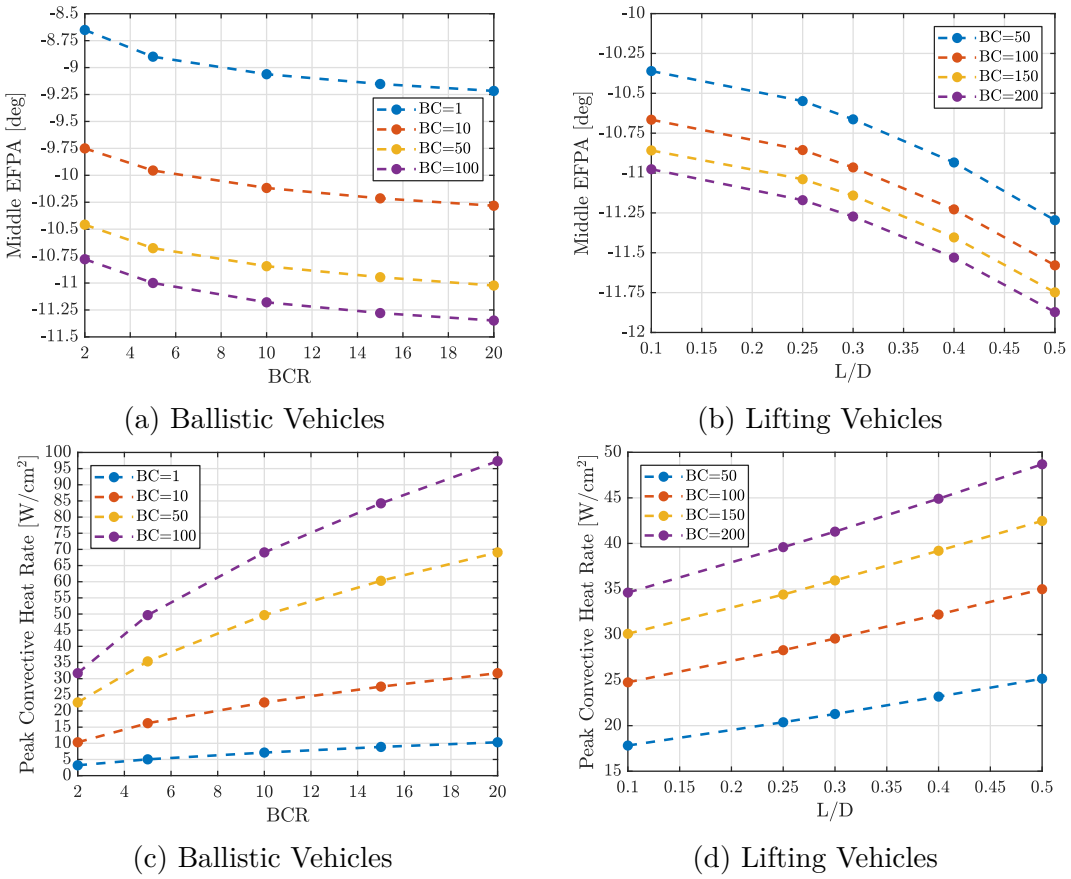

(a) Ballistic Vehicles

(b) Lifting Vehicles

(c) Ballistic Vehicles

(d) Lifting Vehicles

Figure 4.9. Mars middle entry flight path angle and peak convective heat rate as function of vehicle control and base BC for 5.5 km/s entry velocity and target apoapsis altitude of 400 km

Titan

The corridor width assessment for Titan targets a 1700 km circular orbit. Figure 4.10 depicts a comparison between the theoretical corridor width as function inertial entry velocity for different lifting and ballistic vehicles. The range of velocities analyzed as typical for Titan aerocapture mission sets. Note that Titan escape velocity is 2.65 km/s. Figure 4.10a illustrates that the corridor width for ballistic vehicles strongly increases with increasing BCR and generally doesn't change with increasing entry velocities. Figure 4.10b shows that the width strongly increases with both increasing L/D and entry velocity. This width is generally larger than its ballistic vehicle counterpart. At lower entry velocities, a low-L/D vehicle has a similar width as a mid to high BCR vehicle (e.g. L/D=0.25 similar to BCR

= 5 at 3 km/s). But for higher entry velocities, the lifting vehicles produce much larger widths. As compared to other planets, the ballistic vehicles at Titan produce much larger raw values for the width. For a similar entry velocity of 6 km/s, the width produced at Titan is nearly three times as big as on produced at Mars. Likewise for the same entry velocity, the lifting width produced at Titan is nearly double that produced at Mars. In fact, the raw width values produced by lifting vehicles on Titan is nearly comparable to Venus. Combining these two observations suggests that Titan relatively small gravity well and dense atmosphere makes both ballistic and lifting aerocapture vehicles favorable with large levels of control-capability.

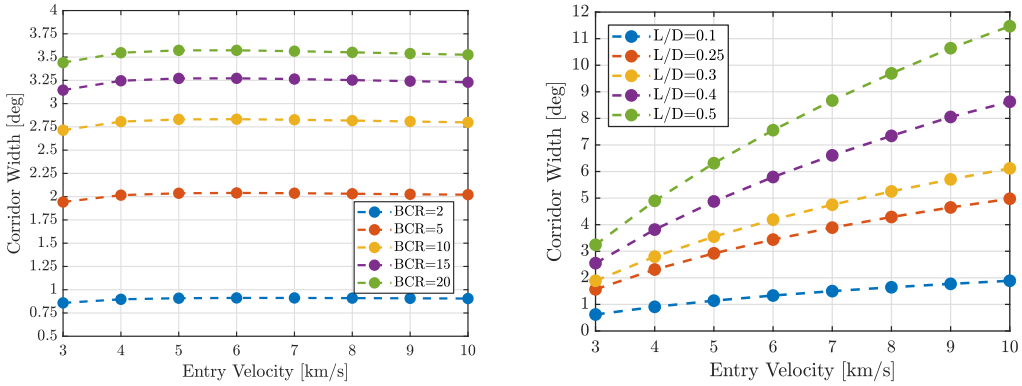

(a) Ballistic Vehicles

(b) Lifting Vehicles

Figure 4.10. Titan corridor width as function of entry velocity and vehicle control for base BC=50 kg/m^2 and target apoapsis altitude of 1700 km

The effect of base BC on the corridor trends for each set of trajectories is shown in Figure 4.11. An entry velocity of 6 km/s is assumed. In Figure 4.11a and Figure 4.11b, decreasing the base BC generously increases the width for ballistic and lifting vehicles respectively.

The effect modifying base BC has on the middle entry flight path angle of the corridor and peak convective heat rate is shown in Figure 4.12. Increasing BC leads to steeper flight path angles as shown in Figure 4.12a and Figure 4.12b. Figure 4.12c shows that increasing the vehicle BC, via increasing BCR or base BC, increases the heat rate. Figure 4.12d shows that increasing L/D increases the peak heat rate. For Titan, the heat rates are well within the current TPS technology capabilities.

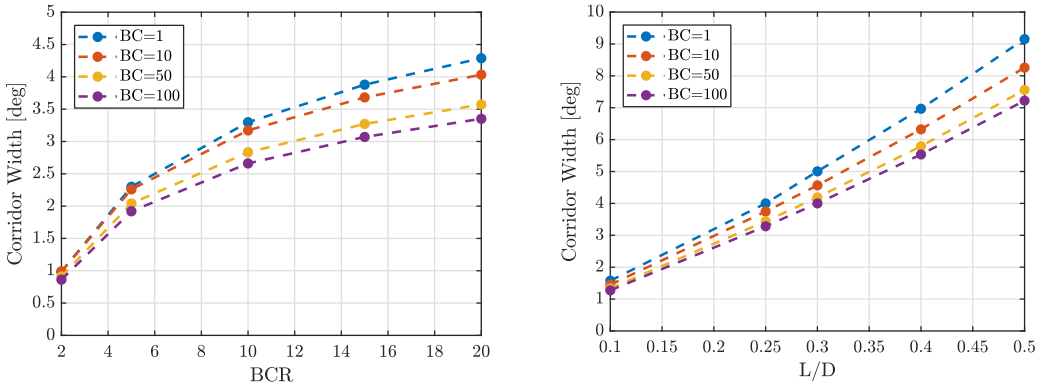

(a) Ballistic Vehicles (b) Lifting Vehicles

Figure 4.11. Titan corridor width as function of vehicle control and base BC for 6 km/s entry velocity and target apoapsis altitude of 1700 km

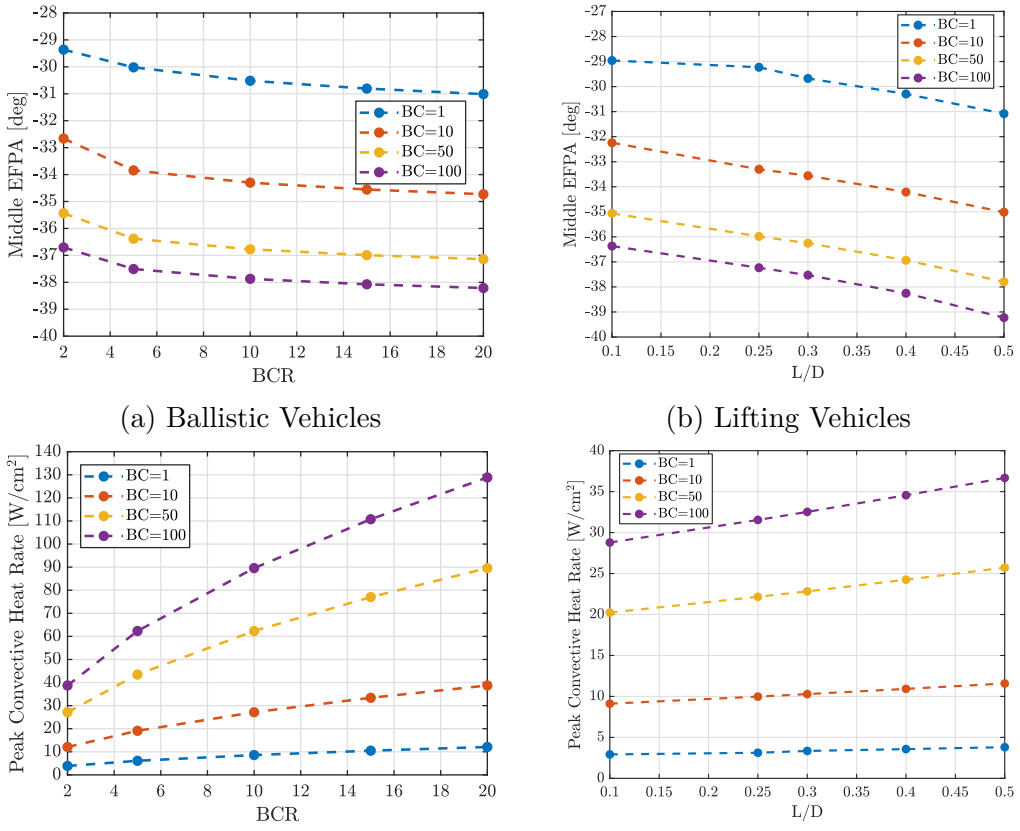

(a) Ballistic Vehicles (b) Lifting Vehicles

(c) Ballistic Vehicles (d) Lifting Vehicles

Figure 4.12. Titan middle entry flight path angle and peak convective heat rate as function of vehicle control and base BC for 6 km/s entry velocity and target apoapsis altitude of 1700 km

Neptune

The corridor width assessment for Neptune targets a 430000 km apoapsis elliptical orbit. Figure 4.13 depicts a comparison between the theoretical corridor width as function of inertial entry velocity for different lifting and ballistic vehicles. Figure 4.13a illustrates that the corridor width for ballistic vehicles strongly increases with increasing BCR but does not generally increase with increasing entry velocities. Figure 4.13b shows that the width strongly increases with both increasing L/D and entry velocity. Comparing the width suggests that lifting trajectories are much wider, even for smaller L/D vehicles. A ballistic vehicle with a large BCR is needed to match a similar width as a lifting vehicle with a low L/D. The trends suggest that for the same BCR, ballistic vehicles may provide for flexibility in the arrival conditions given the unchanging corridor width. On the contrary, the performance of lifting vehicles can be influenced by the arrival conditions. For the same vehicle L/D, higher entry velocities may provide for larger corridor width and shorter interplanetary transit times to Neptune but at the potential expense of higher aeroheating environments since more orbital ΔV needs to be dissipated. Comparing the widths to other planets suggests Neptune's large gravity well can affect lifting vehicle control-capability. The width values at Neptune, even for larger values of L/D and entry velocities, are generally smaller than any other planet. This is in contrast to the comparison for ballistic vehicles as the width produced at Neptune are similar in value to those at Earth and Venus.

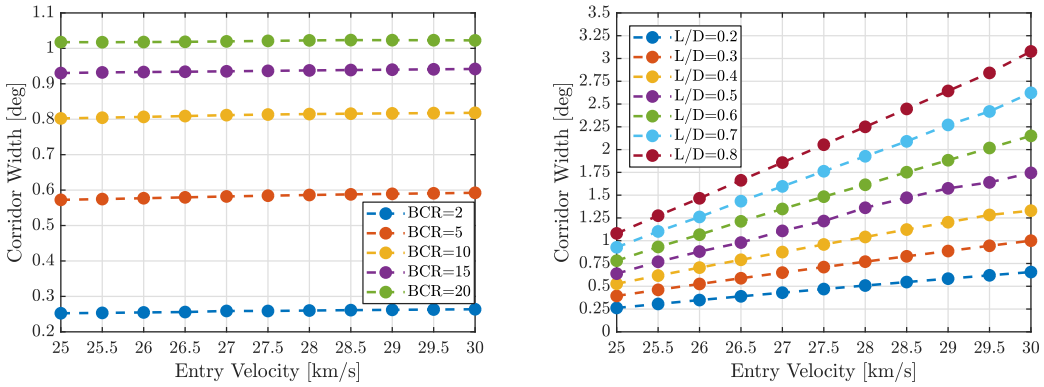

(a) Ballistic Vehicles (b) Lifting Vehicles

Figure 4.13. Neptune corridor width as function of entry velocity and vehicle control for base BC=50 kg/m^2 and target apoapsis altitude of 430,000 km

The effect of base BC on the corridor trends for each set of trajectories is shown in Figure 4.14. Figure 4.14a and Figure 4.14b illustrates that the width generally increases with lower base BC for both ballistic and lifting vehicles, similar to Titan.

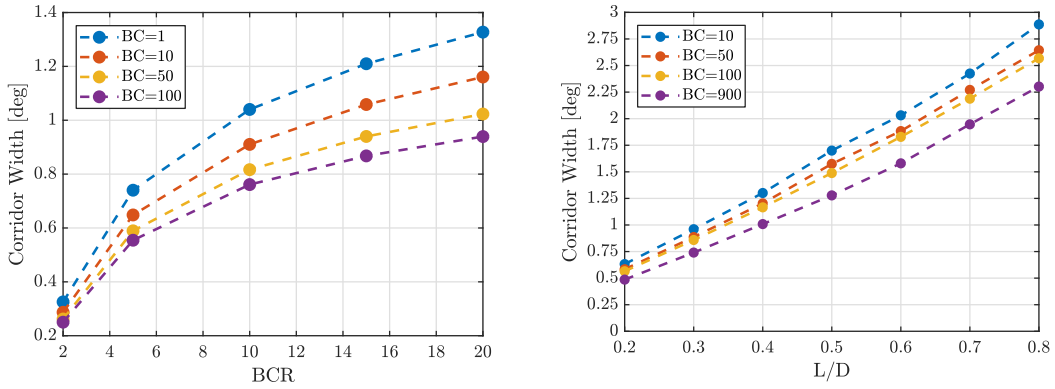

(a) Ballistic Vehicles (b) Lifting Vehicles

Figure 4.14. Neptune corridor width as function of vehicle control and base BC for 29 km/s entry velocity and target apoapsis altitude of 430,000 km

The effect modifying base BC has on the middle entry flight path angle of the corridor and peak convective heat rate is shown in Figure 4.15. Increasing BC leads to steeper flight path angles as shown in Figure 4.15a and Figure 4.15b. Figure 4.15c shows that increasing the vehicle BC, via increasing BCR or base BC, increases the heat rate. Figure 4.15d shows that increasing L/D increases the peak heat rate. Due to the potential large heat rates experienced at Neptune and current TPS technological limitations, it is desirable to utilize ballistic and lifting flight control on low base BC vehicles.

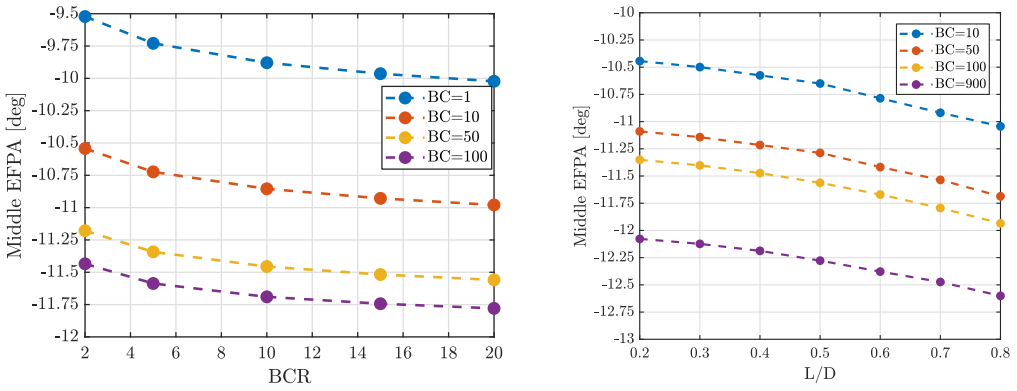

(a) Ballistic Vehicles

(b) Lifting Vehicles

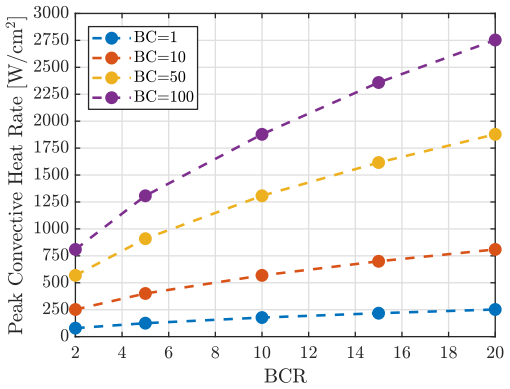

(c) Ballistic Vehicles

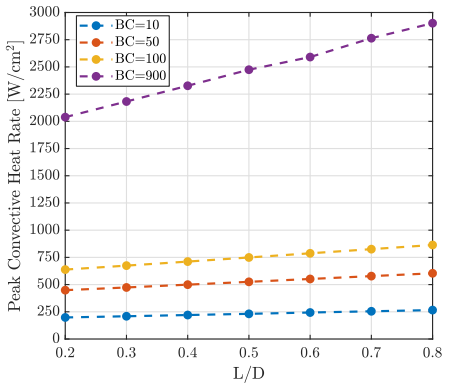

(d) Lifting Vehicles

Figure 4.15. Neptune middle entry flight path angle and peak convective heat rate as function of vehicle control and base BC for 29 km/s entry velocity and target apoapsis altitude of 430,000 km

4.1.2 Aerocapture Flight Envelope

In the previous section, calculations and trends of the theoretical entry flight path angle corridor width are introduced. This width serves as a metric to map vehicle control capability to the entry state. During aerocapture, there can be potential trajectory dispersions that can influence the effectiveness of the control capability. Uncertainties, such as delivery state, atmosphere, and aerodynamics, may serve to reduce the capability potentially leading to lifting and ballistic trajectories that do not successfully capture. Although assessing the aggregate effect of these uncertainties is commonly done in a Monte Carlo fashion, it is difficult to qualitatively assess the implications of each. Rather, their effect can be visualized through a mapping to the entry state. Using a similar setup as in the previous section, the

$\pm 3\sigma$ atmospheric and aerodynamic uncertainties are individually applied and the subsequent steep and shallow side trajectories are computed. From the set of three steep and shallow trajectories, the maximum steep side entry flight path angle and minimum shallow side entry flight path angle form the combined corridor width. The delivery state flight path angle dispersion is applied to narrow this width. The remaining available width is known as the aerocapture flight envelope. Having a positive flight envelope may qualitatively indicate that the vehicle has enough control authority to overcome the applied dispersions. The region enclosed by the envelope can be thought of as the admissible region of guidable aerocapture trajectories. A full quantitative assessment is conducted using Monte Carlo simulations.

Sample flight envelope calculation at each planetary destinations are presented in this section. A few assumptions are made regarding the applied dispersions. For the aerodynamics, the $\pm 3\sigma$ dispersions in L/D are applied. A 70° sphere-cone aeroshell similar to MSL aeroshell is assumed. For the MSL lifting aeroshell, these dispersons were estimated to be $\pm 20\%$ in L/D [114]. Using a similar approach, the resulting L/D uncertainty for a similar sphere-cone flying ballistically is estimated to be ± 0.05. Secondly, the GRAM models are utilized to simulate the atmospheric uncertainty. For Venus, Earth, and Mars, the uncertainty is simulated using the maximum density perturbation scale factor. For Titan and Neptune only, in addition to using the max scale factor, the minimum and maximum atmospheric profiles are set. See Figure 2.15 for a visualization of these settings. Lastly, the values for the delivery state entry flight path angle dispersions are assumed to be 0.4°, 0.5°, 0.22°, 0.4°, and 0.31° for Venus, Earth, Mars, Titan, and Neptune respectively.

Figure 4.16 depicts the individual effects of the uncertainties along with the flight envelope for two sample lifting and ballistic vehicles at Venus. For the ballistic vehicle, the aerodynamic uncertainties significantly reduce the corridor width. Even with the addition of delivery state errors, the flight envelope is quite narrow with a width of 0.153°. A BCR of 20 has just enough controllability to overcome the applied dispersions. Any values lower than this at Venus may yield non-positive flight envelopes potentially leading to uncaptured trajectories. Consequently, ballistic vehicles may not be favorable risk-wise at Venus. Contrasting results can be seen for the lifting vehicle analyzed. Although aerodynamic uncertainties and delivery state errors reduce the corridor width, the remaining flight envelope is quite wide

with a width of 0.824°. A low L/D, potentially heritage, blunt body aeroshell can provide significant controllability, almost 8 times larger than the ballistic vehicle analyzed, within the Venusian atmosphere. Consequently, lifting vehicles might be preferred for aerocapture mission sets at Venus.

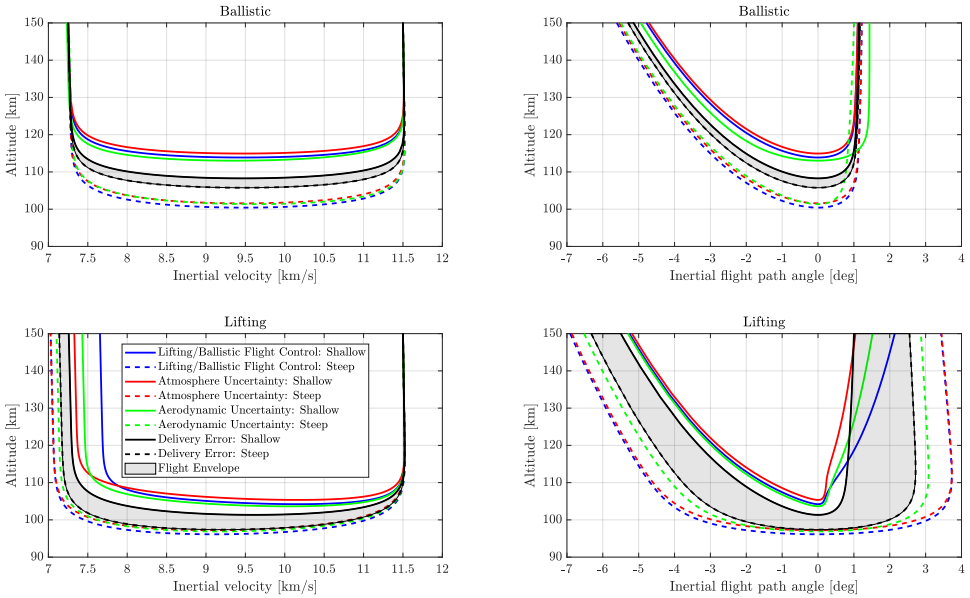

Figure 4.16. Venus flight envelope comparison between lifting (L/D=0.25) and ballistic (BCR=20) trajectories for base BC=50 kg/m^2 and 11.5 km/s entry velocity

Figure 4.17 depicts the individual effects of the uncertainties along with the flight envelope for two sample lifting and ballistic vehicles at Earth. For both the ballistic and lifting vehicle analyzed, the aerodynamic dispersions and delivery errors decrease the corridor width. The resulting flight envelope widths are 0.171° and 1.066° respectively. Unlike Venus, a lower BCR vehicle is capable of providing sufficient controllability potentially indicating that ballistic vehicle are viable for aerocapture applications at Earth. For lifting vehicles, a low L/D aeroshell, such as the Apollo capsule, would be sufficient for Earth aerocapture.

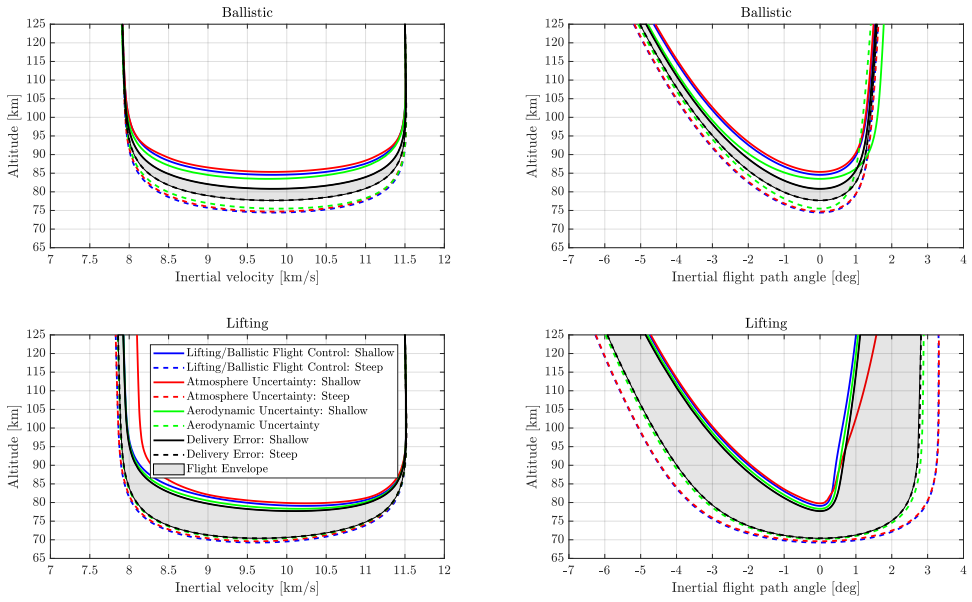

Figure 4.17. Earth flight envelope comparison between lifting (L/D=0.25) and ballistic (BCR=5) trajectories for base BC=50 kg/m^2 and 11.5 km/s entry velocity

Figure 4.18 depicts the individual effects of the uncertainties along with the flight envelope for two sample lifting and ballistic vehicles at Mars. Similar observations as the ones found for Earth can be seen for Mars. The resulting flight envelope width for the ballistic and lifting vehicle analyzed are 0.244° and 0.884° respectively. A low BCR vehicle is capable of providing sufficient controllability potentially indicating that ballistic vehicle are viable for aerocapture applications at Mars. For lifting vehicles, a low L/D aeroshell, such as the MSL aeroshell, would be sufficient for Mars aerocapture.

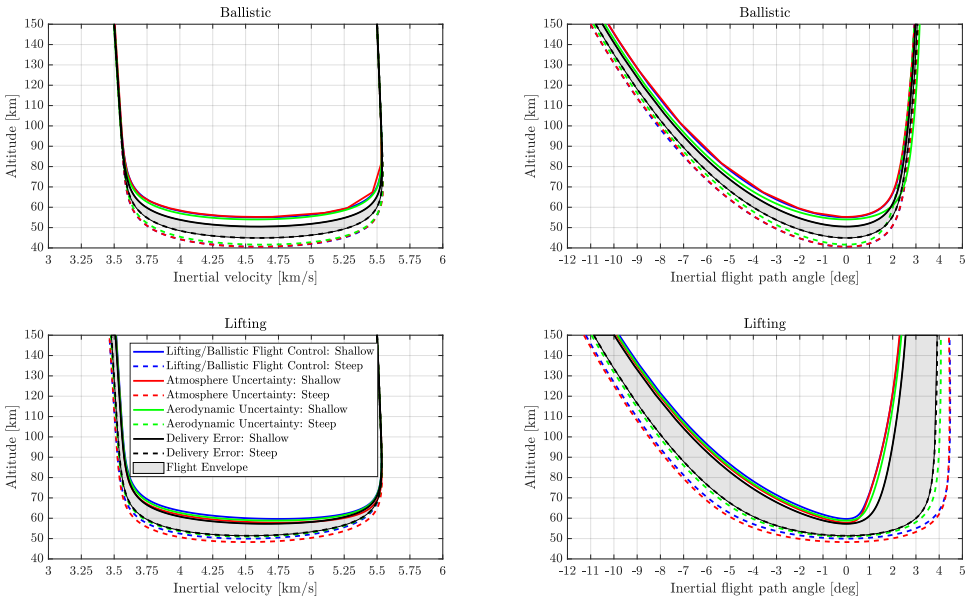

Figure 4.18. Mars flight envelope comparison between lifting (L/D=0.25) and ballistic (BCR=5) trajectories for base BC=50 kg/m^2 and 5.5 km/s entry velocity

Figure 4.19 depicts the individual effects of the uncertainties along with the flight envelope for two sample lifting and ballistic vehicles at Titan. Unlike Venus, Earth, and Mars, the atmospheric dispersions significantly reduce the corridor width along with the delivery state error. The resulting flight envelope width for the ballistic and lifting vehicle analyzed are 0.74° and 0.79° respectively. Similar to Venus, a high BCR vehicle is needed to provide sufficient controllability to overcome the uncertainty in atmospheric profile. If this uncertainty in profile can be improved upon through the integration of Cassini-Huygens flight data, then potentially lower BCR ballistic vehicles may be enabled. For lifting vehicles, a low-L/D vehicle, such as the MSL aeroshell, provides sufficient performance despite the guidable trajectory space being visually thin. This may make the capture success rate of the lifting vehicle susceptible to increased delivery and atmospheric dispersions.

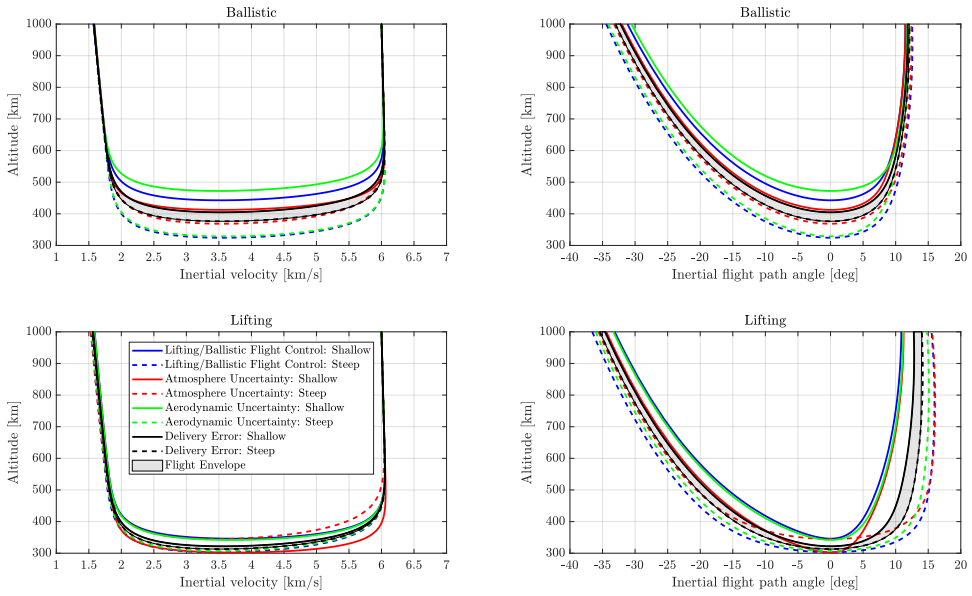

Figure 4.19. Titan flight envelope comparison between lifting (L/D=0.25) and ballistic (BCR=20) trajectories for base BC=50 kg/m^2 and 6 km/s entry velocity

Figure 4.20 depicts the individual effects of the uncertainties along with the flight envelope for two sample lifting and ballistic vehicles at Neptune. Similar to Titan, the atmospheric dispersions significantly reduce the corridor width. The resulting flight envelope width for the ballistic and lifting vehicle analyzed are 0.051° and 1.149° respectively. This width for the large BCR ballistic vehicle is razor thin indicating that ballistic vehicle may not provide enough controllability to overcome uncertainty in atmospheric profile. Unlike Titan, no additional flight data for Neptune is currently available potentially reducing the risk posture of ballistic Neptune aerocapture. For the lifting vehicle, a mid-L/D vehicle is assessed. The relatively large envelope width may indicate that lower-L/D vehicle, say 0.4-0.5, can provide sufficient controllability to overcome the lack in atmospheric knowledge.

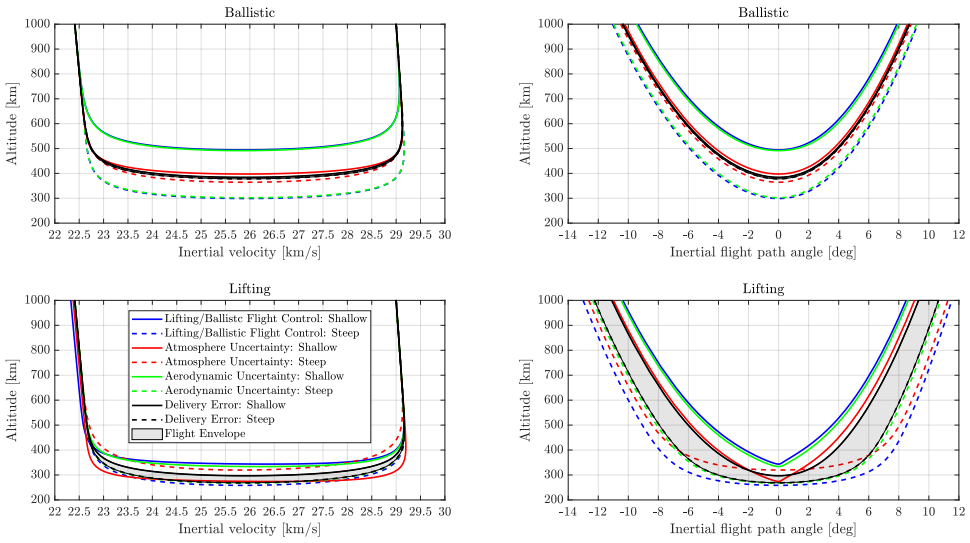

Figure 4.20. Neptune flight envelope comparison between lifting (L/D=0.8) and ballistic (BCR=20) trajectories for base BC=50 kg/m^2 and 29 km/s entry velocity

4.2 Monte Carlo Simulations

A series of Monte Carlo simulations are conducted to assess the performance and robustness of each flight control at different planetary destinations. Two sets of vehicle designs are considered: Discovery-Class vehicles and SmallSat-Class vehicles. The primary difference between the two is the aeroshell sizing to accommodate the science payload delivered to orbit. But, the aeroshells analyzed in this section all belong to the sphere-cone family. The NPC guidance architecture introduced in Section 3 is utilized to conduct the Monte Carlo simulations. A high-fidelity 3DOF truth model is employed. The truth model utilizes the full non-linear aerodynamics model and perturbed atmospheric model produced by each planet's GRAM model. The NPC knowledge of each planetary atmosphere is limited to the nominal atmospheric profile produced by each planet's GRAM model. For DFC flight control only, the NPC is assumed to utilize a linear aerodynamics model as described in Section 2. The flight computer runs the NPC guidance algorithm at the same rate for each flight control but this rate varies for each planet. For Venus, Earth, Mars, Titan, and Neptune, the rates are 0.2 Hz, 0.2 Hz, 0.1 Hz, 0.1 Hz, and 0.5 Hz, respectively. A guidance rate of 0.1 Hz is selected as a baseline. Due to the smaller density scale heights of Venus and Earth, the guid-

ance call rate about the baseline is doubled. Due to the potential large density uncertainties experienced at Neptune, the guidance call rate about the baseline is increased by five times. Each vehicle targets the same sets of orbits that have been analyzed in this dissertation (see Target Orbit category in Table 2.8).

Table 4.1 lists the common atmospheric, aerodynamic, and vehicle attitude dispersions applied to each vehicle. The delivery state dispersions are shown separately in each subsequent planetary destination. The atmospheric dispersions correspond to settings in the GRAM models. The random perturbation seed is used in the random generation on density perturbations. The density and wind scale factor, *rpscale* and *rwscale*, are utilized to control the scale of the corresponding perturbations about the nominal profile. A value of 1 and 2 corresponds to $\pm 3\sigma$ and $\pm 6\sigma$, respectively. For Titan and Neptune only, the variable *fminmax* controls the selection of the atmospheric profile between the Yelle minimum and Yelle maximum profiles. The value can be statically selected for each Monte Carlo run (known as global variation), or can have a sinusoidal latitudinal variation in each Monte Carlo run. The latter case is controlled using the term *fbias*, which keeps *fminmax* within the imposed bounds. This latitudinal variation, as shown in Eq. (4.1), was utilized in both Titan [10] and Neptune [11] NASA aerocapture studies and is replicated in this analysis.

$$fminmax = 0.44 \cos\left(4 * latitude\right) + fbias \tag{4.1}$$

The aerodynamic uncertainties pertain to differences in the on-board atmospheric model and the truth atmospheric model. Viscous and other high-order flow effects that are not captured in the on-board model might be present during flight. The $\pm 3\sigma$ values applied in the Monte Carlo simulations are typical for a 70° sphere-cone [114]. Likewise, similar $\pm 3\sigma$ uncertainties for the vehicle attitude can also be ascertained. These pertain to errors in the vehicle attitude produced from flight actuator inputs, despite the vehicle attitude dynamics not being explicitly simulated in the 3DOF simulations. A nominal value of zero indicates that the vehicle attitude equals the commanded vehicle attitude from the guidance.

Table 4.1. Planetary aerocapture Monte Carlo experimental setup

Category	Variable	Nominal	$\pm 3\sigma$ or min/max	Distribution
Atmosphere	Random perturbation seed	1	1 to 29999	Uniform
	rpscale	0	0 to 1	Normal
	rwscale	0	0 to 1	Normal
	fbias	0	-0.56 to 0.56	Uniform
	fminmax	0	-1 to 1	Uniform
Aerodynamics	Axial force coefficient	1	3%	Normal
	Normal force coefficient	1	5%	Normal
	Side-force coefficient	1	5%	Normal
Vehicle Attitude	Angle of Attack	0°	2°	Normal
	Side-Slip Angle	0°	2°	Normal
	Bank Angle	0°	10°	Normal

4.2.1 Discovery-Class Vehicles

Venus

For Venus, the targeted orbit is a 300 km circular orbit at 90° inclination. A series of different vehicle configurations are assessed. Table 4.2 provides a summary of each configuration consisting of two lifting vehicles and a single ballistic vehicle. Each vehicle is designed to house a 1080 kg satellite payload with a 3.7m diameter antenna (similar to the Magellan spacecraft). A MSL-derived aeroshell is assumed for the lifting vehicles (see Figure 2.12 for vehicle aerodynamics). A morphable sphere-cone aeroshell with a base cone angle of 70°, conical frustrum length of 3.5 m, and payload fairing diameter of 4 m is assumed for the ballistic vehicle (see Figure 2.6 for vehicle aerodynamics). Due to the small scale height of Venus atmosphere, increased control rates as compared to the other planetary destinations are assumed. The atmospheric entry mass of each vehicle is assumed to be 1500 kg. The TPS mass is not formally sized for any of the vehicle designs but a 72% payload over entry mass fraction is assumed from the NASA Venus aerocapture study [8]. Higher fidelity aerothermal heating analysis, not included in the current analysis, is needed to further refine the TPS mass. Note that the NASA Venus aerocapture study formulated a vehicle design with an aeroshell diameter of 2.65 m, L/D of 0.25, and entry mass of 900 kg (BC of 114 kg/m^2) for orbit insertion of a smaller sized science payload into the same target orbit.

Given each vehicle's base BC, L/D and/or BCR, the nominal inertial entry flight path angle is computed using the corridor width assessment introduced in the previous section.

Table 4.2. Venus aerocapture flight control vehicle designs

	Vehicle 1	Vehicle 2	Vehicle 3
Flight Control	BAM	DFC	DMCV
Nose Radius, m	1.125	1.125	5.848
Diameter, m	4.5	4.5	5.3 (at CA = 70)
Control Limits, deg	0 to 180	±16 (±5)[1]	20 to 70
Rate Limit, deg/s	30	7.5 (2)[1]	7.5
Accel Limit, deg/s^2	5	2 (0.3)[1]	2
Base BC, kg/m^2	60	60	10
Max L/D	0.25	0.25	0
Max BCR	–	–	5.5

[1] Angle of Attack (Side-Slip Angle)

These flight path angles are set to -5.825° for Vehicle 1 and Vehicle 2, and -5.359° for Vehicle 3. The nominal delivery state parameters are shown in Table 4.3. Due to the lack of delivery state covariance matrices for each entry condition, a new approach is taken to produce the entry state dispersions. The dispersions are generated through propagation of uncertainties in vehicle position and velocity as applied to the nominal entry hyperbola from the data cut-off point to entry interface using the atmospheric flight equation of motion (with zero density). The a data cutoff-point of 30 hours prior to entry is assumed for Venus. The position and velocity uncertainties are scaled such that the propagated $\pm 3\sigma$ entry flight path angle uncertainty at entry interface is obtained.

Table 4.3. Monte Carlo simulated dispersions for Venus aerocapture

Category	Variable	Nominal	$\pm 3\sigma$ or min/max	Distribution
Delivery State	Inertial entry flight path angle	-5.825° or -5.359°	From propagation	Correlated
	Inertial entry velocity	11.25 km/s	From propagation	Correlated
	Inertial entry altitude	150 km	From propagation	Correlated
	Inertial entry latitude	86°	From propagation	Correlated
	Inertial entry longitude	0°	From propagation	Correlated
	Inertial entry heading angle	90°	From propagation	Correlated

Table 4.4 outlines the various sets of cases run on each flight control. The reference case corresponds to $\pm 3\sigma$ random density variations simulated with the baseline delivery error used in the NASA Venus study [115]. Case 1 serves as the control of the experiment. The second case corresponds to a reduction in the density variation through halving of the perturbation scale multiplier. This case is intended to assess the effects of near nominal atmospheric profile conditions on the orbit insertion performance. The third case corresponds to an increase the random density variations to $\pm 6\sigma$ through doubling of the perturbation scale. This case is

intended to be the worst-case scenario of Venus atmosphere given the simulation capability of VenusGRAM. The fourth case corresponds to an increase in the delivery state uncertainty. This case is intended to simulate the effect of higher entry flight path angle uncertainty on the orbit insertion performance. For this case, the flight path angle uncertainty is increased to the value of 0.4°, which corresponds to a later data cutoff-point of 48 hours prior to entry. Cases 2, 3 and 4 are cases not investigated in the NASA Venus study.

Table 4.4. Summary of Monte Carlo Test Cases for Venus.

Case	Perturbation Scale	$\pm 3\sigma$ Entry Flight Path Angle
1. Reference	1.0	0.28°
2. Reduced Density Perturbations	0.5	0.28°
3. Increased Density Perturbations	2.0	0.28°
4. Increased Delivery State Uncertainty	1.0	0.4°

Reference Case

For the Reference Case, Case 1, a visualization of the Monte Carlo simulation runs for each vehicle is shown in Figure 4.21 and the corresponding orbit insertion statistics is shown in Table 4.5.

Both Vehicle 1 (BAM) and Vehicle 2 (DFC) are sufficiently robust to the applied set of trajectory dispersions, with each producing 100% capture success. Between these two vehicles, the orbit insertion performance slightly differs. Vehicle 1 exhibits half the variance in the apoapsis error statistic leading to slightly lower in-plane ΔV cost on average. On the other hand, Vehicle 2 produces much lower inclination errors leading to significantly lower out-of-plane ΔV statistics. Despite being within 1° of the target inclination, the low circular target orbit along with large gravity well of Venus leads to a costly correction cost for Vehicle 1. Increasing the number of bank reversals may allow for an improvement in the out-of-plane targeting performance. The aggregate total ΔV cost shows Vehicle 2 being cheaper on average with a 99th percentile value that is 50 m/s cheaper. The more precise in-plane performance for the BAM vehicle can be potentially attributed to the control actuator itself. For a small scale height, dense Venusian atmosphere, and short time of flight, the actuator transient response can potentially lead to residual targeting errors each guidance cycle. Using RCS thrusters rather than aerosurfaces, BAM can achieve faster control actuation over the vehicle lift vector than DFC thereby increasing the precision of each control input.

Vehicle 3, DMCV, is generally robust to the applied set of trajectory dispersions producing a 99.6% capture success. Figure 4.21 shows that Vehicle 3 produces lower aeroheating and load factors with peak convective heat rates and decelerations that are five times and 1.4 times lower on average, respectively. The orbit insertion performance exhibits varying levels of accuracy and precision. Vehicle 3 produces minute inclination error statistics that require less than 5 m/s to correct for. Up until the 50th percentile, the apoapsis targeting accuracy is on par with Vehicle 1 and 2. Due to the higher post-aerocapture periapsis altitudes achieved, Vehicle 3 produces lower in-plane ΔV at the 50th percentile. Nevertheless, the small control capability of Vehicle 3 limits the precision of in-plane orbit insertion as seen by the high variance in the apoapsis error and corresponding in-plane ΔV. As was shown in the corridor width assessment for ballistic DMCV vehicles at Venus, increasing the BCR capability to a value near 20 may allow for a mitigation strategy to both improve in capture success rate and orbit insertion performance.

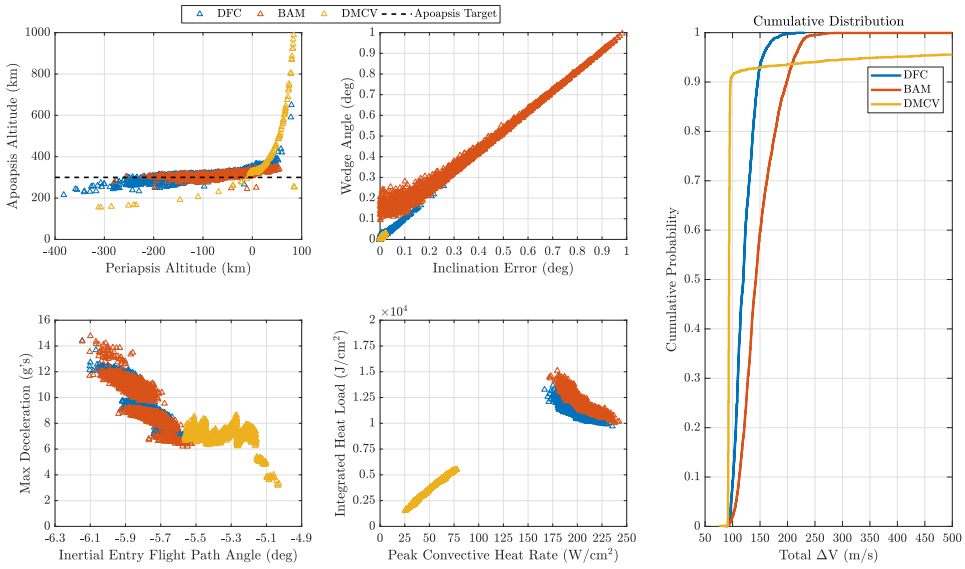

Figure 4.21. Venus Reference Case: Aerocapture orbit insertion performance

Table 4.5. Venus Reference Case: Aerocapture orbit insertion statistics

	Mean	3σ	1st %-tile	Median	99th %-tile	Min	Max
Apoapsis Error, km	10.749	63.130	-40.443	10.683	63.826	-84.416	350.201
	12.510	36.586	-15.633	12.610	39.201	-85.247	52.961
	542.104	10239.587	21.791	23.579	14076.269	-145.147	62050.227
In-plane ΔV, m/s	121	55	93	119	180	90	231
	108	37	87	107	140	82	285
	150	816	91	93	1714	75	2536
Inclination Error, deg	2.848E-05	6.164E-02	-7.131E-02	4.375E-05	6.454E-02	-1.551E-01	2.581E-01
	2.017E-01	1.132E+00	-4.028E-01	1.837E-01	9.204E-01	-6.120E-01	5.190E+00
	-5.377E-03	1.860E-02	-1.936E-02	-5.473E-03	8.604E-03	-2.349E-02	1.408E-02
Out-of-Plane ΔV, m/s	2	8	0	1	15	0	35
	61	100	18	54	133	12	670
	2	3	1	1	4	0	5
Total ΔV, m/s	123	56	95	120	182	90	232
	156	103	116	147	234	111	913
	152	816	92	94	1716	76	2536
Capture Success	100%	100%	99.6%				
Key	DFC	BAM	DMCV				

Reduced Density Perturbations

In Case 2, the density perturbations as simulated by VenusGRAM are halved to assess their effect on the orbit insertion performance. Figure 4.22 provides a visualization of the in-plane orbit insertion performance with the perturbation scale factor *rpscale* mapped to each run for each vehicle. Figure 4.22a shows the performance for Case 1 and Figure 4.22b shows for Case 2. Visual inspection shows that the reduction in density perturbations has no noticeable affect on the in-plane orbit insertion targeting for Vehicles 1 and 2. For Vehicle 3 in Cases 1 and 2, the few uncaptured cases can be classified as failures. Modifying the density perturbation amount has no effect on the outcome of the trajectory. A similar observation can be seen with the trajectories that significantly overshoot the apoapsis target as no significant correlation between density perturbations and apoapsis error can be ascertained visually.

For Case 2, the aerocapture performance statistics for the captured cases are shown in Table 4.6. As compared to Case 1, no significant changes arise in the max deceleration, peak convective heat rate, and integrated heat load with Case 2. However, the reduced density perturbations leads to a small reduction in the total ΔV for both Vehicles 1 and 2 with 99th percentile values of 230 m/s and 177 m/s, respectively. For Vehicle 3, the reduction allows for primarily an improvement in the in-plane orbit insertion targeting as seen by the reduction in the apoapsis error variance and 99th percentile in-plane ΔV value. Additionally, the reduction slightly improves the capture success rate from 99.6% to 99.77%. On average,

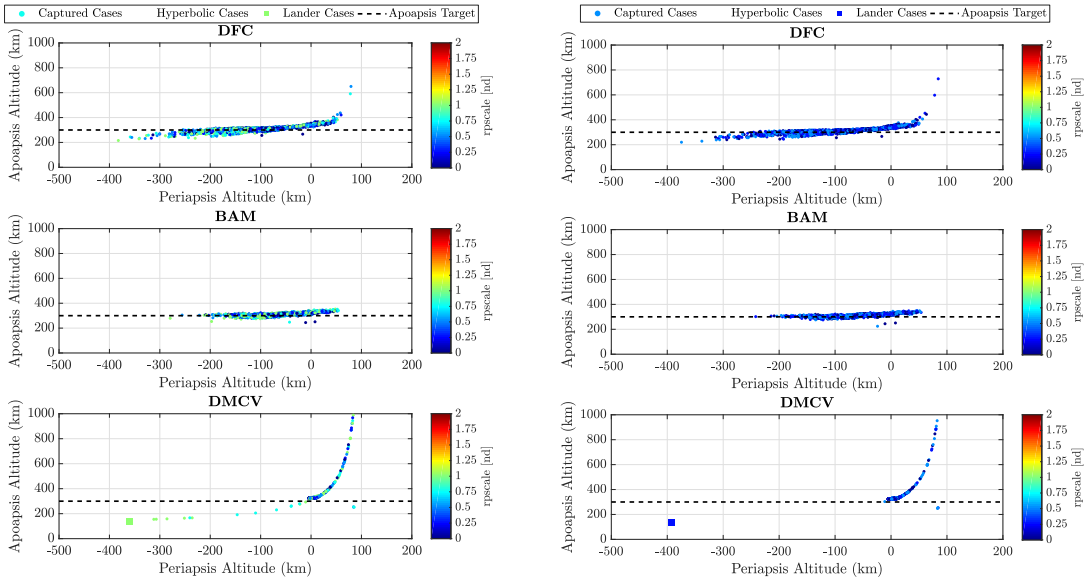

(a) Reference Case

(b) Reduced Density Perturbations

Figure 4.22. Visualization of the effect that reduced Venus density perturbations has on in-plane orbit insertion performance

the total ΔV cost for Vehicle 3 remains similar to Vehicle 1 but is slightly more expensive than Vehicle 2.

Table 4.6. Venus Reduced Density Perturbations Case: Aerocapture orbit insertion statistics

	Mean	3σ	1st %-tile	Median	99th %-tile	Min	Max
Apoapsis Error, km	11.903	61.563	-36.456	10.971	58.439	-80.121	428.856
	12.939	34.005	-12.611	13.138	38.188	-75.510	48.960
	530.238	9854.715	22.118	23.669	13079.896	-51.898	62050.227
In-plane ΔV, m/s	119	53	92	116	175	89	227
	107	35	86	106	139	81	162
	151	807	91	93	1662	75	2536
Inclination Error, deg	-2.987E-05	5.987E-02	-7.005E-02	8.045E-05	6.452E-02	-1.521E-01	2.179E-01
	1.922E-01	1.048E+00	-4.022E-01	1.648E-01	9.047E-01	-6.195E-01	1.333E+00
	-5.383E-03	1.859E-02	-1.936E-02	-5.510E-03	8.679E-03	-2.349E-02	1.408E-02
Out-of-Plane ΔV, m/s	2	8	0	1	14	0	30
	60	89	18	53	131	12	182
	2	3	1	1	4	0	5
Total ΔV, m/s	121	53	94	118	177	89	227
	154	86	116	145	230	111	312
	152	807	92	94	1663	76	2536
Capture Success	100%	100%	99.77%				
Key	DFC	BAM	DMCV				

Increased Density Perturbations

In Case 3, the density perturbations as simulated by VenusGRAM are increased to assess their effect on the orbit insertion performance. Figure 4.23 provides a visualization of the in-plane orbit insertion performance with the perturbation scale factor *rpscale* mapped to each run for each vehicle. Figure 4.23a shows the performance for Case 1 and Figure 4.23b shows for Case 3. Visual inspection shows that the increase in density perturbations has no noticeable effect on the in-plane orbit insertion targeting for Vehicles 1 and 2. Some correlation between rpscale values near 2 and lower periapsis altitudes appears. Like in Case 2 for Vehicle 3, no visible correlation appears between the density perturbation scale factor and apoapsis targeting.

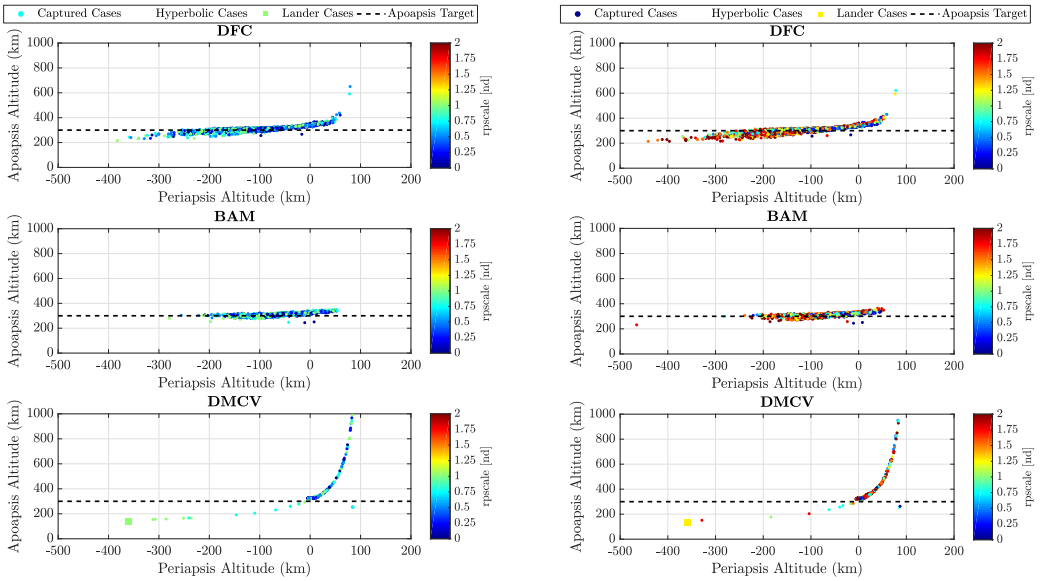

(a) Reference Case (b) Reduced Density Perturbations

Figure 4.23. Visualization of the effect that increased Venus density perturbations has on in-plane orbit insertion performance

For Case 3, the aerocapture performance statistics for the captured cases are shown in Table 4.7. As compared to Case 1, no significant changes arise in the max deceleration, peak convective heat rate, and integrated heat load with Case 2. However, the increased density perturbations leads to a small increase in the total ΔV for each vehicle. For Vehicle 3, the increase slightly worsens the capture success rate from 99.6% to 99.1%. On average, the

total ΔV cost for Vehicle 3 remains similar to Vehicle 1 but is slightly more expensive than Vehicle 2.

Table 4.7. Venus Increased Density Perturbations Case: Aerocapture orbit insertion statistics

	Mean	3σ	1st %-tile	Median	99th %-tile	Min	Max
Apoapsis Error, km	7.562	72.836	-57.778	9.108	63.967	-85.431	321.960
	11.795	40.299	-20.925	12.166	41.379	-68.002	63.710
	576.507	10961.574	21.603	24.183	15209.633	-149.072	63753.532
In-plane ΔV, m/s	125	65	94	121	195	89	250
	110	40	89	108	145	83	253
	151	840	91	93	1769	72	2545
Inclination Error, deg	3.643E-05	6.539E-02	-7.089E-02	7.174E-05	7.296E-02	-1.654E-01	2.876E-01
	2.304E-01	1.129E+00	-4.050E-01	2.280E-01	1.014E+00	-5.399E-01	5.063E+00
	-5.366E-03	1.847E-02	-1.928E-02	-5.510E-03	8.561E-03	-2.348E-02	1.415E-02
Out-of-Plane ΔV, m/s	2	9	0	1	15	0	38
	64	99	18	57	145	12	650
	1	3	1	1	4	0	5
Total ΔV, m/s	127	66	96	123	197	90	251
	160	104	117	151	250	112	885
	152	840	92	94	1770	72	2545
Capture Success	100%	100%	99.1%				
Key	DFC	BAM	DMCV				

Increased Delivery State Uncertainty

In Case 4, the inertial entry flight path uncertainty is increased to assess its effect on the orbit insertion performance. Figure 4.24 provides a visualization of the in-plane orbit insertion performance with the entry flight path angle mapped to each run for each vehicle. Figure 4.24a shows the performance for Case 1 and Figure 4.24b shows for Case 4. A visual correlation between the entry flight path angle and the resulting apoapsis altitude error can be seen. Shallow angles tend to produce trajectories that overshoot the apoapsis target while exiting the atmosphere with a higher periapsis altitude. By making the angles more shallower, via increase in angle uncertainty, more cases overshoot the apoapsis target and potentially remain hyperbolic as shown by Vehicle 3. Too steep angles generally lead to more negative periapsis altitudes and potentially lander trajectories as seen by Vehicle 3.

For Case 4, the aerocapture performance statistics for the captured cases are shown in Table 4.8. As compared to Case 1, no significant changes arise in the max deceleration, peak convective heat rate, and integrated heat load with Case 2. However, the increased delivery state uncertainty primarily affects the in-plane orbit insertion precision of each vehicle. For Vehicles 1 and 2, the variance in apoapsis error increases by more than three times (primarly

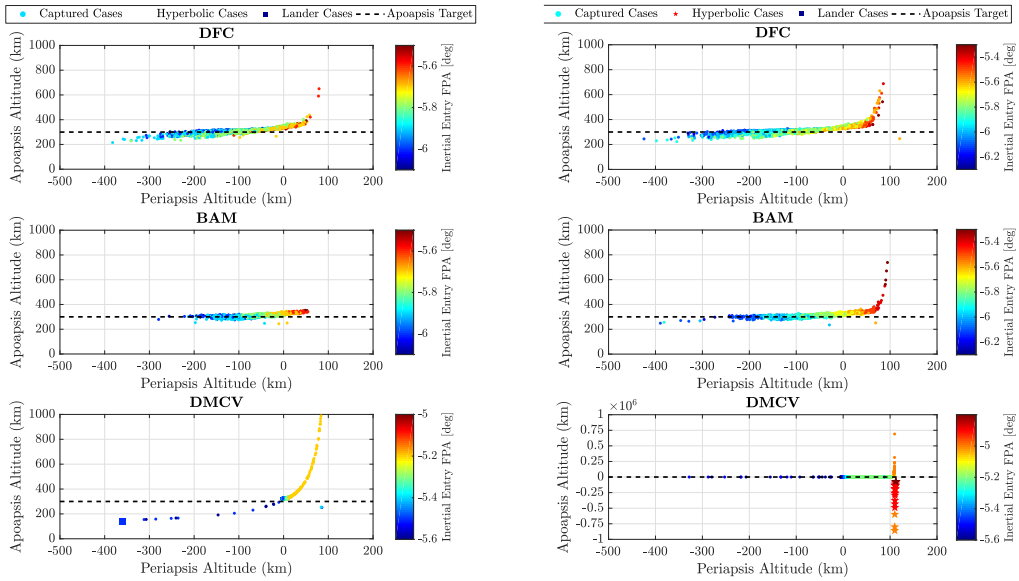

(a) Reference Case

(b) Reduced Density Perturbations

Figure 4.24. Visualization of the effect that increased Venus delivery state uncertainty has on in-plane orbit insertion performance

due to the large maximum cases). This leads to a small increase in the 99th percentile in-plane ΔV and total ΔV. For Vehicle 3, both the mean and variance of the apoapsis error are worsened due to the increase in entry flight path angle error. The leads to a significant increase in both 99th percentile values for in-plane ΔV and total ΔV. Additionally, the capture success rate is worsened from 99.6% to 97.17%. This net change in capture success for Case 4 is much larger than values computed in Cases 2 and 3.

Table 4.8. Venus Increased Delivery State Uncertainty Case: Aerocapture orbit insertion statistics

	Mean	3σ	1st %-tile	Median	99th %-tile	Min	Max
Apoapsis Error, km	16.287	202.833	-43.078	11.593	107.185	-77.178	2750.848
	17.413	199.798	-17.616	13.352	55.711	-65.001	2427.901
	4138.532	90227.906	1.129	25.388	74887.277	-146.617	1215094.23385339
In-plane ΔV, m/s	121	75	89	118	187	67	661
	109	64	82	106	157	78	603
	330	1772	91	93	2599	67	2937
Inclination Error, deg	2.663E-05	6.080E-02	-7.401E-02	8.421E-05	6.594E-02	-1.560E-01	2.678E-01
	2.253E-01	1.181E+00	-3.776E-01	2.206E-01	9.375E-01	-5.501E-01	5.463E+00
	-5.192E-03	2.908E-02	-2.701E-02	-5.256E-03	1.694E-02	-3.296E-02	2.516E-02
Out-of-Plane ΔV, m/s	2	8	0	2	15	0	36
	61	116	17	55	135	12	705
	2	4	0	2	6	0	8
Total ΔV, m/s	123	75	91	119	189	69	663
	157	140	115	148	239	110	879
	331	1772	92	95	2601	68	2938
Capture Success	100%	100%	97.17%				
Key	DFC	BAM	DMCV				

Study Findings

The performance analysis at Venus has shown for the reference set of uncertainties, DFC can enable a 100% successful science orbit insertion within a 182 m/s total ΔV budget for periapsis raise, apoapsis, and inclination corrections. BAM can enable a 100% successful science orbit insertion within a 234 m/s total ΔV budget. DMCV can enable a 99.6% successful science orbit insertion within a 1716 m/s total ΔV budget but at 5 times lower peak stagnation point convective heating than BAM and DFC. Despite being more expensive statistically, DMCV can potentially produce trajectories whose total ΔV is comparable to DFC in cost. Reducing and increasing the density perturbations has little effect on the robustness and orbit insertion performance of DFC, BAM, and DMCV. Increasing the delivery state error via entry flight path angle has most pronounced effect on DMCV where the capture success rate drops by more than 3% and the total ΔV cost significantly increases. Overall, BAM and DFC applied to lifting vehicles producing 0.25 L/D and DMCV applied to ballistic vehicles producing BCR=5.5 are found to be sufficiently robust to the various sets of applied trajectory dispersions. For the given control capability, further decreasing the delivery state error may allow for DMCV to achieve 100% capture success while improving the orbit insertion performance. If not achievable, then increasing the control capability might be warranted. Given near nominal flight conditions, the most accurate orbit insertion, in terms of apoapsis and inclination targeting, can be achieved with DFC.

Mars

For Mars, the targeted science orbit is a 400 km circular orbit at 0° inclination. A series of different vehicle configurations are assessed. Table 4.9 provides a summary of each configuration consisting of two lifting vehicles and a single ballistic vehicle. Each vehicle is sized to house a 1275 kg satellite payload with a 3m diameter antenna (similar to the Mars Reconnaissance Orbiter). A MSL-derived aeroshell is assumed for Vehicles 1 and 2. For Vehicle 1, a maximum of 5 bank reversals is enforced with assumed rate and acceleration limits of an RCS. For Vehicle 2, the corresponding limits are assumed based off trim-tab aerosurface deflections [33]. A morphable sphere-cone aeroshell with a base cone angle of

70°, conical frustrum length of 3.5 m and payload fairing diameter of 4 m is assumed for Vehicle 3. The cone angle rates and acceleration limits are assumed to be identical to the DFC angle of attack limits. To normalize the comparison, the same atmospheric entry mass of 1500 kg is assumed for each vehicle. Both Vehicles 1 and 2 have the same base BC and maximum L/D capability. Vehicle 3, due to the aeroshell geometry, has a smaller base BC but moderate BCR capability. The TPS mass is not formally sized for any of the vehicle designs but a 85% payload over entry mass fraction is assumed from the NASA Mars aerocapture study [9]. Higher fidelity aerothermal heating analysis, not included in the current analysis, is needed to further refine the TPS mass. Note that the NASA Mars aerocapture study formulated an aeroshell design with a diameter of 4.65 m, L/D of 0.24, and entry mass of 7087 kg (BC of 365 kg/m^2) for orbit insertion of an Earth-return vehicle for Mars Sample Return mission.

Table 4.9. Mars aerocapture flight control vehicle designs

	Vehicle 1	Vehicle 2	Vehicle 3
Flight Control	BAM	DFC	DMCV
Nose Radius, m	1.125	1.125	5.848
Diameter, m	4.5	4.5	5.3 (at CA = 70)
Control Limits, deg	0 to 180	±16 (±5)[1]	20 to 70
Rate Limit, deg/s	20	5 (2)[1]	5
Accel Limit, deg/s^2	5	2 (0.3)[1]	2
Base BC, kg/m^2	60	60	10
Max L/D	0.25	0.25	0
Max BCR	–	–	5.5

[1] Angle of Attack (Side-Slip Angle)

Given each vehicle's base BC, L/D and/or BCR, the nominal inertial entry flight path angle is computed using the corridor width assessment introduced in the previous section. These flight path angles are set to -10.5° for Vehicle 1 and Vehicle 2, and -9.96° for Vehicle 3. The nominal delivery state parameters are shown in Table 4.10. The dispersions are generated through propagation of uncertainties in vehicle position and velocity from the data cut-off point to entry interface using the atmospheric flight equation of motion (with zero density). A data cutoff-point of 2.5 days prior to entry is assumed from MSL interplanetary navigation analysis [20]. The position and velocity uncertainties are scaled such that the propagated $\pm 3\sigma$ entry flight path angle uncertainty at entry interface is obtained.

Table 4.10. Monte Carlo simulated dispersions for Mars aerocapture

Category	Variable	Nominal	$\pm 3\sigma$ or min/max	Distribution
Delivery State	Inertial entry flight path angle	-10.5° or -9.96°	From propagation	Correlated
	Inertial entry velocity	5.5 km/s	From propagation	Correlated
	Inertial entry altitude	150 km	From propagation	Correlated
	Inertial entry latitude	0°	From propagation	Correlated
	Inertial entry longitude	342.478°	From propagation	Correlated
	Inertial entry heading angle	90°	From propagation	Correlated

Table 4.11 outlines the various sets of cases run on each flight control. The reference case corresponds to $\pm 3\sigma$ random density variations simulated with MSL-derived delivery state performance. The second case corresponds to an increase the random density variations to $\pm 6\sigma$ through doubling of the perturbation scale. This case is intended to be the worst-case scenario of Mars atmosphere given the simulation capability of MarsGRAM. The third case corresponds to an increase in the delivery state uncertainty. This case is intended to simulate the effect of higher entry flight path angle uncertainty on the orbit insertion performance. For this case, the flight path angle uncertainty is increased to the requirement value used in the MSL navigational analysis [20].

Table 4.11. Summary of Monte Carlo Test Cases for Mars.

Case	Perturbation Scale	$\pm 3\sigma$ Entry Flight Path Angle
1. Reference	1.0	0.11°
2. Increased Density Perturbations	2.0	0.11°
3. Increased Delivery State Uncertainty	1.0	0.2°

Reference Case

In Case 1, the reference set of trajectory uncertainties are applied to each vehicle. Figure 4.25 shows the comparison of the aerocapture orbit insertion performance of each vehicle and Table 4.12 highlights the corresponding statistics. Each vehicle achieves 100% capture success indicating robustness to the applied set of dispersions

Each vehicle produces different-levels of orbit insertion success. The qualitative comparison of the in-plane orbit insertion performance in Figure 4.25 shows that Vehicle 3 is not only the most accurate but the most precise (can also be seen quantitatively by the low mean and variance apoapsis error statistics in Table 4.12). Furthermore, Vehicle 3 generally produces higher periapsis altitudes that allows for the corresponding in-plane ΔV statistics

to be slightly lower than Vehicles 1 and 2. Nevertheless, all three vehicles produces excellent in-plane orbit insertion performance. Despite maintaining the inclination to within 1° of the target, Vehicle 1 produces a much larger correction cost as compared to Vehicles 2 and 3. For both these vehicles, the inclination error and corresponding correction cost are both minute. The total ΔV cost shows that Vehicle 3 produces the lowest value with Vehicle 2 only being a few m/s more expensive.

Comparing the aeroheating and aerodynamic deceleration results, Figure 4.25 shows that all three vehicles generally produce similar peak deceleration values (despite differences in the entry flight path angle) but different peak convective heat rate values. Vehicle 3 is shown to produce nearly 4 times lower peak values as compared to Vehicles 1 and 2. Given BAM as the current state-of-the-art for Mars EDL technology, the result suggests that DMCV can provide both an orbit insertion as well as an aeroheating enhancement.

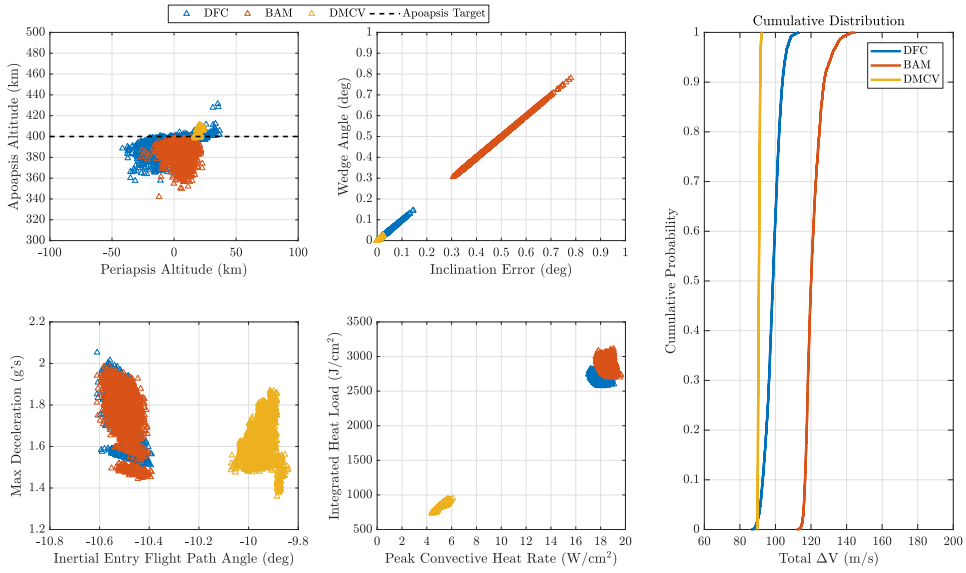

Figure 4.25. Mars Reference Case: Aerocapture orbit insertion performance

Table 4.12. Mars Reference Case: Aerocapture orbit insertion statistics

	Mean	3σ	1st %-tile	Median	99th %-tile	Min	Max
Apoapsis Error, km	-7.430	20.244	-30.167	-6.237	3.711	-42.483	31.428
	-13.788	21.485	-38.322	-11.875	-3.744	-57.921	0.023
	2.587	10.075	-0.993	0.357	9.310	-1.767	11.081
In-plane ΔV, m/s	97	12	88	97	107	86	113
	97	6	93	96	103	91	111
	90	1	90	90	91	89	92
Inclination Error, deg	2.114E-02	5.572E-02	6.915E-04	1.682E-02	9.308E-02	0.000E+00	1.459E-01
	4.209E-01	2.200E-01	3.251E-01	4.006E-01	6.706E-01	3.055E-01	7.803E-01
	7.427E-03	1.296E-02	8.384E-04	6.610E-03	1.990E-02	0.000E+00	2.501E-02
Out-of-Plane ΔV, m/s	1	3	0	1	5	0	9
	25	13	19	23	39	18	46
	0	1	0	0	1	0	1
Total ΔV, m/s	99	13	89	99	108	86	113
	121	14	115	120	138	112	145
	91	2	90	91	92	90	93
Capture Success	100%	100%	100%				
Key	DFC	BAM	DMCV				

Increased Density Perturbations Case

In Case 2, the density perturbations of the Martian atmosphere are increased using the parameter *rpscale*. Figure 4.26 provides a visual comparison of its effect on the in-plane orbit insertion performance. Figure 4.26a and Figure 4.26b shows the in-plane performance for Case 1 and Case 2, respectively. Increasing the density perturbations does not lead to any new uncaptured trajectories to arise indicating that the vehicles are sufficiently robust to the elevated dispersions. Rather, the increasing values have a visual correlation to the apoapsis targeting precision. For *rpscale* values approaching 2, the results in Figure 4.26b for Vehicles 1 and 2 tend to undershoot the apoapsis target leading to an increase in the variance of the apoapsis error statistics. For Vehicle 3, visual comparison shows no such increase demonstrating DMCV in-plane orbit insertion precision advantage.

For Case 2, the aerocapture performance statistics for the captured cases are shown in Table 4.13. As compared to Case 1, no significant changes arise in the max deceleration, peak convective heat rate, and integrated heat load with Case 2. The increased density perturbations has a minute effect on the in-plane orbit insertion performance as seen by the increase in the apoapsis variance but small increase in the in-plane ΔV. This leads to a small increase in the total ΔV for each vehicle with 99th percentile values of 141 m/s, 115 m/s and 92 m/s, respectively.

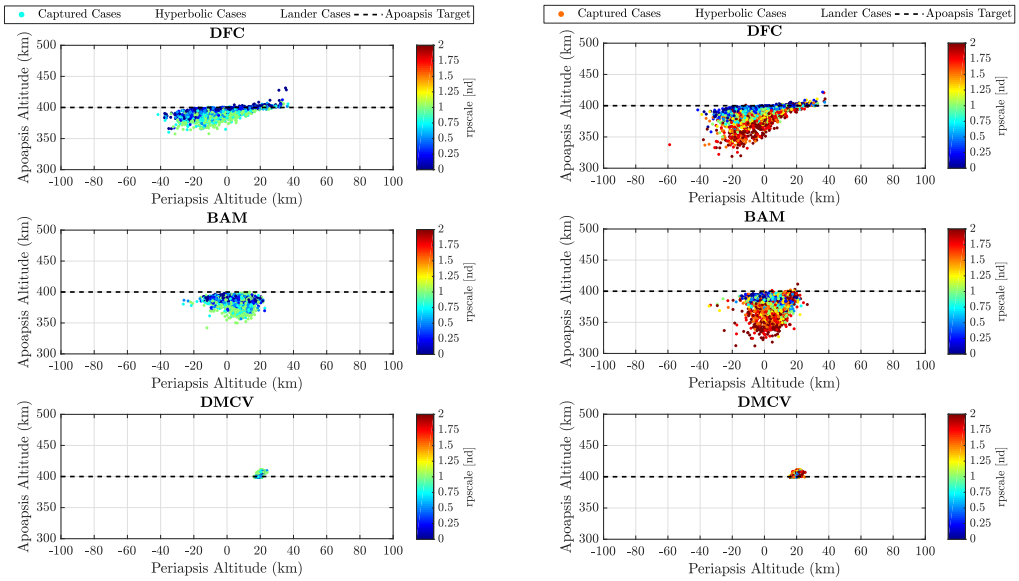

(a) Reference Case (b) Increased Density Perturbations

Figure 4.26. Visualization of the effect that increased Mars density perturbations has on in-plane orbit insertion performance

Table 4.13. Mars Increased Density Perturbations Case: Aerocapture orbit insertion statistics

	Mean	3σ	1st %-tile	Median	99th %-tile	Min	Max
Apoapsis Error, km	-13.253	39.177	-59.093	-9.876	3.213	-81.104	21.724
	-19.779	42.732	-63.943	-14.310	-2.398	-87.882	11.401
	2.892	10.023	-0.898	1.119	9.784	-1.328	11.759
In-plane ΔV, m/s	99	15	88	98	113	86	124
	98	12	92	97	110	90	120
	90	2	89	90	92	89	92
Inclination Error, deg	2.150E-02	5.582E-02	7.280E-04	1.730E-02	9.024E-02	0.000E+00	1.505E-01
	4.325E-01	2.177E-01	3.289E-01	4.164E-01	6.621E-01	2.977E-01	8.393E-01
	7.439E-03	1.298E-02	8.384E-04	6.615E-03	1.990E-02	0.000E+00	2.501E-02
Out-of-Plane ΔV, m/s	1	3	0	1	5	0	9
	25	13	19	24	39	17	49
	0	1	0	0	1	0	1
Total ΔV, m/s	100	16	89	99	115	87	130
	123	18	115	122	141	112	148
	91	2	90	91	92	89	93
Capture Success	100%	100%	100%				
Key	DFC	BAM	DMCV				

Increased Delivery State Uncertainty Case

In Case 3, the delivery state uncertainty, via inertial entry flight path angle, is increased. Figure 4.27 provides a visual comparison of its effect on the in-plane orbit insertion performance. Figure 4.27a and Figure 4.27b shows the in-plane performance for Case 1 and

Case 3, respectively. Increasing the entry flight path angle uncertainty does not lead to any new uncaptured trajectories to arise indicating that the vehicles are sufficiently robust to the elevated values. Rather, the increasing values have a visual correlation to the periapsis altitude. The increased angle range allows for steeper and shallower angle cases that produce lower and higher periapsis altitudes, respectively. In Figure 4.27b for Vehicle 2, some steeper angles produce apoapsis altitudes that undershoots the target. Like in Case 2, visual comparison of Vehicle 3 shows no such increase demonstrating DMCV in-plane orbit insertion precision advantage.

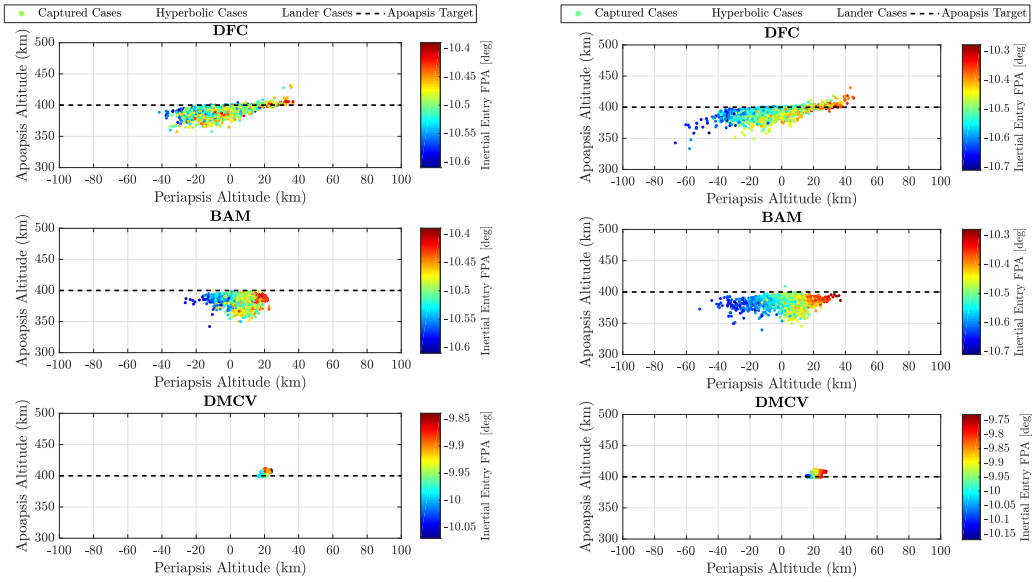

(a) Reference Case (b) Increased Density Perturbations

Figure 4.27. Visualization of the effect that increased Mars delivery state uncertainty has on in-plane orbit insertion performance

For Case 3, the aerocapture performance statistics for the captured cases are shown in Table 4.14. As compared to Case 1, no significant changes arise in the max deceleration, peak convective heat rate, and integrated heat load with Case 3. The increased delivery state uncertainties has generally a minute affect on the orbit insertion statistics and can only be seen in the min and max statistics. The resulting 99th percentile total ΔV for each vehicle are 141 m/s, 112 m/s, and 93 m/s.

Table 4.14. Mars Increased Navigation Uncertainty Case: Aerocapture orbit insertion statistics

	Mean	3σ	1st %-tile	Median	99th %-tile	Min	Max
Apoapsis Error, km	-7.346	22.557	-30.715	-5.684	5.852	-66.600	31.288
	-14.132	21.804	-40.000	-12.258	-3.496	-60.691	9.066
	2.809	10.486	-0.956	0.531	9.919	-1.333	11.415
In-plane ΔV, m/s	97	15	87	97	109	85	125
	97	10	91	97	108	87	114
	90	1	89	90	92	88	92
Inclination Error, deg	2.487E-02	6.146E-02	9.494E-04	2.023E-02	9.697E-02	0.000E+00	1.914E-01
	4.341E-01	2.487E-01	3.053E-01	4.165E-01	6.997E-01	2.704E-01	8.310E-01
	1.657E-02	3.131E-02	1.639E-03	1.437E-02	4.679E-02	0.000E+00	6.050E-02
Out-of-Plane ΔV, m/s	1	4	0	1	6	0	11
	25	15	18	24	41	16	49
	1	2	0	1	3	0	4
Total ΔV, m/s	99	15	88	99	112	86	127
	122	17	114	121	141	109	147
	91	2	90	91	93	89	94
Capture Success	100%	100%	100%				
Key	DFC	BAM	DMCV				

Study Findings

The performance analysis at Mars has shown for the reference set of uncertainties, DFC can enable a 100% successful science orbit insertion within a 108 m/s total ΔV budget for periapsis raise, apoapsis, and inclination corrections. BAM can enable a 100% successful science orbit insertion within a 138 m/s total ΔV budget. DMCV can enable a 100% successful science orbit insertion within a 92 m/s total ΔV budget but at 4 times lower peak stagnation point convective heating than BAM and DFC. Increasing the density perturbations and delivery state error has little effect on the robustness and obrit insertion performance of each vehicle. Overall, BAM and DFC applied to lifting vehicles producing 0.25 L/D and DMCV applied to ballistic vehicles producing BCR=5.5 are found to be sufficiently robust to the various sets of applied trajectory dispersions.

Titan

For Titan, the targeted orbit is a 1700 km circular orbit at 100° inclination. A series of different vehicle configurations are assessed. Table 4.15 provides a summary of each configuration consisting of two lifting vehicles and a single ballistic vehicle. Each vehicle is designed to house a 1000 kg satellite payload with a 3.7m diameter antenna. A scaled MSL aeroshell is assumed for the lifting vehicles (smaller nose radius and diameter but same

nose radius to diameter ratio). A morphable sphere-cone aeroshell with a base cone angle of 70°, conical frustrum length of 3.5 m and payload fairing diameter of 4 m is assumed for the ballistic vehicle. Similar actuator rate and acceleration limits as that used in the Mars study are assumed. The atmospheric entry mass of each vehicle is assumed to be 1500 kg to best match the mass allocation used in the NASA Titan study [10]. The TPS mass is not formally sized for any of the vehicle designs but is implicitly assumed from the NASA study. Higher fidelity aerothermal heating analysis, not included in the current analysis, is needed to further refine the TPS mass.

Table 4.15. Titan aerocapture flight control vehicle designs

	Vehicle 1	Vehicle 2	Vehicle 3
Flight Control	BAM	DFC	DMCV
Nose Radius, m	0.9375	0.9375	5.848
Diameter, m	3.75	3.75	5.3 (at CA = 70)
Control Limits, deg	0 to 180	±16 (±5)[1]	20 to 70
Rate Limit, deg/s	20	5 (2)[1]	5
Accel Limit, deg/s^2	5	2 (0.3)[1]	2
Base BC, kg/m^2	90	90	10
Max L/D	0.25	0.25	0
Max BCR	–	–	5.5

[1] Angle of Attack (Side-Slip Angle)

Given each vehicle's base BC, L/D and/or BCR, the nominal inertial entry flight path angle is computed using the corridor width assessment introduced in the previous section. These flight path angles are set to -35.7° for Vehicle 1 and Vehicle 2, and -33.755° for Vehicle 3. The nominal delivery state parameters are shown in Table 4.16. The dispersions are generated through propagation of uncertainties in vehicle position and velocity from the data cut-off point to entry interface using the atmospheric flight equation of motion (with zero density). From the NASA Titan study, a data cutoff-point of 2 days prior to entry is assumed along with the utilization of optical navigation [16]. The position and velocity uncertainties are scaled such that the propagated $\pm 3\sigma$ entry flight path angle uncertainty at entry interface is obtained.

Table 4.17 outlines the various sets of cases run on each flight control. The reference case corresponds to a latitudinal variation of *fminmax* along with $\pm 3\sigma$ random density variations simulated. The second case corresponds to a single atmospheric profile being utilized in

Table 4.16. Monte Carlo simulated dispersions for Neptune aerocapture

Category	Variable	Nominal	$\pm 3\sigma$ or min/max	Distribution
Delivery State	Inertial entry flight path angle	-35.7° or -33.755°	From propagation	Correlated
	Inertial entry velocity	6.5 km/s	From propagation	Correlated
	Inertial entry altitude	1000 km	From propagation	Correlated
	Inertial entry latitude	-38.065°	From propagation	Correlated
	Inertial entry longitude	-7.937°	From propagation	Correlated
	Inertial entry heading angle	-102.741°	From propagation	Correlated

the simulations. This case is intended to assess the effects of incorporating flight data from the Cassini-Huygens mission on reducing the uncertainty in atmospheric profile. The third case corresponds to a removal of the latitudinal variation of *fminmax*, thereby increasing the uncertainty in the mean profile, as well as increasing the random density variations to $\pm 6\sigma$. This case is intended to be the worst-case scenario of Titan atmosphere given the simulation capability of TitanGRAM. The fourth case corresponds to an increase in the delivery state uncertainty. This case is intended to simulate the effect of not fully achieving the potential benefits of optical navigation with regards to reduced entry flight path angle uncertainty. For this case, the flight path angle uncertainty is selected to match the value used in the NASA Titan study. Case 4 serves as the control of the experiment to best match the reference case setup found in Reference [116]. Cases 1, 2 and 3 are cases not investigated in the NASA Titan study.

Table 4.17. Summary of Monte Carlo Test Cases.

Case	Perturbation Scale	Fminmax	$\pm 3\sigma$ Entry Flight Path Angle
1. Reference	1.0	f(latitude)	0.6°
2. Single Atmospheric Profile	1.0	0	0.6°
3. Increased Density Perturbations	2.0	global	0.6°
4. Increased Delivery State Uncertainty	1.0	f(latitude)	0.93°

Reference Case

A visualization of the orbit insertion performance for Case 1 captured cases is shown in Figure 4.28. Each flight control generally provides sufficient in-plane performance. Vehicle 3 produces cases with the highest post-aerocapture periapsis altitude and most concentration of cases near the apoapsis target. This leads to DMCV producing the lowest apoapsis error variance and in-plane ΔV statistics as shown in Table 4.18 for the reference set of

dispersions. Vehicles 1 and 2 produce varying levels of variance with respect to the apoapsis target. For the same L/D capability and applied dispersions, Vehicle 2 with DFC produces half the variance and lower mean apoapsis error as compared to Vehicle 1 with BAM. With regards to out-of-plane performance, Vehicle 2 produces the lowest inclination error and corresponding ΔV. The residual inclination error and corresponding ΔV for Vehicle 3 is small indicating no significant penalty for the lack of out-plane controllability. For Vehicle 1, the applied bank reversals adequately keeps the inclination to within 1° of the target (99% confidence interval). The higher variance, as compared to the other flight controls, is an indication of the performance limitation of the coupled BAM flight control. The aggregate total ΔV statistics shows that for Case 1, Vehicle 3 produces the cheapest orbit insertion cost in addition to exhibiting the lowest peak convective heat rate and lower deceleration in Figure 4.28. However, Vehicle 3 is the least robust with a capture success of only 98.37% indicating that the BCR capability is not sufficient to overcome the reference set of trajectory dispersions at Titan. Vehicles 1 and 2 both produce 100 % capture success indicating that a lifting vehicle with an L/D of 0.25 is sufficiently robust to these reference set of dispersions. Moreover, Vehicle 1 produces a 99th percentile total ΔV that is nearly 100 m/s cheaper than Vehicle 2. On average, Vehicle 1 is 30 m/s more expensive than Vehicle 3.

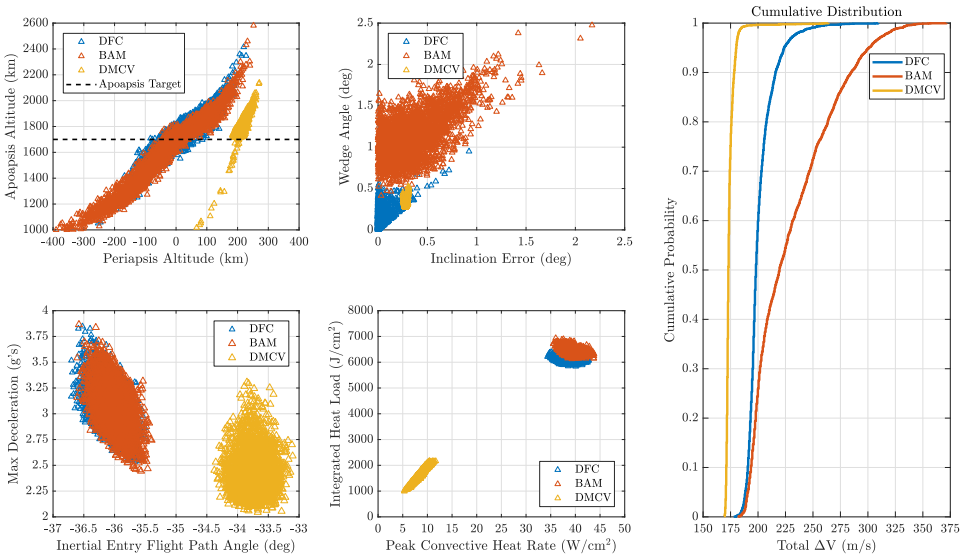

Figure 4.28. Titan Reference Case: Aerocapture orbit insertion performance

Table 4.18. Titan Reference Case: Aerocapture orbit insertion statistics

	Mean	3σ	1st %-tile	Median	99th %-tile	Min	Max
Apoapsis Error, km	3.179	378.848	-328.867	-3.767	357.231	-649.434	715.345
	-115.756	778.981	-646.465	-102.919	452.438	-699.679	881.414
	63.421	211.267	-3.960	42.100	267.351	-682.449	438.402
In-plane ΔV, m/s	201	37	185	198	248	178	307
	222	105	184	210	317	179	340
	167	15	163	166	178	162	257
Inclination Error, deg	1.546E-03	1.636E-01	-2.121E-01	3.632E-03	1.531E-01	-7.189E-01	9.220E-01
	-5.755E-02	1.280E+00	-1.005E+00	-4.881E-02	9.721E-01	-1.421E+00	2.169E+00
	-2.815E-01	3.080E-02	-3.049E-01	-2.815E-01	-2.585E-01	-3.114E-01	-2.526E-01
Out-of-Plane ΔV, m/s	4	9	0	3	14	0	29
	35	30	18	33	65	11	85
	10	6	7	10	16	7	19
Total ΔV, m/s	202	37	185	198	248	178	310
	251	105	209	240	344	198	379
	175	15	171	174	186	170	265
Capture Success	100%	100%	98.37%				
Key	DFC	BAM	DMCV				

Single Atmospheric Profile

A reduction in the atmospheric profile uncertainty at Titan may allow for a significant improvement in the robustness and aerocapture performance. Figure 4.29 provides a visualization of the simulated atmospheric profile uncertainty mapped to the in-plane orbit insertion performance for each simulated vehicle. Figure 4.29a shows Case 1 with its latitudinal variation of the profile controlled by *fbias* and Figure 4.29b shows Case 2 with the utilization of a single atmospheric profile, which is assumed to be the nominal profile. For Case 1, a distinct correlation between *fbias* and periapsis/apoapsis altitude can be inferred. For large *fbias* values, the resulting trajectories undershoot the apoapsis target and have more negative periapsis altitudes. Converse trend is seen for small values of *fbias*. The trajectories that have apoapsis altitudes below 1000 km (atmospheric interface altitude for Titan) are classified as landers. For Case 1, only Vehicle 3 produces lander cases. The physical significance of the *fbias* correlation is that larger values of it produce larger values of *fminmax* that ultimately yield larger than average density profiles. The larger the density, the more effective the aerodynamic forces become thereby potentially leading to too much energy dissipation when targeting the desired orbit. Conversely, smaller than average density profiles may lead to insufficient energy dissipation and targeting performance that overshoots the intended apoapsis altitude with the worst case condition being uncaptured hyperbolic trajectories. In Case 2, the variation of the atmospheric profile is eliminated thus allowing

for both improved orbit insertion performance and elimination of failed cases for Vehicle 3. A visual inspection of Figure 4.29b indicates that Vehicle 3 provides preciser in-plane orbit insertion performance than Vehicle 1 and Vehicle 2, though both vehicles exhibit significant reductions in the apoapsis error variance.

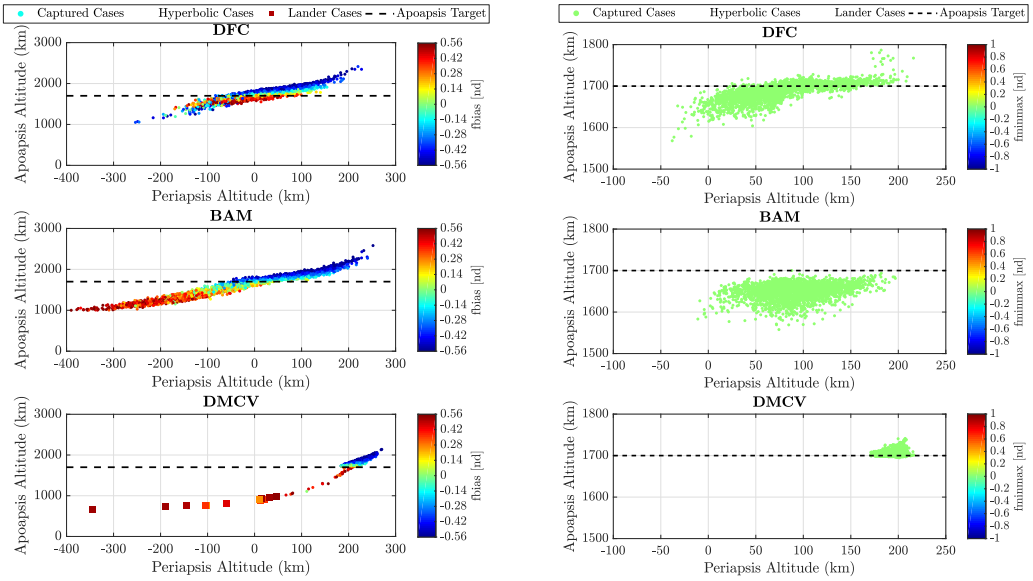

(a) Reference Case (b) Single Atmospheric Profile

Figure 4.29. Visualization of the effect that improved Titan atmospheric knowledge has on in-plane orbit insertion performance

For Case 2, the aerocapture performance statistics for the captured cases are shown in Table 4.19. As compared to Case 1, no significant changes arise in the max deceleration, peak convective heat rate, and integrated heat load with Case 2. However, the reduced atmospheric profile uncertainty leads to a generous reduction in the total ΔV for both Vehicles 1 and 2 with 99th percentile values of 200 m/s and 235 m/s, respectively. For Vehicle 3, the reduction in total ΔV is minute with a 99th percentile values of 177 m/s but remains cheaper than Vehicles 1 and 2.

Table 4.19. Titan Single Atmospheric Profile Case: Aerocapture orbit insertion statistics

	Mean	3σ	1st %-tile	Median	99th %-tile	Min	Max
Apoapsis Error, km	-12.939	65.266	-72.262	-9.039	23.690	-131.707	158.120
	-49.779	55.857	-107.227	-46.199	-18.340	-142.215	0.119
	6.438	17.419	-2.580	7.054	29.960	-5.265	41.353
In-plane ΔV, m/s	183	22	167	183	200	163	212
	184	16	170	184	197	165	206
	165	3	163	165	167	161	168
Inclination Error, deg	3.100E-03	1.399E-01	-1.745E-01	3.438E-03	1.415E-01	-4.145E-01	5.241E-01
	9.412E-01	1.133E+00	1.069E-01	9.461E-01	1.718E+00	-3.847E-02	2.197E+00
	-2.832E-01	3.041E-02	-3.070E-01	-2.833E-01	-2.599E-01	-3.128E-01	-2.542E-01
Out-of-Plane ΔV, m/s	4	9	0	4	14	0	20
	73	35	46	74	97	36	112
	10	6	7	10	17	7	19
Total ΔV, m/s	183	23	167	184	200	163	212
	208	32	187	207	235	184	246
	173	4	170	173	177	169	180
Capture Success	100%	100%	100%				
Key	DFC	BAM	DMCV				

Increased Density Perturbations

Case 3 tests the antithesis of Case 2 being an increase rather than decrease in the atmospheric profile uncertainty. The maximum density perturbations are simulated along with a global rather than latitudinal variation of the atmospheric profile. Figure 4.30 shows the comparison of the in-plane orbit insertion performance between Case 1 and Case 3 for each simulated vehicle configuration. In Figure 4.30b, the global variation using *fminmax* explicitly increases the number of uncaptured cases for each vehicle. For each vehicle, the minimum atmospheric profiles (*fminmax* near -1) yields hyperbolic trajectories or nearly hyperbolic trajectories with large apoapsis altitudes. Like Case 1, the maximum atmospheric profiles (*fminmax* near 1) yield lander trajectories. Note that due to large vertical axes units, not all hyperbolic and lander cases are shown in Figure 4.30.

For Case 3, the aerocapture performance statistics for the captured cases are shown in Table 4.20. As compared to Case 1, no significant changes arise in the max deceleration, peak convective heat rate, and integrated heat load with Case 3. However, the increased density uncertainty leads to a significant increase in the total ΔV for both Vehicles 1 and 3 with 99th percentile values of 313 m/s and 558 m/s, respectively. For Vehicle 2, the increase actually reduces the total ΔV statistics with a 99th percentile value of 278 m/s (though the max stat for Case 3 is larger than Case 1). This can be attributed to the low apoapsis error variance produced with BAM. Despite having the same L/D capability, BAM is more robust to the higher dispersions than DFC as seen by the higher capture success rate. Due to the

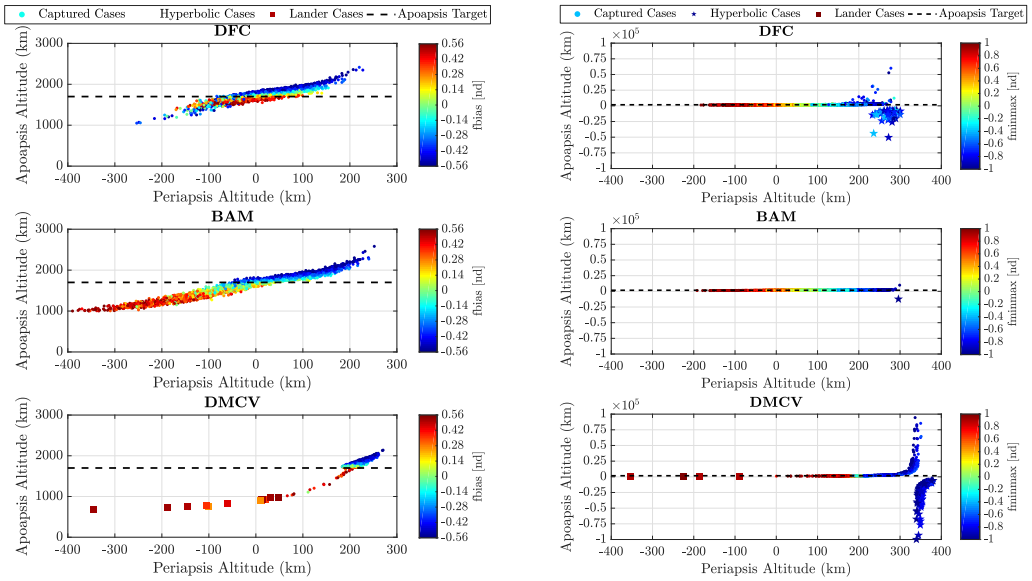

(a) Reference Case (b) Increased Density Perturbations

Figure 4.30. Visualization of the effect that increased Titan atmospheric uncertainty has on in-plane orbit insertion performance

increase number of hyperbolic trajectories, an increase in BCR capability might be needed for Vehicle 3.

Table 4.20. Titan Increased Density Perturbation Case: Aerocapture orbit insertion statistics

	Mean	3σ	1st %-tile	Median	99th %-tile	Min	Max
Apoapsis Error, km	220.182	5773.323	-353.996	-8.544	2534.047	-487.571	58344.185
	16.223	924.611	-413.549	-38.342	739.032	-539.915	8124.554
	3107.974	108135.080	-332.230	6.350	54947.896	-662.201	1239762.426
In-plane ΔV, m/s	202	89	173	196	290	169	557
	197	70	167	189	256	159	405
	190	213	163	167	553	162	598
Inclination Error, deg	1.404E-01	1.284E+00	-3.783E-01	4.529E-03	1.948E+00	-2.193E+00	3.518E+00
	2.022E-01	1.390E+00	-9.039E-01	3.073E-01	1.058E+00	-1.899E+00	2.387E+00
	-2.782E-01	5.936E-02	-3.069E-01	-2.819E-01	-1.962E-01	-3.171E-01	-1.729E-01
Out-of-Plane ΔV, m/s	8	33	0	4	54	0	99
	38	30	18	37	65	3	97
	10	7	6	10	16	5	19
Total ΔV, m/s	207	97	173	199	313	169	573
	226	61	195	223	278	187	453
	198	212	170	175	558	169	604
Capture Success	98.27%	99.97%	93%				
Key	DFC	BAM	DMCV				

Increased Delivery State Uncertainty

In Case 4, the inertial entry flight path angle uncertainty is increased by 55%. Figure 4.31 shows the comparison between the in-plane orbit insertion performance for Cases 1 and 4. Given the same nominal entry flight path angle, increasing the angle uncertainty increases the range of simulated angles. As shown in Figure 4.31b for Vehicles 1 and 2, the steeper angles coupled with higher than average density profiles yield failed trajectories. Shifting the nominal entry flight path angle to be shallower may eliminate these failed trajectories on the steep end but may increase the number of overshooting cases on the shallow end. For Vehicle 3, an increase in the delivery state uncertainty adversely affects the robustness by increasing the number of hyperbolic trajectories. For Case 1 trends in Figure 4.31a, similar flight path angle tuning may allow for a reduction in the number of hyperbolic cases.

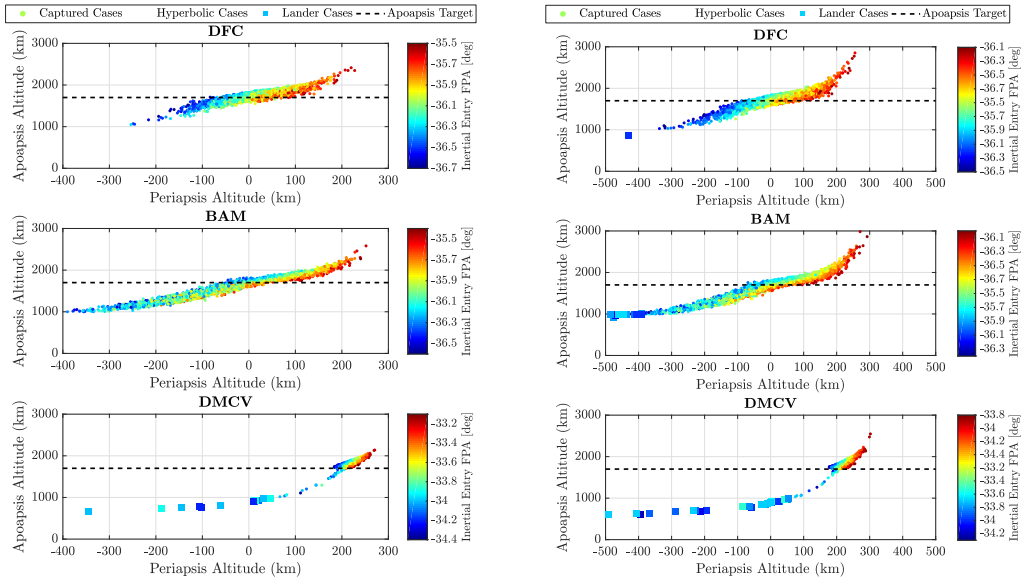

(a) Reference Case

(b) Increased Delivery State Uncertainty

Figure 4.31. Visualization of the effect that increased Titan delivery state uncertainty has on in-plane orbit insertion performance

For Case 4, the aerocapture performance statistics for the captured cases are shown in Table 4.21. As compared to Case 1, no significant changes arise in the max deceleration, peak convective heat rate, and integrated heat load with Case 4. However, the increased

delivery state uncertainty leads to an increase in the apoapsis error variance for each vehicle. The inclination error is not significantly changed. The subsequent affect on the total ΔV is small with corresponding 99th percentile values for Vehicles 1, 2, and 3 of 284 m/s, 356 m/s, and 190 m/s respectively. Despite having the same L/D capability, DFC is more robust to the higher dispersions than BAM as seen by the higher capture success rate. The increase in the number of hyperbolic trajectories decreases the capture success rate for Vehicle 3 by 0.8%.

Table 4.21. Titan Increased Delivery State Uncertainty Case: Aerocapture orbit insertion statistics

	Mean	3σ	1st %-tile	Median	99th %-tile	Min	Max
Apoapsis Error, km	0.861	517.925	-500.476	-6.482	561.420	-670.866	1369.445
	-109.712	864.751	-683.624	-101.113	655.326	-699.854	1457.913
	69.151	236.381	11.444	42.340	350.418	-665.280	847.788
In-plane ΔV, m/s	203	55	181	198	282	175	326
	223	113	180	210	330	175	353
	167	15	162	166	180	161	254
Inclination Error, deg	1.619E-03	1.714E-01	-2.191E-01	3.605E-03	1.506E-01	-7.398E-01	1.214E+00
	-4.441E-02	1.413E+00	-1.114E+00	-3.209E-02	1.177E+00	-1.559E+00	2.795E+00
	-2.814E-01	4.697E-02	-3.184E-01	-2.814E-01	-2.466E-01	-3.309E-01	-2.379E-01
Out-of-Plane ΔV, m/s	5	11	0	5	17	0	35
	36	37	15	34	73	7	104
	11	10	7	11	21	7	25
Total ΔV, m/s	204	55	181	199	284	175	331
	252	113	205	242	356	197	414
	176	16	170	175	190	168	261
Capture Success	99.97%	99.17%	97.57%				
Key	DFC	BAM	DMCV				

Study Findings

The performance analysis at Titan has shown for the reference set of uncertainties, DFC can enable a 100% successful science orbit insertion within a 248 m/s total ΔV budget for periapsis raise, apoapsis, and inclination corrections. BAM can enable a 100% successful science orbit insertion within a 345 m/s total ΔV budget. DMCV can enable a 98.37% successful science orbit insertion within a 186 total ΔV budget but at 4 times lower peak stagnation point convective heating than BAM and DFC. Reduction in the atmospheric profile uncertainty of Titan can allow for all three flight controls to achieve 100% capture success with significant reductions in total ΔV. Increasing the atmospheric dispersions reduces the capture success for each flight control while increasing the variance of the orbit insertion targeting error leading to significant increase in total ΔV. Increasing the delivery state error via entry flight path angle reduces the capture success for each flight control and moderately increases the

total ΔV. Overall, BAM and DFC applied to lifting vehicles producing 0.25 L/D and DMCV applied to ballistic vehicles producing BCR=5.5 are found to be sufficiently robust to the various sets of applied trajectory dispersions. Given near nominal flight conditions, the most accurate orbit insertion, in terms of apoapsis and inclination targeting, can be achieved with DFC while the cheapest, in terms of total ΔV, can be achieved with DMCV. This difference is attributed to the periapsis raise cost, which shows the advantage DMCV might have over DFC.

Neptune

For Neptune, the targeted orbit is an 3986 x 430000 km elliptical orbit at 157° inclination. A series of different vehicle configurations are assessed. Table 4.22 provides a summary of each configuration consisting of four lifting vehicles (two sets of L/D) and a single ballistic vehicle. Each vehicle is designed to house a 1000 kg satellite payload with a 3.7m diameter antenna. A MSL-derived aeroshell is assumed for the lifting vehicles. A morphable sphere-cone aeroshell with a base cone angle of 70°, conical frustrum length of 3.5 m and payload fairing diameter of 4 m is assumed for the ballistic vehicle. The atmospheric entry mass of each vehicle is assumed to be 2200 kg to best match the mass allocation used in the NASA Neptune study [11]. The TPS mass is not formally sized for any of the vehicle designs but is implicitly assumed from the NASA study. Engineering models are utilized to estimate the vehicle aerodynamic heating and sensed deceleration loads. Higher fidelity aerothermal heating analysis, not included in the current analysis, is needed to further refine the TPS mass.

Table 4.22. Neptune aerocapture flight control vehicle designs

	Vehicle 1	Vehicle 2	Vehicle 3	Vehicle 4	Vehicle 5
Flight Control	BAM	BAM	DFC	DFC	DMCV
Nose Radius, m	1.125	1.125	1.125	1.125	5.848
Diameter, m	4.5	4.5	4.5	4.5	5.3 (at CA = 70)
Control Limits, deg	0 to 180	0 to 180	±25 (±5)[1]	±30 (±5)[1]	20 to 70
Rate Limit, deg/s	20	20	5 (2)[1]	5 (2)[1]	5
Accel Limit, deg/s^2	5	5	2 (0.3)[1]	2 (0.3)[1]	2
Base BC, kg/m^2	110	120	110	120	15
Max L/D	0.4	0.5	0.4	0.5	0
Max BCR	–	–	–	–	5.5

[1] Angle of Attack (Side-Slip Angle)

Given each vehicle's base BC, L/D and/or BCR, the nominal inertial entry flight path angle is computed using the corridor width assessment introduced in the previous section. These flight path angles are set to -11.4° for Vehicle 1 and Vehicle 3, -11.6° for Vehicle 2 and Vehicle 4, and -10.6° for Vehicle 5. The nominal delivery state parameters are shown in Table 4.23. The dispersions are generated through propagation of uncertainties in vehicle position and velocity from the data cut-off point to entry interface using the atmospheric flight equation of motion (with zero density). A data cutoff-point of 2 days prior to entry is assumed. The position and velocity uncertainties are scaled such that the propagated $\pm 3\sigma$ entry flight path angle uncertainty at entry interface is obtained.

Table 4.23. Monte Carlo simulated dispersions for Neptune aerocapture

Category	Variable	Nominal	$\pm 3\sigma$ or min/max	Distribution
Delivery State	Inertial entry flight path angle	-11.4° or -11.6° or -10.6°	From propagation	Correlated
	Inertial entry velocity	29 km/s	From propagation	Correlated
	Inertial entry altitude	1000 km	From propagation	Correlated
	Inertial entry latitude	-7.474°	From propagation	Correlated
	Inertial entry longitude	-13.888°	From propagation	Correlated
	Inertial entry heading angle	-154.551°	From propagation	Correlated

A similar experimental procedure as that of Titan is partaken for Neptune. Table 4.24 outlines the various sets of cases run on each flight control. The reference case corresponds to a latitudinal variation of *fminmax* along with $\pm 3\sigma$ random density variations simulated. The second case corresponds to a 50% reduction in the atmospheric variability through halving of the perturbation scale and range of *fbias* term. This case is intended to simulate the effect of having atmospheric data measurements from precursor atmospheric probes might have on the aerocapture performance and robustness. The third case corresponds to a removal of the latitudinal variation of *fminmax*, thereby increasing the uncertainty in the mean profile, as well as increasing the random density variations to $\pm 6\sigma$. This case is intended to be the worst-case scenario given the current knowledge of Neptune's atmosphere. In Cases 1-3, the entry flight path angle dispersion values come from recent advancements in onboard autonomous optical navigation (AutoNav) [117]. When applied to Neptune, optical navigation is shown to achieve reductions in entry flight path delivery uncertainties from ± 0.17 (1σ) to ± 0.11 (1σ) [118]. The fourth case serves to investigate the consequence of not achieving the intended performance enhancements of optical navigation. For this case,

the flight path angle uncertainty is selected to match the value used in the NASA Neptune study [119], which corresponds to a 55% increase in value. With the exception of entry flight path angle, the experimental setup for Cases 1, 2, and 3 exactly match those found in Reference [32]. In particular, Case 3 more rigorously simulates the effects of increased density uncertainty than that found in Reference [32] through doubling the perturbation scale. Case 4 serves as the control of the experiment to best match the reference case setup found in Reference [32].

Table 4.24. Summary of Monte Carlo Test Cases.

Case	Perturbation Scale	Fminmax	$\pm 3\sigma$ Entry Flight Path Angle
1. Reference	1.0	f(latitude)	0.33°
2. Reduced Density Perturbations	0.5	f(latitude)	0.33°
3. Increased Density Perturbations	2.0	global	0.33°
4. Increased Delivery State Uncertainty	1.0	f(latitude)	0.51°

Reference Case

The reference case, Case 1, Monte Carlo simulation is run using the reference set of uncertainties found in Table 4.24. The same set of dispersions associated with delivery error, atmospheric variability, aerodynamic variability, and vehicle attitude are applied to each flight control configuration. A visualization of the orbit insertion performance of the captured cases is shown in Figure 4.32 and the corresponding statistics are shown in Table 4.25.

For Case 1, both BAM configurations, Vehicle 1 and 2, achieve 100% successful capture. Likewise both DFC vehicles, Vehicle 3 and 4, achieve 100% successful capture. For the DMCV vehicle, Vehicle 5, only 92.4% of cases successfully capture. More details on the uncaptured cases are explained in the next section.

Majority of the 3000 simulated cases for both DFC vehicles and the DMCV vehicle produced an absolute apoapsis error of less than 10,000 km with respect to the 430,000 km target. For the DFC vehicles, an increase in L/D allows for significant improvements in the apoapsis targeting as seen in the reduction in the 99th percentile and maximum statistics. For the same L/D capability, DFC flight control provides a significant improvement in the apoapsis targeting as compared to BAM. DMCV generally provides excellent orbit insertion performance. Up until the 50th percentile, DMCV produces apoapsis errors comparable to DFC. The lack of control to mitigate the higher-levels of uncertainty can be attributed to the

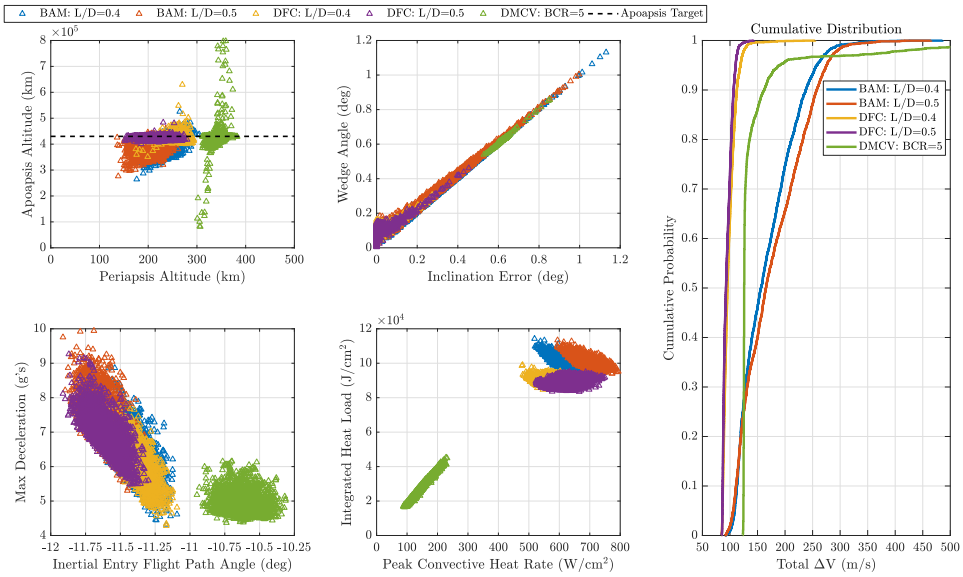

Figure 4.32. Neptune Reference Case: Aerocapture orbit insertion performance

Table 4.25. Neptune Reference Case: Aerocapture orbit insertion statistics

	Mean	3σ	1st %-tile	Median	99th %-tile	Min	Max
Apoapsis Error x 10^3, km	-32.423	83.511	-97.139	-28.579	16.763	-165.593	95.591
	-38.712	87.083	-101.590	-33.677	0.850	-153.656	46.152
	-5.336	32.670	-25.454	-5.756	28.835	-78.891	199.636
	-4.467	18.322	-18.028	-3.377	5.846	-29.254	53.624
	101.291	9687.895	-45.816	-0.094	779.787	-348.218	165236.415
In-plane ΔV, m/s	144	151	85	133	275	85	481
	156	166	87	143	288	86	441
	98	35	85	95	131	85	255
	94	24	86	92	115	85	144
	104	305	82	83	517	82	2075
Inclination Error, deg	3.300E-01	4.909E-01	-9.748E-02	3.410E-01	7.349E-01	-1.656E-01	1.208E+00
	3.016E-01	5.186E-01	-1.048E-01	3.113E-01	7.186E-01	-2.068E-01	9.968E-01
	-4.691E-03	6.510E-02	-1.210E-01	-3.669E-05	3.577E-03	-2.763E-01	8.306E-02
	-9.163E-03	1.202E-01	-2.069E-01	-3.617E-05	1.029E-02	-4.540E-01	1.746E-01
	-6.262E-01	4.503E-02	-6.499E-01	-6.263E-01	-5.834E-01	-8.521E-01	-5.285E-01
Out-of-Plane ΔV, m/s	30	33	6	31	56	1	86
	30	35	7	30	59	2	76
	6	8	2	5	16	1	28
	6	10	2	5	21	0	36
	47	3	43	47	48	41	63
Total ΔV, m/s	167	151	100	156	298	91	486
	177	172	96	165	314	91	465
	98	35	85	95	131	85	255
	95	25	86	93	117	85	144
	147	306	124	126	556	124	2133
Capture Success	100%	100%	100%	100%	92.4%		
Key	BAM: L/D=0.4	BAM: L/D = 0.5	DFC: L/D=0.4	DFC: L/D=0.5	DMCV: BCR=5		

large increase in apoapsis error for the 99th percentile, max, and min statistics. Regarding the in-plane ΔV cost, all three flight controls provide acceptable results. DFC produces the lowest 99th percentile in-plane cost of 115 m/s. DMCV provides a comparable cost up until the 99th percentile. BAM flight control generally produces more expensive aerocapture trajectories as compared to DFC for the same L/D. Only up to the 1st percentile are the two flight control solutions comparable. This is due to the bank reversals needed for handling

the orbital plane error. Figure 4.32 shows high variance in the inclination error for the BAM vehicles as compared to the DFC vehicles. DFC vehicles produced inclination errors within 0.1° of the 153.547° target leading to diminutive out-of-plane ΔV costs. The BAM reversals allow for the inclination errors to be within 1° of the target leading to a moderate correction cost. Vehicle 5 with no out-of-plane control authority produces a rather large inclination error that requires a moderate correction cost, with a value that is nearly half that of the mean in-plane ΔV cost. The aggregate total ΔV statistics shows that DFC produces the cheapest trajectories over the range of applied dispersions. Increasing L/D for DFC is shown to reduce the total ΔV. The same cannot be said for BAM where increasing L/D slightly increases the total ΔV.

In Figure 4.32, subplots of the max sensed deceleration and estimated vehicle aeroheating environment are presented. For the lifting trajectories, the sensed deceleration generally decreases with shallower entry flight path angles. For the same L/D capability, the DFC vehicles can produce lower peak deceleration values than BAM vehicles. These similar low values can be achieved by Vehicle 5. But, Vehicle 5 produces much lower convective heat rate and integrated heat load values. The data suggests that DMCV can provide a 3 times reduction in the convective heating as compared to the BAM and DFC vehicles, whom both have similar heating values though DFC values are slightly smaller. This reduction can be attributed to the larger aeroshell nose radius and smaller BC achieved during flight. A consequence of larger nose radius is potentially larger radiative heating, which is not modeled in this paper. As a result, a high fidelity aerothermal heating analysis is needed to further quantify this reduction.

Overall, a lifting vehicle with a L/D of 0.4-0.5 is sufficiently robust to the given set of dispersions. Lower ΔV can be achieved with DFC flight control. Despite the lower success rate, DMCV flight control is a potentially viable flight control if close to nominal flight conditions are achieved. If achievable, DMCV may provide a performance enhancement in terms of lower apoapsis error and lower stagnation point convective heating.

Reduced Density Perturbation Case

For the reduced density perturbation case, Case 2, the density perturbation scale factor is reduced by half and the bounds on *Fbias* are reduced by half as well. This reduction might be possible with improved knowledge of Neptune's atmosphere from atmospheric entry probes that enter prior to aerocapture. To simulate the effect that this might have on the aerocapture performance, the parameter *rpscale* is reduced from 1 to 0.5 and *Fbias* is reduced from ±0.56 to ±0.28. Figure 4.33 shows a comparison of the in-plane orbit insertion performance for Cases 1 and 2. As shown in Figure 4.33b, reducing the density perturbations and atmospheric profile range improves the apoapsis targeting performance for each flight control as well as improves the capture success rate for the DMCV vehicle (up to 99.3% from 92.4%). For Case 1, as shown in Figure 4.33a, the uncaptured hyperbolic cases for Vehicle 5 directly correlate to large negative *fbias* values. Reducing the increasing the minimum bound on *fbias* is shown to eliminate a majority of the hyperbolic cases. Like the trends found for Titan, the large negative *fbias* values correspond to lower than average density profiles. An increase in BCR capability might allow for the remainder of hyperbolic trajectories to be captured into orbit.

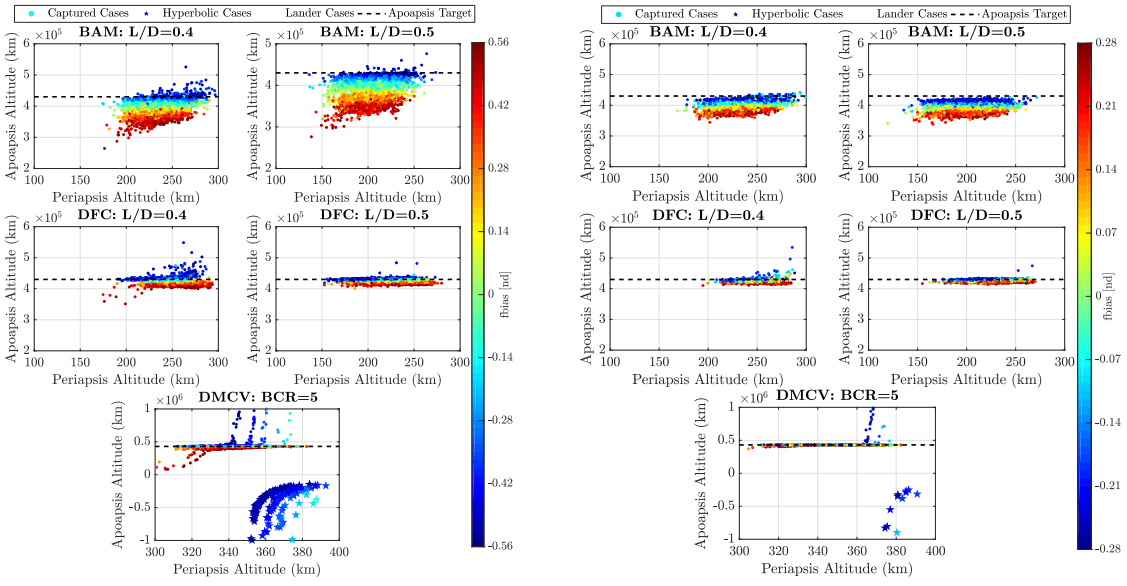

(a) Reference Case (b) Reduced Density Perturbation Case

Figure 4.33. Visualization of the effect that improved Neptune atmospheric knowledge has on in-plane orbit insertion performance. Vertical colorbars map to each subplot in each subfigure.

For Case 2, the aerocapture performance statistics for the captured cases are shown in Table 4.26. As compared to Case 1, no significant changes arise in the max deceleration, peak convective heat rate, and integrated heat load with Case 2. However, the reduced atmospheric profile uncertainty and density perturbations leads to a generous reduction in the total ΔV for both every vehicle with corresponding 99th percentile values of 221 m/s, 238 m/s, 109 m/s, 107 m/s, and 187 m/s. The in-plane ΔV performance for DMCV is on-par if not better than either of the DFC vehicles (lower mean value but larger variance). The out-of-plane cost for each vehicle is generally unaffected by the density perturbation and profile reduction.

Table 4.26. Neptune Reduced Density Perturbation Case: Aerocapture orbit insertion statistics

	Mean	3σ	1st %-tile	Median	99th %-tile	Min	Max
Apoapsis Error x 10^3, km	-30.747	47.746	-64.359	-29.021	-0.552	-85.545	12.247
	-36.849	48.438	-69.570	-35.042	-9.832	-91.890	1.058
	-5.412	15.452	-14.103	-5.793	7.130	-19.646	104.454
	-3.777	11.105	-11.507	-3.620	1.949	-16.148	44.337
	21.550	2223.449	-12.250	-0.055	38.654	-60.282	39502.066
In-plane ΔV, m/s	138	86	90	134	201	85	248
	149	90	101	145	214	87	264
	94	19	85	94	109	85	188
	92	15	85	91	104	85	134
	86	94	82	83	145	82	651
Inclination Error, deg	3.182E-01	3.774E-01	-8.380E-02	3.311E-01	6.164E-01	-1.781E-01	1.042E+00
	3.130E-01	4.437E-01	-9.504E-02	3.255E-01	6.311E-01	-1.238E-01	1.051E+00
	-1.834E-03	3.918E-02	-6.591E-02	1.296E-05	2.818E-03	-1.946E-01	7.254E-02
	-5.168E-03	9.224E-02	-1.641E-01	2.516E-06	5.167E-03	-4.334E-01	1.655E-01
	-6.261E-01	2.989E-02	-6.466E-01	-6.262E-01	-6.026E-01	-6.552E-01	-5.533E-01
Out-of-Plane ΔV, m/s	29	26	7	30	49	1	79
	31	30	8	31	54	4	79
	5	5	2	5	11	1	20
	5	8	2	5	18	1	37
	47	2	45	47	48	41	49
Total ΔV, m/s	159	87	108	156	221	98	252
	171	94	112	168	238	103	327
	95	19	85	94	109	85	188
	92	17	85	92	107	85	134
	129	94	124	125	187	123	689
Capture Success	100%	100%	100%	100%	99.3%		
Key	BAM: L/D=0.4	BAM: L/D = 0.5	DFC: L/D=0.4	DFC: L/D=0.5	DMCV: BCR=5		

Increased Density Perturbation Case

For the increased density perturbation case, Case 3, the density perturbation scale factor is doubled, which increases the applied density perturbation from $\pm 3\sigma$ to $\pm 6\sigma$. Additionally, the latitudinal variation of *fminmax* is removed and replaced with a constant value such that *fminmax* ranges between ± 1. This case is meant to simulate the largest possible density perturbation capability of NeptuneGRAM. Figure 4.34 depicts the in-plane performance comparison between Case 1 and Case 3. As seen in Figure 4.34b, the increase in Case 3 causes an increase in the number of uncaptured hyperbolic trajectories and variance of the

apoapsis targeting for each flight control. These cases generally correlate to *fminmax* values near -1 and shallow entry flight path angles. For BAM and DFC vehicles, an L/D greater than 0.5 is needed to fully capture all the simulated trajectories. Likewise for the DMCV vehicle, a BCR value greater than 5 is needed.

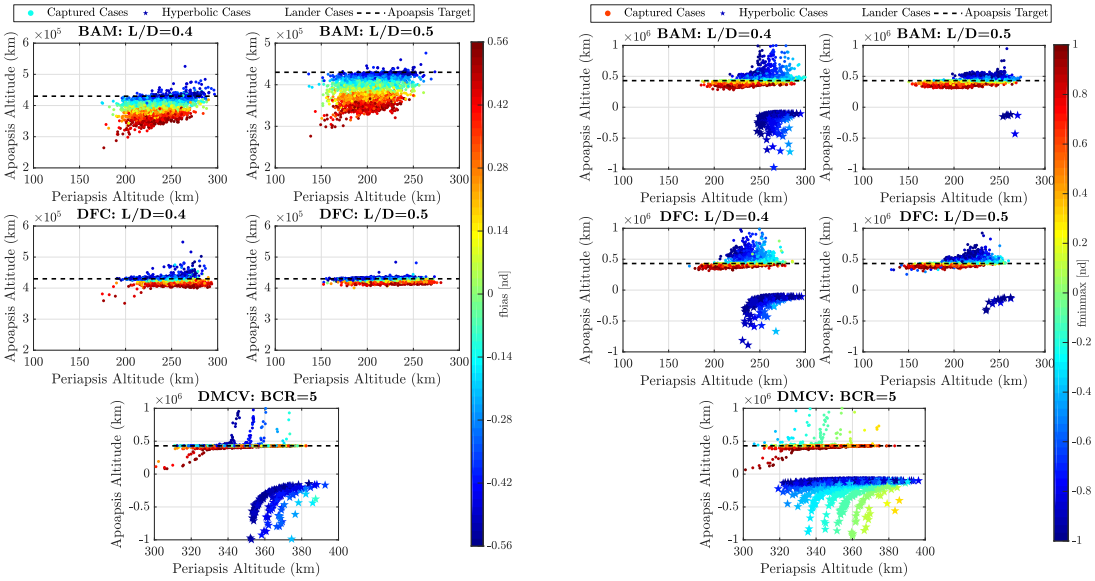

(a) Reference Case

(b) Increased Density Perturbation Case

Figure 4.34. Visualization of the effect that increased Neptune atmospheric uncertainty has on in-plane orbit insertion performance. Vertical colorbars map to each subplot in each subfigure.

For the captured cases in Case 3, Table 4.27 shows the aerocapture orbit insertion statistics. As compared to Case 1, no significant changes arise in the max deceleration, peak convective heat rate, and integrated heat load with Case 3. The low capture success rate of Vehicle 5 may necessitate the need for larger BCR capability. Despite this, the orbit insertion performance of Vehicle 5 on average is as good if not better than the DFC vehicles (lower mean in-plane ΔV value but higher variance). The increase in density perturbations significantly increases the apoapsis error and in-plane ΔV statistics for each vehicle but does not significantly increase the inclination error and out-of-plane ΔV statistics.

Table 4.27. Neptune Increased Density Perturbation Case: Aerocapture orbit insertion statistics

	Mean	3σ	1st %-tile	Median	99th %-tile	Min	Max
Apoapsis Error x 10^3, km	113.621	9461.499	-104.952	-6.478	801.740	-149.423	151205.618
	2.092	1029.745	-106.013	-4.812	121.049	-123.230	17756.747
	49.421	1195.455	-72.946	-1.827	541.290	-115.309	12373.471
	28.358	2105.885	-66.720	0.764	199.927	-175.068	37295.208
	113.070	5762.175	-137.492	-0.190	1817.068	-364.536	71599.483
In-plane ΔV, m/s	159	215	86	144	445	85	657
	148	162	86	135	308	85	643
	145	195	86	125	391	85	637
	133	134	86	121	272	86	651
	118	409	82	83	613	82	2470
Inclination Error, deg	5.271E-01	1.115E+00	-1.086E-01	4.559E-01	1.622E+00	-8.760E-01	2.067E+00
	5.008E-01	9.955E-01	-1.073E-01	4.641E-01	1.442E+00	-2.837E-01	2.427E+00
	-7.660E-03	9.467E-02	-1.535E-01	-1.144E-03	3.450E-02	-4.416E-01	2.234E-01
	-1.149E-02	1.517E-01	-2.563E-01	-1.185E-03	7.994E-02	-5.785E-01	4.003E-01
	-6.261E-01	5.676E-02	-6.621E-01	-6.263E-01	-5.682E-01	-8.999E-01	-5.495E-01
Out-of-Plane ΔV, m/s	43	72	6	38	118	1	149
	42	62	7	41	100	3	180
	8	9	3	7	18	0	35
	8	11	3	8	24	1	45
	47	4	43	47	49	41	67
Total ΔV, m/s	195	238	105	178	503	93	706
	182	170	100	175	340	90	647
	146	196	86	126	391	85	637
	134	134	87	123	273	86	652
	161	410	124	126	652	124	2531
Capture Success	90.9%	99.77%	85.77%	94.67%	53.47%		
Key	BAM: L/D=0.4	BAM: L/D = 0.5	DFC: L/D=0.4	DFC: L/D=0.5	DMCV: BCR=5		

Increased Delivery State Uncertainty Case

For the increased delivery state uncertainty, Case 4, the delivery state uncertainty is increased such that the entry flight path angle uncertainty is increased from $\pm 0.33°$ to $\pm 0.51°$. Figure 4.35 shows the in-plane performance comparison between Case 1 and Case 4. Increase the delivery state uncertainty increases the spread of entry flight path angles as seen by the colorbar limits between Figure 4.35a and Figure 4.35b. This causes for additional hyperbolic cases to arise. For Vehicle 3, three hyperbolic cases arise corresponding to the shallowest entry flight path angle. For the same 0.4 L/D, Vehicle 1 is able to capture these three cases. For 0.5 L/D, both Vehicles 2 and 4 are generally unaffected by the increase in delivery state uncertainty. For Vehicle 5, Case 4 introduces more hyperbolic cases decreasing the capture success rate from 92.4% to 88.2%

For the captured cases in Case 4, Table 4.28 shows the corresponding orbit insertion performance statistics. The increase in delivery state uncertainty does not generally impact the statistics except in the 99th percentile and max values. For Vehicle 5, the 99th percentile in-plane ΔV increases from 517 m/s to 2142 m/s. This significant increase indicates that achieving small delivery state dispersions is most advantageous for DMCV vehicles with low BCR capability.

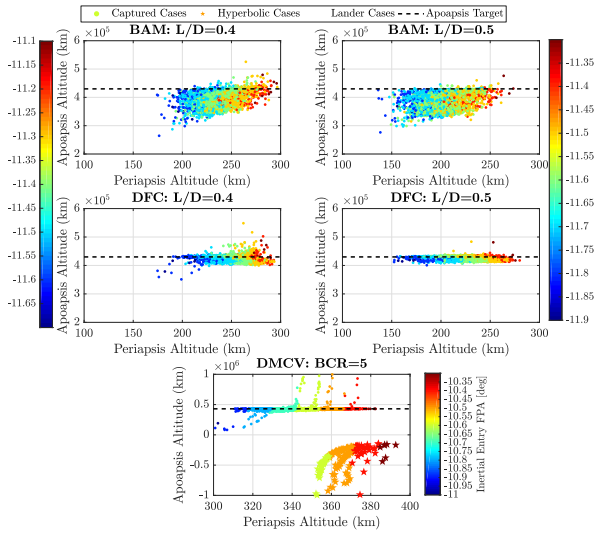

(a) Reference Case

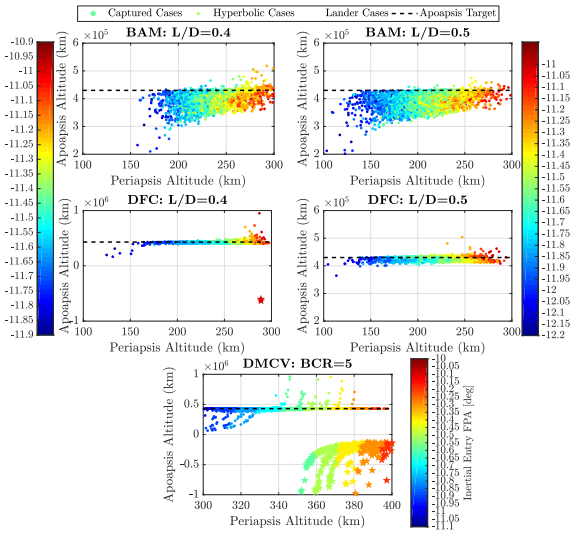

(b) Increased Delivery State Uncertainty Case

Figure 4.35. Visualization of the effect that increased Neptune delivery state uncertainty has on in-plane orbit insertion performance. Left and right vertical colorbars map to 0.4 and 0.5 L/D subplots in each subfigure.

Table 4.28. Neptune Increased Delivery State Uncertainty Case: Aerocapture orbit insertion statistics

	Mean	3σ	1st %-tile	Median	99th %-tile	Min	Max
Apoapsis Error x 10^3, km	-31.977	120.555	-110.313	-28.476	26.597	-269.835	1291.814
	-38.629	110.444	-114.318	-33.521	6.384	-270.360	996.228
	-4.540	81.441	-27.966	-5.831	55.537	-265.085	971.104
	-4.517	20.646	-19.600	-3.825	7.452	-105.376	73.785
	196.426	22366.053	-351.240	-0.128	846.163	-421.761	380122.124
In-plane ΔV, m/s	147	191	85	133	313	84	1053
	158	204	87	143	324	85	1060
	100	95	85	96	164	84	1016
	95	28	85	92	120	85	300
	147	1052	82	84	2142	82	5740
Inclination Error, deg	3.315E-01	6.078E-01	-1.033E-01	3.438E-01	8.835E-01	-1.802E-01	2.328E+00
	2.994E-01	5.841E-01	-1.065E-01	3.202E-01	7.745E-01	-1.506E-01	2.365E+00
	-5.420E-03	7.871E-02	-1.443E-01	-3.728E-05	4.369E-03	-3.858E-01	9.129E-02
	-9.657E-03	1.292E-01	-2.137E-01	-3.264E-05	1.047E-02	-5.540E-01	1.843E-01
	-6.313E-01	1.397E-01	-8.521E-01	-6.263E-01	-5.800E-01	-1.421E+00	-5.400E-01
Out-of-Plane ΔV, m/s	30	41	4	31	66	1	166
	30	41	3	31	63	0	167
	6	9	0	6	17	0	31
	6	12	0	5	22	0	44
	47	10	43	47	64	40	103
Total ΔV, m/s	170	189	97	157	341	90	1055
	179	204	97	165	345	89	1066
	101	95	85	96	167	84	1016
	96	29	85	93	124	85	300
	190	1061	124	127	2200	123	5836
Capture Success	100%	100%	99.9%	100%	88.2%		
Key	BAM: L/D=0.4	BAM: L/D = 0.5	DFC: L/D=0.4	DFC: L/D=0.5	DMCV: BCR=5		

Study Findings

The performance analysis at Neptune has shown for the reference set of uncertainties, DFC can enable a 100% successful science orbit insertion within a 120 m/s total ΔV budget for periapsis raise, apoapsis, and inclination corrections. BAM can enable a 100% successful science orbit insertion with a 300 m/s total ΔV budget. DMCV can enable a 92.4% successful science orbit insertion with a 570 m/s total ΔV budget but at 3 times lower peak stagnation point convective heating than BAM and DFC. Increasing the atmospheric dispersions reduces the capture success for each flight control, with DMCV being impacted the most, while increasing the variance of the orbit insertion targeting error leading to a significant increase in total ΔV. Reduction in atmospheric dispersions can allow for improved orbit insertion performance and capture success for each flight control. Increasing the delivery state error via entry flight path angle increases the 99th percentile total ΔV with most pronounced affect on DMCV. Overall, BAM and DFC flight controls applied to vehicle producing L/D between 0.4-0.5 are found to be sufficiently robust to the various sets of atmospheric, aerodynamic, vehicle attitude, and delivery state dispersions. The best orbit insertion performance and robustness can be achieved with DFC, even for lower L/D vehicles as compared to existing BAM flight control. Despite the lack of sufficient control authority, a DMCV vehicle with a BCR capability of 5.5 is generally robust to the applied dispersions. If lower atmospheric uncertainty and delivery state error are achievable, then DMCV can produce on-par orbit insertion performance as DFC but at potentially much lower aerodynamic heating.

4.2.2 SmallSat-Class Vehicles

The recent decade has seen a surge in the SmallSat vehicle platform. SmallSats are smaller-scaled, lower cost satellite intended to fly as secondary payloads during mission launches. The proliferation of SmallSat missions in low Earth-orbit has both demonstrated the operability of low-cost commercial-off-the-shelf components and the science return augmentation from secondary payloads. The Mars Cube One (MarCO) [120], the first interplanetary SmallSat, demonstrated the capability of utilizing SmallSats on further solar system exploratory missions. NASA's Planetary Science Division in 2016 solicited concept studies

to determine what science missions could be done with SmallSat vehicles [121]. The studies have ranged from orbital studies of Venus upper atmosphere [122] to atmospheric probe delivery to Uranus [123] to orbital flybys of the Martian moons [124].

A key challenge for such interplanetary missions is orbit insertion. Due to the secondary payload fairing constraints, SmallSats are mass and volume constrained and are thus limited on the amount of propellant they can carry. As an example, for a standard Evloved Expendable Launch Vehicle Secondary Payload Adapter (ESPA) secondary payload 5m fairing on a 15" diameter payload port, the maximum port payload mass is 180 kg and maximum payload volume is 24" x 28" x 38" [125]. Note that variants of ESPA may enable slightly larger masses and volumes to be realized. These constraints make propulsive orbit insertion ΔV requirements on the order of a few km/s challenging, if not impossible, at different planetary destinations. As a result, aerocapture can be a potential enabling technology for SmallSat missions by providing the means for payload delivery to orbit within a feasible ΔV budget. Furthermore due to the costs and inherent risks associated with Discovery-class missions, SmallSats may provide a lower-cost alternative to flight-proving aerocapture. Some authors have taken this approach and have developed such aerocapture demonstration mission concepts [48], [49]. Majority of SmallSat aerocapture vehicle designs have employed a form of staged-jettison drag modulation. In this work, a different vehicle design is investigated that can potentially allow for BAM, DFC, and DMCV flight controls.

Vehicle Design

The SmallSat aerocapture system investigated utilizes a deployable aeroshell that stows during launch and is as light weight as possible to maximize the delivered mass to orbit. Deployable aeroshells have the potential to enable the delivery of equivalent scientific payloads with stowed diameters 3 to 4 times smaller than traditional rigid aeroshells [126]. These open backshell designs are either inflated, similar to a ballute, or mechanically deployed, similiar to an umbrella, prior to atmospheric entry. After exiting the atmosphere, the aeroshell is jettisoned and post-aerocapture propulsive burns are conducted.

A deployable vehicle concept that can change its outer mold line offers the opportunity to study three major control strategies for aerocapture: DFC, BAM, and DMCV. For this purpose, a morphable entry system (MES) concept is investigated as the candidate SmallSat aeroshell design [127]. Figure 4.36 depicts the stowed and the baseline deployed configurations of the MES. The system stows into a compact form-factor that adheres with the standard ESPA volume requirements and mechanically deploys into a baseline 70° sphere-cone geometry (note: sphere-cone is a geometrical approximation to the true aeroshell shape). The conical frustrum is made up of six panels that act as aerodynamic control surfaces. They can be actuated through tensioning the six structural ribs. A rigid hemispherical nose attaches to a cylindrical payload fairing that houses the SmallSat vehicle. At the baseline configuration, the sphere-cone has a nose radius of 0.3m, maximum diameter of 1.35m, and has all panels deflected fully at the same angle.

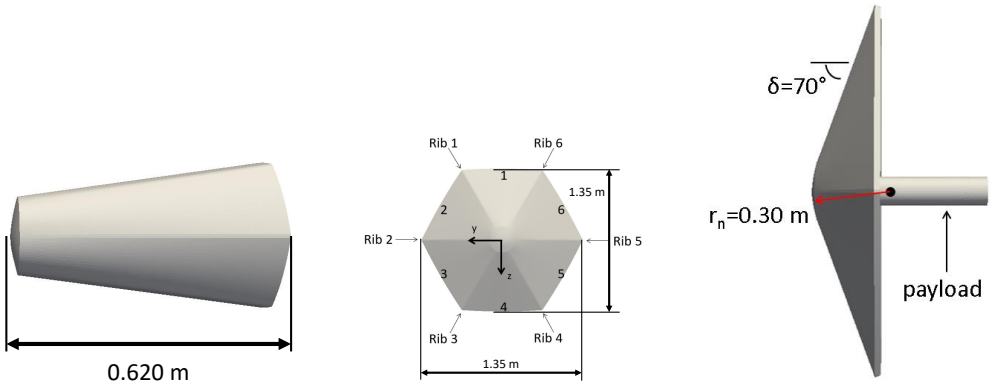

(a) Stowed (b) Deployed Front (c) Deployed Side

Figure 4.36. Stowed and deployed configurations of the morphable entry system.

The deflection angle of each panel can be varied according to the chosen control strategy. For DFC, angle of attack and side-slip angle control can be achieved through panel deflections. Figure 4.37a illustrates a scenario where deflection of panel 1 by δ from the baseline induces a pitching moment for modulating angle of attack. Figure 4.37b shows the scenario of deflecting rib 5 by δ from the baseline induces a yawing motion for modulating side-slip angle. For DMCV symmetrical deflection of the panels by δ, as shown in Figure 4.37d, allows for the cone angle of the morphable sphere-cone to be modified thus allowing for control of the vehicle's ballistic coefficient throughout the trajectory. Lastly as show in Figure 4.37c,

the baseline deployed configuration along with RCS thrusters can allow for control of the bank angle.

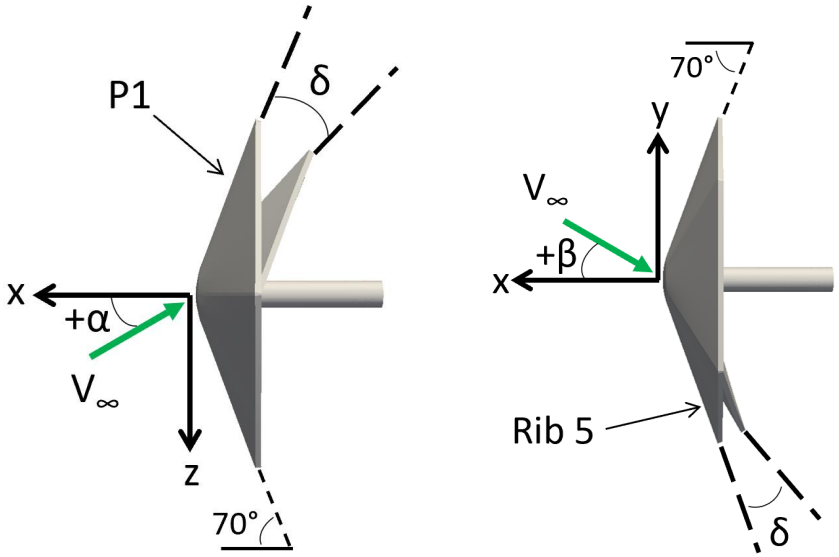

(a) DFC: α modulation

(b) DFC: β modulation

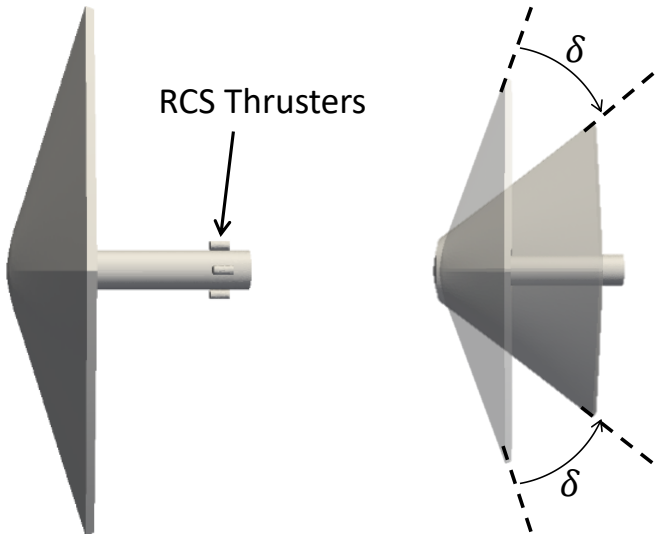

(c) BAM: σ modulation

(d) DMCV: δ_c modulation

Figure 4.37. Aerocapture flight control using the morphable entry system.

This section primarily focuses on assessing the 3DOF aerocapture orbit insertion performance and robustness of the MES vehicle using each flight control technique at different planetary bodies. As a result, some assumptions are made on the vehicle design. Firstly, the thermal protection system is not formally sized due to differences in planetary atmo-

spheres and entry conditions. Rather, the resulting engineering estimates of the aeroheating environment are presented. Higher fidelity models are needed to formally size the TPS. Secondly, the overall aerocapture system mass is assumed to be 180 kg to adhere to ESPA mass requirements. This value allows for a common-ground for each flight control to be compared against. Thirdly, the flight control actuator dynamical response is not modeled in the simulation. Rather, rate and acceleration limits are enforced, similar to the Discovery-Class vehicles analyzed in the previous section. Fourthly, an analytical aerodynamics model, as introduced in Section 2, is assumed. Table I provides a summary of the parameterized SmallSat vehicle design for each flight control assessed at different planetary destinations.

Table 4.29. SmallSat aerocapture flight control vehicle designs

	Vehicle 1	Vehicle 2	Vehicle 3
Flight Control	BAM	DFC	DMCV
Nose Radius, m	0.3	0.3	0.3
Diameter, m	1.35	1.35	1.35 (at CA = 70°)
Control Limits, deg	0 to 180	±16 (±5)[1]	35 to 70
Rate Limit, deg/s	20	5 (2)[a]	5
Accel Limit, deg/s^2	5	2 (0.3)[a]	2
Base BC, kg/m^2	85	85	75
Max L/D	0.25[b]	0.25[b]	0
Max BCR	–	–	5.5[c]

[a] Angle of Attack (Side-Slip Angle)

[b] Value increased for Neptune by increasing trim α (BAM) or α limits (DFC)

[c] Value increased for Venus, Titan, and Neptune by lowering minimum CA limit

Venus

For Venus, the target orbit is a 300 km circular orbit at 90° inclination. For Vehicle 3, the minimum cone angle is decreased from 35° to 20° to increase the BCR capability of the MES vehicle to 20. This increase allows for the vehicle to have a positive flight envelope width and potentially improve the aerocapture orbit insertion performance and success as compared to the Discovery-class DMCV vehicle assessed. The Reference case in Table 4.4 is used in the Monte Carlo experimental setup for each vehicle. The nominal delivery state parameters are shown in Table 4.3. Due to the different base BC and BCR values, the nominal inertial entry flight path angles are recomputed using the corridor width assessment with values of -6.1° for Vehicles 1 and 2 and -6.04° for Vehicle 3.

Reference Case

A visual comparison of the Monte Carlo results are shown in Figure 4.38. For each flight control, 100% of the cases successfully capture. As compared to the Satellite-Class vehicle design results, increasing the BCR capability from 5.5 to 20 allows for the necessary control capability to capture the residual uncaptured cases. Table 4.30 provides a comparison of the simulation statistics.

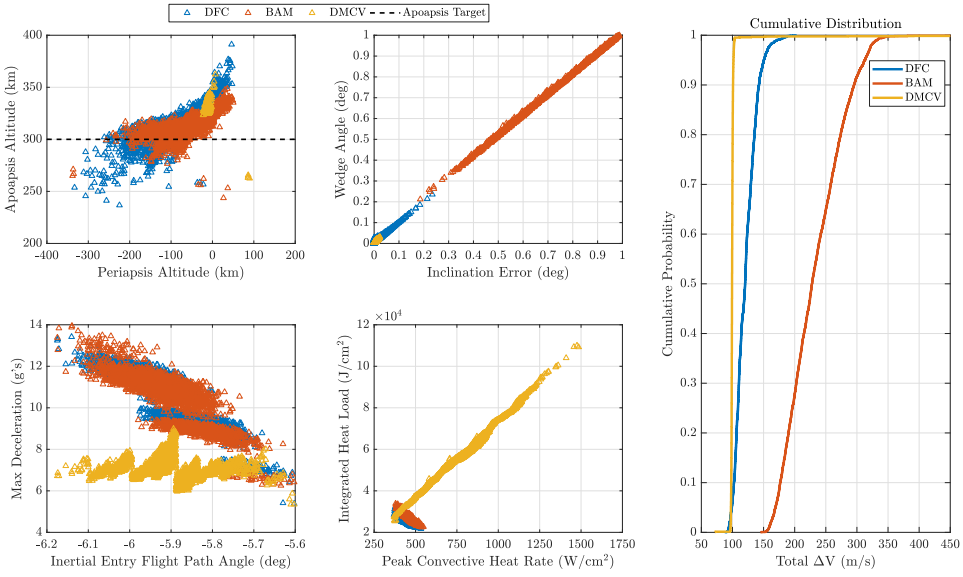

Figure 4.38. Venus SmallSat Case: Aerocapture orbit insertion performance

Table 4.30. Venus SmallSat Case: Aerocapture orbit insertion statistics

	Mean	3σ	1st %-tile	Median	99th %-tile	Min	Max
Apoapsis Error, km	11.511	54.049	-33.659	10.967	55.601	-63.275	349.110
	11.595	31.121	-13.898	11.739	36.597	-56.336	48.650
	36.799	468.544	24.885	29.439	43.327	-37.495	4387.006
In-plane ΔV, m/s	121	49	94	120	171	88	204
	110	41	86	107	146	82	202
	100	90	97	99	102	71	915
Inclination Error, deg	-8.767E-05	5.976E-02	-6.959E-02	1.044E-06	6.835E-02	-1.677E-01	2.345E-01
	9.889E-01	1.058E+00	3.626E-01	9.778E-01	1.649E+00	1.858E-01	5.080E+00
	-5.437E-03	1.844E-02	-1.957E-02	-5.561E-03	8.598E-03	-2.349E-02	1.197E-02
Out-of-Plane ΔV, m/s	2	8	0	1	14	0	32
	143	133	61	142	226	36	655
	1	3	1	1	4	0	5
Total ΔV, m/s	122	50	94	120	172	88	204
	233	144	159	228	332	145	834
	101	90	97	99	103	72	916
Capture Success	100%	100%	100%				
Key	DFC	BAM	DMCV				

The results show that the designed NPC guidance provides sufficient aerocapture performance for each flight control. Vehicle 3 provides excellent in-plane orbit insertion performance with a 99th percentile ΔV of 102 m/s as well as a negligible inclination error and subsequent correction cost. However, the large BCR capability coupled with the large base BC causes Vehicle 3 to achieve much larger peak convective heat rates and integrated heat loads with values nearly triple that of Vehicles 1 and 2. Reducing the BCR capability may allow for lower aeroheating results but at the expense of orbit insertion performance (e.g. Venus Satellite-Class Vehicle 3 results). Increasing the aeroshell nose radius and lowering the base BC can also potentially lower the aeroheating; but, the strict secondary payload stowage requirements may limit achieving this. Unless high-performance flexible TPS materials that can withstand heat rates greater than 1500 W/cm^2 are available, DMCV may not be a preferable flight control option for SmallSat aerocapture at Venus. BAM and DFC can provide potential suitable flight control options for Venus aerocapture. The results show that Vehicles 1 and 2 can provide similar in-plane orbit insertion performance; moreover, Vehicle 2 provides much lower inclination error. This allows for Vehicle 2 to provide 99th percentile orbit insertion total ΔV of 172 m/s, which is approximately half that of the corresponding value for Vehicle 1 being 332 m/s. The aeroheating and sensed deceleration statistics are generally similar between each vehicle. With peak convective heat rate values near 600 W/cm^2, newer flexible TPS material are needed for a Venus SmallSat mission. Such a material might be a 3-D woven carbon fabric similar to what is developed for ADEPT [128].

Earth

The Earth aerocapture study analyzes an Earth-return mission concept. The target orbit is a 500 km circular orbit at 30° inclination. Given the corridor width analysis for each vehicle, the nominal inertial entry flight path angles for each vehicle are -5.581° for Vehicles 1 and 2 and -5.643° for Vehicle 3. The nominal delivery state parameters are shown in Table 4.31. The delivery state dispersions are produced from position and velocity errors propagated from the data cut-off point of 6 hours prior to entry such that the $\pm 3\sigma$ uncertainty in inertial entry flight path angle is 0.25° [129].

Table 4.31. Monte Carlo simulated dispersions for Earth aerocapture

Category	Variable	Nominal	$\pm 3\sigma$ or min/max	Distribution
Delivery State	Inertial entry flight path angle	-5.581° or -5.643°	From propagation	Correlated
	Inertial entry velocity	11.5 km/s	From propagation	Correlated
	Inertial entry altitude	125 km	From propagation	Correlated
	Inertial entry latitude	-5.186°	From propagation	Correlated
	Inertial entry longitude	350.955°	From propagation	Correlated
	Inertial entry heading angle	-29.589°	From propagation	Correlated

Reference Case

A visual comparison of the Monte Carlo results are shown in Figure 4.39. For each flight control, 100% of the cases successfully capture. Table 4.32 provides a comparison of the simulation statistics.

Table 4.32. Earth SmallSat Case: Aerocapture orbit insertion statistics

	Mean	3σ	1st %-tile	Median	99th %-tile	Min	Max
Apoapsis Error, km	-12.938	27.707	-42.319	-11.489	5.437	-70.132	19.311
	-28.113	32.888	-57.651	-26.762	-7.808	-78.682	0.709
	-1.109	2.488	-4.111	-0.979	0.279	-9.416	0.516
In-plane ΔV, m/s	154	29	134	154	178	128	191
	155	23	137	155	174	133	183
	138	2	136	138	140	136	143
Inclination Error, deg	-6.207E-03	7.043E-02	-1.162E-01	-4.457E-04	2.320E-02	-2.217E-01	1.341E-01
	5.391E-01	5.325E-01	2.022E-01	5.225E-01	8.842E-01	1.042E-02	9.800E-01
	-5.447E-01	1.574E-02	-5.569E-01	-5.447E-01	-5.323E-01	-5.629E-01	-5.284E-01
Out-of-Plane ΔV, m/s	2	10	0	1	18	0	32
	97	72	49	95	145	24	159
	75	4	72	75	78	71	79
Total ΔV, m/s	155	30	134	154	181	129	202
	227	70	185	225	275	155	294
	210	3	208	210	213	207	215
Capture Success	100%	100%	100%				
Key	DFC	BAM	DMCV				

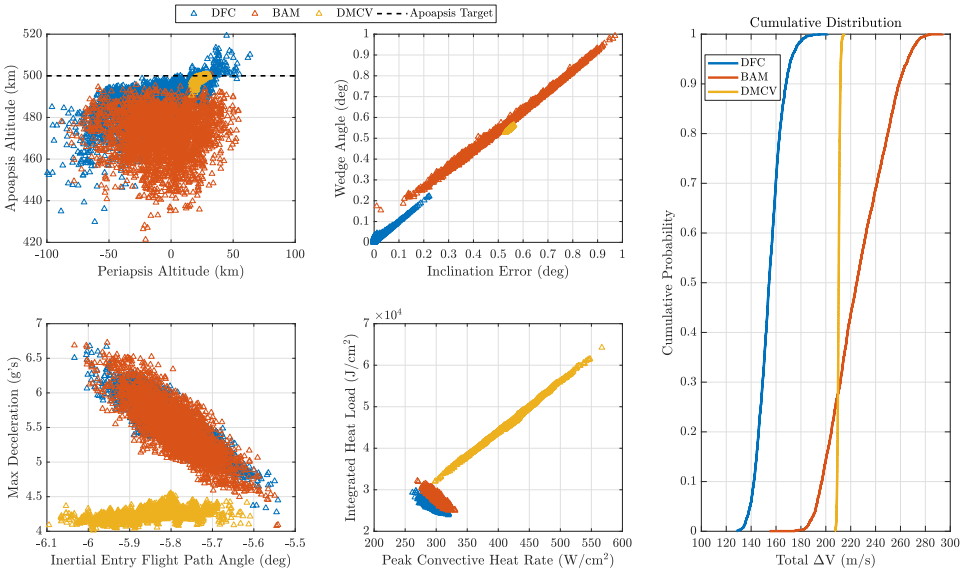

Figure 4.39. Earth SmallSat Case: Aerocapture orbit insertion performance

The results show that the designed NPC guidance provides sufficient aerocapture performance for each flight control. Vehicle 3 provides the most accurate and precise in-plane orbit insertion performance with a 99th percentile ΔV of 140 m/s. Despite the inclination error being small, resulting out-of-plane correction burn is significant being nearly half the value of the in-plane burn ΔV. Similar to Venus, Vehicle 3 produces larger convective heat rates and integrated heat load values than Vehicles 1 and 2. The peak heat rate values for Vehicle 3 at Earth are similar to peak values for Vehicles 1 and 2 at Venus indicating similar TPS material might be needed; but, the larger integrated heat loads experienced at Earth may necessitate increased TPS thickness. For Vehicles 1 and 2 at Earth, similar in-plane orbit insertion performance is achieved with 99th percentile in-plane ΔV costs within 180 m/s. Despite keeping inclination to within 1° of the target, the resulting correction cost for Vehicle 1 is significant. This results in Vehicle 2 producing the lowest total ΔV cost out of the three vehicle designs. Vehicles 1 and 2 have similar peak convective heating and integrated heat loads. As compared to Venus, the integrated heat loads between the two vehicle designs are similar but the the convective heat rate values at Earth are approx. 1.5 times smaller than those at Venus. Despite Earth and Venus having similar gravity wells, the peak deceleration experienced by each vehicle design is distinct. For the same L/D and base BC, Vehicles 1

and 2 at Earth exhibit about half the peak deceleration as the same vehicle applied at Venus, despite having identical nominal entry velocities. This can be attributed to the low density scale height of Venus as well as the slightly steeper nominal entry flight path angles.

Mars

For Mars, the target orbit is a 400 km circular orbit at 0° inclination. The Reference case in Table 4.11 is used in the Monte Carlo experimental setup for each vehicle. The nominal delivery state parameters are shown in Table 4.10. Due to the different base BC values, the nominal inertial entry flight path angles are recomputed using the corridor width assessment with values of -10.85° for Vehicles 1 and 2 and -10.829° for Vehicle 3.

Reference Case

A visual comparison of the Monte Carlo results are shown in Figure 4.40. For each flight control, 100% of the cases successfully capture. Table 4.33 provides a comparison of the simulation statistics.

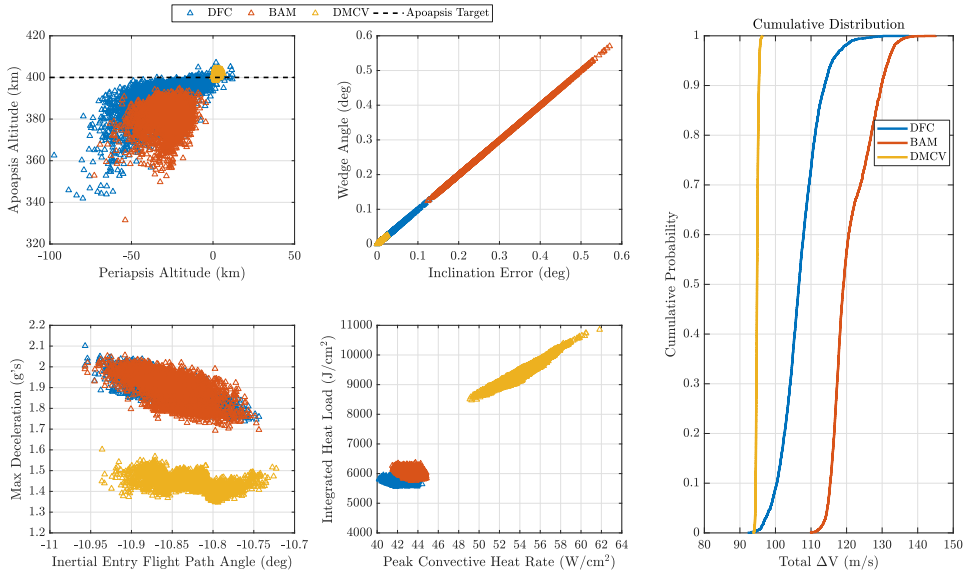

Figure 4.40. Mars SmallSat Case: Aerocapture orbit insertion performance

The results show that the designed NPC guidance provides sufficient aerocapture performance for each flight control. Vehicle 3 provides the most precise and accurate in-plane orbit insertion performance with a 99th percentile ΔV of 95 m/s. The minute residual in-

Table 4.33. Mars SmallSat Case: Aerocapture orbit insertion statistics

	Mean	3σ	1st %-tile	Median	99th %-tile	Min	Max
Apoapsis Error, km	-10.862	24.780	-40.212	-8.853	0.680	-58.106	7.152
	-19.030	19.411	-40.152	-18.160	-8.342	-68.530	-5.224
	1.560	3.746	-0.976	1.270	4.080	-1.474	4.361
In-plane ΔV, m/s	106	16	95	105	120	92	130
	106	9	101	106	115	99	124
	94	1	94	94	95	94	95
Inclination Error, deg	2.137E-02	6.380E-02	7.912E-04	1.610E-02	1.080E-01	0.000E+00	2.454E-01
	2.556E-01	2.701E-01	1.446E-01	2.241E-01	5.047E-01	1.241E-01	5.702E-01
	7.472E-03	1.304E-02	8.414E-04	6.663E-03	1.999E-02	0.000E+00	2.508E-02
Out-of-Plane ΔV, m/s	1	4	0	1	6	0	14
	15	16	8	13	30	7	33
	0	1	0	0	1	0	1
Total ΔV, m/s	107	16	96	107	121	92	138
	121	17	113	119	135	110	145
	95	1	94	95	96	94	96
Capture Success	100%	100%	100%				
Key	DFC	BAM	DMCV				

clination error and corresponding out-of-plane ΔV enables Vehicle 3 to produce the lowest 99th percentile total ΔV cost. Despite increasing the BC during flight, Vehicle 3 produces slightly higher peak convective heat rates and integrated heat loads as well as lower peak decelerations than Vehicles 1 and 2. Vehicles 1 and 2 produce similar in-plane performance with 99th percentile in-plane ΔV of less than 120 m/s. Vehicle 2 provides excellent out-of-plane performance as compared to Vehicle 1. Overall, each flight control provides suitable orbit insertion capability with aeroheating environments that are well within the current acceptable limits for flexible TPS material.

Titan

For Titan, the target orbit is a 1700 km circular orbit at 100° inclination. For Vehicle 3, the minimum cone angle is decreased from 35° to 20° to increase the BCR capability of the MES vehicle to 20. This increase allows for the vehicle to have a positive flight envelope width and potentially improve the aerocapture orbit insertion performance and success as compared to the Discovery-class DMCV vehicle assessed. The Reference case in Table 4.17 is used in the Monte Carlo experimental setup for each vehicle. The nominal delivery state parameters are shown in Table 4.16. Due to the different base BC and BCR values, the nominal inertial entry flight path angles are recomputed using the corridor width assessment with values of -35.678° for Vehicles 1 and 2 and -36.523° for Vehicle 3.

Reference Case

A visual comparison of the Monte Carlo results are shown in Figure 4.41. For each flight control, 100% of the cases successfully capture. As compared to the Satellite-Class vehicle design results, increasing the BCR capability from 5.5 to 20 allows for the necessary control capability to capture the residual uncaptured cases. Table 4.34 provides a comparison of the simulation statistics.

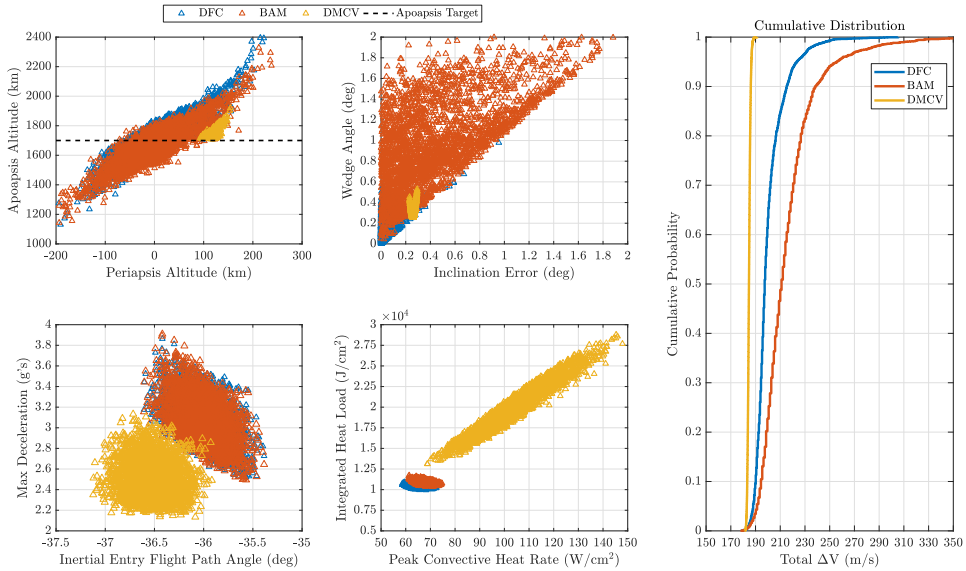

Figure 4.41. Titan SmallSat Case: Aerocapture orbit insertion performance

Table 4.34. Titan SmallSat Case: Aerocapture orbit insertion statistics

	Mean	3σ	1st %-tile	Median	99th %-tile	Min	Max
Apoapsis Error, km	7.851	386.566	-327.055	-2.391	391.693	-639.540	745.591
	-38.075	418.743	-382.320	-46.508	339.706	-684.621	791.525
	37.880	62.428	12.835	34.006	122.394	7.491	220.189
In-plane ΔV, m/s	200	36	184	197	246	179	305
	203	49	181	199	258	172	331
	178	3	176	178	181	175	185
Inclination Error, deg	1.634E-03	1.611E-01	-2.212E-01	3.557E-03	1.511E-01	-6.459E-01	9.548E-01
	2.927E-01	2.037E+00	-8.628E-01	1.718E-01	2.684E+00	-1.444E+00	6.267E+00
	-2.619E-01	3.248E-02	-2.867E-01	-2.620E-01	-2.372E-01	-2.935E-01	-2.310E-01
Out-of-Plane ΔV, m/s	4	9	0	3	14	0	30
	33	54	5	31	97	1	185
	10	7	7	9	16	7	19
Total ΔV, m/s	201	36	185	198	246	179	306
	229	65	199	225	318	186	492
	185	3	182	185	188	181	191
Capture Success	100%	100%	100%				
Key	DFC	BAM	DMCV				

The results show that the designed NPC guidance provides sufficient aerocapture performance for each flight control. Vehicle 3 provides more precise and accurate in-plane orbit insertion performance with a 99th percentile ΔV of 181 m/s. Due to the small gravity well of Titan, the small residual inclination error produced by Vehicle 3 requires a minute correction ΔV. Similar to Venus, the increased BCR capability causes an increase in the peak convective heat rate and integrated heat load. The corresponding values for Vehicle 3 are approx. double the values for Vehicles 1 and 2. The resulting aeroheating environment for each vehicle at Titan is larger but comparable to Mars. Similar peak deceleration values between Vehicles 1 and 2 are achieved. Both vehicles exhibit similar in-plane performance with 99th percentile in-plane ΔV within 260 m/s. The variance in the apoapsis error for Vehicles 1 and 2 are more than 6 times larger than the value for Vehicle 3. Vehicle 2 exhibits better out-of-plane performance than Vehicle 1 as seen by the mean and variance statistics. Overall, each flight control provides suitable orbit insertion capability with aeroheating environments that are generally within the current acceptable limits for flexible TPS material.

Neptune

For Neptune, the target orbit is a 3986 x 430000 km elliptical orbit at 153° inclination. For Vehicle 3, the minimum cone angle is decreased from 35° to 20° to increase the BCR capability of the MES vehicle to 20. This increase allows for the vehicle to have a positive flight envelope width and potentially improve the aerocapture orbit insertion performance and success as compared to the Discovery-class DMCV vehicle assessed. The Reference case in Table 4.24 is used in the Monte Carlo experimental setup for each vehicle. The nominal delivery state parameters are shown in Table 4.23. Due to the different base BC and BCR values, the nominal inertial entry flight path angles are recomputed using the corridor width assessment with values of -11.474° for Vehicles 1 and 2 and -11.504° for Vehicle 3.

Reference Case

A visual comparison of the Monte Carlo results are shown in Figure 4.41. For each flight control, 100% of the cases successfully capture. As compared to the Satellite-Class vehicle design results, increasing the BCR capability from 5.5 to 20 allows for the necessary control

capability to capture the residual uncaptured cases. Table 4.34 provides a comparison of the simulation statistics.

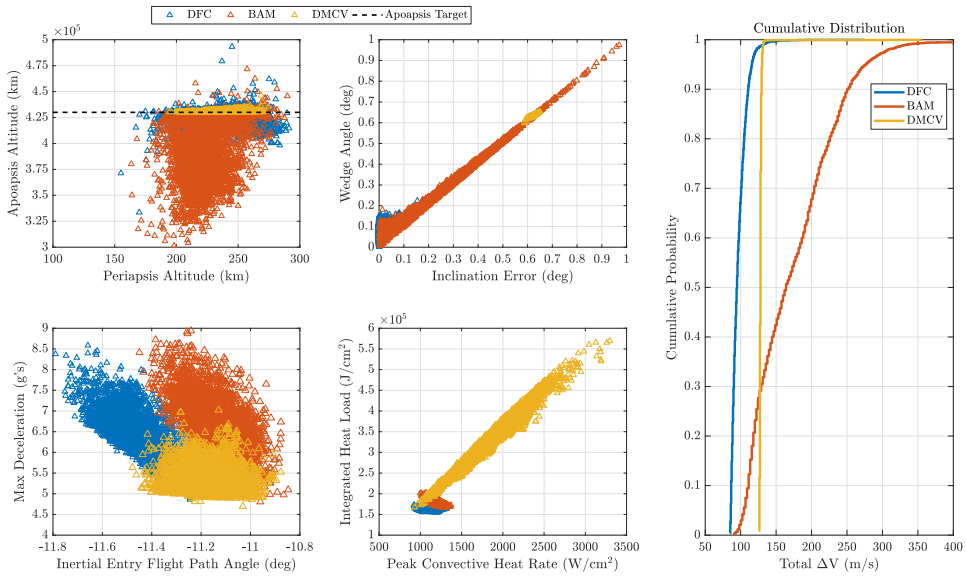

Figure 4.42. Neptune SmallSat Case: Aerocapture orbit insertion performance

Table 4.35. Neptune SmallSat Case: Aerocapture orbit insertion statistics

	Mean	3σ	1st %-tile	Median	99th %-tile	Min	Max
Apoapsis Error x 10^3, km	-6.086	24.178	-26.099	-5.561	8.949	-96.440	94.531
	-39.005	92.988	-112.552	-35.783	3.854	-224.946	41.687
	0.895	21.521	-0.019	0.476	4.086	-0.149	322.606
In-plane ΔV, m/s	97	32	86	94	130	85	275
	156	184	85	146	315	85	748
	86	16	85	86	90	85	317
Inclination Error, deg	-7.112E-03	9.820E-02	-1.679E-01	-3.753E-05	5.276E-03	-4.641E-01	1.186E-01
	2.773E-01	5.545E-01	-1.126E-01	2.968E-01	7.126E-01	-1.823E-01	1.322E+00
	-6.213E-01	2.744E-02	-6.414E-01	-6.212E-01	-6.004E-01	-6.502E-01	-5.872E-01
Out-of-Plane ΔV, m/s	6	9	1	5	18	0	39
	26	36	3	26	55	1	96
	50	2	49	50	52	47	53
Total ΔV, m/s	98	33	86	95	132	85	275
	176	183	97	165	336	89	750
	128	16	126	128	132	126	357
Capture Success	100%	100%	100%				
Key	DFC	BAM	DMCV				

The results show that the designed NPC guidance provides sufficient aerocapture performance for each flight control. Vehicle 3 provides excellent in-plane orbit insertion performance with a 99th percentile ΔV of 90 m/s. As compared to Vehicle 5 in Satellite-Class Neptune reference study, the increase in BCR capability from 5.5 to 20 enables a significant enhancement in the in-plane orbit insertion performance that produced a 99th percentile

ΔV of 517 m/s. Despite having a small residual inclination error, the resulting correction cost for Vehicle 3 is significant being nearly half the value of the in-plane ΔV. For the same L/D capability, Vehicles 1 and 2 have varying levels of orbit insertion performance. Vehicle 2 is more precise in apoapsis targeting allowing for a 99th percentile in-plane ΔV of 130 m/s, which is 185 m/s lower than the corresponding value for Vehicle 2. Likewise, Vehicle 2 produces superior inclination performance as compared to Vehicle 1. The peak decelerations are similar between each vehicle. The aeroheating is also generally comparable for each vehicle but Vehicle 3 produces significantly higher results with more than double the peak convective heat rate and integrated heat load.

The aeroheating environment experienced during Neptune aerocapture is the largest out of the planetary destinations simulated with peak convective heat rates reaching as high as 3250 W/cm^2, which is double the value of the second highest environment being Venus. As a result, a new high performance flexible TPS material would be needed. A potential candidate system is the Heatshield for Extreme Entry Environment Technology (HEEET), which is currently being investigated for application on Ice Giant missions [130]. Although the resulting TPS mass might exceed the maximum weight of the entire SmallSat, the results presented in this section can provide insights into the flight control design trade space. Given a similar Monte Carlo simulation environment, the results show DFC and BAM flight controls are suitable for blunt bodies producing L/D of 0.4 and DMCV flight control is suitable for blunt bodies producing BCR near 20. If similar BC on a larger-scale vehicle can be achieved, then the results presented in Table 4.35 may provide a suitable representation on the anticipated aerocapture performance.

4.2.3 Comparison to Fully-Propulsive Orbit Insertion and Propellant Sizing

Fully-propulsive orbit insertion ΔV costs are computed for each targeted planetary destination. The calculations assume the same hyperbolic excess velocity as the aerocapture entry trajectories. These V_∞ values are computed using the inertial entry velocities and altitudes. The inbound hyperbolic trajectories are assumed to have the same inclination and perigee as the targeted orbit, but do not enter the atmosphere of each planet. The fully-propulsive burn calculations assume a single impulsive in-plane burn at perigee to achieve the desired orbit apogee.

Table 4.36. Orbit Insertion ΔV Comparison. Values in parenthesis are SmallSat-Class vehicle results.

Planet	Aerocapture, m/s			Fully-Propulsive, m/s	Savings, m/s
Venus	182 (172)	234 (332)	1716 (103)	3988	3806 (3885)
Earth	— (181)	— (275)	— (213)	— (3593)	— (3412)
Mars	108 (121)	138 (135)	92 (96)	1994	1902 (3412)
Titan	248 (246)	344 (318)	186 (188)	4987	4801 (1898)
Neptune	131[a](132)	298[a](336)	556 (132)	6884	6753 (6752)
Key	DFC	BAM	DMCV		

[a] L/D = 0.4 Vehicle Design

Table 4.36 provides a comparison between the 99th percentile total ΔV results for the Discovery-Class and SmallSat-Class vehicles and fully-propulsive calculations at each destination. The table also shows the maximum amount of ΔV savings achievable with aerocapture. For each destination, at least 1 km/s of orbit insertion ΔV can be saved using aerocapture. Although fully-propulsive ΔV cost can be potentially reduced through interplanetary trajectory optimization, the results are not expected to significantly change.

The computations of propulsive ΔV costs for aerocapture and fully-propulsive orbit insertion can be translated to propellant mass using the ideal rocket equation as shown in Eq. 4.2. Using the conservation of momentum, the change in velocity is influenced by the specific impulse, I_{sp}, of the propulsion system, Earth sea-level gravitational acceleration, g_0, wet mass of entry vehicle, m_0, and dry mass of entry vehicle, m_f.

$$\Delta V = I_{sp} g_0 \ln \frac{m_0}{m_f} \tag{4.2}$$

The propellant mass is simply the difference between the wet and dry masses. Eq. 4.2 can be re-arraigned to obtain an expression for the propellant mass, m_p, as shown in Eq. 4.3. For both the Discovery-Class and SmallSat-class vehicles, a hydrazine chemical propulsion system is assumed producing an I_{sp} of 200 sec.

$$m_p = m_0(1 - \exp\frac{-\Delta V}{I_{sp}g_0}) \tag{4.3}$$

Table 4.37. Propellant Comparison. Values in parenthesis are SmallSat-Class vehicle results.

Planet	Wet Mass, kg	Aerocapture, kg			Fully-Propulsive, kg	Savings, kg
Venus	1500 (180)	133 (15)	169 (28)	874 (9)	1304 (156)	1171 (147)
Earth	— (180)	— (16)	— (24)	— (19)	— (151)	— (135)
Mars	1500 (180)	80 (11)	102 (12)	69 (9)	957 (115)	889 (106)
Titan	1500 (180)	178 (21)	241 (27)	136 (16)	1382 (166)	1246 (149)
Neptune	2200 (180)	142[a] (12)	310[a] (28)	543 (12)	2134 (175)	1992 (163)
Key		DFC	BAM	DMCV		

[a] L/D = 0.4 Vehicle Design

Table 4.37 provides a comparison between the propellant mass calculations for aerocapture and fully-propulsive orbit insertion. The table also shows the maximum amount of propellant mass savings achievable with aerocapture for SmallSat-Class and Discovery-Class vehicle analyzed. At each destination, aerocapture can substantially reduce the propellant mass requirements need for orbit insertion. For Discovery-Class vehicles, fully-propulsive missions may require nearly all of the vehicle wet mass to be allocated to propellant. This leads to a significant reduction in the delivered mass-to-orbit to the extent where the same satellite payload assumed cannot be delivered to orbit without increasing the wet mass of the vehicle. On the contrary, Discovery-Class aerocapture vehicles requires much smaller amount of propellant mass that are sufficient, given TPS mass allocations, to enable the assumed satellite payload mass to be delivered to orbit at each destination. The propellant mass allocations with respect to the entry mass for Venus, Mars, Titan, and Neptune can be as low as 9%, 5%, 9%, and 6%, respectively.

For SmallSat-class vehicles, Table 4.37 demonstrates aerocapture to be an enabling technology. Without the capability to substantially increase vehicle wet mass, a fully propulsive mission may require nearly all of the vehicle wet mass to be allocated to propellant thereby

reducing the science payload mass delivered to orbit. On the contrary, the aerocapture vehicles analyzed at Venus, Earth, Mars, Titan, and Neptune can have propellant mass allocations with respect to the entry mass as low as 5%, 9%, 5%, 9%, and 7%, respectively. Given TPS mass allocation, it is expected that a generously sized payload mass delivered to orbit is attainable.

5. CONCLUSION

5.1 Summary

Aerocapture has the potential to enable future science missions and increase the payload delivered to orbit across the Solar System and beyond. In preparation for flight implementation, investments in vehicle guidance, navigation, and control might be needed. This dissertation has advanced the current state-of-the-art in the field of aerocapture GNC through the formulation of ΔV-minimizing flight control laws, development of a modular numerical predictor-corrector guidance architecture, and production of numerical simulation results for aerocapture trajectories at a variety of planetary destinations.

Designing flight controls laws that minimize post-aerocapture propulsive ΔV cost can allow for a significant performance advantage over existing methods. Lower costs can reduce propellant mass requirements that could otherwise be used for additional science payload mass. To ascertain these flight control laws for bank angle, direct force control, and drag modulation, optimal control theory is applied. Numerical solutions exhibit a common "bang-bang" structure where the control input switch from one control limit to the other.

Achieving each optimal control solution is computationally expensive. Rather, an unified NPC algorithm incorporating the "bang-bang" structure can allow for similar ΔV costs at a fraction of the computational cost. The algorithm is integrated into a closed-loop guidance architecture to enable numerical simulation studies of aerocapture trajectories for a variety of vehicle configurations, flight controls, and planetary destinations in a unified approach. A series of Monte Carlo simulation studies are conducted to assess aerocapture performance and robustness of Discovery-class and SmallSat-class vehicle designs. The results from these studies have shown a destination-dependence.

The lifting flight controls, BAM and DFC, are shown to be suitable flight controls for blunt bodies at each planetary destination analyzed. At Venus, Earth, Mars, and Titan, having a L/D of 0.25 with either flight control is sufficient for 100% capture success of the reference set of dispersions while an L/D of at least 0.4 is needed for Neptune. Increasing the delivery state error and increasing the atmospheric density uncertainty is shown to have the most pronounced effect on slightly reducing the capture success rate at Titan

and Neptune. With regards to orbit insertion performance, DFC is shown to provide a performance enhancement over BAM at each destination, especially in the out-of-plane and high trajectory perturbation environments. This enhancement is at no expensive to peak deceleration and aerodynamic heating environments as similar values are achieved with both flight controls.

The ballistic flight control, DMCV, is shown to also be suitable for morphable blunt bodies at each planetary destination analyzed. Achieving 100% capture success is found to be highly dependent on the BCR capability of the vehicle. In order to house large satellite payloads, a large nose radius is required thereby limiting the BCR to 5.5. This allowed for DMCV to provide for a reduction in the aerodynamic heating environment as compared to lifting flight controls at each destination analyzed. Moreover, having a BCR of 5.5 is shown to achieve 100% capture success at Mars and Earth only. For Venus, Titan, and Neptune, greater than 90% capture success can be achieved for the corresponding reference set of dispersions. The limited controllability is shown to adversely affect orbit insertion performance at Venus and Neptune with large 99th percentile total ΔV costs. Reducing the atmospheric density and delivery state uncertainties are identified as potential ways to improve both capture success and orbit insertion performance. Alternatively, increasing the BCR capability to 20 is shown to achieve this feat for the reference set of dispersions. For SmallSat payloads, a much smaller nose radius is needed therby allowing for a BCR of 20 to be achievable but at the expense of increasing rather than decreasing aerodynamic heating environment. Consequently, DMCV flight control employed on morphable sphere-cone geometries exhibits a trade-off between BCR capability and aerodynamic heating reduction.

A first-order propellant mass sizing is conducted to correlate aerocapture and fully-propulsive mission ΔV requirements to propellant mass. Aerocapture is demonstrated to provide a significant reduction in orbit insertion propellant mass, on the order of 1000 kg, for Discovery-Class vehicles thereby increasing the payload mass delivered to orbit for the same vehicle wet mass. For mass constrained SmallSat-Class vehicles, fully-propulsive orbit insertion may require at least 60% of the wet mass allocated to propellant. Aerocapture can reduce this allocation to less than 10%.

5.2 Direction of Future Work

This dissertation has identified a few directions for future work. Several limitations of the current approach along with suggestions for how they can be mitigated are described below.

Perfect Navigation Assumption

In the current work, a perfect navigation assumption is made in the uncertainty estimator of the NPC guidance architecture. This assumption is made due to the lack of in-flight navigation sensor specifications, including FADS and IMUs. The implication of this assumption is that the full time history of the truth model each guidance cycle is known by the uncertainty estimator in the calculations of the update gains. In actual flight implementation, the in-flight navigation sensors would provide the in-situ measurements of the truth model accelerations. Sensor noise can potentially introduce measurement error and subsequently influence the gain calculations. To address this, in-flight navigation sensors can be integrated into the closed-loop guidance architecture and subsequent Monte Carlo simulation studies can be conducted to assess their affect on the aerocapture performance.

Aeroshell Geometries Beyond Sphere-Cones

In the current work, rigid and morphable sphere-cone aeroshell geometries are investigated for lifting and ballistic flight control. Newtonian flow theory is employed on the geometries for obtaining analytical aerodynamics solutions. Despite sphere-cones having significant EDL heritage, other aeroshell geometries can also be potentially utilized for aerocapture applications. Biconic and ellipsled geometries can provide higher L/D capability than sphere-cones therby potentially allowing for larger corridor width margin and improved orbit insertion performance. Using a similar methodology, analytical aerodynamics models can be developed for these new geometries and integrated into the NPC guidance architecture. Although sphere-cones are shown in this work to be sufficient for each flight control at each destination, conducting similar Monte Carlo simulation studies may provide further

insight into the potential advantages/disadvantages other aeroshell geometries might have performance-wise.

Additional Planetary Destinations

In the current work, potential aerocapture destinations studies include Venus, Earth, Mars, Titan, and Neptune. Additional planetary bodies with an atmosphere, such as Jupiter, Saturn, and Uranus, can also be viable destinations. The modular framework of NPC guidance architecture allows for such destinations to be readily simulated in future work.

6 DOF Simulation Studies

The current work presents results for 3DOF aerocapture trajectories. The rotational dynamics of the vehicle (equations of motion can be found in Chapter 2), flight actuator dynamics, and subsequent coupling to the kinematic dynamic are omitted. Due to the dependence of the rotational dynamics to the specific vehicle inertia properties and flight actuator models, a 3DOF approach is assumed. As a compromise, a simple control command limiter is developed and integrated into the architecture to emulate the time response of the flight actuators in achieving the NPC control commands each guidance cycle. The idea of the approach taken in the current work is to present the trajectory-based aerocapture results to provide insight into the orbit insertion performance and robustness. Given the data and results produced in Chapter 4, future work can expand using detailed vehicle models for ascertaining the 6DOF aerocapture performance.

REFERENCES

[1] H. London, "Change of satellite orbit plane by aerodynamic maneuvering," *Journal of the Aerospace Sciences*, vol. 29, no. 1, pp. 323–332, 1962.

[2] G. Walberg, "A survey of aeroassisted orbit transfer," *Journal of Spacecraft and Rockets*, vol. 22, no. 1, pp. 3–18, 1985, ISSN: 00224650.

[3] E. Repic, M. Boobar, and F. Chapel, "Aerobraking as a potential planetary capture mode," *Journal of Spacecraft and Rockets*, vol. 5, no. 8, pp. 921–926, 1968, ISSN: 00224650.

[4] J. H. Lichtenstein, "Some considerations on the use of atmospheric braking for a transfer into a martin orbit," National Aeronautics and Space Administration, Technical Note NASA TN D-2837, 1965.

[5] M. Cruz, "The aerocapture vehicle mission design concept-aerodynamically controlled capture of payload into mars orbit," in *Conference on Advanced Technology for Future Space Systems*, 1979. DOI: AIAA79-0893. [Online]. Available: https://doi.org/10.2514/6.1979-893.

[6] D. Spencer and R. Tolson, "Aerobraking cost and risk decisions," eng, *Journal of Spacecraft and Rockets*, vol. 44, no. 6, pp. 1285–1293, 2007. DOI: https://doi.org/10.2514/1.24303.

[7] T. Percy, E. Bright, and T. A.O., "Assessing the relative risk of aerocapture using probabilistic risk assessment," in *41st AIAA/ASME/SAE/ASEE Joint Propulsion Conference and Exhibit*, 2005. DOI: AIAA2005-4107. [Online]. Available: https://doi.org/10.2514/6.2005-4107.

[8] M. K. Lockwood, Y. K. Chen, N. Takashima, M. J. Wright, B. Laub, D. A. Kontinos, C. G. Justus, J. Olejniczak, J. Paulson John W., and B. R. Starr, "Systems analysis for a venus aerocapture mission - nasa/tm-2006-214291," eng, Tech. Rep., 2006. [Online]. Available: http://hdl.handle.net/2060/20060010899.

[9] H. L. Justh, C. H. Westhelle, J. L. Brown, M. M. Munk, D. Y. Oh, K. T. Edquist, J. L. Fisher, H. S. Wright, and R. E. Dyke, "Mars aerocapture systems study - nasa/tm-2006-214522," eng, Tech. Rep., 2006. [Online]. Available: http://hdl.handle.net/2060/20060056070.

[10] E. M. Queen, M. K. Lockwood, D. W. Way, B. R. Hollis, G. A. Hrinda, B. W. Starr, K. Edquist, R. W. Powell, E. V. Zoby, and R. W. Bailey, "Aerocapture systems analysis for a titan mission - nasa/tm-2006-214273," eng, Tech. Rep., 2006. [Online]. Available: http://hdl.handle.net/2060/20060007561.

[11] M. K. Lockwood, K. T. Edquist, G. A. Hrinda, R. W. Bailey, B. R. Hollis, J. L. Hall, T. R. Spilker, N. O'Kongo, M. A. Noca, and B. R. Starr, "Aerocapture systems analysis for a neptune mission - nasa/tm-2006-214300," eng, Tech. Rep., 2006. [Online]. Available: http://hdl.handle.net/2060/20060012088.

[12] J. Hall, M. Noca, and R. Bailey, "Cost-benefit analysis of the aerocapture mission set," *Journal of Spacecraft and Rockets*, vol. 42, no. 2, pp. 309–320, 2005, ISSN: 0022-4650.

[13] T. Spilker, C. Borden, M. Adler, M. Munk, R. Powell, R. Braun, P. Bauchamp, J. Cutts, and P. Wercinski, "An assessment of aerocapture and applications to future missions," Jet Propulsion Laboratory, Technical Document D-97058, 2016.

[14] T. Spilker, M. Adler, N. Arora, P. Beauchamp, J. Cutts, M. Munk, R. Powell, R. Braun, and P. Wercinski, "Qualitative assessment of aerocapture and applications to future missions," *Journal of Spacecraft and Rockets*, vol. 56, no. 2, pp. 536–545, 2019, ISSN: 00224650.

[15] K. Mease, R. J. Weidner, K. J.A., L. Wood, and M. Cruz, "Aerocapture: Guidance, navigation and control," in *9th Atmospheric Flight Mechanics Conference*, 1982. DOI: AIAA82-1381. [Online]. Available: https://doi.org/10.2514/6.1982-1381.

[16] R. Haw, "Approach navigation for a titan aerocapture orbiter," in *39th AIAA/ASME Joint Propulsion Conference and Exhibit*, 2003. DOI: AIAA2003-4802. [Online]. Available: https://doi.org/10.2514/6.2003-4802.

[17] D. Spencer and R. Braun, "Mars pathfinder atmospheric entry: Trajectory design and dispersion analysis," *Journal of Spacecraft and Rockets*, vol. 33, no. 5, pp. 670–676, 1996.

[18] J. Prince, P. Desai, E. Queen, and M. Grover, "Mars phoenix entry, descent, and landing simulation design and modeling analysis," *Journal of Spacecraft and Rockets*, vol. 48, no. 5, pp. 756–764, 2011.

[19] P. Desai, M. Schoenenberger, and F. Cheatwood, "Mars exploration rover six-degree-of-freedom entry trajectory analysis," *Journal of Spacecraft and Rockets*, vol. 43, no. 5, pp. 1019–1025, 2006.

[20] T. Martin-Mur, G. Kruizinga, P. Burkhart, F. Abilleira, M. Wong, and J. Kangas, "Mars science laboratory interplanetary navigation," *Journal of Spacecraft and Rockets*, vol. 51, no. 4, pp. 1014–1028, 2014. DOI: https://doi.org/10.2514/1.A32631.

[21] F. Abilleira, A. Halsell, G. Kruizinga, E. Bonfiglio, R. Grover, M. Chung, K. Fujii, E. Gustafson, Y. Hahn, D. Jefferson, E. Lau, J. Lee, S. McCandless, N. Mottinger, J. Seubert, E. Sklyanskiy, and M. Wallace, "2018 Mars InSight Trajectory Reconstruction and Performance from Launch Through Landing," in *29th AAS/AIAA Space Flight Mechanics Meeting*, Maui, HI, 2019. DOI: AAS19-204.

[22] L. D'Amario, L. Bright, and A. Wolf, "Galileo trajectory design," *Space Science Reviews*, vol. 60, no. 1–4, pp. 23–78, 1992.

[23] T. N. Engineering and S. Center, "Independent technical assessment of cassini/huygens probe entry, descent, and landing (edl) at titan," National Aeronautics and Space Administration, Technical Report NASA RP-05-67, 2005.

[24] M. Lockwood, "Neptune aerocapture systems analysis," in *AIAA Atmospheric Flight Mechanics Conference and Exhibit*, 2004. DOI: AIAA2004-4951. [Online]. Available: https://doi.org/10.2514/6.2004-4951.

[25] C. Karlgaard, P. Kutty, and M. Schoenenberger, "Coupled inertial navigation and flush air data sensing algorithm for atmosphere estimation," *Journal of Spacecraft and Rockets*, vol. 54, no. 1, pp. 128–140, 2017. DOI: https://doi.org/10.2514/1.A33331.

[26] D. J. Lickly, H. R. Morth, and B. S. Crawford, "Apollo Reentry Guidance," National Aeronautics and Space Administration, Contractor Report NASA/CR-52776, Jul. 1963.

[27] D. W. Way, P. R. W., C. A., S. A. D., M. S. M. A., B. D. P., and M. G. F., "Mars Science Laboratory: Entry, Descent, and Landing System Performance," in *2007 IEEE Aerospace Conference*, Big Sky, MT, Mar. 2006. DOI: IEEE1095-323X. [Online]. Available: https://doi.org/10.1109/AERO.2007.352821.

[28] J. C. Harpold and C. A. Graves Jr., "Shuttle entry guidance," *Journal of the Astronautical Sciences*, vol. 27, no. 3, pp. 239–268, 1979.

[29] J. Lafleur and C. C., "Angle of attack modulation for mars entry terminal state optimization," in *AIAA Atmospheric Flight Mechanics Conference*, Chicago, IL, 2009. DOI: AIAA2009-5611.

[30] R. Y. Jits and G. D. Walberg, "Blended control, predictor–corrector guidance algorithm: An enabling technology for mars aerocapture," *Acta Astronautica*, vol. 54, no. 6, pp. 385–398, 2004, ISSN: 0094-5765. [Online]. Available: https://doi.org/10.1016/S0094-5765(03)00159-0.

[31] R. Jits, M. Wright, and Y. Chen, "Closed-loop trajectory simulation for thermal protection system design for neptune aerocapture," *Journal of Spacecraft and Rockets*, vol. 42, no. 6, pp. 1025–1034, 2005, ISSN: 0022-4650. [Online]. Available: https://doi.org/10.2514/1.13428.

[32] B. Starr and J. Westhelle C. Masciarelli, "Aerocapture performance analysis for a neptune-triton exploration mission," in *AIAA Atmospheric Flight Mechanics Conference and Exhibit*, Providence, RI, Aug. 2004. DOI: AIAA2204-4955. [Online]. Available: https://doi.org/10.2514/6.2004-4955.

[33] A. Cianciolo and R. Powell, "Entry, descent, and landing guidance and control approaches to satisfy mars human mission landing criteria," in *AAS/AIAA Space Flight Mechanics Meeting*, Feb. 2017. DOI: AAS17-254. [Online]. Available: https://ntrs.nasa.gov/citations/20170001619.

[34] D. A. Matz and C. C. J., "Development of a Numerical Predictor-Corrector Aerocapture Guidance for Direct Force Control," in *AIAA SciTech Forum*, Orlando, FL, 2020. DOI: https://doi.org/10.2514/6.2020-0847.

[35] R. G. Deshmukh, D. A. Spencer, and S. Dutta, "Investigation of direct force control for aerocapture at neptune," eng, *Acta Astronautica*, vol. 175, no. 1, pp. 375–386, 2020, ISSN: 0022-4650. DOI: https://doi.org/10.1016/j.actaastro.2020.05.047.

[36] A. M. Korzun, M. K. J., and K. T. Edquist, "Supersonic Aerodynamic Characteristics of Blunt Body Trim Tab Configurations," in *31st AIAA Applied Aerodynamics Conference*, San Diego, CA, 2013. DOI: https://doi.org/10.2514/6.2013-2809.

[37] M. C. Ivanov, E. Blood, B. Cook, L. Giersch, M. Grover, J. Jakobowski, T. Rivellini, R. Su, J. Samareh, Z. T.A., R. Winski, A. Olds, and D. Kinney, "Entry, descent, and landing systems analysis study: Phase 2 report on mars science laboratory improvement," National Aeronautics and Space Administration, Technical Memorandum NASA TM-2011-216988, 2011.

[38] B. Yount, S. D'Souza, and A. Cassell, "Pterodactyl: Mechanical designs for integrated control design of a mechanically deployable entry vehicle," in *AIAA Scitech 2020 Forum*, Orlando, FL, 2020. DOI: https://doi.org/10.2514/6.2020-1009.

[39] A. Alunni, S. D'Souza, B. Yount, W. Okolo, B. Nikaido, B. Margolis, B. Johnson, K. Hibbard, J. Barton, G. Lopez, and Z. Hays, "Pterodactyl: Trade study for an integrated control system design of a mechanically deployed entry vehicle," in *AIAA Scitech 2020 Forum*, Orlando, FL, 2020. DOI: https://doi.org/10.2514/6.2020-1014.

[40] R. A. Dillman, A. Slagle, A. M. Korzun, R. Lugo, and A. Cianciolo, "Low lift-to-drag morphing shape design," in *AIAA Scitech 2020 Forum*, Orlando, FL, 2020. DOI: https://doi.org/10.2514/6.2020-1266.

[41] A. Olds, R. Beck, D. Bose, J. White, K. Edquist, B. Hollis, M. Lindell, F. Cheatwood, V. Gsell, and E. Bowden, "Irve-3 post-flight reconstruction," in *AIAA Aerodynamic Decelerator Systems (ADS) Conference*, Daytona Beach, FL, Mar. 2013. DOI: AiAA2013-1390. [Online]. Available: https://doi.org/10.2514/6.2013-1390.

[42] A. Cassell, P. Wercinski, S. B.P., B. Yount, S. Ghassemieh, O. Nishioka, C. Kruger, C. Brivkalns, A. Makino, S. Wu, N. Mai, R. McDaniel, A. Guarneros-Luna, J. Williams, D. Hoang, R. Rowan, S. Dutta, A. Korzun, J. Green, J. Tynis, and C. Karlgaard, "Adept sounding rocket one flight test review," in *AIAA Aviation 2019 Forum*, Dallas, TX, Jun. 2019. DOI: AiAA2019-2896. [Online]. Available: https://doi.org/10.2514/6.2019-2896.

[43] E. Venkatapathy, J. Arnold, I. Fernandez, K. Hamm Jr., D. Kinney, B. Laub, A. Makino, M. McGuire, K. Peterson, D. Prabhu, D. Empey, I. Dupzyk, L. Huynh, P. Hajela, P. Gage, A. Howard, and D. Andrews, "Adaptive deployable entry and placement technology (adept): A feasibility study for human missions to mars," in *21st AIAA Aerodynamic Decelerator Systems Technology Conference and Seminar*, May 2011. DOI: AIAA2011-2608. [Online]. Available: https://doi.org/10.2514/6.2011-2608.

[44] A. D. McRonald, "A Light-Weight Hypersonic Inflatable Drag Device for Neptune Orbiter," in *AAS/AIAA Spaceflight Mechanics Meeting*, Clearwater, FL, 2000. DOI: AAS00-170.

[45] D. T. Lyons and W. Johnson, "Ballute Aerocapture Trajectories at Neptune," in *AIAA Atmospheric Flight Mechanics Conference and Exhibit*, Providence, RI, 2004. DOI: AIAA2004-5181.

[46] Z. Putnam and R. Braun, "Drag-modulation flight-control system options for planetary aerocapture," *Journal of Spacecraft and Rockets*, vol. 51, no. 1, pp. 139–150, 2014.

[47] E. Roelke, J. McMahon, and P. Hattis, " Mutli-event drag modulation aerocapture guidance under uncertainty," in *AAS/AIAA Astrodynamics Specialist Conference*, Lake Tahoe, UT, 2020. DOI: AAS20-566.

[48] M. Werner and R. Braun, "Mission design and performance analysis of a smallsat aerocapture flight test," *Journal of Spacecraft and Rockets*, vol. 56, no. 6, pp. 1704–1713, 2019. DOI: https://doi.org/10.2514/1.A33997.

[49] A. Austin, A. Nelessen, B. Strauss, J. Ravich, M. Jesick, E. Venkatapathy, R. Reck, P. Wercinski, M. Aftosmis, M. Wilder, G. Allen, R. Braun, M. Werner, and E. Roelke, "SmallSat Aerocapture to Enable a New Paradigm of Planetary Missions," in *2019 IEEE Aerospace Conference*, Clearwater, FL, 2019. DOI: IEEE1095-323x.

[50] P. Moseley, "The apollo entry guidance: A review of the mathematical development and its operational characteristics," NASA Johnson Space Center, Houston, TX, TRW Note 69-FMT-791, Dec. 1969.

[51] O. Hill, "An adaptive guidance logic for an aeroasisted orbital transfer vehicle," in *AAS Astrodynamics Specialist Conference*, Lake Placid, NY, 1983, pp. 495–518. DOI: AAS83-357. [Online]. Available: https://ui.adsabs.harvard.edu/abs/1984AdAnS..54..495H/abstract.

[52] T. Ro and E. Queen, "Study of martian aerocapture terminal point guidance," in *23rd Atmospheric Flight Mechanics Conference and Exhibit*, Boston, MA, 1998. DOI: AIAA98-4571. [Online]. Available: https://doi.org/10.2514/6.1998-4571.

[53] F. J. Regan, *Dynamics of atmospheric re-entry*, eng, ser. AIAA education series. Washington, D.C.: American Institute of Aeronautics and Astronautics, 1993, ISBN: 160086046X.

[54] H. J. Allen and A. J. Eggers, "A study of the motion and aerodynamic heating of ballistic missiles entering the earth's atmosphere at high supersonic speeds," National Advisory Committee for Aeronautics, Technical Report NACA-TR-1381, 1958.

[55] C. Cerimele and J. Gamble, "A simplified guidance algorithm for lifting aeroassist orbital transfer vehicles," in *23rd Aerospace Science Meeting*, Reno, NV, 1985. [Online]. Available: https://doi.org/10.2514/6.1985-348.

[56] L. Bryant, M. Tigges, and D. Ives, "Analytic drag control for precision landing and aerocapture," in *23rd Atmospheric Flight Mechanics Conference*, Boston, MA, 1998. [Online]. Available: https://doi.org/10.2514/6.1998-4572.

[57] J. Masciarelli, "Aerocapture Guidance Algorithm Development and Testing," in *2007 NASA Science Technology Conference*, University of Maryland University College, 2007. DOI: NSTC2007.

[58] J. Masciarelli and E. Queen, "Guidance algorithms for aerocapture at titan," in *39th AIAA/ASME/SAE/ASEE Joint Propulsion Conference and Exhibit*, Huntsville, AL, 2003. [Online]. Available: https://doi.org/10.2514/6.2003-4804.

[59] J. Masciarelli, C. Westhelle, and C. Graves, "Aerocapture guidance performance for the neptune orbiter," in *AIAA Atmospheric Flight Mechanics Conference and Exhibit*, Providence, RI, 2004. [Online]. Available: https://doi.org/10.2514/6.2004-4954.

[60] J. Gamble, C. Cerimele, T. Moore, and J. Higgins, "Atmospheric guidance concepts for an aeroassist flight experiment," *Journal of the Astronautical Sciences*, vol. 36, no. 1, pp. 45–71, 1988, ISSN: 0021-9142. [Online]. Available: https://ntrs.nasa.gov/citations/19880058486.

[61] R. D. Braun and R. W. Powell, "Predictor-corrector guidance algorithm for use in high-energy aerobraking system studies," *Journal of Guidance, Control, and Dynamics*, vol. 15, no. 3, pp. 672–678, 1992, ISSN: 0731-5090. [Online]. Available: https://doi.org/10.2514/3.20890.

[62] R. W. Powell and R. D. Braun, "Six-degree-of-freedom guidance and control analysis of mars aerocapture," *Journal of Guidance, Control, and Dynamics*, vol. 16, no. 6, pp. 1038–1044, 1993, ISSN: 0731-5090. [Online]. Available: https://doi.org/10.2514/3.21125.

[63] R. W. Powell, "Numerical roll reversal predictor corrector aerocapture and precision landing guidance algorithms for the mars surveyor program 2001 missions," in *AIAA Atmospheric Flight Mechanics Conference and Exhibit*, Boston, MA, 1998. [Online]. Available: https://doi.org/10.2514/6.1998-4574.

[64] P. Lu, "Entry guidance: A unified method," *Journal of Guidance, Control, and Dynamics*, vol. 37, no. 3, pp. 713–728, 2014, ISSN: 07315090. [Online]. Available: https://doi.org/10.2514/1.62605.

[65] K. Webb, P. Lu, and A. Cianciolo, "Aerocapture guidance for human mars missions," in *AIAA Guidance, Navigation, and Control Conference*, Grapevine, TX, 2017. DOI: AIAA2017-1900. [Online]. Available: https://doi.org/10.2514/6.2017-1900.

[66] A. Miele, T. Wang, and Z. Zhao, "Optimal trajectories for the aeroassisted flight experiment," *Acta Astronautica*, vol. 69, no. 11/12, pp. 735–747, 1990. [Online]. Available: https://doi.org/10.1016/0094-5765(90)90116-3.

[67] A. Miele, T. Wang, and A. Deaton, "Decomposition technique and optimal trajectories for the aeroassisted flight experiment," *Journal of Optimization Theory and Applications*, vol. 69, no. 2, pp. 201–234, 1991. [Online]. Available: https://link.springer.com/article/10.1007/BF00940640.

[68] J. Lafleur, "The Conditional Equivalence of ΔV Minimization and Apoapsis Targeting in Numerical Predictor-Corrector Aerocapture Guidance," National Aeronautics and Space Administration, Technical Memorandum NASA/TM-2011-216156, Aug. 2011.

[69] P. Lu, C. J. Cerimele, M. A. Tigges, and D. A. Matz, "Optimal aerocapture guidance," *Journal of Guidance, Control, and Dynamics*, vol. 38, no. 4, pp. 553–565, 2015, ISSN: 07315090. [Online]. Available: https://doi.org/10.2514/1.G000713.

[70] N. X. Vinh, *Hypersonic and planetary entry flight mechanics*. Ann Arbor: University of Michigan Press, 1980, ISBN: 0472093045.

[71] C. Lanczos, *The variational principles of mechanics.* eng, 4th ed.., ser. Mathematical expositions ; no. 4. Toronto: University of Toronto Press, 1970, ISBN: 0802017436.

[72] D. T. Greenwood, *Classical dynamics*, eng, ser. Prentice-Hall international series in dynamics. Englewood Cliffs, N.J.: Prentice-Hall, 1977, ISBN: 0131360361.

[73] D. T. Greenwood, *Principles of dynamics*, eng, 2nd ed. 1988, ISBN: 0137099819.

[74] J. Anderson, *Hypersonic and high-temperature gas dynamics*, eng, Third edition., ser. AIAA education series. Washington, D.C.: American Institute of Aeronautics and Astronautics, 2019, ISBN: 9781624105142.

[75] N. Sir Isaac, *The Principia: The Authoritative Translation : Mathematical Principles of Natural Philosophy.* University of California Press, 2016, ISBN: 9780520290730.

[76] L. Lees, "Hypersonic flow," *Institute of Aeronautical Sciences*, pp. 241–276, 1955.

[77] E. Clark and L. Trimmer, "Equations and charts for the evaluation of the hypersonic aerodynamic characteristics of lifting configurations by the newtonian theory," Arnold Engineering Development Center Arnold AFB TN, Technical Report AEDC-TDR-64-25, 1964.

[78] E. Clark, "Equations and charts for the evaluations of forces on spherically blunted cones by the newtonian theory," Arnold Engineering Development Center Arnold AFB TN, Technical Report AEDC-TR-66-16, 1966.

[79] W. Wells and W. Armstrong, "Tables of aerodynamic coefficients obtained from developed newtonian expressions for complete and partial conic and spheric bodies at combined angles of attack and sideslip with some comparisons with hypersonic experimental data," National Aeronautics and Space Administration, Technical Report NASA TR R-127, 1962.

[80] M. Grant and R. Braun, "Analytic hypersonic aerodynamics for conceptual design of entry vehicles," in *48th AIAA Aerospace Sciences Meeting*, Orlano, FL, 2010. DOI: AIAA2010-1212.

[81] M. Grant, "Rapid simultaneous hypersonic aerodynamic and trajectory optimization for conceptual design," Doctor of Philisophy in Aerospace Engineering, Mar. 2012. [Online]. Available: https://smartech.gatech.edu/handle/1853/43685.

[82] D. Kinney, "Aero-thermodynamics for conceptual design," in *42nd AIAA Aerospace Sciences Meeting and Exhibit*, Reno, NV, 2004. DOI: AIAA04-31962.

[83] A. Dyakonov, M. Schoenenberger, and J. Van Norman, "Hypersonic and supersonic state aerodynamics of mars science laboratory entry vehicle," in *43rd AIAA Thermophysics Conference*, New Orleans, LA, 2012. DOI: AIAA2012-2999.

[84] C. G. Justus, A. Duval, and V. W. Keller, "Atmospheric Models for Aerocapture Systems Studies," in *AIAA Atmospheric Flight Mechanics Conference and Exhibit*, Providence, RI, 2004. DOI: AIAA2004-3844.

[85] F. Leslie and C. Justus, "The nasa marshall space flight center earth global reference atmospheric model-2010 version," National Aeronautics and Space Administration, Technical Memorandum NASA TM-2011-216467, Jun. 2011.

[86] H. Justus, "Mars global reference atmospheric model 2010 version: Users guide," National Aeronautics and Space Administration, Technical Memorandum NASA TM-2014-217499, Feb. 2014.

[87] H. L. Justus and A. D. Cianciolo, "Venus Global Reference Atmospheric Model Status and Planned Updates," in *Venus Modeling Workshop*, Cleveland, OH, 2017.

[88] R. Yelle, D. Strobell, E. Lellouch, and D. Gautier, "Engineering models for titan's atmosphere," European Space Agency, Huygens Science Payload and Mission ESA SP-1177, Aug. 1997.

[89] D. P. Cruikshank, "Neptune and triton," Tuscon, AZ: University of Arizona Press, 1995, ISBN: 9780816536092.

[90] P. Gnoffo, "Planetary-entry gas dynamics," *Annual Review of Fluid Mechanics*, vol. 31, pp. 459–495, Jan. 1999, ISSN: 00664189.

[91] J. Fay and F. Riddell, "Theory of stagnation point heat transfer in dissociated air," *Journal of Aeronautical Sciences*, vol. 25, no. 121, pp. 73–85, 1958.

[92] G. Chapman, "Theoretical laminar convective heat transfer and boundary-layer characteristics on cones at speeds to 24 km/sec," National Aeronautics and Space Administration, Technical Note NASA TN-D-2463, Aug. 1964.

[93] K. Sutton and R. Graves, "A general stagnation point convective heating equation for arbitrary gas mixtures," National Aeronautics and Space Administration, Technical Report NASA TR-R-376, Nov. 1971.

[94] M. Tauber and K. Sutton, "Stagnation point radiative heating relations for earth and mars entries," *Journal of Spacecraft and Rockets*, vol. 28, no. 1, pp. 40–42, 1991.

[95] D. Vallado, *Fundamentals of astrodynamics and applications*, eng, 2nd ed., ser. Space technology library. El Segundo, California: Microcosm Press ; Kluwer Academic Publishers, 2001, ISBN: 0792369033.

[96] J. Longuski, J. Guzman, and J. Prussing, *Optimal Control with Aerospace Applications*, eng, ser. Space Technology Library. New York, NY: Springer, 2014, ISBN: 978-1-4614-8944-3. [Online]. Available: https://doi.org/10.1007/978-1-4614-8945-0.

[97] A. Bryson Jr and Y. Ho, *Applied Optimal Control*, eng. Routledge, 2018, ISBN: 1138472034.

[98] L. Pontryagin, V. Boltyanskii, Q. Gramkreledze, and E. Mishchenko, *The Mathematical Theory of Optimal Processes*, eng. New York, NY: Interscience Publishers, 1962, ISBN: 1138472034.

[99] K. Graichen, A. Kugi, N. Petit, and F. Chaplais, "Handling constraints in optimal control with saturation functions and sytem extension," *System and Control Letters*, vol. 59, no. 11, pp. 671–679, 2010, ISSN: 0167-6911. [Online]. Available: https://doi.org/10.1016/j.sysconle.2010.08.003.

[100] T. Antony and M. Grant, "Path constraint regularization in optimal control problems using saturation functions," in *2018 AIAA Atmospheric Flight Mechanics Conference*, Kissimmee, FL, 2018. DOI: AIAA2018-0018. [Online]. Available: https://doi.org/10.2514/6.2018-0018.

[101] J. Kierzenka and L. Shampine, "A bvp solver that controls residual and error," *Journal of Numerical Analysis, Industrial and Applied Mathematics*, vol. 3, no. 1-2, pp. 27–41, 2008, ISSN: 1790-8140.

[102] G. Dahlquist, *Numerical methods in scientific computing*, eng. Philadelphia, PA, 2008, ch. 6, ISBN: 9780898716443.

[103] R. Brent, *Algorithms for Minimization without Derivatives*, ser. Prentice-Hall series in automatic computation. Englewood Cliffs, NJ: Prentice-Hall, 1973, ch. 5, ISBN: 0130223352.

[104] *Numerical recipes in C : the art of scientific computing*, eng, 2nd ed. New York, NY: Cambridge University Press, 1995, ch. 10, ISBN: 0521431085.

[105] L. Shampine and M. Gordon, *Computer Solution of Ordinary Differential Equations: The Initial Value Problem*, eng. San Francisco, CA: W.H. Freeman, 1975, ISBN: 9780716704614.

[106] K. M. Smith, "Predictive lateral logic for numerical entry guidance algorithms," in *26th AAS/AIAA Space Flight Mechanics Meeting*, Napa, CA, 2016. DOI: AAS16-216.

[107] S. Striepe, R. Powell, P. Desai, E. Queen, D. Way, J. Prince, A. Cianciolo, J. Davis, D. Litton, R. Maddock, J. Shidner, R. Winski, S. O'Keefe, A. Bowes, J. Aguirre, C. Garrison, J. Hoffman, A. Olds, S. Dutta, C. Zumwalt, J. White, G. Brauer, S. Marsh, R. Lugo, J. Green, and M. Engel, *Program to optimize simulated trajectories ii (post2)*, English, version Version 4.1.0.r1359, National Aeronautics and Space Administration, 706 pp., December 16, 2017.

[108] A. Cianciolo, J. Davis, D. Komar, M. Munk, J. Samareh, J. Williams-Byrd, T. Zang, R. Powell, J. Shidner, D. Stanley, A. Wilhite, D. Kinney, M. McGuire, A. J.O., A. Howard, R. Sostaric, J. Studak, C. Zumwalt, E. Llama, J. Casoliva, M. Ivanov, I. Clark, and A. Sengupta, "Entry, descent and landing systems analysis study: Phase 1 report," National Aeronautics and Space Administration, Technical Memorandum NASA TM-2010-216720, Jul. 2010.

[109] A. Cianciolo, J. Davis, W. Engelund, D. Komar, E. Queen, J. Samareh, D. Way, T. Zang, J. Murch, S. Krizan, A. Olds, R. Powell, J. Shidner, D. Kinney, M. McGuire, A. J.O., M. Covington, R. Sostaric, C. Zumwalt, and E. Llama, "Entry, descent and landing systems analysis study: Phase 2 report on exploration feed-forward systems," National Aeronautics and Space Administration, Technical Memorandum NASA TM-2011-217055, Feb. 2011.

[110] B. Johnson, C. Cerimele, S. Stachowiak, R. Sostaric, and D. Matz, "Mid-Lift-to-Drag Ratio Rigid Vehicle Control System Design and Simulation for Human Mars Entry," in *2018 AIAA Guidance, Navigation, and Control Conference*, Kissimmee, FL, 2018. DOI: AIAA2018-0615.

[111] C. Brunner and P. Lu, "Skip entry trajectory planning and guidance," *Journal of Guidance, Control, and Dynamics*, vol. 31, no. 5, pp. 1210–1219, 2008. [Online]. Available: https://doi.org/10.2514/1.35055.

[112] C. Brunner and P. Lu, "Comparison of fully numerical predictor-corrector and apollo skip entry guidance algorithms," *Journal of the Astronautical Sciences*, vol. 59, no. 3, pp. 517–540, 2012. [Online]. Available: https://link.springer.com/article/10.1007/s40295-014-0005-1.

[113] H. Musoff and P. Zarchan, *Fundamentals of Kalman Filtering: A Practical Approach*, eng, Second edition., ser. AIAA education series. Washington, D.C.: American Institute of Aeronautics and Astronautics, 2005, ch. 15, ISBN: 978-1-56347-694-5.

[114] S. A. Striepe, D. W. Way, and A. M. Dwyer-Cianciolo, "Mars science laboratory simulations for entry, descent, and landing," eng, *Journal of Spacecraft and Rockets*, vol. 43, no. 2, pp. 311–323, 2015, ISSN: 0022-4650.

[115] B. Starr and C. Westhelle, "Aerocapture performance analysis of a venus exploration mission," eng, 2005, pp. 1–14. [Online]. Available: http://search.proquest.com/docview/28636022/.

[116] D. Way, R. Powell, J. Masciarelli, B. Starr, and K. Edquist, "Aerocapture simulation and performance for the titan explorer mission," eng, in *American Institute of Aeronautics and Astronautics. AIAA Conference Papers*, Reston: American Institute of Aeronautics and Astronautics, 2003. [Online]. Available: http://search.proquest.com/docview/1433234821/.

[117] S. Bhaskaran, "Autonomous navigation for deep space missions," in *SpaceOps 2012 Conference*, 2012. DOI: AIAA2012-1267135. [Online]. Available: https://doi.org/10.2514/6.2012-1267135.

[118] A. P. Girija, S. J. Saikia, J. M. Longuski, S. Bhaskaran, M. S. Smith, and J. A. Cutts, "Feasibility and performance analysis of neptune aerocapture using heritage blunt-body aeroshells," eng, *Journal of Spacecraft and Rockets*, vol. 1, no. 1, pp. 1–17, 2020, ISSN: 0022-4650.

[119] R. J. Haw, "Aerocapture Navigation at Neptune," in *AAS/AIAA Astrodynamics Specialist Conference*, Big Sky, MT, 2003. DOI: AAS03-643.

[120] A. Klesh, B. Clement, C. Colley, J. Essmiller, D. Forgette, J. Krajewski, A. Marinan, T. Martin-Mur, J. Steinkraus, D. Sternberg, T. Werne, and B. Young, "MarCO: Early Operations of the First CubeSats to Mars," in *32nd Annual AIAA/USU Conference on Small Satellites*, Logan, UT, 2018. DOI: SSC18-WKIX-04.

[121] C. Mercer, "Small Satellite Mission for Planetary Science," in *33rd Annual AIAA/USU Conference on Small Satellites*, Logan, UT, 2019. DOI: SSC19-WKV-06.

[122] C. Sotin, G. Avice, J. Baker, A. Freeman, S. Madzunkov, T. Stevenson, N. Arora, M. Darrach, G. Lightsey, and B. Marty, "Cupid's Arrow: a small satellite to measure noble gases in Venus atmosphere," in *Planetary Science Deep Space SmallSat Mission Concepts*, The Woodlands, TX, 2018. [Online]. Available: https://www.hou.usra.edu/meetings/smallsat2018/pdf/07_Sotin.pdf.

[123] K. Sayanagi, R. Dillman, D. Atkinson, A. Simon, M. Wong, T. Spilker, S. Saikia, J. Li, D. Hope, and W. Edwards, "Small Next-generation Atmospheric Probe," in *Planetary Science Deep Space SmallSat Mission Concepts*, The Woodlands, TX, 2018. [Online]. Available: https://www.hou.usra.edu/meetings/smallsat2018/pdf/11_Sayanagi.pdf.

[124] D. Minton, D. A. Spencer, B. Horgan, Z. Putnam, J. Puig-Suari, and P. Christensen, "Chariot to the Moons of Mars," in *Planetary Science Deep Space SmallSat Mission Concepts*, The Woodlands, TX, 2018. [Online]. Available: https://www.hou.usra.edu/meetings/smallsat2018/pdf/05_Minton.pdf.

[125] *Espa user's guide*, 1, Rev. 0, MOOG Space and Defense Group, Oct. 2018. [Online]. Available: https://www.moog.com/content/dam/moog/literature/Space_Defense/spaceliterature/structures/moog-espa-users-guide-datasheet.pdf.

[126] B. Smith, A. Cassell, C. Kruger, E. Venkatapathy, C. Kazemba, and K. Simonis, "Nano-ADEPT: An entry system for secondary payloads," in *2015 IEEE Aerospace Conference*, Big Sky, MT, 2015. DOI: 1095-323X.

[127] J. Cabrera, R. Deshmukh, and D. Spencer, "Aerodynamic Database Development using a Bridging Function for a Conceptual Morphable Entry System," in *AIAA SciTech 2021 Forum*, Virtual, 2021. DOI: AIAA2021-0935.

[128] J. Arnold, K. Pterson, B. Yount, N. Schneider, and J. Chavez-Garcia, "Thermal and Structural Performance of Woven Carbon Cloth for Adaptive Deployable Entry and Placement Technology," in *AIAA Aerodynamic Decelerator Systems (ADS) Conference*, Daytona Beach, FL, 2013. DOI: AIAA2013-1370.

[129] C. D'Souza and R. Zanetti, "Navigation Design and Analysis for the Orion Earth-Moon Mission," in *24th AAS/AIAA Space Flight Mechanics Meeting*, Santa Fe, NM, 2014. DOI: AAS14-263.

[130] E. Venkatapathy, D. Ellerby, P. Gage, D. Prabhu, M. Gasch, C. Kazemba, C. Kellerman, L. S., B. Libben, M. Mahzari, F. Milos, A. Murphy, O. Mishioka, K. Peterson, C. Poteet, S. Splinter, M. Stackpoole, W. J., and Z. Young, "Entry system technology readiness for ice-giant probe missions," eng, *Space Science Reviews*, vol. 216, no. 22, pp. 1–21, 2020. DOI: https://doi.org/10.1007/s11214-020-0638-2.

A. SINGULAR ARC OPTIMAL FLIGHT CONTROL SOLUTIONS

This section highlights the investigation of the singular optimal control solution for direct force control and drag modulation analyzed in the optimal aerocapture problem. For each flight control control, a similar methodology is devised to assess the potential non-existence of singular arc solutions. The work by Lu et al [69] has previously investigated the potential non-existence of the singular arc solution for bank angle modulation.

Following the formulation in 2.2.4, the Hamiltonian is defined by Eq. (A.1) where $\dot{r}$ is defined by Eq. (2.39), $\dot{\theta}$ is defined by Eq. (2.40), $\dot{\phi}$ is defined by Eq. (2.41), $\dot{v}$ is defined by Eq. (2.57), $\dot{\gamma}$ is defined by Eq. (2.58), and $\dot{\psi}$ is defined by Eq. (2.59).

$$H = \lambda_r \dot{r} + \lambda_\theta \dot{\theta} + \lambda_\phi \dot{\phi} + \lambda_V \dot{V} + \lambda_\gamma \dot{\gamma} + \lambda_\psi \dot{\psi} \tag{A.1}$$

The co-state vector, $\vec{\lambda}$ is defined by $\vec{\lambda} = \begin{bmatrix} \lambda_r & \lambda_\theta & \lambda_\phi & \lambda_V & \lambda_\gamma & \lambda_\psi \end{bmatrix}^T$. Its dynamics are computed using Euler-Lagrange equations from Eq. (2.142). Applying the equation and decomposing the components yields the following six coupled differential equations.

$$\dot{\lambda}_r = -\lambda_v \left(\frac{2J_2\mu R_p^2 \sin(\gamma)\left(1.5 - 4.5\sin^2(\phi)\right)}{r^5} + \frac{2\mu\sin(\gamma)\left(\frac{J_2 R_p^2\left(1.5-4.5\sin^2(\phi)\right)}{r^2}+1\right)}{r^3} \right.$$
$$\left. + \omega^2\cos(\phi)(\cos(\gamma)\sin(\psi)\sin(\phi)+\sin(\gamma)\cos(\phi)) - \frac{12J_2\mu R_p^2\cos(\gamma)\sin(\psi)\sin(\phi)\cos(\phi)}{r^5} \right)$$
$$- \frac{\lambda_\gamma}{v}\left(\cos(\gamma)\left(\frac{2J_2\mu R_p^2\left(1.5 - 4.5\sin^2(\phi)\right)}{r^5} + \frac{2\mu\left(\frac{J_2 R_p^2\left(1.5-4.5\sin^2(\phi)\right)}{r^2}+1\right)}{r^3} - \frac{v^2}{r^2} \right) \right.$$
$$\left. + \omega^2\cos(\phi)(\cos(\gamma)\cos(\phi)-\sin(\gamma)\sin(\psi)\sin(\phi)) + \frac{12J_2\mu R_p^2\sin(\gamma)\sin(\psi)\sin(\phi)\cos(\phi)}{r^5} \right)$$
$$- \frac{\lambda_\psi}{v}\left(\omega^2\sec(\gamma)\cos(\psi)\sin(\phi)\cos(\phi) - \frac{12J_2\mu R_p^2\sec(\gamma)\cos(\psi)\sin(\phi)\cos(\phi)}{r^5} \right.$$
$$\left. - \frac{v^2\cos(\gamma)\cos(\psi)\tan(\phi)}{r^2} \right) + \frac{\lambda_\theta v\cos(\gamma)\cos(\psi)\sec(\phi)}{r^2} - \frac{\lambda_\phi v\cos(\gamma)\sin(\psi)}{r^2} \tag{A.2}$$

$$\dot{\lambda}_\theta = 0 \tag{A.3}$$

$$
\begin{aligned}
\dot{\lambda}_\phi = -\lambda_v \Bigg(& \frac{3J_2\mu R_p^2 \cos(\gamma)\sin(\psi)\cos^2(\phi)}{r^4} - \frac{3J_2\mu R_p^2 \cos(\gamma)\sin(\psi)\sin^2(\phi)}{r^4} \\
& + \frac{9J_2\mu R_p^2 \sin(\gamma)\sin(\phi)\cos(\phi)}{r^4} + r\omega^2\cos(\phi)(\cos(\gamma)\sin(\psi)\cos(\phi) - \sin(\gamma)\sin(\phi)) \\
& - r\omega^2\sin(\phi)(\cos(\gamma)\sin(\psi)\sin(\phi) + \sin(\gamma)\cos(\phi)) \Bigg) \\
- \frac{\lambda_\psi}{v} \Bigg(& \frac{3J_2\mu R_p^2 \sec(\gamma)\cos(\psi)\cos^2(\phi)}{r^4} - \frac{3J_2\mu R_p^2 \sec(\gamma)\cos(\psi)\sin^2(\phi)}{r^4} \\
& + r\omega^2\sec(\gamma)\cos(\psi)\cos^2(\phi) - r\omega^2\sec(\gamma)\cos(\psi)\sin^2(\phi) + \frac{v^2\cos(\gamma)\cos(\psi)\sec^2(\phi)}{r} \\
& + 2v\omega(\cos(\phi) - \tan(\gamma)\sin(\psi)\sin(\phi)) \Bigg) \\
- \frac{\lambda_\gamma}{v} \Bigg(& \frac{3J_2\mu R_p^2 \sin(\gamma)\sin(\psi)\sin^2(\phi)}{r^4} - \frac{3J_2\mu R_p^2 \sin(\gamma)\sin(\psi)\cos^2(\phi)}{r^4} \\
& + \frac{9J_2\mu R_p^2 \cos(\gamma)\sin(\phi)\cos(\phi)}{r^4} + r\omega^2\cos(\phi)(-\sin(\gamma)\sin(\psi)\cos(\phi) - \cos(\gamma)\sin(\phi)) \\
& - r\omega^2\sin(\phi)(\cos(\gamma)\cos(\phi) - \sin(\gamma)\sin(\psi)\sin(\phi)) - 2v\omega\cos(\psi)\sin(\phi) \Bigg) \\
- & \frac{\lambda_\theta v\cos(\gamma)\cos(\psi)\tan(\phi)\sec(\phi)}{r}
\end{aligned}
\tag{A.4}
$$

$$
\begin{aligned}
\dot{\lambda}_v = \frac{\lambda_\gamma}{v^2}\Bigg(\cos(\gamma)\left(\frac{v^2}{r} - \frac{\mu\left(\frac{J_2 R_p^2\left(1.5-4.5\sin^2(\phi)\right)}{r^2}+1\right)}{r^2}\right) + \frac{AC_L\rho v^2\cos(\sigma)}{2m} + \frac{AC_Q\rho v^2\sin(\sigma)}{2m} \\
- \frac{3J_2\mu R_p^2\sin(\gamma)\sin(\psi)\sin(\phi)\cos(\phi)}{r^4} \\
+ r\omega^2\cos(\phi)(\cos(\gamma)\cos(\phi) - \sin(\gamma)\sin(\psi)\sin(\phi)) + 2v\omega\cos(\psi)\cos(\phi)\Bigg) \\
+ \frac{AC_D\lambda_v\rho v}{m} + \frac{\lambda_\psi}{v^2}\Bigg(\frac{AC_L\rho v^2\sec(\gamma)\sin(\sigma)}{2m} - \frac{AC_Q\rho v^2\sec(\gamma)\cos(\sigma)}{2m} \\
+ \frac{3J_2\mu R_p^2\sec(\gamma)\cos(\psi)\sin(\phi)\cos(\phi)}{r^4} + r\omega^2\sec(\gamma)\cos(\psi)\sin(\phi)\cos(\phi) \\
+ \frac{v^2\cos(\gamma)\cos(\psi)\tan(\phi)}{r} + 2v\omega(\tan(\gamma)\sin(\psi)\cos(\phi) + \sin(\phi))\Bigg) \\
- \frac{\lambda_\gamma}{v}\left(\frac{AC_L\rho v\cos(\sigma)}{m} + \frac{AC_Q\rho v\sin(\sigma)}{m} + \frac{2v\cos(\gamma)}{r} + 2\omega\cos(\psi)\cos(\phi)\right) \\
- \frac{\lambda_\psi}{v}\Bigg(\frac{AC_L\rho v\sec(\gamma)\sin(\sigma)}{m} - \frac{AC_Q\rho v\sec(\gamma)\cos(\sigma)}{m} \\
+ 2\omega(\tan(\gamma)\sin(\psi)\cos(\phi) + \sin(\phi)) + \frac{2v\cos(\gamma)\cos(\psi)\tan(\phi)}{r}\Bigg) \\
- \lambda_r\sin(\gamma) - \frac{\lambda_\theta\cos(\gamma)\cos(\psi)\sec(\phi)}{r} + \frac{\lambda_\phi\cos(\gamma)\sin(\psi)}{r}
\end{aligned}
\tag{A.5}
$$

$$\dot{\lambda}_\gamma = -\lambda_v \left(-\frac{\mu\cos(\gamma)\left(\frac{J_2 R_p^2\left(1.5-4.5\sin^2(\phi)\right)}{r^2}+1\right)}{r^2} - \frac{3J_2\mu R_p^2 \sin(\gamma)\sin(\psi)\sin(\phi)\cos(\phi)}{r^4} \right.$$
$$\left. + r\omega^2\cos(\phi)(\cos(\gamma)\cos(\phi) - \sin(\gamma)\sin(\psi)\sin(\phi)) \right)$$
$$- \frac{\lambda_\gamma}{v}\left((-\sin(\gamma)) \left(\frac{v^2}{r} - \frac{\mu\left(\frac{J_2 R_p^2\left(1.5-4.5\sin^2(\phi)\right)}{r^2}+1\right)}{r^2} \right) \right.$$
$$\left. - \frac{3J_2\mu R_p^2\cos(\gamma)\sin(\psi)\sin(\phi)\cos(\phi)}{r^4} \right.$$
$$\left. + r\omega^2\cos(\phi)(\sin(\gamma)(-\cos(\phi)) - \cos(\gamma)\sin(\psi)\sin(\phi)) \right)$$
$$- \frac{\lambda_\psi}{v}\left(\frac{AC_L\rho v^2\tan(\gamma)\sec(\gamma)\sin(\sigma)}{2m} - \frac{AC_Q\rho v^2\tan(\gamma)\sec(\gamma)\cos(\sigma)}{2m} \right.$$
$$+ \frac{3J_2\mu R_p^2\tan(\gamma)\sec(\gamma)\cos(\psi)\sin(\phi)\cos(\phi)}{r^4} + r\omega^2\tan(\gamma)\sec(\gamma)\cos(\psi)\sin(\phi)\cos(\phi)$$
$$\left. - \frac{v^2\sin(\gamma)\cos(\psi)\tan(\phi)}{r} + 2v\omega\sec^2(\gamma)\sin(\psi)\cos(\phi) \right)$$
$$+ \frac{\lambda_\theta v\sin(\gamma)\cos(\psi)\sec(\phi)}{r} - \frac{\lambda_\phi v\sin(\gamma)\sin(\psi)}{r} - \lambda_r v\cos(\gamma) \tag{A.6}$$

$$\dot{\lambda}_\psi = -\lambda_v \left(\frac{3J_2\mu R_p^2\cos(\gamma)\cos(\psi)\sin(\phi)\cos(\phi)}{r^4} + r\omega^2\cos(\gamma)\cos(\psi)\sin(\phi)\cos(\phi) \right)$$
$$- \frac{\lambda_\psi}{v}\left(-\frac{3J_2\mu R_p^2\sec(\gamma)\sin(\psi)\sin(\phi)\cos(\phi)}{r^4} - r\omega^2\sec(\gamma)\sin(\psi)\sin(\phi)\cos(\phi) \right.$$
$$\left. - \frac{v^2\cos(\gamma)\sin(\psi)\tan(\phi)}{r} + 2v\omega\tan(\gamma)\cos(\psi)\cos(\phi) \right)$$
$$- \frac{\lambda_\gamma}{v}\left(-\frac{3J_2\mu R_p^2\sin(\gamma)\cos(\psi)\sin(\phi)\cos(\phi)}{r^4} - r\omega^2\sin(\gamma)\cos(\psi)\sin(\phi)\cos(\phi) \right.$$
$$\left. - 2v\omega\sin(\psi)\cos(\phi) \right) + \frac{\lambda_\theta v\cos(\gamma)\sin(\psi)\sec(\phi)}{r} + \frac{\lambda_\phi v\cos(\gamma)\cos(\psi)}{r} \tag{A.7}$$

For the optimal aerocapture problem, the final time is free to vary. The transversality condition allows for the terminal state of the Hamiltonian to be computed. Since both the terminal cost nor the terminal constraints explicitly depend on time, the Hamiltonian

computed at t_f must equal zero. Furthermore, the Hamiltonian itself does not explicitly depend on time; as a result, it must be a constant. Putting these two finding together indicates that $H = 0 \; \forall \; t \in [t_0, t_f]$. The condition can be used in determining the existence of the singular control.

For each flight control assessed in the following sections, a similar investigation is employed. The singular arc solution is assumed to exist in a finite time interval $[t_1, t_2] \subset [t_0, t_f]$. The potential solutions for the state and co-state variables are explored. Although not all mathematical solutions are analyzed, insight into the physically realizable solutions is presented.

A.0.1 Drag Modulation

From the derivation in 2.2.4, the singular optimal control for DM occurs when the switching function equals zero. From Eq. (2.165), this condition necessitates that $\lambda_v(t) \equiv 0$ in $[t_1, t_2]$. Consequently, $\dot{\lambda}_v = 0$ in $[t_1, t_2]$. Substituting $\lambda_v = \dot{\lambda}_v = 0$ into Eq. (A.5) yields

$$
\begin{aligned}
0 = \frac{\lambda_\gamma}{v^2}\Bigg(\cos(\gamma)\left(\frac{v^2}{r} - \frac{\mu\left(\frac{J_2 R_p^2\left(1.5 - 4.5\sin^2(\phi)\right)}{r^2} + 1\right)}{r^2}\right) + \frac{AC_L\rho v^2\cos(\sigma)}{2m} + \frac{AC_Q\rho v^2\sin(\sigma)}{2m} \\
- \frac{3J_2\mu R_p^2\sin(\gamma)\sin(\psi)\sin(\phi)\cos(\phi)}{r^4} + r\omega^2\cos(\phi)(\cos(\gamma)\cos(\phi) - \sin(\gamma)\sin(\psi)\sin(\phi)) \\
+ 2v\omega\cos(\psi)\cos(\phi)\Bigg) + \frac{\lambda_\psi}{v^2}\Bigg(\frac{AC_L\rho v^2\sec(\gamma)\sin(\sigma)}{2m} - \frac{AC_Q\rho v^2\sec(\gamma)\cos(\sigma)}{2m} \\
+ \frac{3J_2\mu R_p^2\sec(\gamma)\cos(\psi)\sin(\phi)\cos(\phi)}{r^4} + r\omega^2\sec(\gamma)\cos(\psi)\sin(\phi)\cos(\phi) \\
+ \frac{v^2\cos(\gamma)\cos(\psi)\tan(\phi)}{r} + 2v\omega(\tan(\gamma)\sin(\psi)\cos(\phi) + \sin(\phi))\Bigg) \\
- \frac{\lambda_\gamma}{v}\left(\frac{AC_L\rho v\cos(\sigma)}{m} + \frac{AC_Q\rho v\sin(\sigma)}{m} + \frac{2v\cos(\gamma)}{r} + 2\omega\cos(\psi)\cos(\phi)\right) \\
- \frac{\lambda_\psi}{v}\left(\frac{AC_L\rho v\sec(\gamma)\sin(\sigma)}{m} - \frac{AC_Q\rho v\sec(\gamma)\cos(\sigma)}{m} + 2\omega(\tan(\gamma)\sin(\psi)\cos(\phi) + \sin(\phi))\right. \\
\left. + \frac{2v\cos(\gamma)\cos(\psi)\tan(\phi)}{r}\right) - \lambda_r\sin(\gamma) - \frac{\lambda_\theta\cos(\gamma)\cos(\psi)\sec(\phi)}{r} + \frac{\lambda_\phi\cos(\gamma)\sin(\psi)}{r}
\end{aligned}
\tag{A.8}
$$

The zero value of the Hamiltonian can be utilized. Setting Eq. (A.1) equal to zero, expanding, and substituting $\lambda_v = 0$ yields

$$\begin{aligned}0 = \frac{\lambda_\gamma}{v}\Bigg(\cos(\gamma)\left(\frac{v^2}{r} - \frac{\mu\left(\frac{J_2 R_p^2\left(1.5-4.5\sin^2(\phi)\right)}{r^2}+1\right)}{r^2}\right) + \frac{AC_L\rho v^2\cos(\sigma)}{2m} + \frac{AC_Q\rho v^2\sin(\sigma)}{2m} \\ - \frac{3J_2\mu R_p^2\sin(\gamma)\sin(\psi)\sin(\phi)\cos(\phi)}{r^4} + r\omega^2\cos(\phi)(\cos(\gamma)\cos(\phi) - \sin(\gamma)\sin(\psi)\sin(\phi)) \\ + 2v\omega\cos(\psi)\cos(\phi)\Bigg) + \frac{\lambda_\psi}{v}\Bigg(\frac{AC_L\rho v^2\sec(\gamma)\sin(\sigma)}{2m} - \frac{AC_Q\rho v^2\sec(\gamma)\cos(\sigma)}{2m} \\ + \frac{3J_2\mu R_p^2\sec(\gamma)\cos(\psi)\sin(\phi)\cos(\phi)}{r^4} + r\omega^2\sec(\gamma)\cos(\psi)\sin(\phi)\cos(\phi) \\ + \frac{v^2\cos(\gamma)\cos(\psi)\tan(\phi)}{r} + 2v\omega(\tan(\gamma)\sin(\psi)\cos(\phi) + \sin(\phi))\Bigg) \\ + \frac{\lambda_\theta v\cos(\gamma)\cos(\psi)\sec(\phi)}{r} - \frac{\lambda_\phi v\cos(\gamma)\sin(\psi)}{r} + \lambda_r v\sin(\gamma)\end{aligned} \tag{A.9}$$

Eq. (A.8) and Eq. (A.9) can be algebraically combined. Adding Eq. (A.9) to v times Eq. (A.8) yields

$$\begin{aligned}0 = \frac{\cos(\phi)}{r^4 v}\Big(\sin(\psi)\left(\lambda_\gamma\sin(\gamma)\sin(\phi)\left(-6J_2\mu R_p^2 - 2r^5\omega^2\right) + 2\lambda_\psi r^4 v\omega\tan(\gamma)\right) \\ + \cos(\psi)\left(\lambda_\psi\sec(\gamma)\sin(\phi)\left(6.J_2\mu R_p^2 + 2.r^5\omega^2\right) + 2\lambda_\gamma r^4 v\omega\right)\Big) \\ + \frac{\lambda_\gamma\cos(\gamma)}{r^4 v}\left(\mu\left(9J_2 R_p^2\sin^2(\phi) - 3J_2 R_p^2 - 2r^2\right) + 2r^5\omega^2\cos^2(\phi)\right) + 2\lambda_\psi\omega\sin(\phi)\end{aligned} \tag{A.10}$$

There are potentially many ways in which Eq. (A.10) can mathematically equal zero. For instance, the term $2\lambda_\psi\omega\sin(\phi)$ may necessitate either λ_ψ or ϕ to equal zero. The latter case is physically possible over the finite time interval $[t_1, t_2]$ where the latitude of the aerocapture trajectory remains equatorial. To keep Eq. (A.10) equal to zero, $\gamma = \pm 90°$ and $\psi = \pm 90°$ over the same time interval. However, such angles would not be physically achievable with an aerocapture trajectory.

Although other achievable solutions to Eq. (A.10) may exist, they are not obvious to obtain analytically. A potentially achievable solution on the singular arc is to have λ_γ and

λ_ψ both equal zero over time interval $[t_1, t_2]$. Substituting λ_γ and λ_ψ constants expressions into Eq. (A.8) yields

$$0 = -\lambda_r \sin(\gamma) - \frac{\lambda_\theta \cos(\gamma)\cos(\psi)\sec(\phi)}{r} + \frac{\lambda_\phi \cos(\gamma)\sin(\psi)}{r} \tag{A.11}$$

Like Eq. (A.10), Eq. (A.11) has numerous mathematical solutions. A potentially achievable solution on the singular arc is to have $\lambda_\theta = \lambda_r = \lambda_\phi = 0$ over time interval $[t_1, t_2]$. Given this and the previous solution, the co-state vector on the singular arc may become $\vec{\lambda} = \begin{bmatrix} \lambda_r & \lambda_\theta & \lambda_\phi & \lambda_V & \lambda_\gamma & \lambda_\psi \end{bmatrix}^T = \vec{0}$. Since the co-state differential equations have linear relationship with the co-state vector components and the co-state vector is continuous over time domain $[t_0, t_f]$, the resulting co-state vector integrated over this time domain will equal zero. Having a zero co-state vector over this time domain is a contradiction of the Maximum Principle which states that the co-state vector is non-zero. The cause for this contradiction is the assumption of a singular arc in the optimal solution and assumption of this particular solution to Eq. (A.10) and Eq. (A.11). **As a result, the singular arc optimal control solution for DM is shown to potentially not exist.**

A.0.2 Direct Force Control

From the derivation in 2.172, the singular optimal control for angle of attack occurs when the switching function equals zero. From Eq. (2.170), this condition necessitates that $\lambda_\gamma(t) \equiv 0$ in $[t_1, t_2]$. Consequently, $\dot{\lambda}_\gamma = 0$ in $[t_1, t_2]$. Substituting $\lambda_\gamma = \dot{\lambda}_\gamma = 0$ into Eq. (A.6) yields

$$
\begin{aligned}
0 = -\lambda_v \Bigg(& -\frac{\mu\cos(\gamma)\left(\frac{J_2 R_p^2\left(1.5-4.5\sin^2(\phi)\right)}{r^2}+1\right)}{r^2} - \frac{3J_2\mu R_p^2\sin(\gamma)\sin(\psi)\sin(\phi)\cos(\phi)}{r^4} \\
& + r\omega^2\cos(\phi)(\cos(\gamma)\cos(\phi)-\sin(\gamma)\sin(\psi)\sin(\phi)) \Bigg) \\
& - \frac{\lambda_\psi}{v}\Bigg(\frac{\alpha A C_{L_\alpha}\rho v^2\tan(\gamma)\sec(\gamma)\sin(\sigma)}{2m} - \frac{A\beta C_{Q_\beta}\rho v^2\tan(\gamma)\sec(\gamma)\cos(\sigma)}{2m} \\
& + \frac{3J_2\mu R_p^2\tan(\gamma)\sec(\gamma)\cos(\psi)\sin(\phi)\cos(\phi)}{r^4} + r\omega^2\tan(\gamma)\sec(\gamma)\cos(\psi)\sin(\phi)\cos(\phi) \\
& - \frac{v^2\sin(\gamma)\cos(\psi)\tan(\phi)}{r} + 2v\omega\sec^2(\gamma)\sin(\psi)\cos(\phi)\Bigg) \\
& + \frac{\lambda_\theta v\sin(\gamma)\cos(\psi)\sec(\phi)}{r} - \frac{\lambda_\phi v\sin(\gamma)\sin(\psi)}{r} - \lambda_r v\cos(\gamma)
\end{aligned}
\tag{A.12}
$$

The zero value of the Hamiltonian can be utilized. Setting Eq .(A.1) equal to zero, expanding, and substituting $\lambda_\gamma = 0$ yields

$$
\begin{aligned}
0 = \lambda_v \Bigg(& -\frac{\mu\sin(\gamma)\left(\frac{J_2 R_p^2\left(1.5-4.5\sin^2(\phi)\right)}{r^2}+1\right)}{r^2} - \frac{AC_D\rho v^2}{2m} \\
& + \frac{3J_2\mu R_p^2\cos(\gamma)\sin(\psi)\sin(\phi)\cos(\phi)}{r^4} \\
& + r\omega^2\cos(\phi)(\cos(\gamma)\sin(\psi)\sin(\phi)+\sin(\gamma)\cos(\phi)) \Bigg) \\
& + \frac{\lambda_\psi}{v}\Bigg(\frac{\alpha A C_{L_\alpha}\rho v^2\sec(\gamma)\sin(\sigma)}{2m} - \frac{A\beta C_{Q_\beta}\rho v^2\sec(\gamma)\cos(\sigma)}{2m} \\
& + \frac{3J_2\mu R_p^2\sec(\gamma)\cos(\psi)\sin(\phi)\cos(\phi)}{r^4} + r\omega^2\sec(\gamma)\cos(\psi)\sin(\phi)\cos(\phi) \\
& + \frac{v^2\cos(\gamma)\cos(\psi)\tan(\phi)}{r} + 2v\omega(\tan(\gamma)\sin(\psi)\cos(\phi)+\sin(\phi))\Bigg) \\
& + \frac{\lambda_\theta v\cos(\gamma)\cos(\psi)\sec(\phi)}{r} - \frac{\lambda_\phi v\cos(\gamma)\sin(\psi)}{r} + \lambda_r v\sin(\gamma)
\end{aligned}
\tag{A.13}
$$

Eq. (A.12) and Eq. (A.13) can be algebraically combined. Adding $cos(\gamma)$ times Eq. (A.13) to $sin(\gamma)$ times Eq. (A.12) yields

$$
\begin{aligned}
0 = & \frac{\cos(\gamma)}{2m}\left(\lambda_\psi m\omega\sin(\phi) - AC_D\lambda_v\rho v^2\right) \\
& + \frac{\cos(\phi)}{mr^4}\left(r^3 v\sec(\phi)\left(\frac{1}{2}\alpha AC_{L_\alpha}\lambda_\psi\rho r\left(1-\tan^2(\gamma)\right)\sin(\sigma) - \lambda_\phi m\sin^2(\gamma)\sin(\psi)\right)\right. \\
& \qquad + m\sin(\psi)\left(\lambda_v\sin^2(\gamma)\sin(\phi)\left(3J_2\mu R_p^2 + r^5\omega^2\right) + 2\lambda_\psi r^4\omega\sin(\gamma)\right. \\
& \qquad \left.\left. - 2\lambda_\psi r^4\omega\tan(\gamma)\sec(\gamma)\right)\right) + \frac{A\beta C_{Q_\beta}\lambda_\psi\rho v\sec^2(\gamma)\cos(\sigma)}{2m} \\
& + \frac{(\cos(\psi)\cos(\phi))}{r^4 v}\left(\lambda_\psi\cos(2\gamma)\sec^2(\gamma)\sin(\phi)\left(3J_2\mu R_p^2 + r^5\omega^2\right) + \lambda_\theta r^3 v^2\sin^2(\gamma)\sec^2(\phi)\right. \\
& \qquad \left. + \lambda_\psi r^3 v^2\tan(\phi)\sec(\phi)\right) \\
& + \frac{\cos^2(\gamma)}{r^4}\left(\sin(\psi)\left(\lambda_v\sin(\phi)\cos(\phi)\left(3J_2\mu R_p^2 + r^5\omega^2\right) - \lambda_\phi r^3 v\right) + \lambda_\theta r^3 v\cos(\psi)\sec(\phi)\right)
\end{aligned}
\tag{A.14}
$$

There are potentially many ways in which Eq. (A.14) can mathematically equal zero. One way is to make the individual components in the addition equal zero. For instance, to make the term $\frac{A\beta C_{Q_\beta}\lambda_\psi\rho v\sec^2(\gamma)\cos(\sigma)}{2m}$ equal to zero, λ_ψ must equal zero for non-zero β and zero σ. Having $\gamma = \pm 90°$ and $\phi = \pm 90°$ would also make Eq. (A.14) equal to zero. The latter case is physically possible over the finite time interval $[t_1, t_2]$ where the latitude of the aerocapture trajectory remains polar but the former case would not be physically achievable with an aerocapture trajectory.

Another possible solution is having $\phi = \pm 90°$, $\psi = \pm 90°$, $\lambda_\phi = 0$, $\lambda_\psi = 0$, and $\lambda_v = 0$ over the finite time interval $[t_1, t_2]$. This would make their corresponding time derivatives equal to zero. Using Eq. 2.41 for $\dot{\phi}$ and Eq. 2.59 for $\dot{\psi}$, the singular arc solution would require $\gamma = \pm 90°$ and $\beta = 0$. Using the reasoning as the previous solution, this potential solution would not be physically achievable.

As one can see, there are potentially infinitely many mathematical solutions to Eq. (A.14) with some possibly being physically realizable. However, they are not obvious to obtain analytically. A potentially achievable solution on the singular arc is to have λ_v, λ_θ, λ_ϕ, and λ_ψ all equaling zero over time interval $[t_1, t_2]$. The case in which $\lambda_\psi = 0$ corresponds to the singular optimal control for side-slip angle as denoted by Eq. (2.171). This indicates that both angle of attack and side-slip angle are on their respective singular arcs over the same time domain, given this assumed solution. Substituting these constants into Eq. (A.12) yields

$$0 = -\lambda_r v \cos(\gamma) \tag{A.15}$$

Due to physical significance for Eq. (A.15) to remain zero along the interval $[t_1, t_2]$, $\lambda_r = 0$. Aggregating all necessary co-state variable expressions, the co-state vector on the singular control arc becomes $\vec{\lambda} = \begin{bmatrix} \lambda_r & \lambda_\theta & \lambda_\phi & \lambda_V & \lambda_\gamma & \lambda_\psi \end{bmatrix}^T = \vec{0}$. Since the co-state differential equations have linear relationship with the co-state vector components and the co-state vector is continuous over time domain $[t_0, t_f]$, the resulting co-state vector integrated over this time domain will equal zero. Note that this same result would be achieved if side-slip angle singular arc condition, $\lambda_\psi = \dot{\lambda}_\psi = 0$ is assessed and expanded using the same approach and assumed zero-costate solutions. Having a zero co-state vector over this time domain is a contradiction of the Maximum Principle which states that the co-state vector is non-zero. The cause for this contradiction is the assumption of a singular arc in the optimal solution and the assumption of this particular solution to Eq. (A.14) and Eq. (A.12). **As a result, the singular arc optimal control solution for DFC is shown to potentially not exist.**

VITA

Rohan Gajanan Deshmukh

Rohan Deshmukh is a doctoral candidate at Purdue University. His research interests include guidance, navigation, and control of planetary aeroassist/EDL vehicles, mission design, and systems engineering. He has previously interned at the National Aeronautics and Space Administration Langley Research Center in the Atmospheric Flight and Entry Systems Branch where he worked on planetary aerocapture mission studies. Since 2020, he is employed by Analytical Mechanics Associates working at NASA Langley as a flight mechanics engineer. His hometown is Fairfax, Virginia.

Education

Ph.D. Aeronautics and Astronautics, Purdue University, May 2021. Thesis title: "System Analysis of a Numerical Predictor-Corrector Aerocapture Guidance Architecture."

M.S. Aeronautics and Astronautics, Purdue University, May 2018.

B.S. Aerospace Engineering, Georgia Institute of Technology, May 2016.

Journal Publications

R.G. Deshmukh, D.A. Spencer, and S. Dutta, "Investigation of direct force control for aerocapture at Neptune," *Acta Astronautica*, vol. 175, no. 1, pp. 375-386, 2020.

R.G. Deshmukh, D.A. Spencer, and S. Dutta, "Flight control methodologies for Neptune aerocapture trajectories," *Journal of Spacecraft and Rockets*, submitted, 1 March, 2021.

J.V. Cabrera, R.G. Deshmukh, and D.A. Spencer, "Development of an Aerodynamics Database for a Conceptual Morphable Entry System," *Journal of Spacecraft and Rockets*, submitted, 9 March, 2021.

Conference Publications

R.G. Deshmukh, S. Dutta, and D.A. Spencer, "Investigation of Direct Force Control for planetary aerocapture at Neptune," 29th AAS/AIAA Space Flight Mechanics Meeting, AAS 19-212, Ka'anapali, HI, 13-17 January, 2019.

R.G. Deshmukh, D.A. Spencer, and J.M. Longuski, "Derivation of Atmospheric Flight Equations of Motion using Lagrangian Dynamics and its Application to Aerocapture," AIAA SciTech 2020 Forum, AIAA 2020-1742, Orlando, FL, 6-10 January, 2020.

R.G. Deshmukh, D.A. Spencer, and S. Dutta, "Flight control methodologies for Neptune aerocapture trajectories," 31st AAS/AIAA Space Flight Mechanics Meeting, AAS 21-202, Virtual, 1-4 February, 2021.

R.G. Deshmukh, J.V. Cabrera, and D.A. Spencer, "SmallSat aerocapture using a generalized numerical predictor-corrector guidance architecture," AIAA SciTech 2021 Forum, AIAA 2021-1066, Virtual, 11-15 January, 2021.

J.V. Cabrera, R.G. Deshmukh, and D.A. Spencer, "Aerodynamic Database Development using a Bridging Function for a Conceptual Morphable Entry System," AIAA SciTech 2021 Forum, AIAA 2021-0935, Virtual, 11-15 January, 2021.